



*Ministero dell'Università
e della Ricerca*



*Università degli Studi di
Palermo*

DIN
Dipartimento di
Ingegneria Nucleare
Università di Palermo

*Dipartimento di
Ingegneria Nucleare*

Suspension phenomena in solid-liquid agitated systems

PhD thesis of **Alessandro Tamburini**

Supervisors

Prof. Giorgio Micale

Prof. Michele Ciofalo

Prof. Alberto Brucato

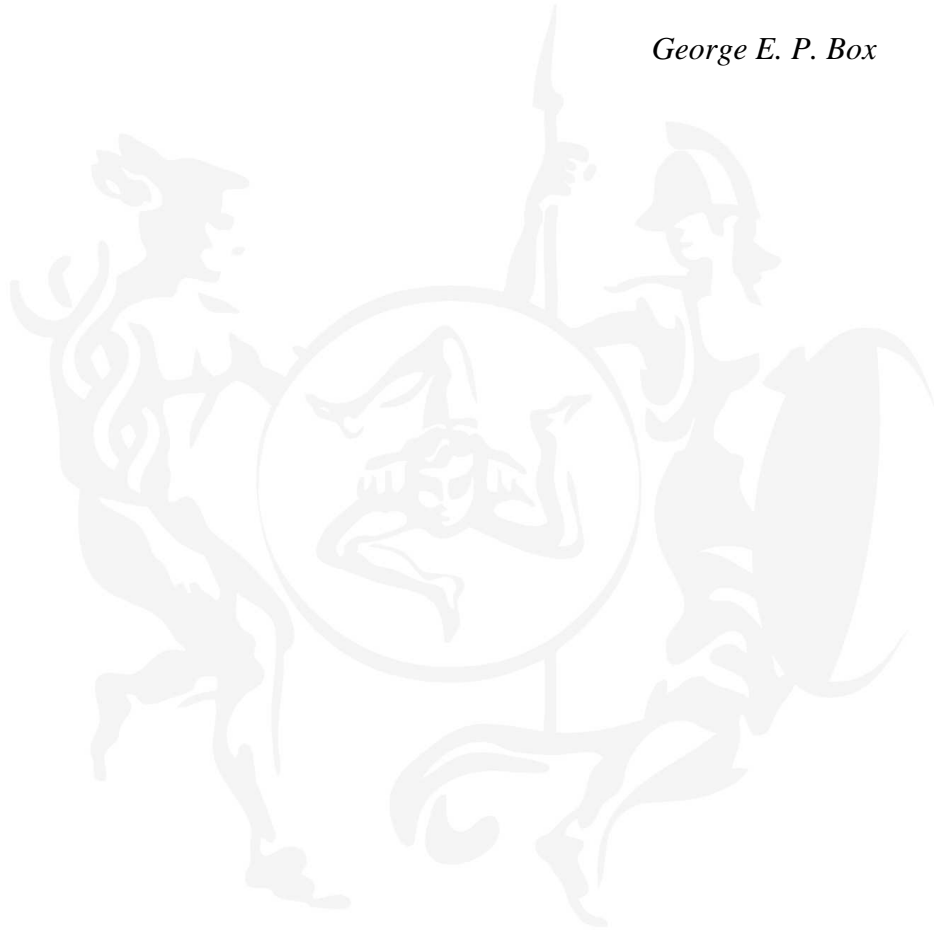
Head of the PhD board

Prof. Francesco Castiglia

Ciclo XXII: 2008-2010

All models are wrong, but some are useful.

George E. P. Box



INTRODUCTION	9
SOLID-LIQUID SUSPENSION IN STIRRED TANKS	13
Mixing fundamentals	13
States of suspension	16
Nomenclature	18
PART I: EXPERIMENTAL	23
Introduction	23
CHAPTER 1	25
LASER SHEET IMAGE ANALYSIS TECHNIQUE (LSIA)	25
1.1 Abstract	25
1.2 Literature review	25
1.2.1 Invasive measurement techniques	26
1.2.2 Non-invasive measurement techniques	32
1.3 Experimental information	44
1.3.1 Fluorescent particles	50
1.4 LSIA fundamentals	52
1.4.1 The grey-level parameter	55
1.4.2 The number of images to acquire and the median filter	56
1.4.3 The mean and the minimum particle area: A_{mean} and A_{min}	59
1.4.4 Light reflection issues	59
1.4.5 Shifting from a probability distribution map to a normalized concentration map	62
1.4.6 Reproducibility	64
1.5 LSIA application: dilute suspensions in unbaffled vessels	65
1.5.1 Introduction	65
1.5.2 Attractors for solid particles	66

1.5.3 Top-covered unbaffled tank stirred by standard Rushton Turbine with a clearance $C=T/3$: toroidal attractors for solid particles	67
1.5.4 Top-covered unbaffled tank stirred by a marine propeller with a clearance $C=T/4$.	76
1.6 Final remarks	81
1.7 Nomenclature	82
CHAPTER 2	85
STEADY CONE RADIUS METHOD (SCRM)	85
2.1 Abstract	85
2.2 Literature review	86
2.3 Experimental information	88
2.3.1 Investigated systems	88
2.3.2 Steady Cone Radius Method (SCRM)	93
2.3.3 Power consumption assessment apparatus	95
2.4 Just suspended speed (N_{js}) measurements	97
2.4.1 N_{js} dependence on solid concentration B	97
2.4.2 N_{js} dependence on particle diameter d_p	99
2.4.3 N_{js} dependence on normalized relative density $\Delta\rho/\rho_L$	101
2.4.4 N_{js} dependence on fluid kinematic viscosity ν	102
2.5 Power Number (N_p) measurements	105
2.6 Scale-up criterion assessment	111
2.7 N_{js} correlation for top-covered unbaffled vessels	113
2.8 Conclusive remarks	115
2.9 Nomenclature	116
PART II: MODELLING AND SIMULATION	119
Introduction	119
CHAPTER 3	121

DENSE OFF-BOTTOM SUSPENSION DYNAMICS	121
3.1 Abstract	121
3.2 Literature review	121
3.3 Physical system	126
3.4 CFD modelling	128
3.4.1 Inter-phase Drag Force and Drag Coefficient	131
3.4.2 Computational approaches and numerical simulations	135
3.5 Results and discussion	146
3.6 Final remarks	154
3.7 Nomenclature	155
CHAPTER 4	157
INCOMPLETE SUSPENSION REGIME MODELLING	157
4.1 Abstract	157
4.2 Literature review	158
4.3 Experimental information	164
4.3.1 Pressure Gauge Technique (PGT) apparatus and fundamentals	165
4.3.2 Snapshots of the investigated vessel	167
4.4 Numerical modelling	168
4.4.1 Equations of motion	168
4.4.2 Inter-phase transfer terms	170
4.4.3 Turbulence closure	171
4.4.4 Drag Coefficient C_D	175
4.5 Other tested modelling procedures	178
4.5.1 Dense Particle Effect approach (DPE)	178
4.5.2 Homogeneous k- ϵ approach (Turb-Turb)	178
4.5.3 Modified $C_{a\beta}$ approach (Mod- $C_{a\beta}$)	180
4.6 Numerical details	181
4.6.1 Discretization of the computational domain	181
4.6.2 Initial conditions, time step and number of iterations	183
4.6.3 Excess Solid Volume Correction Algorithm (ESVC)	185
4.7 Unsuspended Solid Criterion (USC)	190

4.8 Results and analysis	191
4.8.1 PGT curves	192
4.8.2 Concentration maps	194
4.8.3 Velocity vector plots	195
4.8.4 Time step dependence	197
4.8.5 Sliding Grid versus Multiple Reference Frames	198
4.8.6 Initial conditions	200
4.8.7 Grid dependence analysis	201
4.8.8 Solid loading	204
4.8.9 Particle diameter and drag coefficient	205
4.8.10 Alternative modelling approaches	206
4.8.11 Snapshots of the investigated vessel	208
4.8.12 Validation with literature data	216
4.9 Conclusions	224
4.10 Nomenclature	225
 CHAPTER 5	 229
 N_{JS} PREDICTION	 229
5.1 Abstract	229
5.2 Literature review	230
5.2.1 Vessel-bottom observation method or Zwietering's method	231
5.2.2 Liquid free surface observation method	233
5.2.3 Particle bed height method	233
5.2.4 Cloud height method	234
5.2.5 Power Number method	235
5.2.6 Mixing Time method	236
5.2.7 Radioactive tracer method	237
5.2.8 Local Particle Concentration method	238
5.2.9 Acoustic Emission method	239
5.2.10 Variation Coefficient method	240
5.2.11 Pressure Gauge Technique method	241
5.2.12 Large scale methods	243
5.2.13 Theoretical methods	244
5.2.14 Computational Fluid Dynamics method	245
5.3 Numerical modelling and details	248
5.4 Case Description and Analysis of Results	249
5.4.1 Cloud height method	249
5.4.2 Particle Bed Height method	254

5.4.3 Power Number method	256
5.4.4 Local Particle Concentration method	261
5.4.5 Variation Coefficient method	265
5.4.6 Mak (1992) and Hosseini et al. (2010b) or Intersection method	268
5.4.7 Wang et al. (2004) or Particle Axial Velocity method	271
5.4.8 Kee and Tan (2002) or Transient r_β Profile method	277
5.4.9 Unsuspended Solid Criterion method	282
5.4.10 Sufficient Suspension Speed Prediction	284
5.5 Final remarks	286
5.6 Nomenclature	287
CONCLUSIONS	291
REFERENCES	297
ACKNOWLEDGMENTS	322

INTRODUCTION



INTRODUCTION

Mechanically agitated tanks are widely employed in process industry: in particular in food, chemical, pharmaceuticals, mining, oil and water remediation industry, etc.

One of the more common and notable application of stirred tanks is represented by the suspension of solid particles in a liquid phase, unit operation which concerns crystallization, precipitation, dissolution, adsorption, ionic exchange processes and chemical reactions with heterogeneous catalysis.

In order to successfully carry out these processes it is necessary to guarantee a suitable suspension degree of particles in the liquid phase. A sound understanding of the mechanisms of suspension and dispersion of particles is, hence, important for a rational design of mechanically agitated vessels.

The problem of suspending solids in liquids by mechanical agitation requires the knowledge of:

- the minimum impeller speed necessary to suspend all particles in the vessel, so that all the particle area is available for mass transfer which represents one of the most important design requirements. Operating a solid-liquid system at impeller speeds much below the minimum for complete off-bottom suspension could be detrimental to chemical reaction and mass transfer being particles non-uniformly exposed to the liquid;
- the conditions for creating, if possible, and maintaining a relatively homogeneous suspension, particularly when this is used to prepare materials for successive processes. However, a significant power input enhancement is required for attaining a homogeneous suspension regime with respect to complete suspension conditions. Therefore, most industrial apparatuses are designed to operate at the minimum suspension speed for complete off-bottom suspension which is often considered sufficient to satisfy the process requirements as well as guarantee energy savings;

- the fluid-particle mechanics within the stirred vessels by means of information on the local characteristics of the solid-liquid agitated suspension, such as local particle-liquid slip velocity and particle flow behaviour.

Even though solid-liquid stirred tanks are largely encountered in the process industries, nowadays there is still a poor understanding of the complex phenomenon of particle suspension in a turbulent liquid mechanically agitated by a stirrer. A lot of scientific efforts have been devoted to this issue, but resolute results have not been provided yet. This poor knowledge of suspension dynamics generates a large uncertainty in the design of these solid-liquid contactors. The total absence of predictive models on suspension phenomenon is close linked to the lack of suitable objective methods for the evaluation of the main design parameters for stirred tanks. This lack of design certainties determines direct and strong economical repercussions as design errors cause economical costs which are estimated to be of some milliard dollars only in the United States every year (Smith, 1990).

The present PhD thesis starts from this background with the final goal of contributing to increase the understanding of such unit operation which is so frequently employed and not so well understood.

Two different methodologies were adopted to investigate suspension phenomena in solid-liquid agitated systems: i) experimental studies, ii) modelling via *Computational Fluid Dynamics (CFD)* techniques. These two complementary investigation approaches started in parallel with the same common aim.

The experimental studies will be detailed in Part I of the present PhD thesis, CFD modelling efforts will be minutely presented throughout Part II.

In the following the content of the present PhD thesis will be briefly summarized, in order to help the reader to easily identify the topics investigated.

Part I

Chapter 1 presents the design and development of an innovative measurement technique which is non-intrusive and able to directly provide 2-D concentration maps at acceptable costs and in reasonable times.

Chapter 2 focuses on the evaluation of unbaffled stirred tanks as suitable devices to successfully perform solid-liquid mixing operations.

Part II

Chapter 3 deals with the modelling of an off-bottom solid-liquid suspension start-up until steady state is attained.

Chapter 4 aims at the development of a novel CFD simulation approach able to reliably predict the suspension of unsuspended solid particles at any agitation speed below and up to the complete suspension speed.

Chapter 5 focuses on the proposition of a CFD-aided reliable and universally accepted criterion for solid-suspension which could constitute a powerful innovative tool for solid-liquid stirred contactor design and operation.

SOLID-LIQUID SUSPENSION IN STIRRED TANKS

Mixing fundamentals

In the process industry, fluid agitation within mechanically agitated systems is performed by means of different types of stirrers, depending on the specific aim to fulfil.

Typical aims of mechanical agitation are listed in the following:

- suspension of solid particles;
- blending of immiscible liquids;
- dispersion of gas in liquids;
- dispersion of both gas and particles in liquids;
- heat exchange promotion.

It is important to underline that the choice of a suitable impeller type is fundamental for the success of the process to be carried out. Agitators can be divided into two main classes:

- radial flow impellers, which mainly generate streams in the radial and tangential directions;
- axial flow impellers, which, in addition to the tangential components, generate streams mainly directed along the impeller axis.

In general, it is possible to state that, at the same mechanical power requirements, axial impellers provide a higher movimentation of fluids (i.e. higher pumping capacity), while the radial ones determine, in regions close to themselves, a high turbulence (and consequently a smaller overall circulation in the tank). Because of this feature, the use of radial impellers is particularly suitable for processes involving the dispersion of immiscible phases, where it is necessary to maximize the interfacial area between phases (*shear rate controlled processes*). Conversely, axial impellers are more suitable for those processes where convective motion is essential,

that is processes where the operation effectiveness is closely linked to fluid movimentation (*bulk motion controlled processes*).

The particular flow field that establishes within a stirred tank depends not only on impeller type, but also on fluid physical properties, tank size and shape, baffles presence and type, etc. The most commonly employed tank has a cylindrical shape, it is equipped with four lateral baffles, it is provided with a flat or rounded bottom and it is equipped with one or more impellers. In this regard, in order to avoid any dependence on geometrical features, a “*standard geometry*” was codified and accepted in literature (Fig. 1).

Fluid velocity has three components in each point of the vessel: the *radial* component acts perpendicularly to impeller axis, the *axial* component acts in a direction parallel to the same axis and the *circumferential* (or *tangential* or *azimuthal*) component acts in the direction of the tangent to the circumference coaxial to the impeller shaft, which passes through the considered point. The tangential flux generates circular trajectories around the shaft and, in absence of baffles, creates on the liquid free surface a vortex whose deepness depends on the impeller speed. In addition, if a vortex is present, the low relative velocities between impeller and fluid result in a small pumped flow rate, with a consequent poor mixing of tank contents. Because of this reason, baffles are commonly employed: generally, four equally spaced baffles located perpendicularly on the vessel lateral wall are employed.

The assessment of the exact mechanical power which has to be conferred to the impeller is an issue of crucial importance. In this regard, the dimensionless *Power Number* N_p is defined as:

$$N_p = \frac{P}{\rho \cdot N^3 \cdot D^5} \quad (1)$$

where ρ is liquid density, P is mechanical power, D is impeller diameter and N is impeller speed.

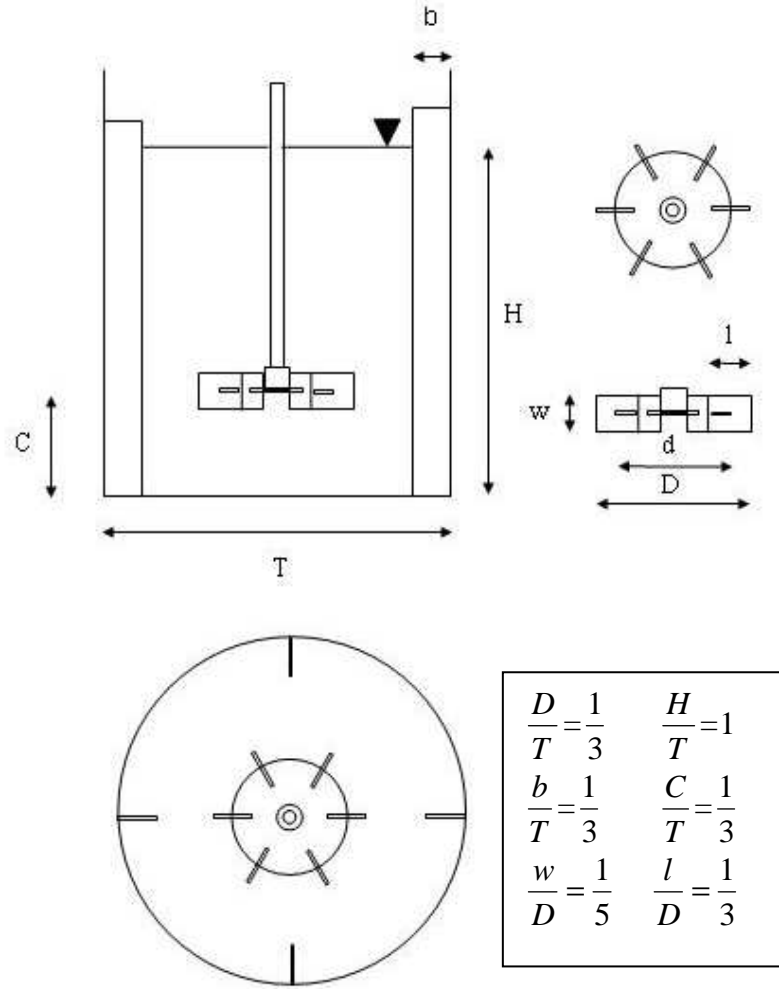


Fig. 1: “Standard geometry” stirred tank.

When blending processes are to be carried out, it is important to ensure that the entire fluid volume circulates through the impeller (which in this case can be assimilated to a pump) in reasonable times as a function of the particular process considered. In this regard, another dimensionless number can be introduced named *Flow Number* or *Pumping Number* N_Q :

$$N_Q = \frac{Q}{N \cdot D^3} \quad (2)$$

where Q is the fluid flow rate pumped by the impeller. In the case of radial impellers, Q is the flow rate crossing through the cylindrical surface swept by the tip of impeller blades.

Theoretically (not shown here for the sake of brevity) it is possible to demonstrate that, for a given impeller type and configuration, both N_p and N_Q should be expected to be functions of the Reynolds and Froude numbers, which for stirred tanks are defined as:

$$\text{Re} = \frac{\rho N D^2}{\mu} \quad \text{Fr} = \frac{N D^2}{g} \quad (3)$$

where μ is fluid viscosity and g is gravity acceleration. Notably the dependence on Fr vanishes when the liquid free surface either does not exist (covered vessels entirely filled by the liquid) or is reasonably flat (as occurs in most baffled vessels). In such cases, when the regime is fully turbulent (i.e. when $\text{Re} > 10000$), both N_p and N_Q approach constant values which are specific for a given impeller type and system geometry.

States of suspension

For measuring the performance of solid suspension equipment, it is necessary to know the different states of suspension occurring in a stirred vessel with respect to the increasing impeller speed. Independently on the stirred tank geometrical configuration adopted for particle suspension, three possible suspension regimes can be identified. They are listed in the following from the lowest to the highest power input (Fig. 2).

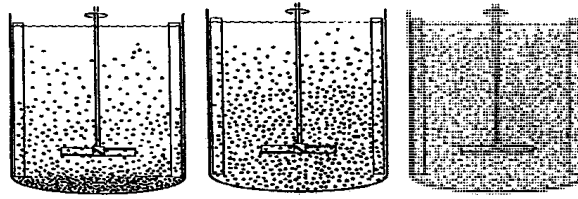


Fig. 2: States of suspension. From the left: *Partial Suspension Conditions*, *Complete Suspension Conditions*, *Homogeneous Suspension Conditions*.

Filletting regime or Partial Suspension Regime

It generally occurs at low impeller speeds. Solids are partially suspended, the motionless ones stay still on the vessel bottom as sediments (*fillets*). The positions where fillets are present depend on the flow patterns.

Complete Suspension Regime

Complete suspension conditions can be considered as achieved when all particles are suspended. At this stage the applied power input is sufficient to guarantee that no particles rest on the bottom for more than 1 or 2 seconds. Concentration gradients as well as a free liquid layer on the top of the vessel could however be present.

This regime can be divided into two sub-regimes.

- *Complete on-bottom Suspension Conditions*: no particle rests on the bottom for more than 1-2 seconds; some are lift off while others roll on vessel bottom;
- *Complete off-bottom Suspension Conditions*: no particle stays on the bottom for more than 1-2 seconds.

Homogeneous Suspension Regime

Homogeneous suspension conditions can be considered as achieved when particle concentration and distribution are constant throughout the vessel and no concentration gradients are observable anywhere. The achievement of homogeneous

conditions requires a large increase of impeller speed and power inputs with respect to complete suspension regime.

It is not possible to attain this regime for all cases: systems where gravitational force highly dominates over the drag force cannot achieve homogeneous conditions (Mersmann et al., 1988; Ochieng and Lewis, 2006a).

It is worth noting that in the incomplete suspension regime the liquid phase in contact with the particles inside the stationary fillets is not efficiently replaced; as a consequence transport phenomena are not suitably promoted and the solid-liquid apparatus performance decreases.

Impeller speeds higher than that corresponding to complete suspension conditions can lead to higher homogeneity degree, but this increase is typically followed only by moderate increases of overall process performance. Conversely, increasing impeller speed implies a dramatic increase of power requirements, as power increases with the cube of impeller speed.

According to these considerations, the assessment of complete suspension conditions and in particular of the minimum impeller speed able to guarantee this regime is a problem of crucial importance for stirred tank design. In most industrial cases, the minimum agitation speed for complete off-bottom suspension (N_{js}) can be regarded as a reference agitation condition that gives rise to an optimal compromise between mass transfer process promotion and power requirements.

Theoretical and experimental investigations on suspension phenomena of solid particles in stirred tanks are complex because of the large variety of both the properties of particles to suspend and typologies of stirred tank (impeller and tank types and/or impeller-tank configurations).

Nomenclature

b	<i>baffle width, m</i>
C	<i>impeller clearance, m</i>
D	<i>impeller diameter, m</i>

d	<i>impeller disc diameter, m</i>
H	<i>fluid height in the vessel, m</i>
l	<i>impeller blade width, m</i>
N	<i>impeller speed, RPM or RPS</i>
N_{js}	<i>just suspended agitation speed, RPM or RPS</i>
N_P	<i>Power Number, (-)</i>
N_Q	<i>Pumping Number, (-)</i>
P	<i>power consumption, Watt</i>
Q	<i>flow rate pumped by the impeller, (-)</i>
T	<i>tank diameter, m</i>
w	<i>impeller blade thickness, m</i>

Greek letters

α	<i>liquid phase</i>
β	<i>solid phase</i>
ρ	<i>density, kg/m³</i>
μ	<i>viscosity, Pa m</i>



PART I: EXPERIMENTAL

PART I: EXPERIMENTAL

Introduction

Many experimental studies have been devoted so far to the investigation of suspension phenomena in solid-liquid agitated systems. Notwithstanding all the scientific efforts carried out by researchers in order to enhance the knowledge degree of this unit operation, some dark points still exist.

Several experimental techniques have been proposed and applied over the decades to investigate solid-liquid agitated systems, but all of them are affected by a number of drawbacks which significantly influence their reliability and/or applicability.

On the other hand, most studies carried out up today have dealt with baffled stirred tanks as they are considered more efficient mixers than tanks unprovided of baffles (*unbaffled*). In a number of industrial cases, the presence of baffles can be undesirable thus leading to an increasing interest towards unbaffled stirred tanks. Also, recent studies have demonstrated that at a given power input, higher mass transfer coefficients can be obtained inside solid-liquid unbaffled stirred tanks than inside corresponding baffled systems.

The main aim of this section is to clarify and to develop these points providing also an original contribution to the increase of understanding of this unit operation.

Particularly, a novel technique to investigate solid-liquid suspension within stirred vessels was developed and suitably applied to solid-liquid dispersions in an unbaffled stirred tank provided with a top-cover.

Moreover, a purposely prepared method was proposed to assess objective measurements of minimum impeller speeds for on-bottom suspension in top-covered unbaffled tanks stirred by a radial impeller. Finally, the economical advantage of

performing solid-liquid suspension processes within unbaffled stirred tanks was addressed and critically discussed.

These aspects are minutely developed and described in the following two chapters.

CHAPTER 1

LASER SHEET IMAGE ANALISYS TECHNIQUE (LSIA)

1.1 Abstract

Detailed knowledge of the local particle-fluid dynamics is often the key to get effective design and scale-up of solid-liquid stirred reactors. The availability of experimental information on particle distribution inside stirred tanks is a topic of great importance in several industrial applications such as catalysis and polymerization. The measurement of solid particle distribution in turbulent multiphase flow is not simple and the development of suitable measurement techniques is still an open problem in chemical engineering research.

In this chapter a novel non-invasive optical technique for measuring particle concentration distributions in solid-liquid systems is critically presented and described. The technique makes use of a laser sheet, a high sensitivity digital camera for image acquisition and a Matlab procedure for post-processing the acquired images. It is able to provide solid concentration distribution maps on the laser sheet plane.

Application examples are presented for the case of an unbaffled stirred vessel provided with a cover in order to avoid vortex formation: experimental results are presented and discussed.

1.2 Literature review

Stirred vessels are the most commonly employed apparatuses in the process industries for mixing operations. It is very difficult to find an industrial chemical process not involving the mixing of one or more phases. Particularly, suspension of solid particles in liquids is largely employed in a number of applications. Due to the importance of this unit operation, several investigations aimed at suitably quantifying stirred tank performance have been carried out over the decades. The

rational design and operation of these tanks remain a challenging problem because of the intrinsic complexity of the 3-D circulating and turbulent multiphase flow in the reactor. A deep understanding of the mechanisms of suspension and dispersion of solids in liquids requires the knowledge of the minimum agitation speed necessary to suspend all the particles in the tank and some local characteristics of the stirred suspension like solid-liquid slip velocities and solid concentration fields. In addition, the availability of reliable experimental data on particle distribution is very important for modelling purposes and CFD validation applications.

A number of different types of experimental techniques have been devoted to obtain detailed local fluid dynamics information in solid-liquid multiphase systems.

Today, in scientific literature, two macro-categories of methods for solid particle distribution assessment inside a stirred vessel exist, i.e. invasive techniques and non-invasive techniques.

1.2.1 Invasive measurement techniques

Sampling method and measurement probe techniques belong to the class of invasive measurement techniques.

The *sampling method* was the first measuring technique used for investigating solid-liquid suspensions in stirred tanks. Its best peculiarity is clearly the simplicity: it provides for taking samples withdrawal from suspensions in many different points of the stirred tank thus successively analysing and measuring their solid concentration value (McLaren White and Sumerford, 1933; Barresi and Baldi, 1987a,b; Buurman et al., 1986). The sample is withdrawn by means of a probe and of a sample-tube which have to enter inside the vessel (through holes purposely prepared in the lateral wall) to carry out such operation.

The main drawback of this method is closely linked to its intrinsic high intrusivity: the presence of a probe and of a tube inside the vessel can strongly alter the liquid flow field, interfering with the suspended particle movement and consequently compromising reliability of result. Many research efforts (MacTaggart et al., 1993; Godfrey and Zhu, 1994; Nasr-el-din et al., 1996; Kuzmanic and Kessler, 1997) showed that such methodology strongly suffers of a poor reproducibility of

results because they are highly dependent on both the shapes and the entrance of the used sampling probes. In particular Nasr-el-din et al. (1996) measured the local solids concentration in a mixing tank using both sample withdrawal and a conductivity probe (see below). Conductivity measurements were used to assess the errors associated with various sampling techniques: they examined in detail the effects of sampling tube design (tip shape, face angle and inside diameter), sampling position, bulk solids concentration and particle size on the sampling errors. Their results showed that on the impeller plane, the sample withdrawal technique provides particle concentrations lower than the right ones at the isokinetic sampling velocity. Errors relevant to sampling techniques were found to be dependent on the sample tube shape and location in the tank, especially with coarse sand particles of 1000 μm .

Finally, when sampling at right angle to the flow, sampling errors were found to increase with particle size, especially when a small diameter tube was used. Van der Westhuizen and Deglon (2006) used the sampling method to predict the critical impeller speed for solid suspensions in a pilot-scale mechanical flotation cell.

Kuzmanic and Kessler (1997) and Kondo et al. (2008) investigated floating solids suspension in a stirred tank. Kondo et al. (2008) examined the influences of diameter and impeller position on drawing from the liquid surface and on the dispersion of solid particles lighter than liquid in a vessel stirred by dual impellers. They used measurements to define the *just drawdown condition* as the state in which no lighter-than-liquid particles were floating on the liquid surface at the just suspension speed for heavier-than-liquid particles. Kuzmanic and Kessler (1997) built up a continuous wall sampling method: suspension was continuously removed using a variable speed impeller pump. Sampling were drawn by the flow being diverted into the collecting device by means of a solenoid valve controlled by a timer allowing adaptation and control of the sampling time. They investigated in detail the sampling efficiency dependence on suspension characteristics, sample tube design and sampling technique. Results showed that at complete suspension state it is practically impossible to obtain a representative sample of floating suspended particles from a mixing tank with markedly axial flow using the wall sampling

technique. In addition they stated that sampling errors can be minimized changing suspension conditions and sampling technique even if all conclusions point to the fact that this method may be applied in practice with extreme caution.

The measurement probe techniques can be grouped into three different sub-categories on the basis of the specific variable they measure, i.e. impedance, optic and acoustic techniques.

Impedance techniques (McKee et al., 1995; Ceccio and George, 1996; Brunazzi et al., 2001; Paglianti and Pintus, 2001; Micheletti et al., 2003; Brunazzi et al., 2004; Spidla et al., 2005) provide for assessing the impedance (which can be reduced to capacitance or conductance depending on the working fluid electrical properties) between two (or four, Considine and Considine, 1985; Shirhatti et al., 2006) electrodes present inside the probe by measuring the current between the electrodes at a given voltage: the value resulting depends on the local solid particle quantity met by the electric flow lines and it allows the local solid concentration calculation. Impedance techniques are extensively used for measurement of the dispersed phase in two-phase systems (Hewitt, 1978; Wang et al., 2000).

Also, impedance methods can be used for both local (Takenaka and Takahashi, 1996; Andreussi et al., 1999) and integral measurements of the phase hold-ups (Andreussi et al., 1988; Brunazzi et al., 2001). Such techniques are strongly sensitive to the local flow conditions thus requiring caution during their use. Micheletti et al. (2003) used a conductivity probe consisting of a Y-shaped Perspex body and a stainless steel handle (for robustness and minimum flow disturbance purposes). Two platinum black coated electrodes were mounted at the end of the Perspex body giving a measuring volume of a 1 cm^3 . Authors carried out in situ measurements in order to investigate impeller clearance, particle size and concentration effect on particle distribution in a standard geometry stirred vessel. Shirhatti et al. (2006) determined the minimum agitation speed for complete solid suspension using a four electrodes conductivity method. Spidla et al. (2005) provided both axial and radial local concentration profiles for the case of a moderately concentrated suspension in

a pilot plant stirred vessel concluding that the higher was the average solid concentration and the smaller were the solid particles, the more homogeneous was the suspension obtained. Authors proposed a two stainless steel electrode conductivity probe whose action volume was of 6.3 cm³. The outer electrode was formed of six parallel rods placed in the corners of a regular hexagon and conductively connected by a ring. The inner electrode consisted of a single rod placed in the centre of the former ring.

Paglianti and Pintus (2001) and later Brunazzi et al. (2004) proposed an innovative probe based on the measurement of the electrical impedance. It can measure mixing time and solid/hold up in stirred tank reactors working with high solid concentration. The main advantage of this probe concerns its complete non-intrusivity: it uses the shaft and a circular baffle support as electrodes, which can both move in axial direction. Therefore, each measurement is relevant to the horizontal section bound by the two electrodes. Also, the probe does not require particular attention for its calibration and it can be used both for laboratory-scale and industrial-scale stirred vessels.

Concerning technique limit, electrical flow lines move from an electrode towards the other, but they do not move only along the investigated section thus possibly leading to unreliable results. Clearly, such method allows to get average solid concentration profiles in the axial direction and no information on concentration radial variation are obtainable.

Optical techniques provide for the employment of photoelectric capillaries or fibre-optic probe (Lu et al., 1993; Thompson and Worden, 1997; Shan et al., 2008; Shan et al., 2008; Shan et al., 2008) or endoscopies (Angst and Kraume, 2006; Angst and Kraume, 2005; Alban et al., 2004; Lacknermeier et al., 2001) or turbidimetric analysis (Sessieq et al., 1999), all instruments and equipments (characterized by an emitter and a receiver) able to transform light scattering measurement in an indirect local particle concentration assessment.

Thompson and Worden (1997) suggested the use of a fibre-optic probe for measuring the local value of gas/liquid/solid hold-ups in a three phase magneto-

fluidized bed. Shan et al. (2008) investigated solid-liquid unbaffled vessels by using a PS-6A fiber-optic probe, composed of two bundles of quartz fibers (the one working as light projector, the other as light receiver), in order to measure solid particle concentration and collect data for CFD validation purposes.

The endoscope system proposed by Angst and Kraume (2006) is based on the principle of back scattering. The particles at the measuring point just in front of the endoscope tip are temporarily brightened by a flashlight connected to the endoscope via fibre optics. An amount of light that is proportional to the number of particles in front of the endoscope tip is scattered back into the front lens and to an attached CCD camera. The mean value of the back-scattered light intensity is calculated by a computational grey-scale analysis, such value directly corresponds to the particle concentration at the measuring point. For concentration measurements at the tank wall, the endoscope can be adjusted to be flushed with the wall thus avoiding any invasive disturbance.

Turbidimetry analysis of a particle-liquid suspension concerns the attenuation measurement of the transmitted light beam intensity due to light scattering. Sessiecq et al. (1999) adopted a sensor to evaluate the turbidity spectrum of the suspension: a polychromatic light beam is passed to the sensor by optical fibres; after this beam has crossed the sensor window, where it is scattered by the particles in suspension, the transmitted light is led again via optical fibres to a photodiode array spectrophotometer which provides the suspension turbidity. Local concentration can be deduced via turbidity measurements by means of the Mie theory (Kerker, 1969) application.

The last category of measurement probe techniques makes use of *acoustic techniques* (Alba, 1992; Alba et al., 1999; Bamberger et al., 1998; Bamberger and Greenwood, 2004). The acoustic properties of a transmitted sound beam (such as sound speed, amplitude) measured in a continuous single-phase liquid system become different if solid particles or gas bubbles are present as dispersed media. When a liquid contains such unhomogeneities, the sound wave is reflected or transmitted at the boundary of two media with different characteristic impedances.

The acoustic energy dissipates faster in an inhomogeneous medium than in a homogeneous one due to absorption and scattering which result in distinct changes in sound velocity and attenuation (Zheng and Zhang, 2004). Practically, by quantifying this attenuation that the acoustic wave undergoes while crossing the two-phase medium, it is possible to calculate the relevant dispersed phase hold-up (Chang et al., 1984).

Alba et al. (1999) developed an instrument which can measure the particle size distribution and dispersed phase concentration of samples of low contrast density, such as emulsions as well as high density contrast systems such as suspensions of rigid particles. This can be achieved both over a wide size range from 0.01 μm to 1000 μm and concentration range from 0.5% v/v to 50% v/v, dependent on the application. The technique, based on termed acoustic attenuation spectroscopy consists of propagating ultrasonic waves of a range of frequencies through the particulate system and accurately measuring the attenuation at each frequency. This attenuation spectrum can be converted to a particle size distribution and a measure of the concentration of the dispersed phase.

Bamberger and Greenwood (2004) adopted a simple single frequency ultrasonic measurement technique to monitor the progress of mixing of a silicon dioxide–water slurry in an open tank by providing real-time in-situ measurement of slurry concentration. The ultrasonic sensor consists of two parallel and coaxial transducers (a transmitter and receiver separated by 10.2 cm) suspended in the slurry. The transmitter operates by sending a swept frequency pulse (0.1–3 MHz) through the slurry to the receiver. A peak detector captures the amplitude of the received signal.

All the intrusive techniques have the intrinsic negative feature of requiring the probe presence (for sampling or measurement) inside the stirred tank: such a presence could change the system flow field and consequently alter the deduced results. Moreover, most of these methods allow only local assessments, thus requiring too much measurements as well as many interpolations among the obtained local data. In addition, stirred tanks are non-stationary systems: local

concentration varies with time thus leading to a number of measurements for the same position (with a significant increase in operation time).

However it is worth nothing that, in some industrial operating conditions, non-invasive techniques become ineffective for example because of particular physico-chemical characteristics, opaque walls (as for image analysis technique) and non stationary phenomena: some non-invasive techniques provide discrete or time-averaged information, thus resulting in an impossible statistical or spectral analysis (Boyer et al., 2002). In addition, such techniques are often very expensive or however difficult to apply.

1.2.2 Non-invasive measurement techniques

There are a number of non-intrusive techniques reported in literature, among them the following techniques will be briefly discussed:

- light techniques;
- radiation techniques;
- acoustic/ultrasonic attenuation techniques;
- Magnetic Resonance Imaging (MRI) technique;
- polarographic techniques;
- radioactive particle tracking;
- tomographic techniques.

The main non-intrusive light technique is the *light attenuation technique* (Bohnet and Niesmak, 1980; Fajner et al., 1985; Shamlou and Koutsakos, 1988; Magelli et al., 1990; Godfrey and Zhu, 1994; Montante et al., 2001; Nocentini et al., 2002). It provides for the presence of a light emitting diode as light source and a silicon photo-diode as receiver. Both of them are placed outside the vessel and they measure the attenuation that a light beam undergoes while crossing (horizontally along a chord) the vessel itself: a ray light is more adsorbed when it passes through a suspension than a poor liquid.

The results obtainable by this method are very reliable, but, they concern only the mean solid concentration along the line covered by the beam. Such particle mean

concentration measurements along the chord are considered representative of the mean concentration in the whole horizontal section as radial profiles often are fairly flat (Barresi and Baldi 1987a). Though it sometimes represents a clear approximation (as example, see Angst and Kraume, 2006) a lot of experiments would be necessary to avoid the use of too much interpolations in getting a solid concentration distribution map on the same horizontal plane.

Other light-based techniques concern the fluid flow velocity evaluation (like Particle Image Velocimetry, PIV, and Laser Doppler Anemometry, LDA) or the micro- and macro-mixing quantification (like Laser Induced Fluorescence, LIF) in stirred tanks.

In the case of PIV, a laser sheet is used to illuminate a well defined slice of the fluid containing seeding particles; two or more pictures of the sheet are taken at short time intervals. The distances between the positions of seeding particles yield the instantaneous velocity field of the liquid. Different variants have been proposed: particle streak velocimetry (long exposure), particle tracking velocimetry (video recording of particle motion). Full details are available on the reviews of Murai et al. (2000) and Chaouki et al. (1997).

The principle and the main applications of LDA are briefly described in the following: if there is a relative motion between a wave source (laser) and a wave receiver (seeding particle of the liquid or bubble in the liquid), there will be a shift of wave frequency; this phenomenon is called the Doppler effect; measuring this frequency shift by using interference fringes gives access to the velocity. This technique has been applied to the determination of local velocities for some time. LDA provides well-localized values of velocity; the measurements are very fast, allowing to determine velocity fluctuations Chaouki et al. (1997).

LIF is suitable to measure small-scale structures either point by point or in a two dimensional plane. Fluorescent dyes (molecules) can absorb light at one frequency and subsequently (after some time, usually in the order of few nanoseconds to microseconds) de-excite and reemit (fluoresce) light at a different wavelength, larger than the excitation one. This light fluorescence is measured. In experiments, the dyes are excited by laser light whose frequency closely matches the excitation

frequency of the dye. The intensity of light emitted from a dyed region of flow is proportional to the intensity of excitation energy and to the concentration of dye. If the excitation energy is locally uniform, then the emitted light intensity will be linearly related to the dye concentration. Then, through a simple calibration, the emitted light intensity can be directly converted to dye concentration. In addition it is possible to get two- and three-dimensional images since fluorescence takes place in all directions (i.e. the fluorescence signal is isotropic). The signal-to-noise ratio of the fluorescence signal is very high, providing a good sensitivity to the process. It is also possible to distinguish between more species, since the lasing wavelength can be tuned to a particular excitation of a given species which is not shared by other species (Guilbault, G. 1973; Walker, 1987; Hannoun and List, 1988).

Such technique is able to yield information both on micro- and macro-mixing (Distelhoff and Marquis, 2000; Guillard et al., 2000; van Vliet et al., 2000; Slazai et al., 2003) process simply injecting a mixture of two different dyes in the stirred vessel: one of the dyes is an inert dye and its distribution inside the tank is analyzed to assess macro-mixing even if it does not provide information on nano-scale mixing quality; the other dye (the reactant dye) undergoes a fast chemical reaction with the vessel contents allowing to indirectly visualize micro-mixing since chemical reaction requires mixing on the molecular scale (Kling and Mewes, 2004).

PIV, LDA and LIF are mainly applied to investigate single-phase system or multiphase flows with very low hold-ups of the dispersed phase (Rammohan et al., 2003).

In recent years, Unadkat et al. (2009) proposed a new technique combining Fluorescent PIV and digital image analysis to quantify turbulence properties of solid-liquid stirred suspensions. They managed to investigate the flow field of both phases simultaneously by using two different cameras, the one for the liquid, the other for the solid phase. In addition, this technique is able to provide information on particle distribution, even if the presented results appear too qualitative.

Clearly, light based technique main limit concerns dense suspensions applicability: all of such techniques are completely useless in the case of suspension with high solid loading since the light beam is not able to pass through the system.

By the way, such drawback can be resolved by matching the refractive indexes of the suspended phase and the liquid as a number of works have already shown (Cui and Adrian, 1997; Micale et al., 2000; Kohnen and Bohnet, 2001; Boyer et al., 2002; Micheletti and Yianneskis, 2004, Virdung and Rasmuson, 2008).

The same theoretical principle lies behind the *radiation techniques* (Fournier et al., 1993; Hewitt, 1978), but instead of a ray light, they employ X-rays, or γ -rays, or neutrons beams: when crossing a two-phase mixture, all kinds of radiation are attenuated (Boyer et al., 2002). Radiation techniques are extensively used to measure hold-up of the dispersed phase in two-phase systems. Particularly some cases not involving attenuation measurement exist: x rays radiography is essentially the technique widely used in medical facilities, the difference being that a sequence of images can be made thus showing the dynamics of particle motion (Mondy et al., 1986; Milliken et al., 1989).

Typical difficulties concerning radiation techniques are related to measurement uncertainty due to the natural statistical fluctuation of photons. Theoretically this kind of technique is really useful because it has no limitations to time resolution but, safety and/or price (they require access to a nuclear reactor) may be an issue for its application especially for high solid hold-ups (Boyer et al., 2002): measurement can be affected by void distribution on the test section and it cannot often be carried out in industrial stirred tank reactors, because of common problems associated with the use of radiation (Paglianti and Pintus, 2001; Powell, 2008).

In addition, radiation technique can be used in an invasive way by the adoption of a suitable probe (Hewitt, 1978) and they also are the basis of a number of tomographic techniques (see below).

The *ultrasonic attenuation techniques* general principle is practically the same described for the corresponding invasive techniques. The only difference concerns the fact that the sensors are placed outside the system like the case of light attenuation techniques. In addition, acoustic method is quite similar to the optical

one but, as a matter of fact, an acoustic wave can pass through very dense suspensions, an impossible objective for a light beam.

Currently, no works so far have dealt with the ultrasonic non-invasive estimation of solid concentration for the case of stirred tanks. Uchida et al. (1989), Zheng and Zhang (2004), Vatanakul et al. (2004) and Vatanakul et al. (2005) investigated fluidized beds by means of the above mentioned ultrasonic technique. Zheng and Zhang (2004) and Vatanakul et al. (2004) also used differential pressure transducers and conductivity probe for the same measurement cases (for comparison purposes) and a good agreement with ultrasound method data was found, thus demonstrating the soundness of the technique.

In more recent years, a Chinese research group presented some interesting works (Ren et al. 2008a,b,c) dealing with acoustic measurements: they did not carry out hold-up assessments, but they proposed a new non-invasive acoustic emission method (based on multi-scale analysis) to determine the critical speed for complete solid suspension. Authors validate their approach by comparisons with visual observation of the just suspended speed.

Magnetic Resonance Imaging has been adopted to investigate multiphase flows since a couple of decades (Majors et al., 1989; Stapf and Han, 2006). A number of works focused their attention on the application of this technique to multiphase systems (Altobelli et al., 1991; Sinton and Chow, 1991; Maneval et al., 1993; Fukushima, 1999; Powell, 2008). Briefly, by applying a magnetic field with a linear gradient to a fluid sample, it is possible to detect the sample response consisting in some peaks with different intensities in the frequency domain (frequency responses are obtainable via Larmor relation).

Frequency differences give information on spatial distribution. Conversely, the magnitude of the signal centered at each frequency is directly related to the amount of fluid at this position. The latter represents the crucial point in multiphase flow application: when the technique is applied to a solid-liquid suspension (to estimate particle concentration), it yields the local amount of the liquid phase by which it is possible to get the local volume fraction relevant to the solid phase. More precisely,

a first image is got by placed in the magnetic field a sample consisting of liquid only as benchmark. Clearly, such reference image representing signal intensity as a function of position should show the same result for each position. Successively, MRI is used to image a sample with both phases. Comparing the two images, the one with the particles will appear as less intense because of the decrease in liquid quantity. The consequent decrease in signal intensity is directly proportional to the volume fraction of solid phase.

In addition, MRI can be adopted to measure velocity fields or to determine size distribution of droplets. On a one hand, MRI offers a non-invasive way of measuring local solid concentration as a function of position even for very dense suspensions without requiring the match of two phase refractive indices. On the other hand, MRI apparatus is usually located in a research laboratory with a person very skilled in NMR or MRI or in a facility with specialized technical support.

The equipment is very expensive and needs to be designed around system which has to be investigated (Powell, 2008).

Polarographic technique (Latifi et al., 1992; Rode et al., 1994; Magaud et al., 2001) is generally adopted to provide information on flow field in the immediate vicinity of the wall system. Particularly, it concerns local wall shear stress measurement by quantifying the current delivered by the fast electrochemical reduction of a reagent (generally reduction of hexacyanoferrate III to hexacyanoferrate) dissolved in the analyzed fluid (Reiss and Hanratty, 1963).

Clearly, technique characteristics require a conductive liquid and a support electrolyte whose presence could alter liquid coalescence behavior. About advantages, polarography is able to provide data on the flow behavior in the proximity of the walls; also, it can be miniaturized via microelectrodes and yielding even information on velocity fluctuations near the wall (Boyer et al., 2002).

The radioactive particle tracking techniques are the Positron Emission Particle Tracking (PEPT) and the Computer Automated Particle Tracking (CARPT). They are non-intrusive techniques, unique in flow visualization terms, being able to

resolve Lagrangian particle trajectories in opaque fluids and through opaque apparatuses, which is an invaluable piece of information in the study of complex fluid motion, such as in stirred vessels.

About fluid velocity assessment, radioactive techniques present a distinct advantage over other optical methods, such as LDS or PIV, which yield Eulerian type measurements and, as a result, only an average velocity field can be measured. PEPT and CARPT yield more detailed results on individual particle behavior and provide local information which are important in the study of complex multiphase flow, though a long and complicated calibration procedure is required. Particularly, differences between instantaneous and average velocities allow the estimation of the fluctuating velocities and all their auto- and cross-correlations lead to estimate turbulent kinetic energy and Reynolds stresses (Dudukovic, 2002).

On the other hand, at the present time, they do not provide a fine spatial or temporal resolution (Boyer et al., 2002; Dudukovic, 2002).

PEPT technique (Parker et al., 1993; Fangary et al., 2000; Parker et al., 2002; Fangary et al., 2002; Barigou et al., 2003; Barigou, 2004; Fishwick et al., 2005; Pianko-Oprych et al., 2009; Guida et al., 2009) was developed at the University of Birmingham: it primarily involves the use of a labelled tracer particle, a positron camera and a location algorithm for computing the tracer location. The tracer particle is labelled with a positron-emitting isotope. A positron emitted by the particle tracer rapidly annihilates with an electron emitting a pair of almost collinear 511 keV γ -quanta in opposite directions, 180 degrees apart. These two γ -rays can be detected by two position-sensitive detectors of the positron camera which are mounted in the middle of the stirred vessel. Each detector contains a single rectangular sodium iodide crystal optically coupled to an array of photomultiplier tubes. When a positron annihilation occurs the γ -rays emitted produce two coincident scintillations in the crystals, the related photomultipliers generate positional signals and two 2D centroids are calculated by the associated software. The joining line is the photon-trajectory related to the annihilation event. With a small number of annihilation events (theoretically only two) the position of a single

positron-emitting particle can be located at the crossing (centroid) of the photon-trajectories. Only coincidence events in which γ -rays are simultaneously detected by both detectors are recorded. The location algorithm (Parker et al., 1993) calculates the Lagrangian radioactive tracer trajectory allowing to track it in space and time. As a matter of fact, some γ -rays are scattered prior to detection, but this tracking algorithm adopted is able to discard these events (Barigou et al., 2003).

For solid-liquid flows as well as for suspensions in stirred tanks, both phases can be simultaneously tracked: two different tracer particles have to be used in this case, the one representative for liquid, the other representative for solid particles (Guida et al., 2009).

Ergodicity or iso-probability condition is the theoretical base which guarantees that a tracer is representative of all the solid or liquid phase. Theoretically, this ideal state could be approached only after an infinite tracking time, even if it can be mathematically demonstrate that, if the probability of visit is sufficiently high everywhere (i.e. when the trajectory of the tracer is recorded over a sufficiently long time to achieve adequate data resolution in every region) ergodicity can be safely assumed (Wittmer et al., 1998). Clearly, turbulence and/or aimed-homogeneous conditions, very often achieved in stirred tanks, give soundness to such assumption.

CARPT (Larachi et al., 1997; Rammohan et al., 2001a,b,c; Dudukovic, 2002; Guha et al., 2007) was developed at the Washington University of St Louis: its basic principles are the same already described for PEPT. As a difference with PEPT, *CARPT* typical set up consists of 16 scintillation detectors mounted on aluminium supports, which are arranged on an octagonal base. There are eight aluminium supports placed around the tank at 45° to each other. The configuration generally adopted optimizes the extent to which the particle can be seen by each detector in the tank (for full details see Rammohan et al., 2001,b). Each detector unit is a cylinder containing an active cylindrical Sodium Iodide crystal.

Rammohan et al. (2003) addressed the strengths and the limitations of the *CARPT/PEPT* technique by numerically simulating the same Eulerian flow field experimentally generated, for comparison purposes. They stated that three types of

errors are possible in CARPT/PEPT measurements: (1) errors in reconstructing the trajectories from detector signals, (2) errors in estimating the Eulerian information from the reconstructed trajectories, and (3) errors due to tracer particle not following the flow faithfully. However, information on these error minimization/solution are available in literature (Parker et al., 1993; Larachi et al., 1997; Rammohan et al., 2001c; Guida et al., 2009). Error (3) is strictly linked to size and density of the liquid radioactive tracer. Clearly, density should be equal to the liquid one to avoid buoyant effects as well as size should be as small as possible to faithfully follow liquid turbulence. In CARPT, typically, a 2300 μm size tracer is adopted. Rammohan et al. (2003) stated that the larger the particle size, the less likely it is to respond to liquid phase turbulence. They found that turbulent kinetic energy estimated from the trajectories of a neutrally buoyant tracer particle larger than 2300 μm could be highly underpredicted (by as much as 50% in their case). Conversely, in PEPT, a 600 μm size tracer is utilized. Barigou (2004) addressed this problem by considering both the Kolmogorov length scale theory and the particle Stokes number (see the relevant paper for other details) and he concluded that the 600 μm PEPT tracer was able to follow faithfully the fluid streamlines. Other PEPT aspects concerning geometric efficiency, improved elimination of corrupted tracer locations (due to scattering phenomena), trajectory interruptions (due to accidental low frequency acquisition) were addressed by Guida et al. (2009) (see for full details) resulting in a good optimization of the present technique. Moreover, authors managed to provide for the first time PEPT information on local solid concentration in the case of a high solid loading stirred vessel, with the unique hypothesis of dividing the solution domain (the entire tank) in *all equal control volumes* during data processing. Other obvious drawbacks regarding radioactive particle tracking techniques concern the equipment high price and the dangerous use of radioactive tracers (Boyer et al., 2002). Finally, they cannot be applied to solid-liquid suspension where particles are not completely suspended, because the tracer could be entrapped in the sediment without providing any useful/reliable information.

The *tomographic techniques* (Williams and Beck, 1995) were born and developed in recent years both for medical and industrial applications. They are advantageous because they are able to provide non-invasive information on phase volume fraction distribution inside different types of systems. The general principle consists in measuring inside the system a physical property that can be related to the phase volumetric fraction. Measurements are carried out at different angular positions and give the average values of the property over the corresponding diameters. By adopting a reliable reconstruction algorithm, the acquired signals are then analyzed to provide the phase fraction image on a cross-section of the system.

Different tomographic technique exist (PET, optical, infrared, ultrasonic) but mainly two of them have been developed and utilized so far for multiphase flow investigation: *photon attenuation tomography* or *γ -ray Computed Tomography (CT)* and *Electrical Impedance Tomography (EIT)*.

Computed tomography (CT) has been largely employed so far (Kumar et al., 1995; Chaouki et al., 1997; Froystein, 1997; Kumar et al., 1997; Schmitz, and Mewes, 2000; Dudukovic, 2002). Its principle is simple. From the measured attenuation of photon rays such as γ or X-ray through the two phase mixture (projections) it is possible to calculate the distribution of phases in the cross-section that was scanned, since different phases show different attenuations. In other words, this attenuation being directly proportional to the material density for a given energy, the resulting image gives the density at each pixel and then the phase fraction map. Reconstruction algorithms are based on the inversion of 2D Fast Fourier Transform since all the measured attenuations are linear functions of density.

Technique limits regarding price, safety, low spatial distribution, very high power requirement for high solid loading system and high measurement time in industrial application cases. Moreover, it should be used with rather stationary flow. Technique potential errors concern statistical error due to random emission of γ photons, the dynamic bias due to gas fraction fluctuations and the reconstruction

error (Boyer et al, 2002). To my knowledge no works dealing with CT application on solid-liquid suspension in stirred tanks exist.

Tomography systems based on electrostatic fields (Electrical Impedance Tomography, EIT) for imaging the conducting (or dielectric) properties of a medium are called electrical tomography systems. Practically, the distribution of electrical properties inside the system is obtained from measurements of electrical quantities, such as capacitance (*ECT*) (Warsito and Fan, 2001) or conductance (*ERT*), between all couples of electrodes, suitable placed around the system periphery: outside the system in the case of ECT and flush with the inner surface of the system in the case of ERT (in the case of ERT electrodes have to be in direct contact with the investigated media to allow the electrical current to enter the imaging domain) (Dyakowski et al., 2000). Such information is elaborated by applying an appropriate reconstruction algorithm which mathematically links the measured values with that distribution.

The aim of ERT is to reconstruct the conducting (or dielectric) properties of an object from (ERT) measurements of electrical signals, taken from all possible views of the sensing electrodes. Multiple alternating current-driven and voltage sensing electrodes can be used. A measurement protocol is based on injecting current, using a pair of neighboring electrodes and measuring the voltage differences, using all other pairs of neighboring electrodes, and repeating this process by injecting current using different pairs of neighboring electrodes. Therefore, spatial gradients of electrical conductivity, which are a function of concentration gradients, can be measured. Additionally, the use of multi-plane electrical sensors provides for a description of mixing processes in three dimensions.

Similarly, the aim of ECT is to reconstruct the dielectric properties of an object from the measurement of electrical capacitance recorded between all possible pairs of electrodes. Electrodes are excited one by one and the capacitance values between the excited electrode and the remaining ones are measured.

Electrical tomography is, in certain cases, the most attractive for real-time imaging of industrial processes, because of its inherent simplicity, rugged

construction and high-speed imaging capability, typically between 100 and 200 frames per second (Dyakowsky et al., 2000). It is easy to implement with relatively low costs. Its characteristic response dynamics is very fast thus allowing reliable descriptions of flow rapid evolutions or flow configuration changes (Boyer et al., 2002).

Nevertheless, the limited number of measurements and the presence of electrical noise causes difficulties in obtaining an accurate solution (Mann et al., 1997a). Also, the applied electrical fields are low so that complex (i.e. iterative) reconstruction algorithms may be needed to reduce inherent image distortion. Spatial resolution is very poor and a compensation may also be needed to increase sensitivity near the centre of the image. With this regard, Stephenson et al. (2008) addressed the dramatic effect that measurement strategy, reconstruction algorithm and reconstruction parameters can have on electrical impedance tomography images. Authors concluded that all these operating parameters have to be chosen carefully because they can lead to high mismatches with real quantities.

A number of scientific works were devoted to electrical tomography applications to stirred tanks (McKee et al., 1995; Williams et al., 1996; Mann et al., 1997a,b; Williams and Mann, 2000; Stanley et al., 2002; Bolton and Primrose, 2005; Rodgers et al., 2009; Hosseini et al., 2010a).

Particularly, Williams et al. (1996) described the application of ERT for three-dimensional imaging of the concentration of solids in a slurry mixer as a function of key process variables (particle size, impeller type, agitation speed).

Bolton and Primrose (2005) presented an overview about electrical tomography applications on pharmaceutical and related industrial processes investigating, among others solid distribution in stirred tanks and crystallizers.

Recently, Rodgers et al. (2009) demonstrated for the first time the capability of three-dimensional EIT to monitor reactive stirred systems under realistic process conditions and scale. Authors investigated the semi-batch precipitation of barium sulphate from barium chloride and sodium sulphate in a 200 litre, semi-tech scale, stirred tank reactor.

Taking into full account the limits and disadvantages concerning all the techniques described so far, the idea of proposing a new measurement technique arises. Obviously, it would be innovative, non-invasive, very simple and able to directly produce reliable 2D solid distribution maps at acceptable costs and in reasonable times. This new technique was namely *Laser Sheet Image Analysis* and it will be described in detail in the relevant paragraph.

It is the aim of the present PhD work to apply the *LSIA* technique to the case of a dilute solid-liquid suspension in completely unbaffled stirred tanks: the one stirred by a Rushton turbine, the other stirred by a marine propeller. For the case of the radially stirred system, the formation of two stable toroidal structures resulting in attractors for non-Brownian solid particles, heavier than the fluid was observed.

The practical assessment and the existence conditions of the former two stable toroidal zones, was investigated under turbulence conditions by the adoption of the reliable and accurate measurements provided by *LSIA* technique. Naturally, the obvious vortex formation typical of liquid stirring within unbaffled vessels is avoided by both covering and degassing the vessel, thus consequently eliminating the dependence of the *Power number* on the *Froude number*.

1.3 Experimental information

The experimental system is constituted by three main parts: the investigated vessel, the degassing unit and the *LSIA* apparatus.

The investigated vessel consists of a cylindrical, flat-bottomed, 0.5 cm thick unbaffled tank with a inner diameter of $T=0.19\text{m}$ and a height $H=T$, as depicted in Fig.1.1.

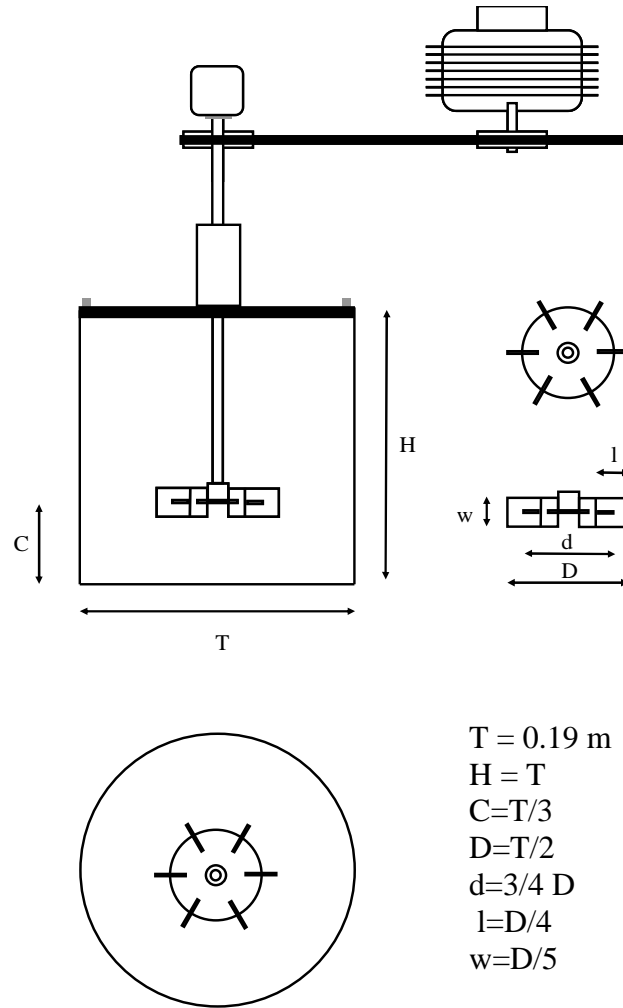


Fig. 1.1: Stirred vessel.

Two different impellers were investigated in the suspension experiments: a standard six bladed Rushton turbine with a diameter $D=T/2$ placed at a clearance $C=T/3$ and a marine propeller with a diameter $D=T/2.4$ placed at a clearance $C=T/4$. In order to avoid optical distortion problems, the stirred vessel was inserted inside a bigger tank, with a rectangular plant (Fig.1.2), accurately placed with the faces perpendicular to the laser and the videocamera action directions.

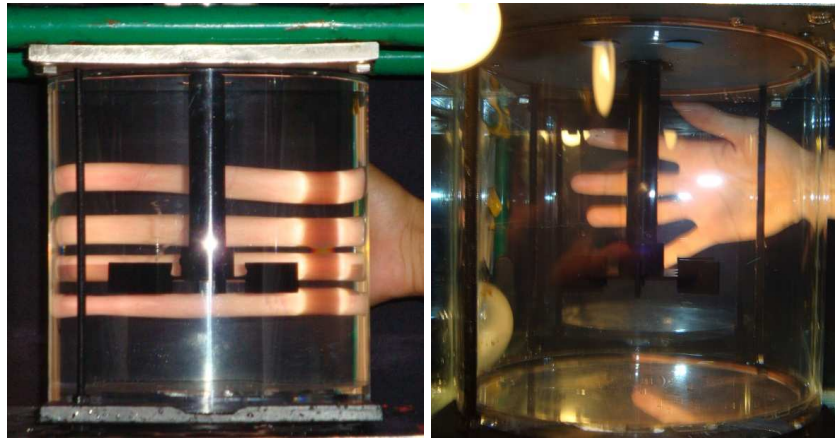


Fig. 1.2: The optical distortion problem and the relevant solution.

The impeller is moved by an electric synchronous engine *MAVILOR*, *MSS-8 type*, supplied by continuous current by an external controller-feeder. It is on its side equipped with a feedback (PID) *INFRANOR* controller able to ensure the angular velocity set point.

A fundamental task in conducting experiments is to avoid the presence of air or simply air bubbles within the stirred vessel. Air could generate vortex under turbulent regime and bubbles could be mistaken for solid particles in acquisition procedure, thus altering result reliability. In order to answer to this task, the investigated vessel is covered by a holed metal plate and contemporaneously connected, by means of two 3/8 inches gum tubes, with a purposely developed degassing system well described in Fig.1.3. A air-water mixture is drawn by the submerged pump through the tube B and successively pure water is reintroduced in the vessel after the degassing by means of the tube A. The particles are introduced in the vessel by a syringe through the inlet C.

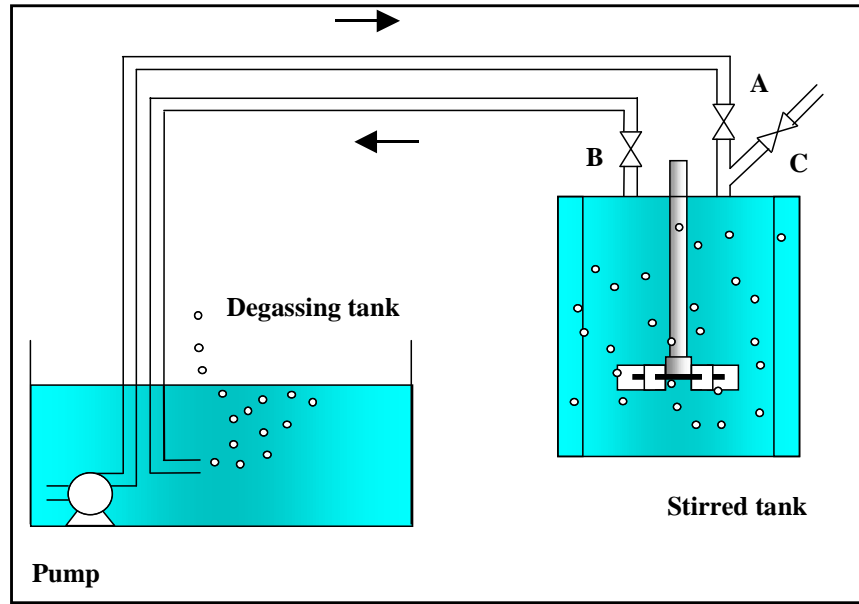


Fig. 1.3: The degassing system: A) water inlet; B) water + air outlet; C) particles inlet.

The *LSIA* apparatus is depicted in Fig.1.4: it is constituted by the illumination system, the acquisition system, the synchronization system and the PC with the relevant software.

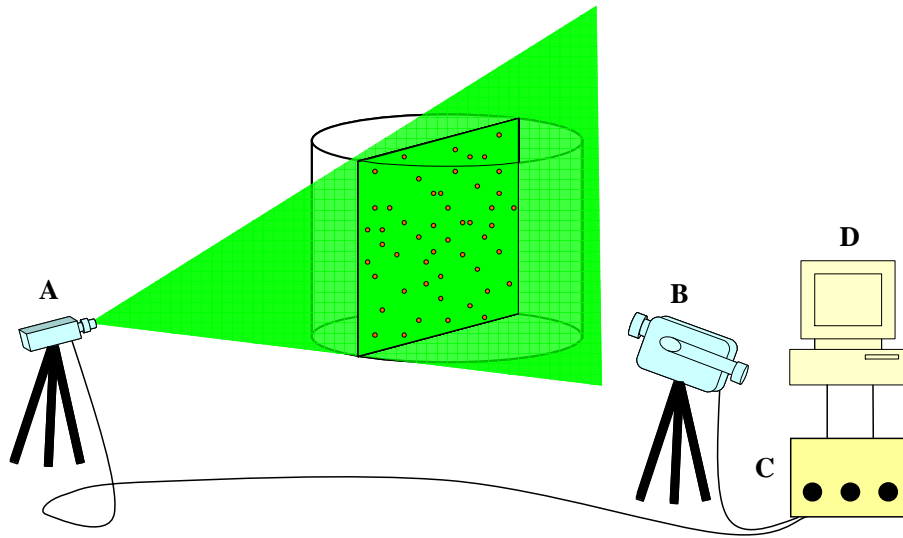


Fig. 1.4: LSIA apparatus: A) pulsed laser; B) videocamera; C) control-acquisition unit; D) personal computer.

The illumination equipment is a double cavity ND:YAG pulsed laser of the *NEW WAVE RESEARCH, Solo III 15Hz* model. It is a state solid laser emitting an infrared radiation which is transformed in a luminous radiation by a suitable frequency doubler. Finally, such a laser is equipped with a semi-cylindrical optics *Dantec 80x11* able to transform the ray emitted in a light sheet in order to light up the section to investigate.

The acquisition system is a *Dantec 80C60 Hisense PIV* characterized by a 1280x1240 pixel CCD. It has a very high sensibility to light and it is equipped by a pass-band filter of the *Edmund Scientific* centred on the wave length of 532 nm in order to limit the luminous noise due to other external light sources. Obviously, the videocamera-vessel relative position is to be accurately chosen in order to avoid any parallax error, but keeping a good image resolution.

The synchronization of the emitting-acquisition times of laser and videocamera are guaranteed by an acquisition-control unit with a *DANTEC* processor, *Flow Map 1500* model.

This processor is connected via Ethernet peer to peer connection to a PC. The software utilized are the *Flow Manager ver.3.7* and the *Matlab*. The parameters set inside the *Flow Manager* software are shown in Tab.1.1. Naturally the time between two subsequent recordings has not to be a multiple of the impeller rotation frequency in order to avoid that all the acquired images are relevant to the same impeller position.

Time between pulses	111 μ s
Light pulses per recording	1
Duration of each pulse	0.01 μ s

Tab. 1.1: Flow Manager acquisition parameters

All the experiments were performed by filling the tank with deionised water and particles with a concentration of 0.2 g/l. Glass ballottini (density of about 2500 kg/m³), white corundum particles (density of about 3450 kg/m³) and made-house fluorescent particles (density of about 1400 kg/m³) (see the following paragraph) of different sizes were utilized in the experiments. In addition, a number of angular velocities were investigated. For need of clarity, all data are summarized in Tab. 1.2.

Top-covered unbaffled vessel stirred by a standard Rushton turbine					
Glass ballottini or Corundum Particles					
<i>Diameter 125-150 μm</i>	<i>300 RPM</i>	<i>400 RPM</i>	<i>500 RPM</i>	<i>600 RPM</i>	
<i>Diameter 212-250 μm</i>	<i>300 RPM</i>	<i>400 RPM</i>	<i>500 RPM</i>	<i>600 RPM</i>	
<i>Diameter 250-300 μm</i>	<i>300 RPM</i>	<i>400 RPM</i>	<i>500 RPM</i>	<i>600 RPM</i>	
<i>Diameter 425-500 μm</i>	<i>300 RPM</i>	<i>400 RPM</i>	<i>500 RPM</i>	<i>600 RPM</i>	
<i>Fluorescent particles</i>					
<i>Diameter 425-500 μm</i>	<i>300 RPM</i>	<i>400 RPM</i>	<i>500 RPM</i>	<i>600 RPM</i>	
Top-covered unbaffled vessel stirred by marine propeller					
<i>Fluorescent particles</i>					
<i>Diameter 425-500 μm</i>	<i>200RPM</i>	<i>300 RPM</i>	<i>400 RPM</i>	<i>500 RPM</i>	<i>600 RPM</i>

Tab. 1.2: Investigated cases

1.3.1 Fluorescent particles

As it will be better described in the following paragraph, luminous reflections can be erroneously considered as particles by the technique so leading, to unreliable solid concentration assessments. The adoption of particles labelled with the rhodamine B (fig.1.5) allows to resolve the reflection problem.

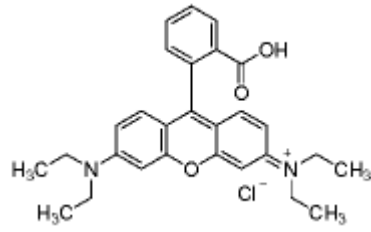


Fig. 1.5: Rhodamine B: molecular structure

These particles were prepared by mixing a thermosetting resin with its relevant catalyst (weight ratio 2:1), a glass charge (necessary to increase the density of the final polymer) constituted by particles whose diameter has to be very low ($<40\mu\text{m}$) and the rhodamine B. It is important to obtain a homogeneous solution during the mixing process in order to avoid gradients in the final material properties. After the hardening, the obtained polymer pieces were ground and sieved. Finally, the density of the obtained particles was experimentally measured (by means of a volumetric flask): it was about 1400 kg/m^3 .

It is worth noting that during the experiments performed by using such type of particles, the pass-band filter was substituted by a high-pass filter with a threshold wave length value of 570nm : the rhodamine B hit by the laser sheet emits the light at a wave length of about 590nm . Therefore, with the adoption of the high-pass filter, only the illuminated fluorescent particles are visible (Fig.1.6).

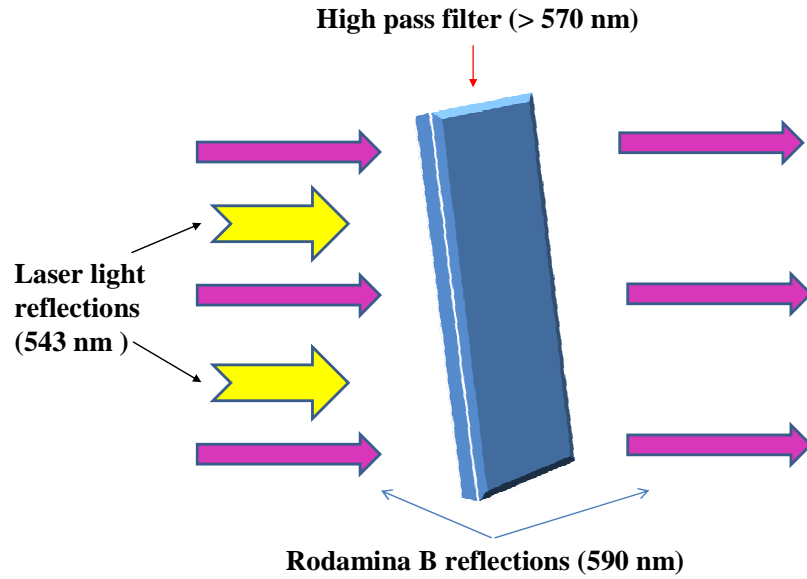


Fig. 1.6: High pass filter working

1.4 LSIA fundamentals

The novel *Laser Sheet Image Analysis* technique (summarized in Fig.1.7) is based on the probabilistic elaboration of acquired images. A horizontal or vertical section of the investigated vessel is illuminated by a pulsed laser sheet; in this work only a half diametrical vertical section is investigated. Solid particles are stochastically intercepted by the laser blade and they are lightened as bright little points, whose spatial disposition is captured by the videocamera, purposely placed perpendicularly to the illuminated plane. By suitably synchronizing the pulsed laser and the videocamera, it is possible to obtain an image. It is a grey-scale background image with some white peaks that may correspond to the presence of particles. The images obtained in this way are elaborated in order to identify the particles and their position, accurately filtering the reflections and other spurious white peaks, that are

not linked to the presence of particles. All these elaborations are carried out by means of specific functions of the *Matlab image tool-kit*.

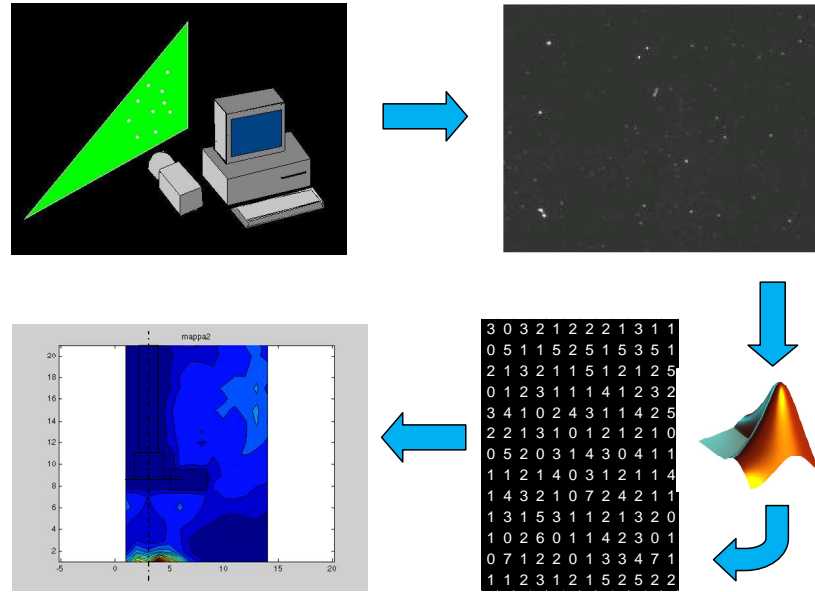


Fig. 1.7: *LSIA* main phases.

More precisely, the acquired snapshots are transformed in a matrix, whose dimensions are equal to videocamera CCD pixels. Each coefficient of this matrix corresponds to a single pixel, exposed in the CCD. It has a grey scale value variable from 0 (corresponding to black) to 255 (corresponding to white). By choosing a suitable *grey-level* parameter (see below), this initial matrix is transformed in a binary position matrix constituted of 0 and 1 signs. The signs 1 correspond to the brightness centre of all the white peaks identified as objects by the *Matlab* procedure. Therefore, by acquiring a sufficient *number of images* (about 2000, see below) and by summing all their relevant position matrixes, it is possible to get a bidimensional particle presence probability ($counts_{r,z}$) distribution map. The sum-

position matrix is compressed about 25 times (each matrix area whose dimensions are $\Delta r = \Delta z \approx 5$ pixels is substituted by only one coefficient: the sum of all the coefficients belonging to that area) in order to average results and consequently reduce data probabilistic scattering. Such a map, multiplied by a α constant (see below), corresponds to a solid phase concentration $C_{r,z}$ map on the same vessel section.

An example of the information which it is possible to get by means of the LSIA technique is shown in Fig.1.8 (C_m is the average solid concentration in the vessel).

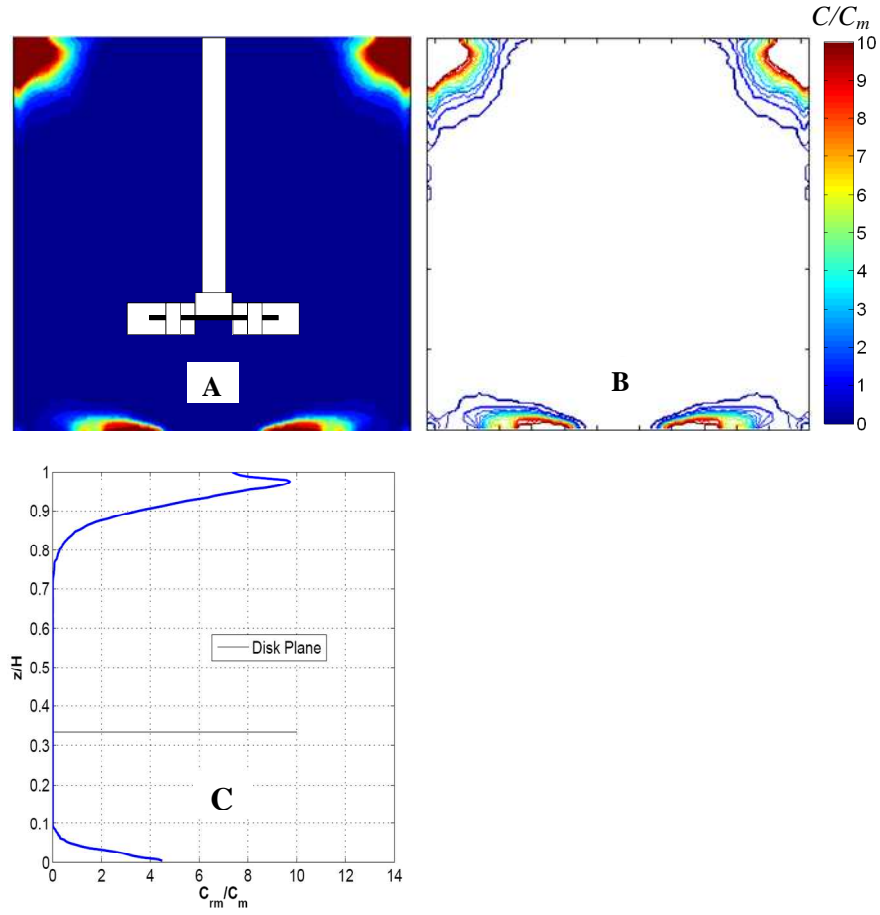


Fig. 1.8: Example of information obtainable by the LSIA technique (for the case of glass ballottini particles of 425-500 μm at 600RPM in the tank stirred by the Rushton turbine): A) Colour Maps; B) Contour Plots; C) Radially averaged integral axial profile.

1.4.1 The grey-level parameter

The elaboration procedure needs the choice of a threshold value for the matrix bynarization in order to discriminate the brightness belonged to the illuminated particles placed on the laser sheet plane from the brightness of the background: all the coefficient values higher than this parameter are considered signs 1, the others are considered signs 0. In order to correctly choose such a parameter, it is necessary to analyze the histogram of some acquired images. An example of this histogram, typical for all the acquired images, is shown in Fig.1.9.

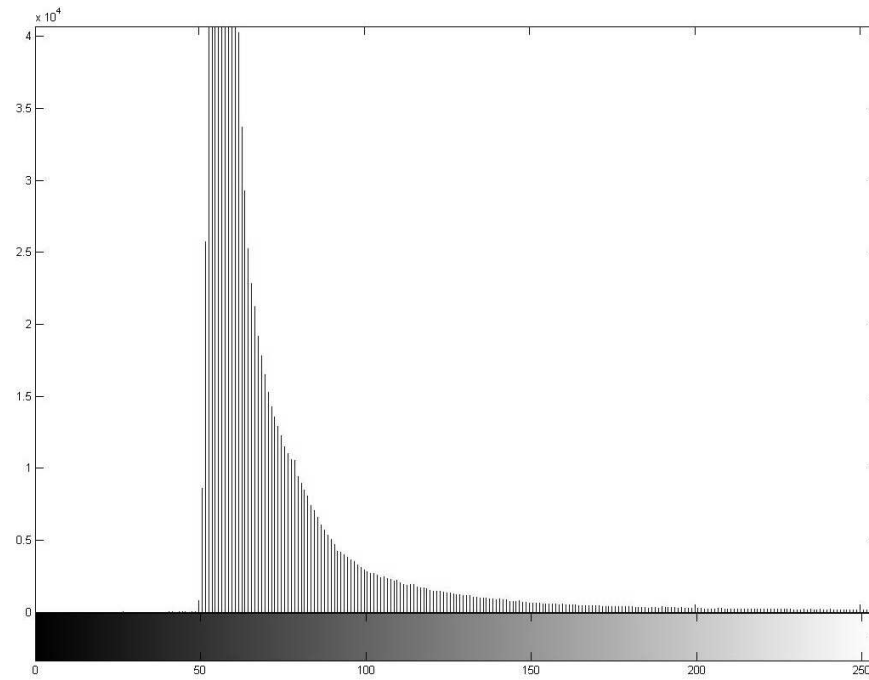


Fig. 1.9: Typical acquired image histogram: brightness value versus number of occurrences.

This figure shows that the bright peaks distribution is bimodal (there is a very narrow peak at 255).

All the value relevant to the first mode of the histogram are representative of the background brightness, conversely, particles located on the laser sheet plane are directly hit by the light blade showing the maximum brightness value, i.e. 255. Any parameter value higher than 200 guarantees the obtaining of practically the same results: two different elaborations of the same set of images were performed by adopting a *grey-scale* parameter of 240 and 253 respectively. Results are practically identical and they are not shown for the sake of brevity.

1.4.2 The number of images to acquire and the median filter

Obviously, a higher number of images guarantees more defined and reliable particle distribution, but requiring increasing elaboration times. In order to find a compromise and choose the best value, a set of tests were carried out. Obtained results (some of these are shown in Figs.1.10 and 1.11) suggest the use of 2000 as the *number of images* to acquire: in fact, as matter of fact, results obtained with 6000 acquired images are very similar to those relevant to 2000. In particular, the contours of the concentration plot relevant to the 6000 images case (Fig.1.10B) are smoother and more defined than the 2000 images one (Fig.1.10A), but the two maps are qualitatively the same. In addition, the radially averaged axial profiles shown in the Fig.1.11a provide a quantitative comparison between the two cases confirming that 2000 images are sufficient to guarantee reliable results by a statistical point of view.

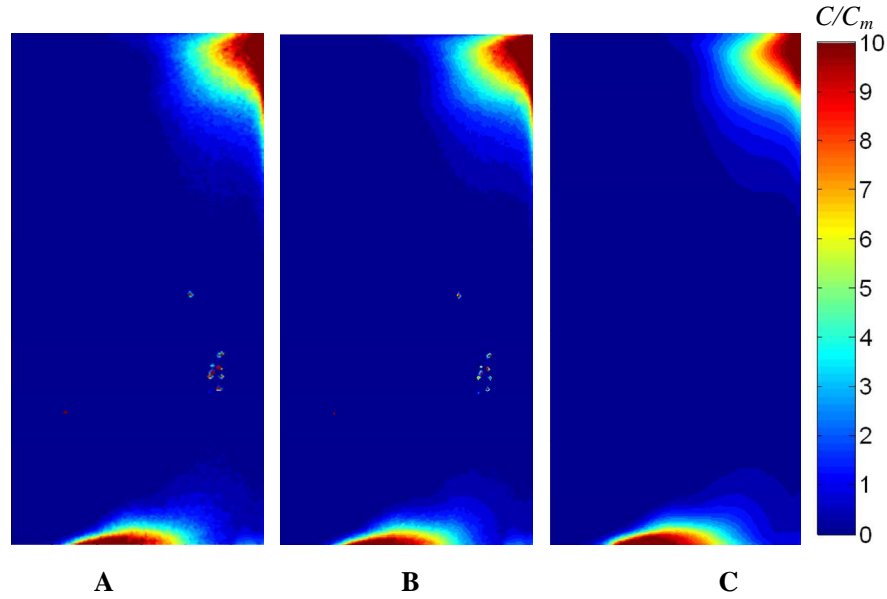


Fig. 1.10: Examples of the same distribution map relevant only to half section because of obvious symmetry reasons (for the case of corundum particles of 212-250 μm at 500RPM in the tank stirred by the Rushton turbine) obtained by acquiring: A) 2000 images; B) 6000 images; C) 2000 images elaborated with the adoption of the median filter.

These axial profiles present some little peaks likely relevant to light reflections which are also visible as red points in the contour plots (Figs 1.10A and B). The adoption of a *median filter* represents a good way to delete their presence. For each value of the final compressed counts matrix, the median filter analyzes a squared window of surrounding values (3x3 pixels) whose centre is the initially considered value: these values are ordered and the considered central value is substituted by the median value of the succession.

As a matter of fact this operation does not have a physical meaning, but it provides a good global effect: the undesired peaks are deleted as shown in Fig.1.10C and in Fig.1.11B and C. In addition the contours of the normalized solid concentration depicted in Fig.1.10C appear to be perfectly smooth and defined.

Probably, increasing greatly the number of acquired images would lead to the same contour plot obtained by means of the median filter. It is worth noting that this filter can be used only when concentration variations are smooth and sharp gradients are not present: a characteristic of all the maps presented in this section.

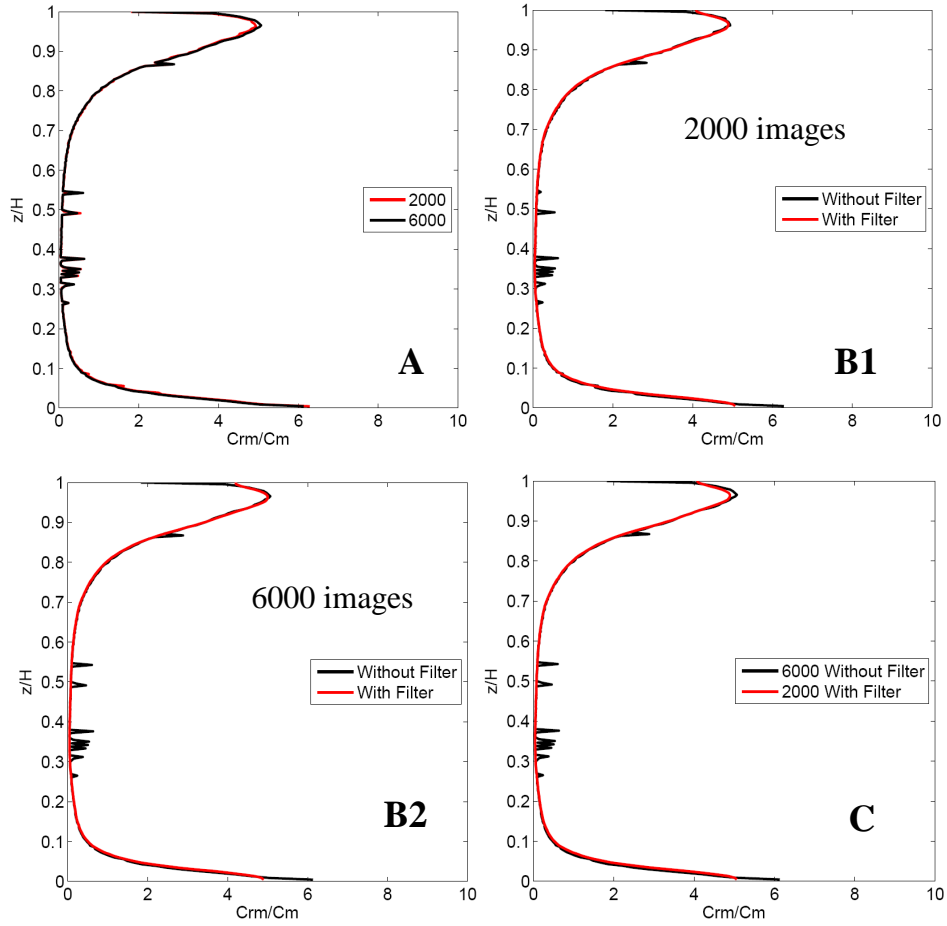


Fig. 1.11: Comparisons of radially averaged axial profiles for corundum particles of 212-250 μm at 500RPM.

1.4.3 The mean and the minimum particle area: A_{mean} and A_{min}

After the binarization, the Matlab procedure takes into account all the agglomerates of signs 1 and labels each of them as an object. Each of these agglomerates is substituted with an only sign 1 placed in the centre of the object. This choice is dependent on the fact that the brightened crown of each illuminated particle has the same particle luminosity and it has also size comparable with the particle one (this effect is greater for smaller particle size). Clearly, some particles could be one near the other, like in the sediment, appearing as a unique brightened object. The A_{mean} is an important value allowing to divide the big agglomerates (bigger than $A_{mean}+A_{min}$) in the correct number of constituting objects.

A_{min} is another important parameter which has to be considered. The light sheet is a narrow plane (about 2-3 mm), some particles are completely contained in it, others are partially outside the plane appearing as small objects. All particles partially hit by the laser sheet show an area smaller than A_{min} and have not to be taken into account. Moreover, the adoption of an inferior limit have also the function of eliminating all the little reflections (see below).

The two parameters were chosen by a visual observation of the acquired images: little differences due to operator sensibility did not provide significant variations in the obtained results.

1.4.4 Light reflection issues

This novel *LSIA* technique suffers of a bothersome drawback: the presence of light reflections relevant to some physical components of the vessel. In order to reduce the problem incidence, the rotating compounds (impeller and shaft), the bottom and the cover were blacken by an opaque paint. However, even optimizing the spatial disposition and the physical elements painting, some reflections appear permanent.

Light reflections can be classified into two different categories: random and fixed ones. Random reflections are generally small size reflections: typically they are smaller than the particle size. They are identified and deleted by a filter

implemented inside the Matlab procedure which does not take into account all the objects having an area (in pixel) smaller than the minimum particle area A_{min} .

Conversely, fixed reflections have big size and are not linked to the particle presence or movement. They are identified and deleted by a “mask” (Fig. 1.12), a particular binary matrix which is created by processing some images acquired in the tank filled with liquid only. Moreover, in the mask the impeller and a little region surrounding it (areas which are clearly not involved in an eventual particle presence) are manually shaded. Such a mask eliminate all the fixed reflections, but resulting in a loss of data in the zones where reflections are present (all the mask coefficients relevant to reflections are set to 0).

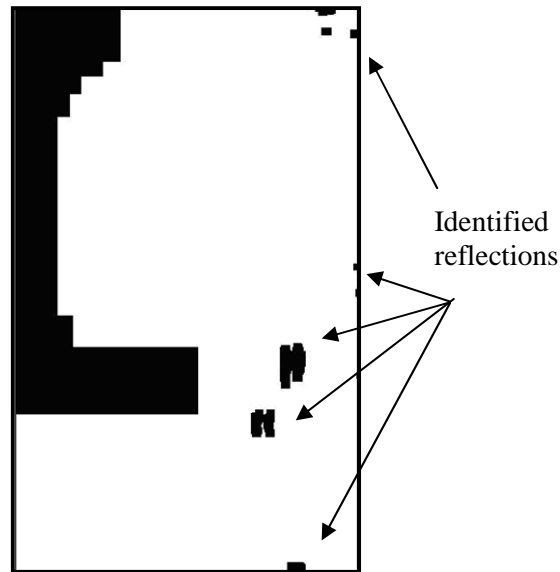


Fig. 1.12: The “mask”

This data holes in the final counts matrix are filled by interpolating the coefficients of the cells surrounding these holes (Fig.1.13).

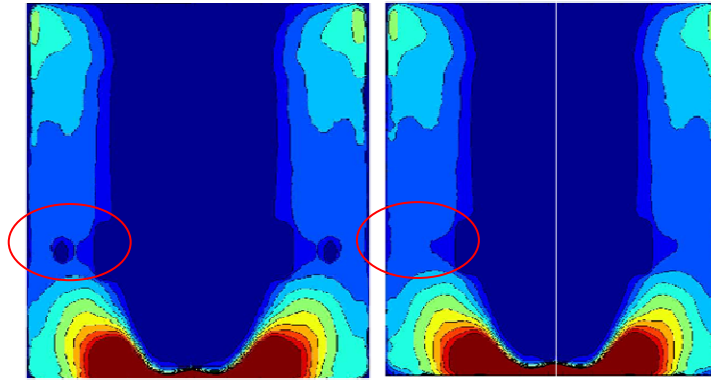


Fig. 1.13: Examples of data hole filleting

The most valuable solution for avoiding almost all the reflections (fixed or random) is the adoption of fluorescent particles as the Fig. 1.14 shows, though it is worth noting that some reflections will however be present if the black paint is not applied. For example, Unadkat et al. (2009) find high values of solid concentrations in the proximity of the impeller and they do not provide a convincing explanation about this evidence: in fact the light reflected by particles can hit the metal-made shaft and the impeller thus resulting in a secondary reflection which can pass over the filter and provide the unphysical highlighted areas near the stirrer.

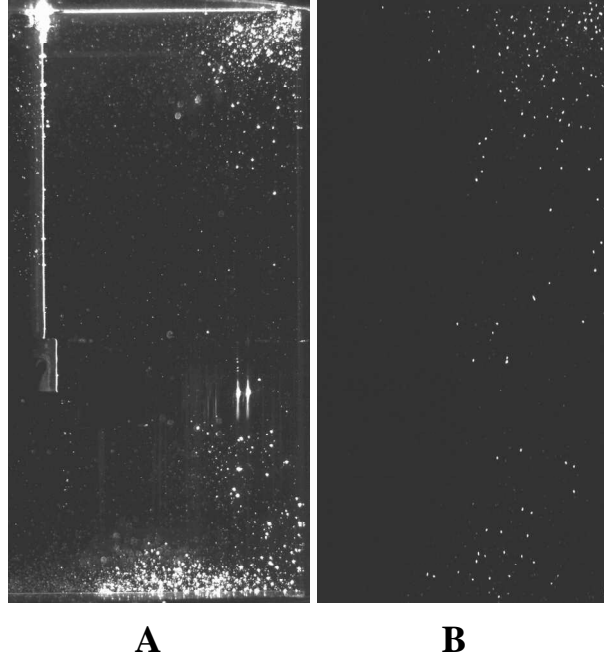


Fig. 1.14: Two examples of acquired images: A) 425-500 μm glass particles;
B) 425-500 μm fluorescent particles

1.4.5 Shifting from a probability distribution map to a normalized concentration map

Each coefficient of the compressed sum-position matrix (that is a number of $\text{counts}_{r,z}$) refers to a little area of the illuminated plane (whose size are clearly Δr and Δz) and it represents the probability of finding a particle in that area. Because of the axial symmetry of the unbaffled vessel, there is the same probability in the volume generated by the azimuthal rotation of the considered area around the shaft. The α constant allows to shift from this local probability to the local concentration value $C_{r,z}$ which is the concentration value relevant to the former rotational volume. In formula:

$$C_{r,z} = counts_{r,z} \cdot \alpha \quad (1.1)$$

Therefore, the relevant local mass value $M_{r,z}$ can be estimated by multiplying the local concentration by the relevant rotational volume:

$$M_{r,z} = counts_{r,z} \cdot \alpha \cdot 2\pi(\Delta r \cdot \Delta z) \quad (1.2)$$

The sum of all the local mass values results in the total mass value:

$$M_{TOT} \cong \sum_{r=1}^{T/2} \sum_{z=1}^H 2\pi r \cdot \Delta r \cdot \Delta z \cdot counts_{r,z} \cdot \alpha \quad (1.3)$$

In this way it is possible to estimate α since the total mass loaded in the tank is a known value:

$$\alpha = \frac{M_{TOT}}{2\pi \cdot \Delta r \cdot \Delta z \cdot \sum_{r=1}^{T/2} \sum_{z=1}^H r \cdot counts_{r,z}} \quad (1.4)$$

However, it is more interesting to obtain final maps where the local concentration is normalized as regards to the mean concentration inside the vessel C_m . Therefore inside the Matlab procedure it is used another constant, named K which is equal to the ratio of α to the mean concentration C_m .

$$\frac{C_{r,z}}{C_m} = \frac{counts_{r,z} \cdot \alpha}{\frac{M_{TOT}}{\pi R^2 H}} = counts_{r,z} \cdot K \quad (1.5)$$

The equation for the computation of the constant K is obtained by dividing α by the mean concentration.

$$K = \frac{\alpha}{\frac{M_{TOT}}{\pi R^2 H}} = \frac{R^2 H}{2 \cdot \Delta r \cdot \Delta z \cdot \sum_{r=1}^{T/2 H} \sum_{z=1}^H r \cdot counts_{r,z}} \quad (1.6)$$

Summarizing, it is possible to directly transform the probability map into a normalized concentration map simply multiplying the compressed sum-position matrix by this K value.

1.4.6 Reproducibility

A statistical assessment of the LSIA technique reproducibility was not carried out. However, two runs of the same experiments were reproduced and quite similar results were obtained. An example is reported in Fig.1.15.

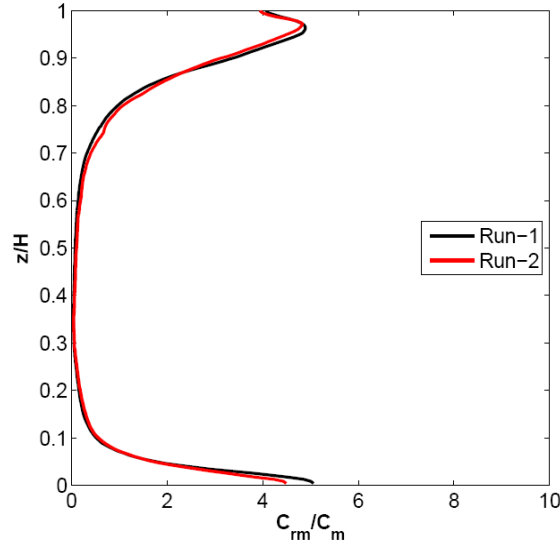


Fig. 1.15: Reproducibility assessment (for the case of corundum particles of 212-250 μm at 500RPM in the tank stirred by the Rushton turbine).

1.5 LSIA application: dilute suspensions in unbaffled vessels

1.5.1 Introduction

The most industrial stirred vessels are equipped with baffles breaking the undesired tangential component of velocity, and consequently avoiding the vortex formation at high angular speeds. Moreover baffle presence increases the axial velocities thus guaranteeing a better axial circulation and mixing than the vessels without baffles (Nagata, 1975). Although baffled tanks are widely used for better mixing of liquids or of solid particles and liquid, there are many cases where the use of unbaffled tanks may be desirable. Unbaffled systems are, in fact, usually used in some specific applications (Assirelli et al., 2008; Pacek et al., 2001) where the baffles could be determine some precise drawbacks. For example, in food and pharmaceutical industries it is a matter of primary importance to keep the reactor as clean as possible. In crystallization processes (Hekmat et al., 2007) and biological application (Aloi and Cherry, 1996) it is necessary to avoid any damage on growing particles or on cells culture respectively. In precipitation processes baffles could be suffer from incrustation problems (Rousseaux et al., 2001). Finally, unbaffled vessels are commonly adopted for the case of laminar mixing of viscous systems, typically in conjunction with large close-clearance impellers, since dead regions may form in the proximities of baffles (Lamberto et al., 1996). Notably, higher values of the mass transfer coefficient may be obtained in unbaffled vessels, at the same value of mechanical power dissipation, especially when high density differences exist between the liquid and solid phases (Grisafi et al., 1994; Yoshida et al., 2008).

Scientific literature emphasizes a continuous increasing interest towards unbaffled stirred vessels: both experimental (Abatan et al., 2006; Kagoshima and Mann, 2006; Montante et al., 2006; Rao and Kumar, 2007; Tezura et al., 2007; Shan et al., 2007; Shan et al., 2008; Yoshida et al., 2008; Hirata et al., 2009; Brucato et al., 2010) and computational studies (Ciofalo et al., 1996; Lamberto et al., 2001;

Shekhar and Jayanti, 2002; Alcamo et al., 2005; Derksen, 2006; Sbrizzai et al., 2006; Shan et al., 2008) were carried out, often showing good perspectives about a massive industrial use of such equipments (Brucato et al., 2010).

However, at the present time, unbaffled vessels are still preferentially adopted for the case of laminar mixing: they are preferred for this flow regime because in baffled systems some dead regions may exist in front of baffles. Moreover, at these low velocities, the swirling-tangential flow produced by a radial impeller is not so strong as to determine the formation of a pronounced vortex. In a such regime, some studies have shown the presence of two main poor mixing regions, bounded by surfaces with a typical toroidal shape, placed over and below the impeller respectively (Yianneskis et al., 1987; Dong et al., 1994; Lamberto et al., 1996; Lamberto et al., 2001; Alvarez et al. 2002). Such surfaces, separating the non-chaotic regions from the outside flow (except through molecular diffusion), are the known invariant tori described by the Kolmogorov-Arnold-Moser (*KAM*) theory (Fountain et al., 2000; Abatan et al., 2006). All the studies involving the laminar flow in unbaffled vessels have the same common aim, that is to break the poor mixing tori and to increase axial and radial mixing. Typical solutions provide the choice of a shaft eccentrically located (Montante et al. 2006; Galletti and Brunazzi, 2008) or the use of a time dependent angular velocity (Lamberto et al., 1996, Tezura et al., 2007; Yoshida et al., 2008).

1.5.2 Attractors for solid particles

It is quite known that in a solid-liquid flow, particles, as big as to consider any Brownian effect negligible, can follow streamlines up to reach non-trivial equilibrium positions in a number of different flow types (Segré and Silberberg, 1962; Mauri and Papageorgiou, 2002). Abatan et al. (2006) investigated this particle migration in a tank stirred by multiple impellers rotating at low velocities. They observed the migration of non-neutrally buoyant particles, both lighter and heavier than the continuous fluid (glycerine in their work), towards the two *KAM* tori and they investigated the non-trivial asymptotic behaviour of such a migration. They stated that both particle types can migrate across streamlines to position themselves

in repeatable equilibrium locations. In accordance with their study, such a behaviour is the result of a balance between: centrifugal buoyancy forces, wall interactions and particle inertial effects, as a function of the local shear environment.

The practical assessment of this phenomenon requires the adoption of a reliable and accurate measurement technique. LSIA technique was used to assess such a phenomenon.

1.5.3 Top-covered unbaffled tank stirred by standard Rushton Turbine with a clearance $C=T/3$: toroidal attractors for solid particles

Starting to operate from still conditions, all the particles begin to move from the bottom until they form the first torus (the *lower torus*) below the impeller. Increasing the impeller rotational velocity, some particles run away from the lower torus to constitute the *upper torus* in the upper part of the vessel. Increasing further the agitation velocity, the number of particles moving from the lower torus towards the upper torus increases gradually. Therefore, at high impeller speeds particles prefer the upper torus more than the lower one. This evolution is well captured by the LSIA technique and it is visible for 425-500 μm glass ballottini in Fig.1.16: at 300RPM particles are all over the bottom, some as sediment and some circulating within the lower torus, at 400RPM many of them move towards the upper part of the vessel and form the second upper torus, at 500RPM and finally at 600RPM the amount of particles shifting from the lower torus to the upper one increases with the angular velocity. In addition, at 600RPM all the particles are suspended and no sediments are present. At velocities much higher than 600RPM, i.e. about 800RPM for the present case (glass ballottini of 425-500 μm), all the particles leave the lower torus transferring themselves in the upper one. These very high velocities were not investigated since the seal between the shaft and the upper part of the cover becomes less effective and some air bubbles enter inside the vessel compromising the experiments. However, at these high velocities, all the experiments performed showed the existence of the upper torus only. It is worth noting that, negligible concentration of particles are present in other vessel zones at any agitation speed, because almost all particles are essentially attracted by the two tori.

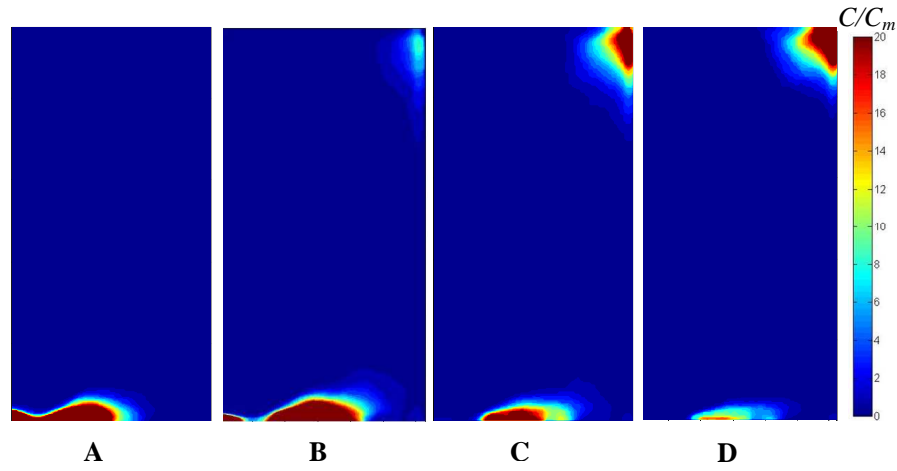


Fig. 1.16: Contour plots of solid concentration for 425-500 μm glass ballottini at: A) 300RPM; B) 400 RPM; C) 500 RPM; D) 600 RPM.

The same behaviour is observable in Fig.1.17 where the relevant radially averaged axial profiles are shown: increasing the impeller velocity, the particle concentration decreases in the lower part of the vessel (where the lower torus is located) and it increases at the quote where the upper torus is placed. Moreover such profiles confirm that almost all particles are essentially attracted by the two tori showing a very low concentration at any agitation speed in the rest of the tank.

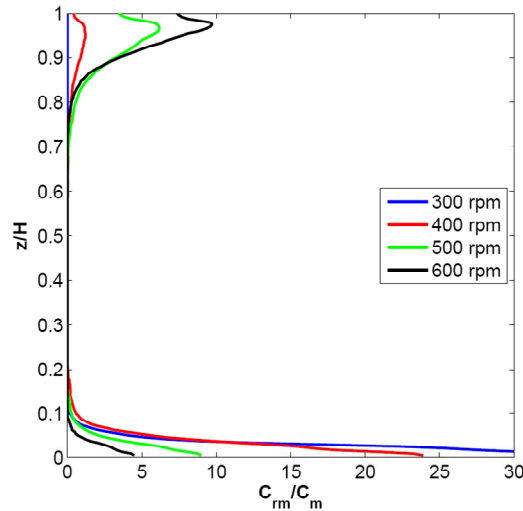


Fig. 1.17: Radially averaged axial profile for glass ballottini of 425-500 μm at different angular velocities.

The tori formation has been rarely investigated so far (Abatan et al., 2006). They are likely to result from the complex equilibrium arising among gravity, buoyancy, wall constraining reactions, centrifugal forces, drag forces and particles inertia.

It is a dynamic equilibrium because under turbulent fluctuations particles escape from one of the two attractors to assume a new equilibrium position in the other one. It is worth noting that such equilibrium result in two different stable positions below and upon the impeller thus leading to two tori with a different diameter: the upper torus has got a diameter comparable with the tank one, conversely the lower torus diameter is found to be significantly lower.

If particles were without their own inertia they would follow the liquid flow field and they would be distributed more or less homogeneously in all the vessel, on the contrary, increasing particle inertia, their tendency to constitute the tori likely increases consequently. In order to better clarify this relationship between particle inertia and tori attraction, the influence of particle diameter and density were investigated.

Figs.1.18 and 1.19 show the behaviour of 125-150 μm glass ballottini particles at different angular velocities. It is clear that particles however move preferentially in proximity of the two tori, in fact the particle concentration is higher in the upper and in the lower part of the vessel just where the two tori are placed. But particles with smaller size intrinsically possess a smaller inertia and are more subject to turbulent dispersion forces. This results in a higher homogeneity degree with respect to the case of larger particles.

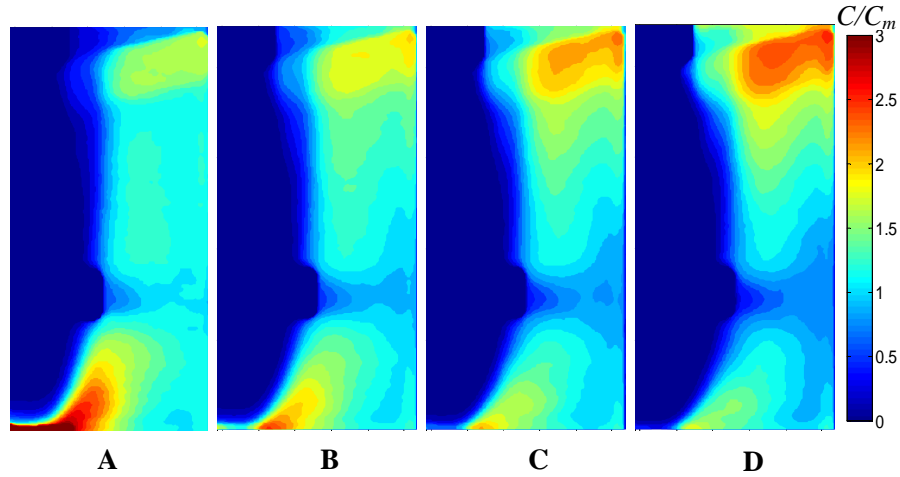


Fig. 1.18: Contour plot of glass ballottini of 125-150 μm at: A) 300RPM; B) 400 RPM; C) 500 RPM; D) 600 RPM.

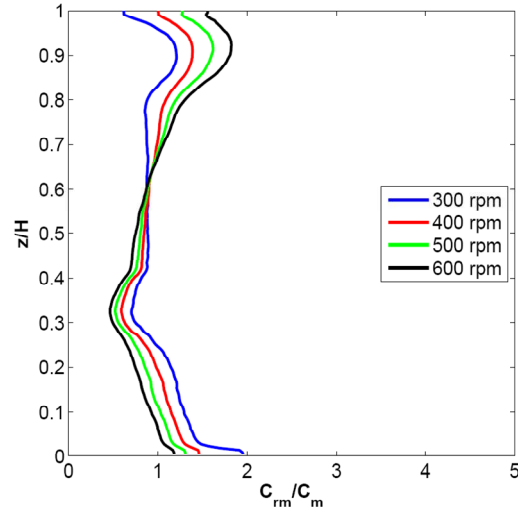


Fig. 1.19: Radially averaged axial profile for glass ballottini of 125-150 μm at different angular velocity.

The dependence of particle distribution on particle diameter is better shown in Fig.1.20 where contour plots and radially averaged axial profiles relevant to different particle size at constant agitation speed and particle density are shown. Larger particles are less dispersed and more concentrated in the tori zones because particles with a higher diameter have got higher inertia.

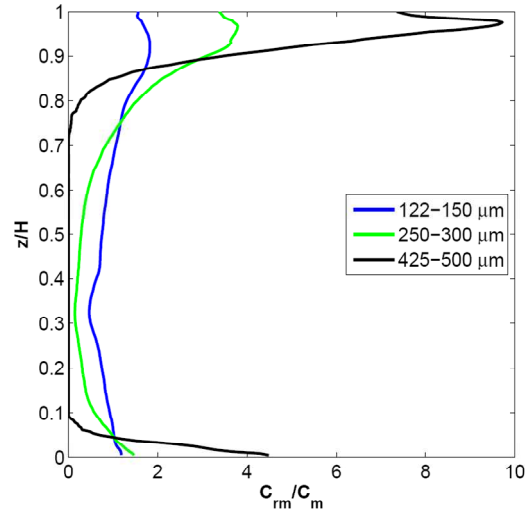
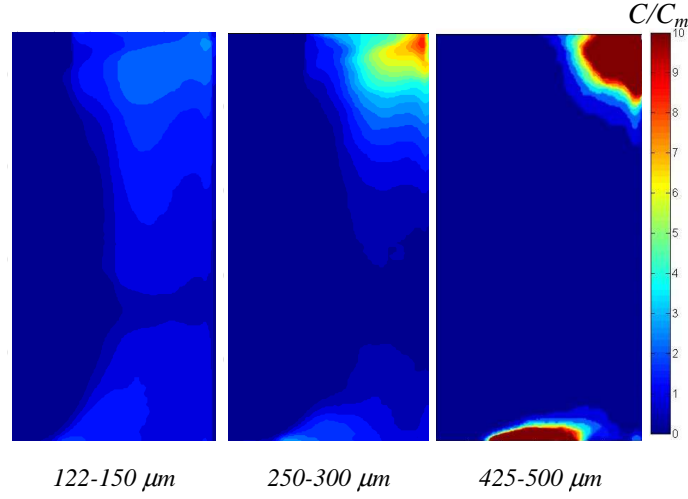


Fig. 1.20: Particle diameter influence: contour plots and radially averaged axial profile of glass ballottini of different size at 600RPM.

Also the effect of particle density on the two tori consistency was investigated and a representative example of the obtained results is reported in Fig.1.21. Increasing particle density at given agitation speed and particle diameter leads to an

increase of particle inertia. Even in this case the particle homogeneity degree decreases and the concentration consequently increases near the tori zones.

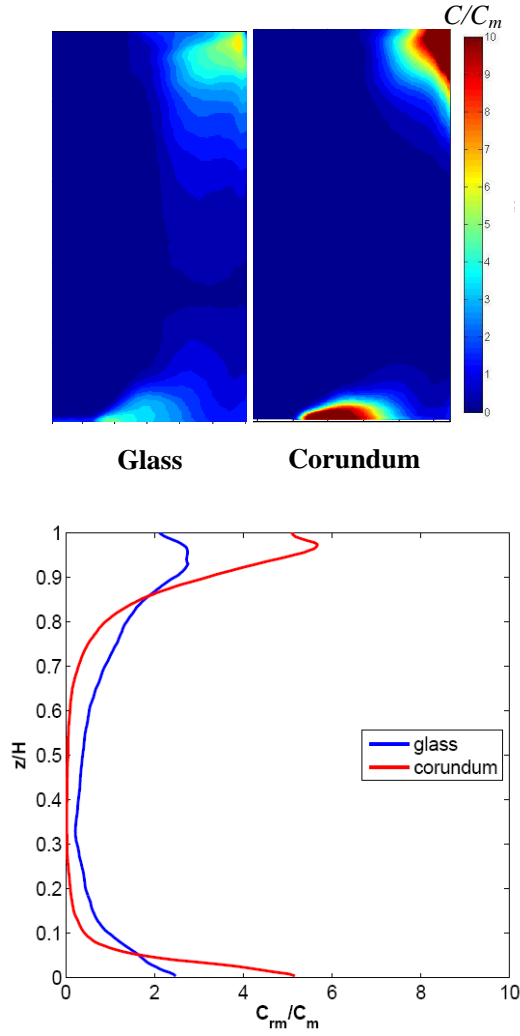


Fig. 1.21: Particle density influence: contour plots and radially averaged axial profile of 250-300 μm particles with difference density at 500 RPM.

Summarizing, particles with a higher inertia have got a higher tendency not to follow the liquid main flow and concentrate in the toroidal attractors, thus resulting in a lower dispersion degree.

The close effect of particle inertia on solid distribution degree was quantified by calculating the standard deviation of the normalized particle distribution matrixes: The standard deviation as defined by Bohnet and Niesmak (1980) is:

$$\sigma = \sqrt{\frac{1}{n} \sum_{i=1}^n \left(\frac{C_i}{C_m} - 1 \right)^2} \quad (1.7)$$

This value is commonly called standard deviation though it is actually a variation coefficient (i.e. a normalized standard deviation).

Results concerning the standard deviation are depicted in Fig.1.22, they confirm the considerations described so far.

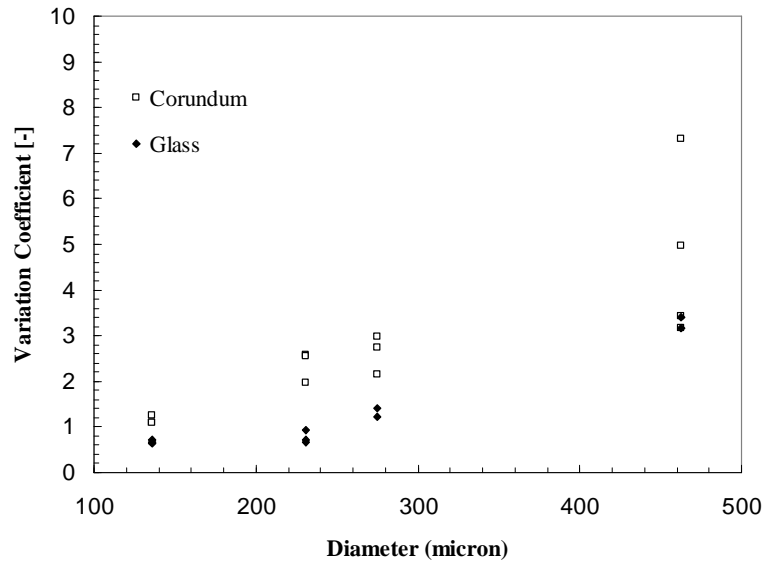


Fig. 1.22: Inertia influence on particle dispersion degree.

In this figure only the results relevant to cases where the agitation speed is higher than the just suspended speed are presented. This is because under incomplete suspension conditions the standard deviation would be heavily affected by the presence of particles resting on the bottom instead of circulating along the two toruses.

Finally, some experiments were carried out with 425-500 μm made-house particles in order to verify the effectiveness of light reflection removal procedure. Two identical set of particles were prepared with the procedure described along the paragraph 1.3.1, but for one of this set, no Rhodamine B was added for comparison purposes. The radially averaged axial profiles resulting from these experiments are shown in Fig.1.23: the two profiles are not the same, but they are quite similar confirming the soundness of the light reflections removal procedure and the reliability of the results presented so far.

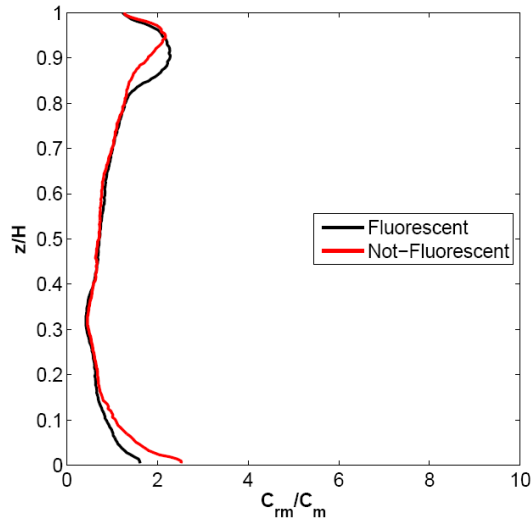


Fig. 1.23: Radially averaged axial profile of normalized solid concentration relevant to made-house particles of 425-500 μm (density of about 1400 kg/m^3) at 400RPM.

1.5.4 Top-covered unbaffled tank stirred by a marine propeller with a clearance $C=T/4$.

Propeller are very useful for mechanical mixing of *bulk motion controlled systems* like suspensions of solid particles into a liquid. Only some explorative experiments were carried out by adopting fluorescent particles of 425-500 μm (density of about 1400 kg/m^3). Five different impeller velocities were investigated and the relevant results are depicted in Fig.1.24.

A number of differences from the Rushton turbine system are observable. Clearly, distribution effects linked to the flow induced by a propeller show a mainly convective character, conversely, in the case of a Rushton turbine, distribution is strictly close to turbulence.

At very low velocities (200RPM) a big grouping of particles is present on the tank bottom underneath the propeller. These grouped particles are not a stable sediment, but they move dynamically rolling upon the bottom. In fact just suspension speed N_{js} was estimated by visual observation and found lower than 200RPM. Increasing agitation speed the extent of this *dynamic sediment* gradually decreases and almost disappears at 600RPM.

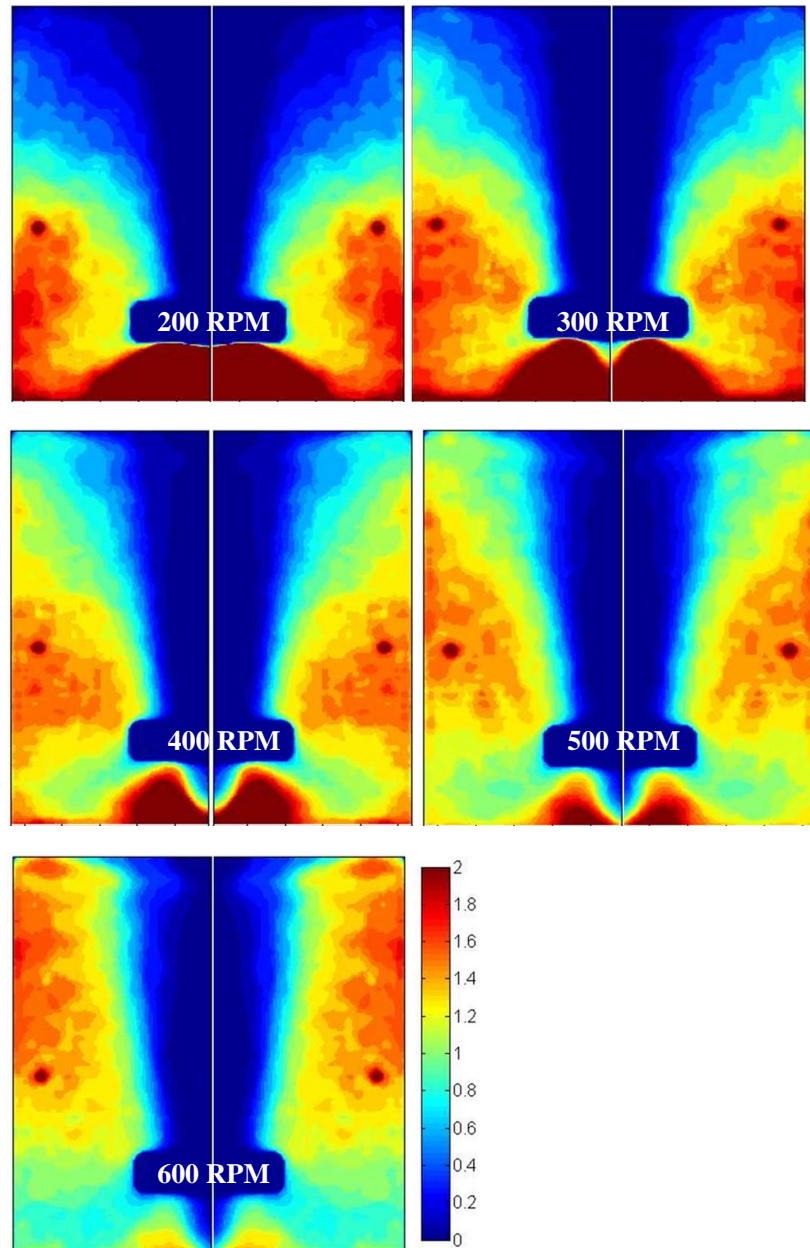


Fig. 1.24: Contour plots of normalized solid concentration for 425-500 μm fluorescent particles at different propeller rotational velocities.

However, no attractors for solid particles were recognized in this case. Starting from 200RPM and increasing propeller angular velocity, particles do not move from the dynamic sediment to constitute a lower torus on the vessel bottom, liquid radial velocities and centrifugal forces act towards the same directions, on the contrary they oppose each other in the Rushton turbine system. By the way, the dynamic sediment presence appears quite stable, though reduced, even at high velocities suggesting that considering liquid flow as characterized by a single circulation loop is too simplistic. Probably the fluid pumped by the propeller moves away from the axis due to flow radial components, thus generating flow lines lapping on the dynamic sediment. Contemporaneously, a smaller secondary circulation loop (whose character is turbulent) is present just below the propeller driving the sediment in the opposite direction, i.e. towards the lateral wall (see Fig.1.25).

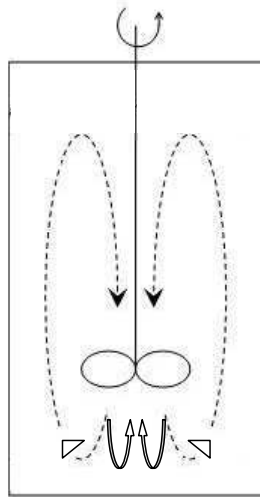


Fig. 1.25: Sketch of liquid flow circulating rings in a top-covered unbaffled tank stirred by a marine propeller

These two effects are contrary, they generate different equilibrium conditions at different angular velocities: at high velocities the secondary ring effect increases because of higher turbulence thus favoring the suspension of a higher amount of particles from the dynamic sediment. In addition, an increase in propeller rotational velocity leads the primary circulation loop to increase its extension, thus allowing more suspended particles to reach higher heights before moving downwards towards the propeller. This effect is clearly observable in Fig.1.24: at a given angular velocity, particle concentration is higher just where axial velocities are low and residence times are consequently high. However, as shown in Fig.1.26, no clear liquid layer is visible at all the investigated velocities. This figure confirms that an increase in impeller speed leads to a decrease of normalized solid concentration in the lower part of the vessel and a consequent increase in the upper part of the vessel.

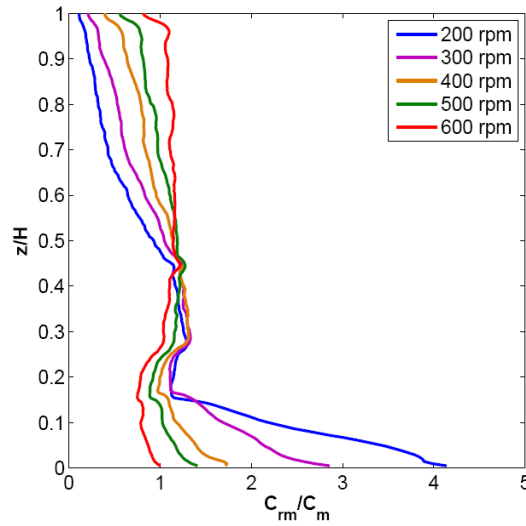


Fig. 1.26: Radially averaged axial profiles of normalized solid concentration for 425-500 μm fluorescent particles at different propeller rotational velocities.

By comparing these results with the ones obtained in the case of the radial impeller it is clear that the two impeller provide a very different effect on solid particle distribution. Increasing rotational speed the propeller generates a better dispersion of solid particles, conversely, Rushton turbine leads to concentrate them towards the two tori. This evidence suggests the adoption of one impeller instead of the other depending on the kind of process involving. The different behaviour shown by the two cases is also visible in Fig.1.27 where standard deviation are compared at different rotational speed for the same particles: marine propeller tendency to particle dispersion is represented by a decrease in standard deviation with impeller speed, conversely, Rushton turbine effect of particle concentration is represented by an increase of standard deviation.

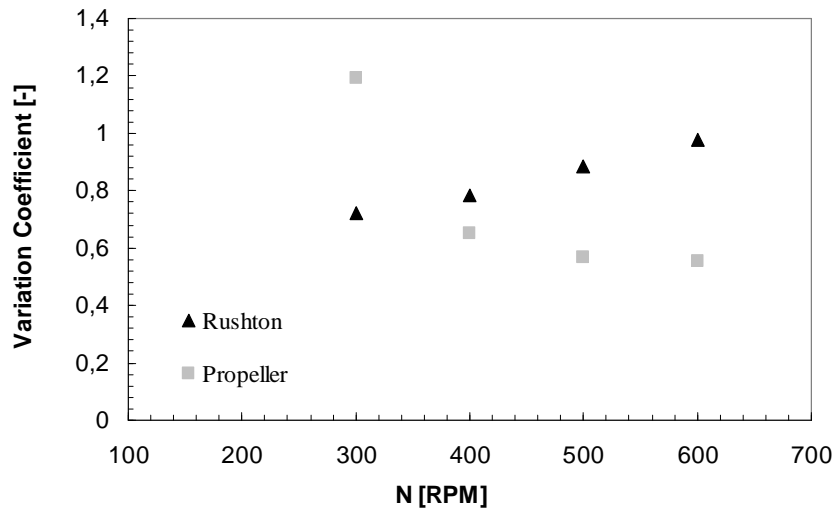


Fig. 1.27: Comparison of standard deviations for the two types of impeller (425-500 μm fluorescent particles).

1.6 Final remarks

A novel very simple technique named *Laser Sheet Image Analysis* for solid concentration assessments in dilute solid-liquid stirred vessels was developed and accurately described. It is not-invasive allowing to get experimental information on particle distribution without adopting any equipment inside the investigated system and consequently avoiding possible result alteration. This innovative technique appears to be very promising: it is characterized by a good reproducibility and result reliability. It is able to provide directly 2-D (composed of about 35'000 point by point measurement information) solid particle distribution maps in stirred tanks without requiring neither too complex and long elaborations nor too expensive measurement apparatuses. In addition, it could be possible to use LSIA technique to get simultaneous PIV information on fluid flow field inside the vessel simply by using another acquisition camera (Unadkat, 2009).

Anyway, the technique development is at the beginning and there is still room for future improvements. At the present time *LSIA* main limit is represented by solid concentration. As all other optical techniques, *LSIA* cannot be applied to dense solid-liquid systems because the laser ray is not able to cross high solid concentration suspensions. Ad-hoc experiments aimed to quantify such a limit were not carried out. By the way, it is possible to resolve this drawback simply coupling *LSIA* technique with a suitable *Refractive Index Matching* of the two phases (Cui and Adrian, 1997; Micheletti and Yianneskis 2004, Virdung and Rasmuson, 2008).

In this study *LSIA* technique was applied to solid-liquid dispersions in two different unbaffled vessels both provided with a cover at the top: one stirred by a standard six bladed Rushton turbine with a diameter $D=T/2$ placed at a clearance $C=T/3$, the other stirred by a marine propeller with a diameter $D=T/2.4$ placed at a clearance $C=T/4$.

Visual observations of the first unbaffled system show the existence of two stable toroidal attractors for non-Brownian solid particles heavier than the fluid. The existence conditions and possible influences on the formation of these two tori for solid particles were investigated. *LSIA* technique was found be very useful and promising: it was able to reproduce the same system behaviour visually observed.

Results showed that particle diameter and density affect the attraction of the two tori and the particle suspension degree consequently. By discussing these results it can be stated that the tori formation, opposing to particle dispersion, is favoured by an increase in particle inertia properties.

Conversely, no attractors for solid particles were recognized in the system stirred by the marine propeller. Analysis of the collected data suggests that the fluid flow field is characterized by two contrasting circulation loops generating different equilibrium conditions at different angular velocities.

Finally, it can be stated that *LSIA* technique can be successfully applied to solid-liquid dispersions providing useful data which may constitute a good validation tool for computational studies.

1.7 Nomenclature

A_{mean}	mean particle area, m^2
A_{min}	minimum particle area, m^2
C	impeller clearance, m
$C_{r,z} / C_i / C$	local particle concentration, g/l
C_{rm}	radially averaged particle concentration, g/l
C_m	mean particle concentration, g/l
$counts_{r,z}$	probability of finding a particle at a given r,z position, (-)
D	impeller diameter, m
d	impeller disc diameter, m
H	fluid height in the vessel, m
K	constant which allows the shift from local probability to normalized local concentration value, (-)
l	impeller blade width, m
$M_{r,z}$	local solid mass value, g
M_{tot}	total solid mass value, g
n	number of cells within the matrix, (-)
N	impeller speed, RPM or RPS

N_{js}	<i>minimum impeller speed for complete off-bottom suspension, RPM</i>
r	<i>radial coordinate, m</i>
R	<i>tank radius, m</i>
T	<i>tank diameter, m</i>
w	<i>impeller blade thickness, m</i>
z	<i>axial coordinate, m</i>

Greek letters

α	constant which allows the shift from local probability to local concentration value, g/l
σ	variation coefficient, (-)

CHAPTER 2

STEADY CONE RADIUS METHOD (SCRM)

2.1 Abstract

As already emphasized in Chapter 1, unbaffled stirred tanks are seldom employed in the process industry as they are considered poorer mixers than baffled vessels. However they may be expected to provide significant advantages in a wide range of applications (e.g. crystallization, food and pharmaceutical processes, etc) where the presence of baffles is often undesirable. In this second Chapter solid-liquid suspensions in an unbaffled stirred tank are investigated. The tank was equipped with a top-cover in order to avoid vortex formation. A novel experimental method (the “*steady cone radius method*”, *SCRM*) was proposed to determine experimentally the minimum impeller speed at which solids are completely suspended. Experimental N_{js} and power consumption data were provided over fairly wide ranges for particle size, density and concentration. N_{js} dependence on fluid viscosity and system scale was investigated as well. Dependence of N_{js} on particle density and concentration was similar to that observed in baffled tank. Conversely, a negligible dependence of N_{js} on particle diameter was observed in the unbaffled tank, a difference from baffled vessels with important practical implications: it may advice the adoption of unbaffled tanks when large heavy particles are to be dealt with. As another difference from baffled vessels N_{js} was found to decrease when liquid viscosity increases.

The mechanical power required to achieve complete suspension in unbaffled tanks is shown to be much smaller than in baffled vessels. This, in conjunction with a previously ascertained excellent particle-fluid mass-transfer promotion (Grisafi et al., 1994), could make unbaffled tanks a best choice for many solid-liquid operations where mass transfer is the main limiting factor.

On the other hand, a smaller exponent for the scale-up rule was found with respect to baffled tanks, which implies the need for larger specific power

consumptions the larger the vessel size and may limit useful applications to small to medium plant sizes. Finally, a correlation akin to Zwietering's correlation was proposed for top-covered unbaffled stirred tanks.

2.2 Literature review

Mechanically agitated vessels are widely employed for a variety of chemical processes involving particulate solids suspension. Almost invariably the solid phase is required to participate in mass transfer phenomena, and therefore it is important to provide enough agitation to suspend all particles. Below this full suspension state the total solid-liquid interfacial area is not completely or efficiently utilized, while above this speed the solid-liquid mass transfer rate increases only slowly with agitation intensity.

Many research efforts have been devoted to the determination of the minimum rotational speed required to attain full particle suspension, N_{js} , and its dependence on a number of geometrical, physical, and operational variables (Zwietering, 1958, Nienow, 1968, Baldi *et al.*, 1978, Raghava Rao and Joshi, 1988, Armentante and Nagamine, 1998, among the others). A number of studies focused on three phase systems; among these Nienow *et al.*, (1986), Frijlink *et al.*, (1990), Micale *et al.*, (2000), Dohi *et al.*, (2004) addressed the problem of correlating the agitator speed for complete suspension under gassed conditions. Recently Kuzmanic and Lubic (2001), Bao *et al.* (2005), Tagawa *et al.* (2006), investigated the draw-down of floating solid particles in aerated baffled vessels.

Many of these works relied on the visual assessment of N_{js} according to the method first introduced by Zwietering (1958) which, apart from being subject to substantial uncertainties, gives no information on what happens at agitation speeds below N_{js} . Many other methods and techniques, both experimental and theoretical, were adopted in order to evaluate this minimum agitation speed for complete solid suspension. For full details regarding all the existing techniques as well as their advantages and limits refer to Chapter 5. Another fundamental parameter regarding particle suspension performance within stirred tank is the Power Number: it is a

dimensionless number which indicates the mechanical power requirement for a given impeller size and velocity. A significant effort has been devoted so far to investigating the power consumption requirements of solid liquid suspensions in baffled stirred tanks (Bohnet and Niesmak, 1980; Chudacek, 1982; Raghava Rao *et al.*, 1988; Rewatkar *et al.*, 1991; Bubbico *et al.*, 1998; Bujalski *et al.*, 1999; Micheletti *et al.*, 2003) as well as in aerated solid liquid stirred vessels (Frijlink *et al.*, 1990; Pantula and Ahmed, 1997; Birch and Ahmed, 1997).

Bohnet and Niesmak (1980) were the first to show that Power Number depends on particle loading. Bubbico *et al.* (1998) highlighted that the increase in power consumption due to the presence of particles cannot be satisfactorily predicted by simply substituting the average suspension density for liquid density. This is especially true when large particles are involved and particle fraction exceeds 4% by volume, allegedly due to energy dissipations connected with solid-liquid friction and particle-particle collisions. Also Micheletti *et al.* (2003) investigated Power Number (N_p) dependence on impeller speed, particle loading and particle size, for baffled tanks stirred by a Rushton turbine. They observed that N_p increases with N until complete suspension conditions are achieved. At higher rotational speeds they did not observe further variations of N_p , whose final values (computed by considering the average mixture density) did not exactly collapse on the relevant single phase (liquid-only) value, as a difference from Heringe, (1979).

A similar trend of N_p versus N was observed by Raghava Rao *et al.* (1988) and by Rewatkar *et al.* (1991). These authors also suggested that N_{js} may be directly assessed from power measurements as the first impeller speed at which N_p reaches its final constant value. Finally, for a tank equipped with a propeller Bohnet and Niesmak (1980) found an increasing-decreasing behaviour of N_p with a relative maximum practically coinciding with N_{js} .

Very little attention has been devoted so far to solid-liquid suspension in *unbaffled* stirred tanks. Very few works have addressed so far such topic. These concern unsteadily forward-reverse moving impellers, either rotating (Tezura *et al.*, 2007; Yoshida *et al.*, 2008) or axially moving (Hirata *et al.* 2009). In particular Tezura *et al.* (2007) experimentally assessed just suspended conditions and the

relevant power consumption. Their results were found to follow a slightly modified version of the well known Zwietering's equation commonly employed for baffled tanks (Zwietering, 1958). In addition, the just suspended power consumption was found to be lower than that required in a conventional baffled tank. Yoshida *et al.* (2008) measured the liquid and particle flow fields, while Hirata *et al.* (2009) measured power consumption and mixing times in particle suspensions by using a mixing system with a disk impeller moving up and down in a cylindrical vessel (recipro-mixing).

In the present chapter the problem of particle suspension in unbaffled tanks stirred by common (continuously rotating) impellers is addressed for the first time. A special “*steady cone radius method*” (*SCRM*) was devised to assist the N_{js} assessment. Power consumption measurements for a number of operating conditions were also performed. Finally, just suspended power requirements (power consumption corresponding to the N_{js} value) were collected and compared with the relevant values in baffled tanks. The vortex formation problem has been addressed and resolved by the adoption of a top-cover. It is worth noting that, though this choice limits the extent of the present PhD work to a specific system, it represents an easy design solution to avoid vortex formation.

2.3 Experimental information

2.3.1 Investigated systems

Experiments were performed using a cylindrical tank with internal tank diameter $T=0.19\text{m}$ and square configuration ($H=T$), equipped with a six bladed Rushton turbine with diameter equal to $T/2$ and impeller clearance equal to $T/3$, (Fig.2.1).

A bigger unbaffled tank was used to investigate scale-up effects. This bigger tank was geometrically similar to the former and had a diameter $T=0.48\text{m}$ (Fig. 2.2).

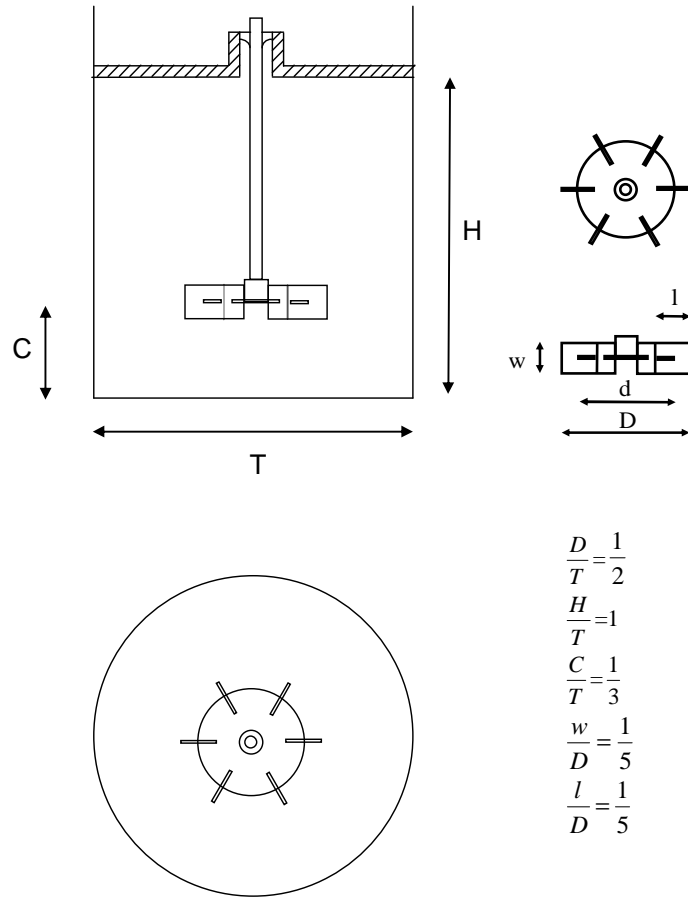


Fig. 2.1: Stirred vessel employed for the experimentation ($T=0.19$ m).

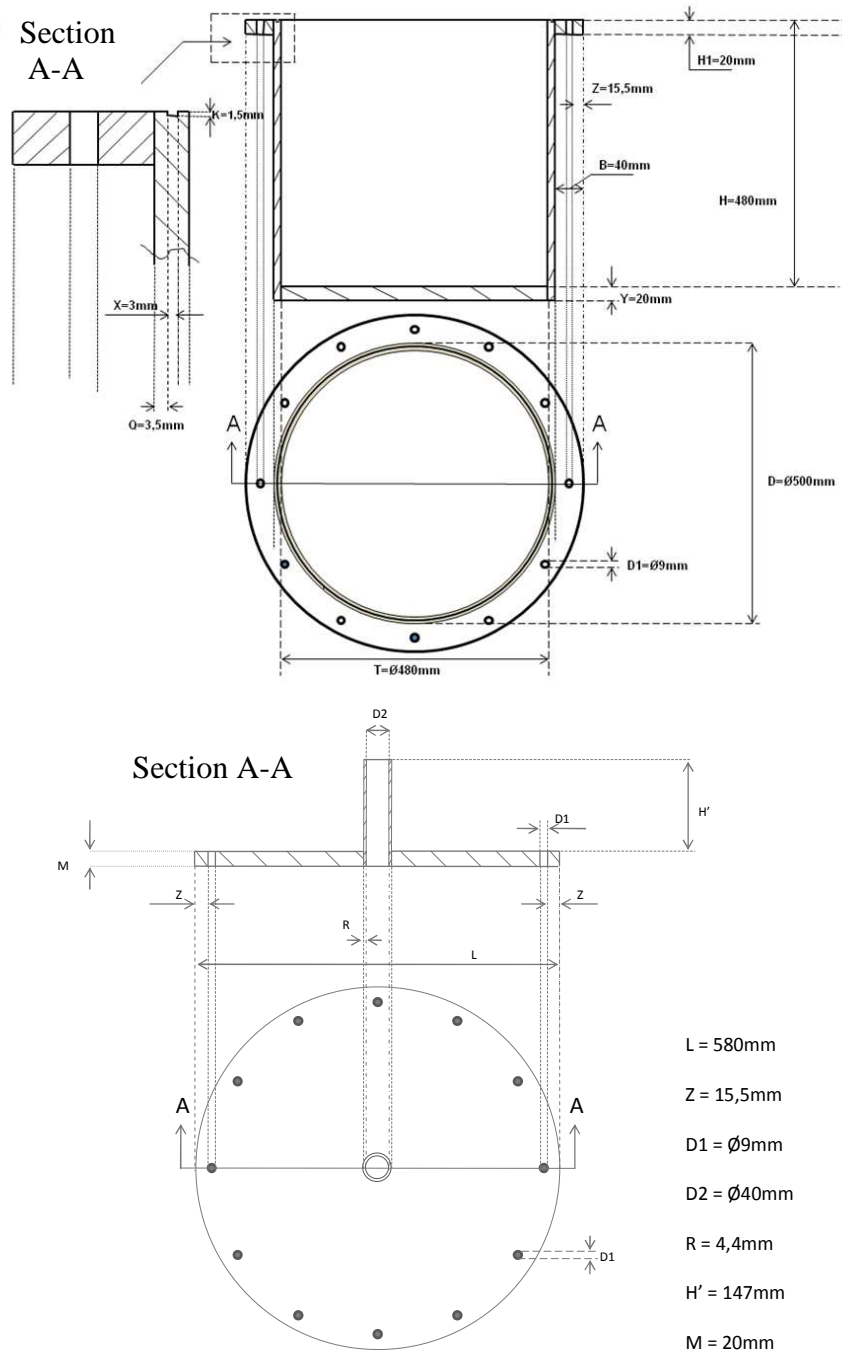


Fig. 2.2: Big stirred vessel employed for the experimentation ($T=0.48\text{ m}$) and its relevant cover (below).

The tank was provided with a top-cover to avoid vortex formation on the free surface. The seal between the cover and the tank was guaranteed by a gasket o-ring. A plexiglass vessel together with a transparent support and a 45° inclined mirror (positioned below the tank support) were used in order to ease visual observation of tank bottom. A simple compact digital camera, allowing shutter speed to be manually set, was used for image acquisition. The mirror was employed only for visual observation while the digital camera was used for N_{js} assessment.

Distilled water and solid particles of different materials and size, as summarised in Table 2.1, were employed for the experimentation.

Material	dp [μm]	average dp [μm]	Density [kg/m^3]	Particles concentration [%w/w]
Silica particles	212-250	231	2400	2.5 – 5 – 7.5 – 10 – 12.5
	250-300	275	2400	2.5 – 5 – 7.5 – 10 – 12.5
	355-425	390	2400	2.5 – 5 – 7.5 – 10 – 12.5
	425-500	463	2400	2.5 – 5 – 7.5 – 10 – 12.5
	500-600	550	2400	2.5 – 5 – 7.5 – 10 – 12.5
	850-1000	925	2400	2.5 – 5 – 7.5 – 10 – 12.5
Glass ballottini	500-600	550	2500	2.5 – 5 – 7.5 – 10 – 12.5
	850-1000	925	2500	2.5 – 5 – 7.5 – 10 – 12.5
Corundum	212-250	231	3850	2.5 – 5 – 7.5 – 10 – 12.5
	425-500	463	3850	2.5 – 5 – 7.5 – 10 – 12.5
	500-600	550	3850	2.5 – 5 – 7.5 – 10 – 12.5

Tab. 2.1: Experimental suspensions investigated.

Different ratios of water and glycerol were used to prepare solutions of different kinematic viscosity ν . Standard Ubbelohde viscometers (Fig. 2.3) were employed to measure the viscosity of these solutions.

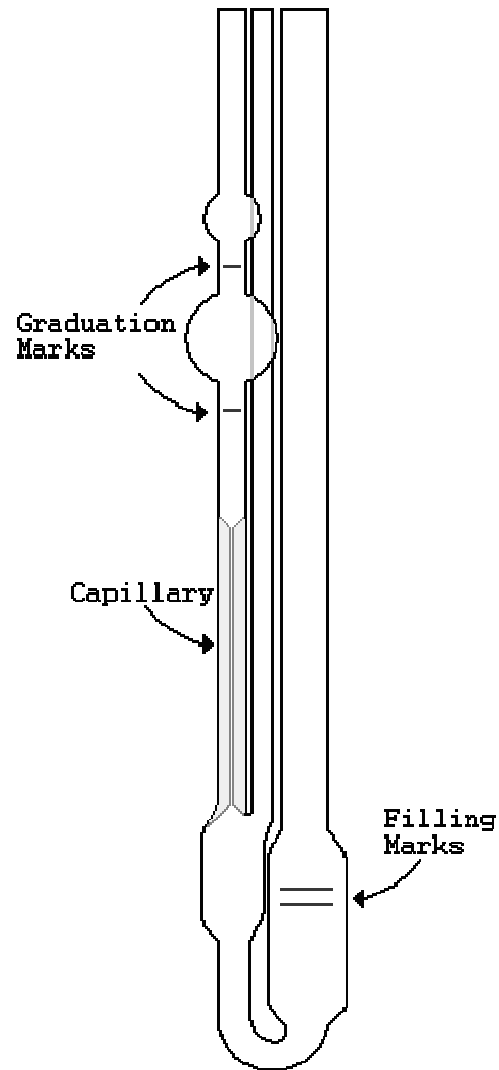


Fig. 2.3: Standard Ubbelohde viscometer employed for measurements

2.3.2 Steady Cone Radius Method (SCRM)

Particle “just suspended” conditions may refer to the original Zwietering definition (off-bottom suspension) or to “on-bottom” suspension (more realistic with heavy particles). In any case what is important is insuring that the surrounding liquid phase is continuously renewed around all particles so that they are allowed to effectively participate into mass transfer phenomena.

For N_{js} assessment, in the present case, a suitable “*steady cone radius method*” (SCRM) was devised to assist the identification of on-bottom just-suspended conditions in unbaffled vessels. It takes advantage from the observation that in the unbaffled vessel here adopted, at any rotational speed below N_{js} the unsuspended particles form a sort of steady cone laying over bottom centre. The steady cone radius is quite easily discriminated from the moving particles in images of the tank bottom taken with relatively low shutter speeds (large image capture times), as steady particles are neatly visible while moving particles are strongly blurred and therefore can be easily distinguished from the former, as it can be observed in Fig. 2.4.

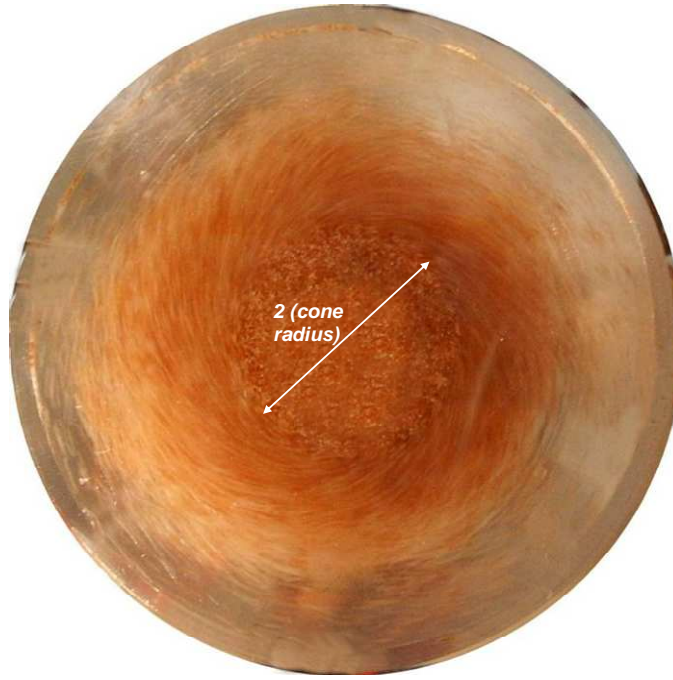


Fig. 2.4: Picture of tank bottom with indication of the solid cone radius (silica particles, $d_p=850-1000 \mu\text{m}$, $B=5\%$, $N=250 \text{ rpm}$).

The exposure times needed are typically of the order of one tenth of second, though larger exposure times are even more effective. All the acquired images are collected and then analyzed after the end of the experiment. Cone radius measurement is performed by comparing the observable cone radius with a reference length included in all images. The steady particle cone radius decreases while increasing rotational speed, as shown in Fig.2.5. The observed trend can therefore be exploited for reducing the uncertainties on the exact velocity at which no particles remain steady on the tank bottom, as illustrated in Fig.2.5. The SCRM has the advantage of avoiding measurement subjectivity and was found to result into excellent reproducibility: even changing the operator, errors remain lower than 5%. A graph similar to that shown in Fig.2.5 was obtained for all the cases here investigated, so resulting in the relevant N_{js} values.

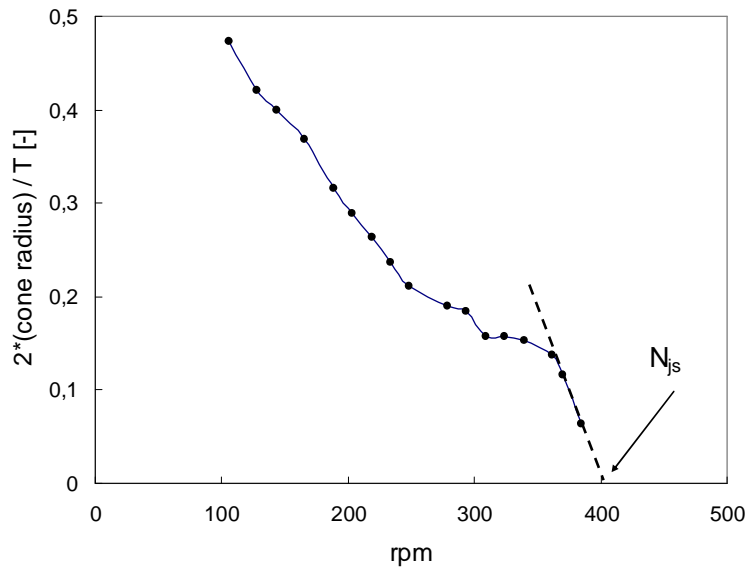


Fig. 2.5: Typical trend of particle-cone-radius versus impeller speed with linear extrapolation of the last data points to locate N_{js} (Silica particles, $d_p=231 \mu\text{m}$, $B=2.5\%$)

2.3.3 Power consumption assessment apparatus

Power measurements were finally performed by assessing the torque transmitted by the impeller to the tank with the apparatus described in Grisafi et al. (1998). A sketch of the power measurement apparatus is conveniently depicted in Fig. 2.6. It is a “static-frictionless” turntable consisting of a granite dish (D) able to rotate around its central axis: this dish is provided with a pivot pin (protruding from its lower surface centre) that is inserted inside a hard steel tube placed in the upper part of a granite table surface (C). Clearly, the facing surfaces of the granite dish and the granite table are suitably polished. This tight coupling pivot pin-steel tube and the polished surface coupling are lubricated by means of a small flow rate (about 2 millilitres per minute) of a fairly viscous oil coming from a reservoir (B). The oil

was fed by compressing the camera (B) by compressed air (over pressure of about 2 atm) coming from a valve (A). This arrangement practically deleted the static friction between the surfaces, but allowing the dynamic friction to be present in order to damp unavoidable oscillations of the torque. The tank (E) was placed on the granite dish in order to rotate integrally with it. This rotation (induced by the stirrer rotation during experiments) is hampered by a flexible nylon thread, tightly attached to the external vessel wall and connected by a pulley (G) to a weight (H) (of about 2 kg) which is placed upon an electronic balance (I).

Practically, the torque exerted by the stirrer on the vessel was assessed by measuring the force acting on the flexible string in order to inhibit vessel rotation. This force was measured by subtracting the reading of the balance in agitation conditions from that observed without agitation (still stirrer).

Measurement are estimated to be around ± 0.05 Newton. This order of magnitude of errors did not significantly affect the precision of the measurements performed. Notably, errors are most recorded at very low impeller speeds, so measurements were taken by approaching the desired agitator speed from both higher and lower speeds, and then taking the arithmetic mean of the two readings obtained.

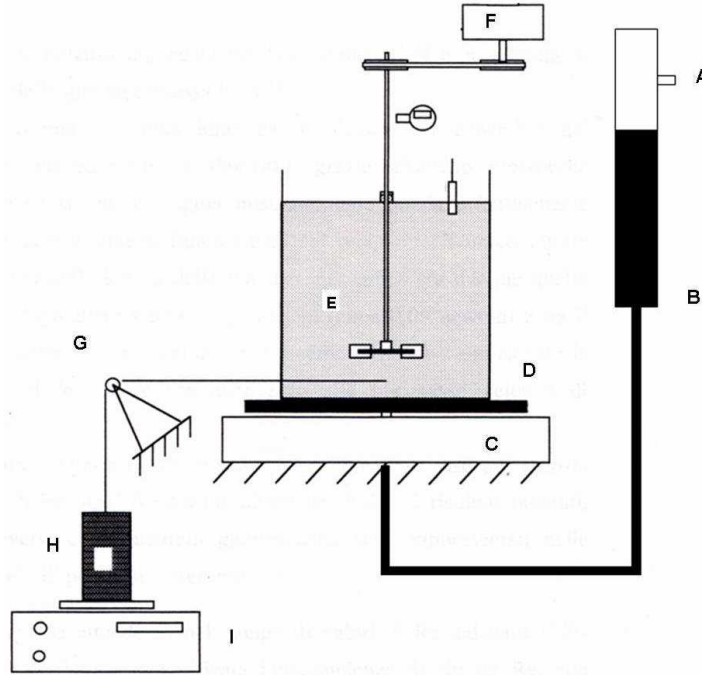


Fig. 2.6: Power measurement apparatus: A) compressed air inlet; B) compressed oil tank; C) granite plane; D) rotating granite disc; E) tank; F) DC motor; G) pulley; H) weight, I) electronic scale.

2.4 Just suspended speed (N_{js}) measurements

Firstly, N_{js} dependence on particle concentration, particle diameter and particle density was investigated.

2.4.1 N_{js} dependence on solid concentration B

In Figs. 2.7 a, b and c the dependence of N_{js} on particle concentration (B , %) is reported for silica, glass and corundum particles respectively.

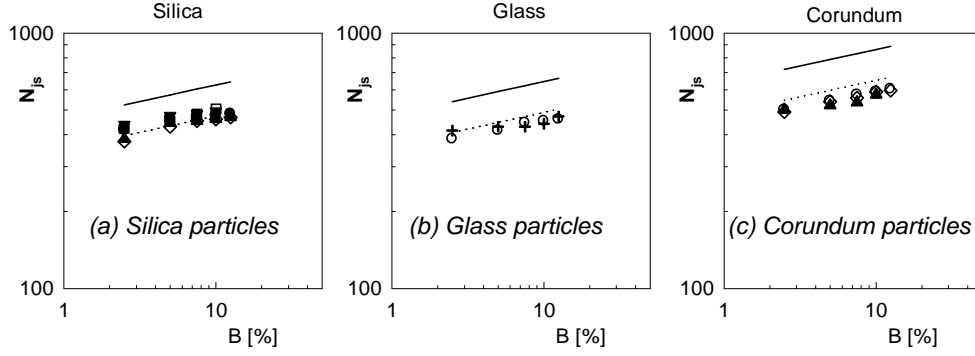


Fig. 2.7: Dependence of N_{js} on particle concentration. Symbols: particle size [μm]: ▲ 231; ● 275; □ 390; ◇ 462; ○ 550; +1000. Lines report Zwitering's correlation for standard baffled system (Eq. 1): dotted line, $d_p=231$ μm; solid line, $d_p=925$ μm

In the same figures, lines reporting the relevant N_{js} values predicted by the well known Zwitering's correlation (Zwitering, 1958) for standard baffled vessels (S=5.2, Nienow, 1968) are also reported for comparison purposes (Eq. 2.1).

$$N_{js} = \frac{S \cdot v^{0.1} \cdot d_p^{0.2} \cdot \left(\frac{g \cdot \Delta \rho}{\rho_L} \right)^{0.45} \cdot B^{0.13}}{D^{0.85}} \quad (2.1)$$

Only the lowermost (smallest particle size) and the uppermost (largest particle size) lines are shown. As it can be seen, in the top-covered unbaffled vessel the N_{js} dependence on particle concentration seems to be very similar to that predicted by Zwitering's correlation for baffled tanks ($N_{js} \propto B^{0.13}$). Notably most of the data points obtained in the unbaffled tank are below the dotted lines, which implies that most of the N_{js} values obtained in the unbaffled tank are significantly smaller than the relevant values in baffled systems. The only exception is the case of the smallest silica particles, for which the two values of N_{js} are almost identical (Fig. 2.7a).

2.4.2 N_{js} dependence on particle diameter d_p

In Figs 2.8 a,b,c the unbaffled N_{js} values obtained are reported versus particle size. On the same figures Zwietering's predictions for the lowest and highest particle concentrations (for baffled tanks) are also reported for comparison purposes.

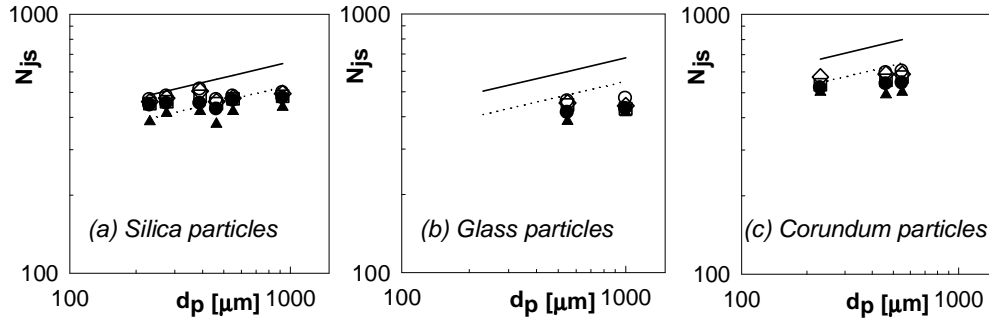


Fig. 2.8: Dependence of N_{js} on particle size. Symbols: B%: ▲ 2.5; ● 5.0; □ 7.5; ◇ 10.0; ○ 12.5. Lines report Zwietering's correlation for standard baffled system (Eqn. 1): dotted line B=2.5%; solid line B=12.5%.

It can be seen that, as a difference from particle concentration, the dependence of N_{js} on particle size for top-covered unbaffled tanks is much weaker than for baffled tanks (a feature that could have been noticed also by closer inspection of Fig. 2.7). In practice, all the points relevant to different particle mean diameters at the same particle concentration are quite well fitted by lines with a negligible slope.

In order to verify this singular finding, other specific experiments were carried out and discussed (Fig. 2.9a): particularly, N_{js} was assessed for the cases of 275 μm and 655 μm (mean diameter) silica particles at different particle concentrations and no differences (at a given solid loading) were found. Mixture of these two particle types (resulting in a suspension with a bimodal distribution of solid particles) provided the same results as well. Analogous experiments were provided by

employing silica un-sieved particles whose particle size distribution cumulative curve is plotted in Fig. 2.9b. At $B=2.5\%$ and $B=5\%$ identical N_{js} values were obtained while at $B=10\%$ a lower N_{js} was found. This finding is allegedly due to the lower voidage of the particle bed: this leads to a reduction of the flow able to cross the bed and the lateral thrust undergone by the sediment increases consequently. At N_{js} the sediment shows a rigid motion where interstitial liquid is scarcely replaced, thus suggesting that *SCRM* may be misleading in this case.

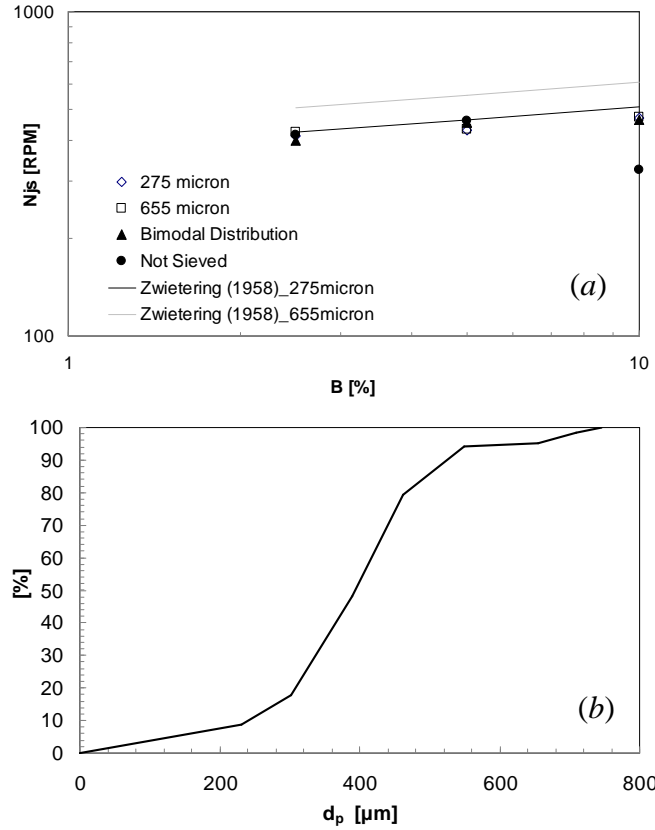


Fig. 2.9: (a) dependence of N_{js} on particle diameter (and solid concentration); (b) particle size distribution cumulative curve for the case of not sieved particles.

This finding marks an important difference between unbaffled and baffled tanks as concerns their particle suspension capabilities: in top-covered unbaffled systems one may ideally think to use particles of larger size without sensibly increasing the impeller speed needed to achieve complete suspension conditions. Clearly extrapolation of this result outside the size range here investigated is risky, as one may guess that this behaviour cannot be extended to very large particle sizes.

2.4.3 N_{js} dependence on normalized relative density $\Delta\rho/\rho_L$

Finally, N_{js} dependence on relative density difference between particles and liquid ($\Delta\rho/\rho_L$) is reported in Fig. 2.10, where the N_{js} values obtained for different solid concentrations and three different particle diameters are reported.

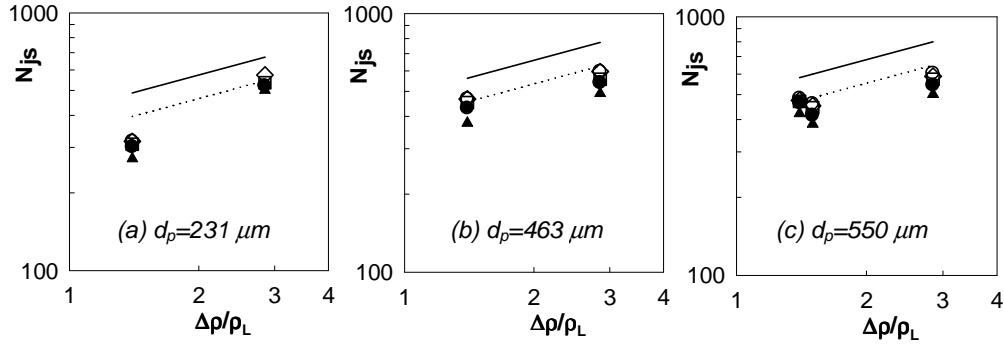


Fig. 2.10: Dependence of N_{js} on relative density difference ($\Delta\rho/\rho_L$). Symbols: particle concentration B%: \blacktriangle 2.5; \bullet 5.0; \square 7.5; \diamond 10.0; \circ 12.5. Lines report Zwiering's correlation for standard baffled system (Eq. 1): dotted line B=2.5%; solid line B=12.5%.

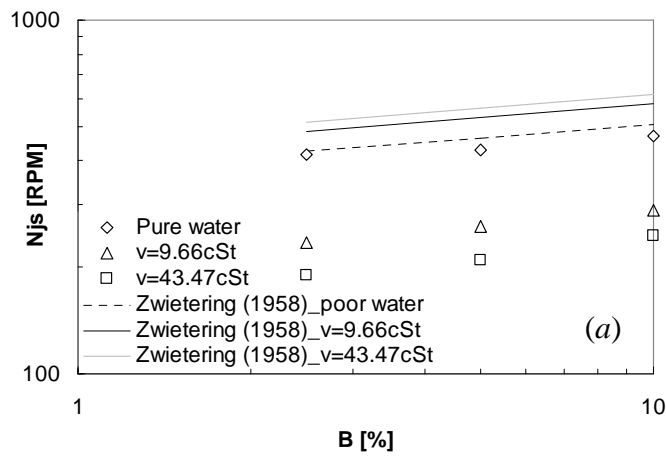
Also in this figure the two lines reporting the N_{js} values assessed by means of the Zwiering's correlation for the lowest and the highest solid concentration values (2.5% and 12.5%) are reported for comparison purposes. As it can be seen here, N_{js} shows a dependence similar to that predicted by the Zwiering's correlation, i.e. a dependence of N_{js} on ($\Delta\rho/\rho_L$) with an exponent of 0.45, with the only exception of

particles with the smallest size (231 μm) for which a stronger dependence seems to apply.

These results are similar to those obtained by Tezura *et al.* (2007) in an unsteadily stirred unbaffled vessel with the exception of the N_{js} dependence on particle size, that in their system was similar to Zwietering's one. The different behaviour observed with the present system concerning N_{js} dependence on particle size may be explained by considering that in the present case the particle suspension mechanism may be well different and likely to be related to fluid mean velocities near tank bottom rather than to velocity turbulent fluctuations, as is instead the case of both baffled tanks and unsteadily stirred unbaffled tanks. In any case, this finding suggests that top-covered unbaffled tanks may be much better suited than baffled tanks when relatively large particles need to be suspended in liquid phases.

2.4.4 N_{js} dependence on fluid kinematic viscosity ν

As far as N_{js} dependence on kinematic viscosity is concerned, Fig. 2.11 shows that an increase in kinematic viscosity leads to a large decrease of N_{js} (for both the investigated particle diameters).



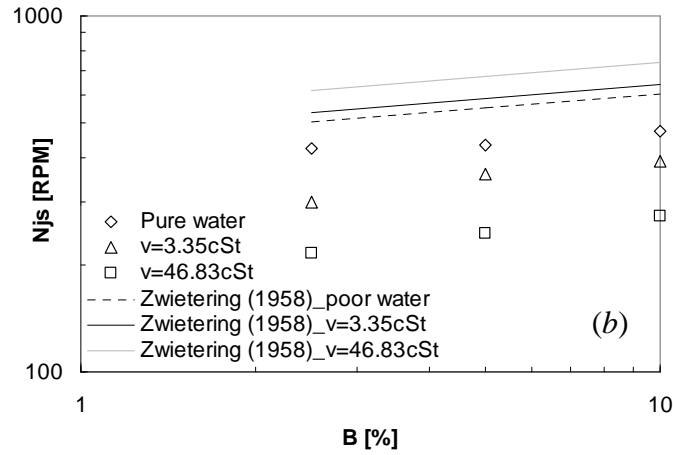
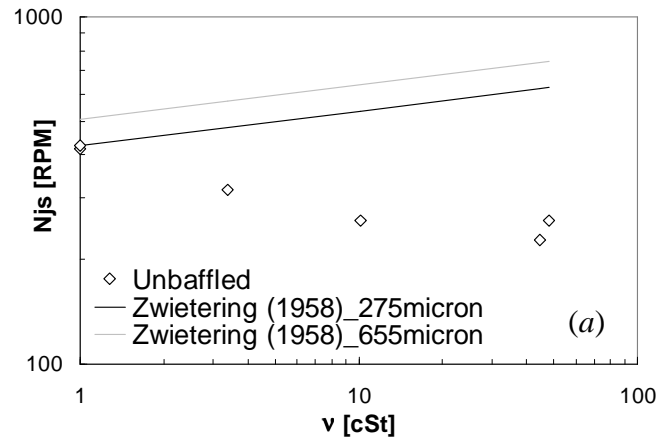


Fig. 2.11: Dependence of N_{js} on kinematic viscosity (and particle concentration). (a) 250-300 μm ; (b) 600-710 μm .

This behaviour marks an important difference between unbaffled and baffled tanks (Fig. 2.12) as in baffled vessels N_{js} increases with the kinematic viscosity according with Zwietering's correlation.



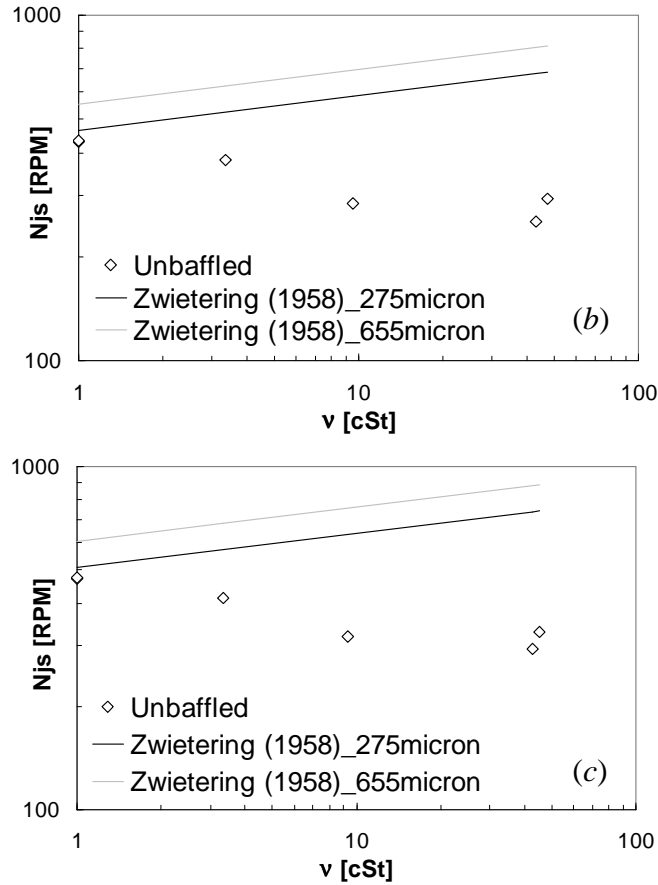


Fig. 2.12: Dependence of N_{js} on kinematic viscosity. (a) $B=2.5\%$; (b) $B=5\%$; (c) $B=10\%$.

Actually, a globally accepted dependence of N_{js} on ν does not exist for baffled vessels as some authors disagree with the dependence predicted by Zwietering. Tezura et al. (2007) carried out N_{js} assessments in unbaffled vessels stirred by unsteadily radial impellers and they found that this parameter does not depend on the kinematic viscosity.

This difference between Zwietering (1958), Tezura et al. (2007) and the present PhD work is likely linked to the different suspension mechanisms involved. For

baffled and unsteadily stirred unbaffled vessels the suspension phenomenon is linked to velocity turbulence fluctuations near the tank bottom, while for the present case of top-covered unbaffled vessels it is due to fluid mean velocities. Clearly, an increased fluid viscosity damps turbulent fluctuations as well as enhances the drag coefficient thus resulting in different dependence of N_{js} on viscosity for the two suspension mechanisms.

Fig. 2.11 shows that the larger the kinematic viscosity, the higher the difference between N_{js} values for Zwietering-baffled and top-covered unbaffled vessels at each solid loading. Notably, in relation to the independence of N_{js} on particle diameter, results relevant to different particle diameters are plotted indistinctly in each graph of Fig. 2.12. By fitting the experimental data of each graph by a power law and by averaging the relevant exponents the following dependence was found: $N_{js} \propto \nu^{-0.13}$.

Most data points obtained in the top-covered unbaffled tank are below Zwietering's correlation lines especially when big particles and/or solutions with high kinematic viscosities are employed.

2.5 Power Number (N_p) measurements

From the smaller N_{js} values observed in unbaffled *versus* baffled tanks, in conjunction with the typically smaller power number values exhibited by the former, one may infer that mechanical power requirements to achieve fully suspended conditions are bound to be smaller in the absence than in the presence of baffles. In order to quantify this feature, power consumption measurements were made, as described in the paragraph 2.3.3.

The data collected will be discussed with reference to a dimensionless power number N_p based on an average suspension density, ρ_{susp} :

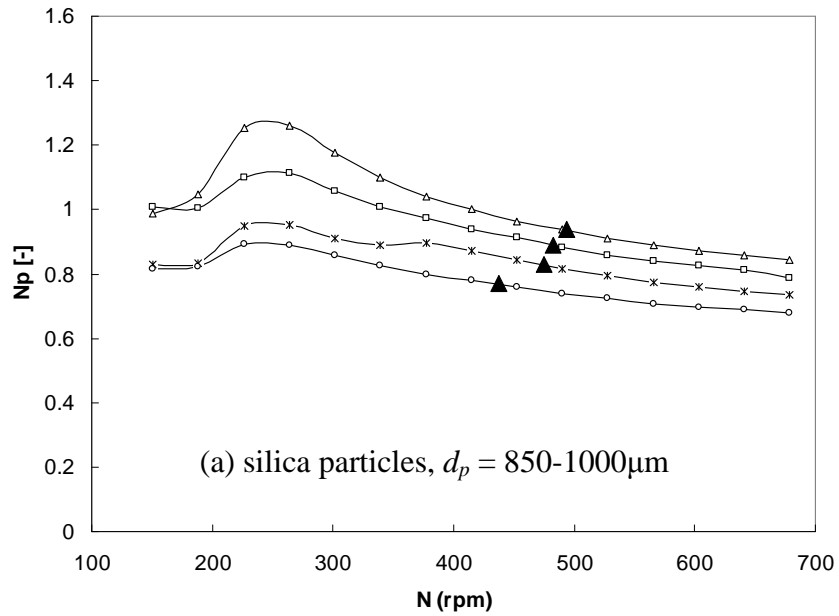
$$N_p = \frac{P}{\rho_{susp} \cdot N^3 \cdot D^5} \quad (2.2)$$

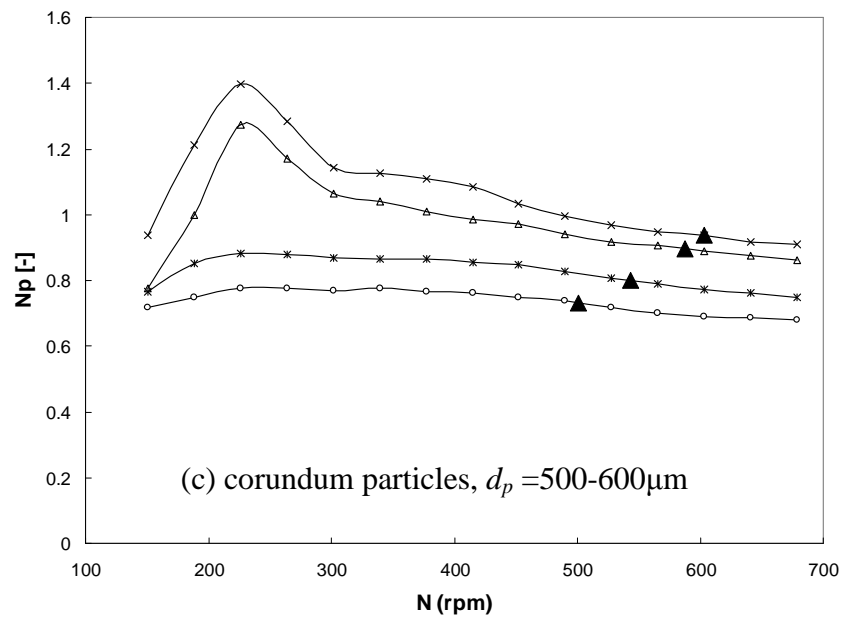
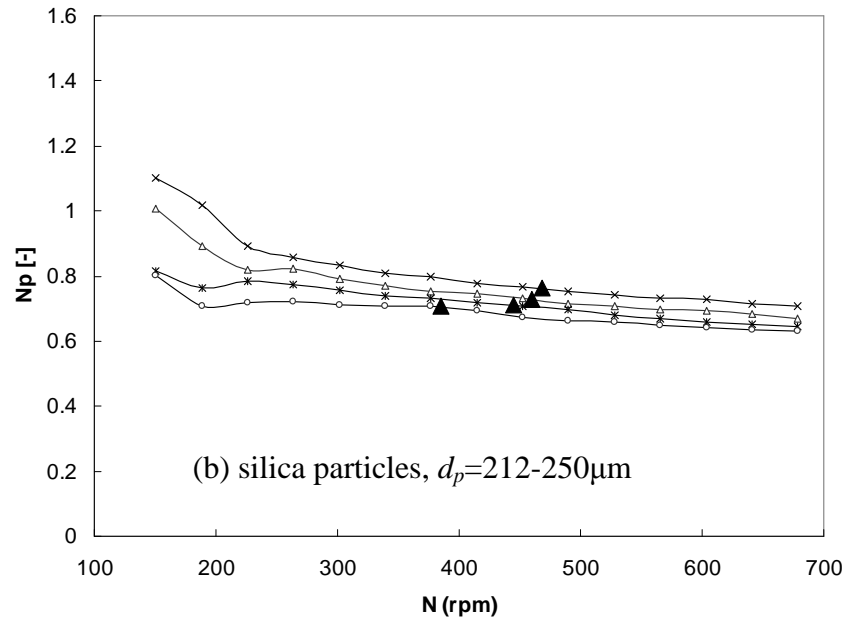
where ρ_{susp} is estimated in the following way,

$$\rho_{susp} = (1 - r_\beta) \rho_\alpha + r_\beta \rho_\beta \quad (2.3)$$

where P is power consumption, r_β is overall particle volume fraction, N is agitator speed and D is impeller diameter.

In Figs 2.13 a-d the dependence of N_p on impeller rotational speed for silica and corundum particles at different solid loadings and two different particle sizes is shown. Similar trends (not reported here for the sake of brevity) were obtained with all other particles here investigated.





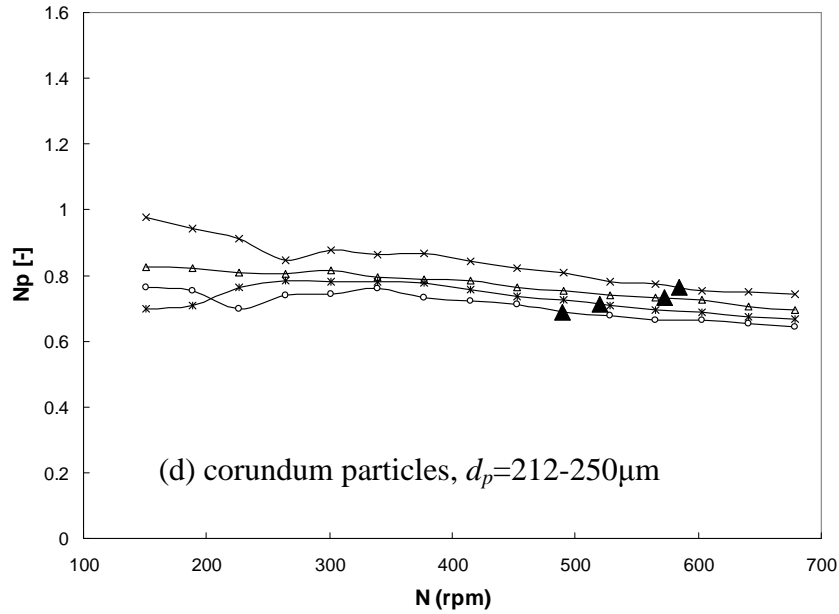


Fig. 2.13: N_p versus impeller speed at different particle concentrations concentrations B%: \circ 2.5, $*$ 5, \square 7.5, Δ 10, \times 12.5. Solid triangles indicate the relevant N_{js} .

The trends reported in Figs. 2.13 show that power number increases both with solid concentration and particle size, as already pointed out by previous works (Micheletti *et al.*, 2003; Bubbico *et al.*, 1998).

In Fig. 2.13 the N_{js} values assessed by the cone radius method are also reported (solid triangles). It may be worth noting that in this case it is not possible to infer N_{js} from N_p versus N curves, as a difference from baffled vessels where N_{js} has been claimed to be deducible from the N_p versus N graphs (Bohnet and Niesmak, 1980; Raghava Rao *et al.*, 1988; Rewatkar *et al.* 1991).

As regards curve shape, it may be observed that in the case of the largest particles (Fig 2.13 a and c) power number curves show a non-monotonic trend versus impeller speed, which suggests the existence of different factors affecting the

N_p dependence on N . These factors are likely to be *bottom reshaping* and *suspension local density*.

As a matter of fact, it is well known that for single-phase baffled tanks equipped with Rushton turbines, Power Number increases when increasing impeller clearance (Hemrajani and Tatterson, 2004). In the present case the distance of the impeller from tank bottom is significantly modified by the presence of unsuspended particles, especially at high solid loading. At low agitation speeds this results in smaller impeller clearances which, in conjunction with bottom itself to become more streamlined due to fillets shape, result into smaller N_p values. While increasing rotational speed, a larger proportion of particles is brought into suspension, impeller clearance increases, bottom reshaping becomes less effective, and power number increases. Clearly, all these effects become less important when decreasing the amount of particles introduced in the tank, i.e. average particle concentration.

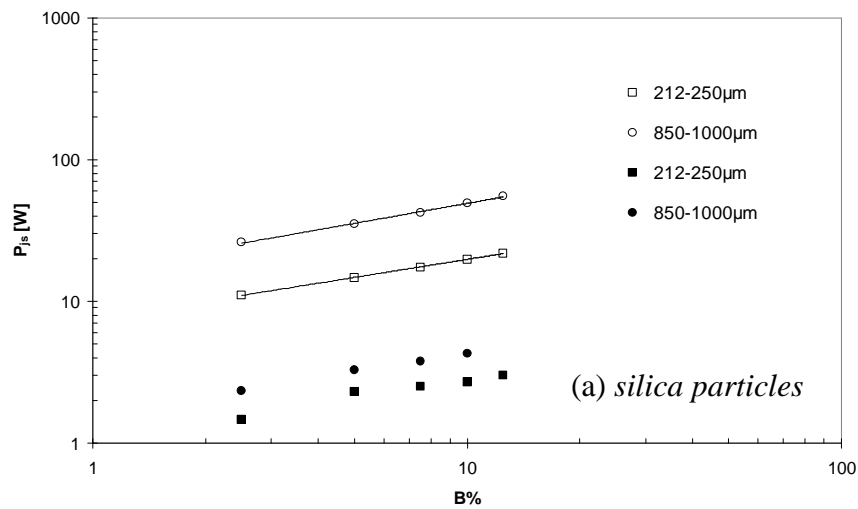
The other parameter involved in the dependence of N_p on N is the effective (two-phase) density seen by the impeller, *viz.* suspension local density in the proximities of impeller blades. This is clearly different from average suspension density. In particular, at very low impeller speeds (when most particles are laying on tank bottom) this coincides with liquid density. By increasing agitation speed some particles get suspended while others remain on the bottom. Due to the relatively low agitation speed particles remain in the lower part of the tank, possibly leading to a local density (near impeller blades) larger than average suspension density and therefore a particularly high power number. At still larger agitation speeds the local density seen by the impeller is bound to decline because particles are increasingly well distributed along vessel height as well as moved radially outwards by the increasing centrifugal forces, so leading to decreasing power numbers.

Clearly, at very low rotational speeds bottom reshaping prevails and N_p values are quite low; while increasing agitation speed the reduced bottom reshaping effect (due to more particle getting suspended), together with increase of suspension local density, brings up an important increase of N_p . At still larger agitation speeds particle redistribution prevails, the suspension local density reduces and power number declines, so leading to the relative maxima observable in Fig. 8a and 8c. As

a difference from baffled tanks, where the final almost homogeneous conditions result in a constant N_p value (Micheletti *et al.*, 2003; Bohnet and Niesmak, 1980; Raghava Rao *et al.*, 1988), here the increasing effect of centrifugal forces leads to a continuous decrease of N_p , asymptotically approaching some final N_p value.

It is worth noting that only part of this behaviour is observable with 231 μm particles (Fig. 2.13b,d) as due to their smaller settling velocity they are suspended earlier, and the effects related to bottom reshaping occur only at very low impeller speeds, where power consumption assessment is made difficult by disturbances overwhelming the very small forces to be measured.

It is now interesting to compare P_{js} values (i.e. power consumption needed to achieve complete suspension conditions) in baffled and unbaffled systems. The comparison is made in Figs 2.14a and 2.14b, where the P_{js} values obtained in the investigated top-covered unbaffled system are reported for silica and corundum particles with different average diameters and particle loadings, together with the values for the relevant baffled system, as predicted on the basis of Zwietering's correlation and a fixed N_p value of 4.9 (Bates *et al.*, 1963; Micheletti *et al.*, 2003).



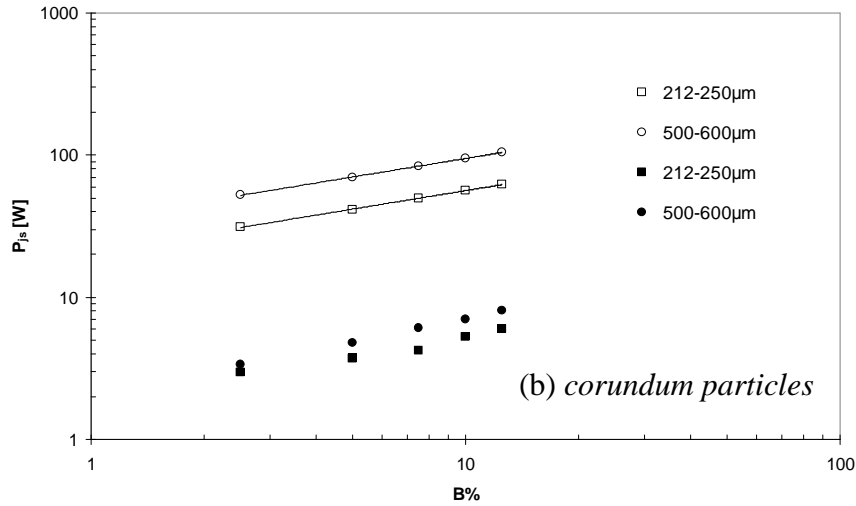


Fig. 2.14: Dependence of P_{js} on particle concentration for different particles. Solid symbols: experimental data for the unbaffled system; empty symbols: P_{js} for the baffled vessel predicted by Zwietering's equation and $N_p=4.9$.

Observing this figure it is quite evident that the P_{js} values in the top-covered unbaffled tank are much smaller (by about one order of magnitude) than the relevant values in baffled systems. Notably, the comparison with unsteadily reversing impellers is also favourable, as these were found to be about three times smaller than the corresponding (Zwietering's predicted) values in baffled tanks (Tezura *et al.*, 2008). Hence the use of a cover instead of an unsteadily stirring device, besides being mechanically and electrically simpler, leads to lower power requirements for suspending solid particles in stirred tanks.

2.6 Scale-up criterion assessment

Typical mixing tank employed for industrial applications have very large size and investigations on solid-liquid suspension on apparatuses of these size at plant scale are really complex. Therefore, in order to obtain reliable and necessary

parameter design, studies and experiments are carried out on laboratory scale stirred vessel. Relevant results are successively extrapolated at plant scale by means of suitable scale-up criterions. Clearly, effectiveness of final design depends on laboratory-scale experimental data reliability and scale-up procedure soundness.

Different investigation approaches and consequent different results concerning solid-liquid suspension lead to different scale-up rules, especially if the power per unit volume criterion is considered (Mersmann, 1985). In fact, even little differences concerning N_{js} assessment correlations can lead to very different criteria for the estimation of specific power requirement because of the dependence of mechanical power on the cube of impeller speed (see equation 2.2).

More precisely, for geometrically similar systems:

$$N_{js} = (\text{scale factor})^{-b} \quad (2.4)$$

In relation to equation 2.2 and supposing that the power number N_p is independent on system scale and agitation speed the mechanical power per unit volume can be expressed as in the following:

$$(P/V)_{js} = (\text{scale factor})^{2-3b} \quad (2.5)$$

Accordingly, specific power requirement increases, remains constant, decreases with system scale if $b < 2/3$, $b = 2/3$, $b > 2/3$ respectively. Therefore, exponent b value can greatly affect laboratory-scale data extrapolation and defines the scale-up criterion.

In order to evaluate a reliable scale-up criterion for top-covered unbaffled vessels some experiments with the larger tank ($T=0.48\text{m}$) were performed and the relevant results are reported in Fig. 2.15. These experiments confirmed the independence of N_{js} on particle diameter as well as its dependence on particle concentration (similar to that predicted by Zwietering). Conversely, dependence of N_{js} on factor scale D was found different than that of baffled vessels: Zwietering found that $N_{js} \propto D^{-0.85}$ while experiments performed in the present top-covered

unbaffled vessel showed that $N_{js} \propto D^{-0.5}$. The scale factor exponent 0.5 is lower than 2/3 thus resulting in an increase of power input per unit volume with an increase of the scale factor. Conversely, in accordance with Zwietering's correlation, an increase of the scale produces a reduction of power per unit volume.

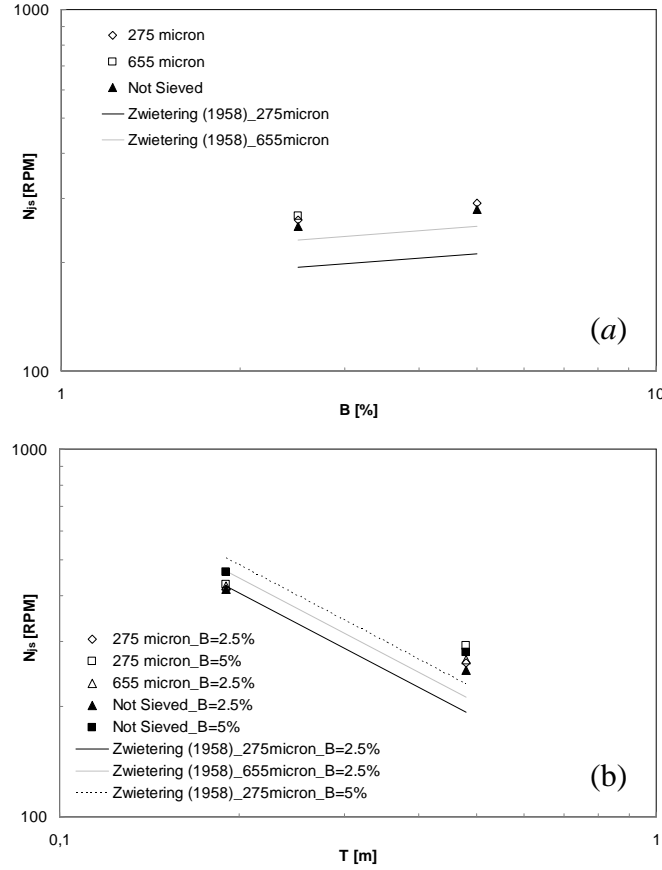


Fig. 2.15: Scale-up effects. (a) dependence of N_{js} on particle concentration and diameter; (b) dependence of N_{js} on the vessel diameter.

2.7 N_{js} correlation for top-covered unbaffled vessels

A correlation for the prediction of N_{js} in unbaffled vessels provided of a top-cover was devised in accordance with the mathematical form of Zwietering's correlation (1958). This was obtained by carrying out a multiple regression of all presently collected data resulting in the exponents showed in the following equation:

$$N_{js} = \frac{9.85 \cdot d_p^{0.0352} \cdot \left(\frac{g\Delta\rho}{\rho} \right)^{0.3315} \cdot B^{0.1133}}{v^{0.142} \cdot D^{0.4344}} \quad (2.6)$$

Experimental N_{js} values were compared with corresponding N_{js} values calculated by means of the equation 1: the comparison is depicted in Fig. 2.16.

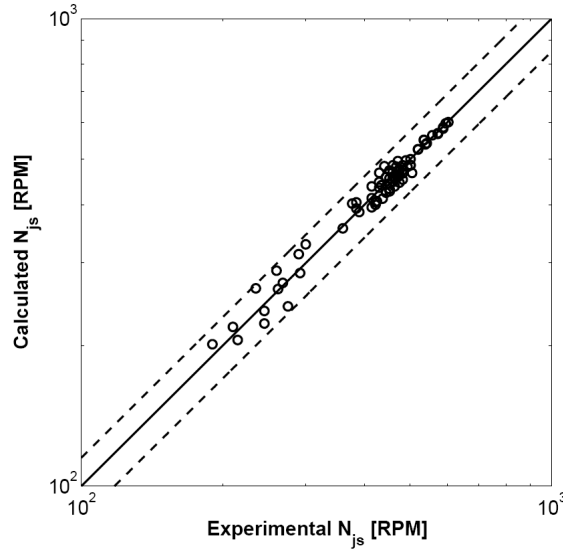


Fig. 2.16: Experimental N_{js} versus N_{js} calculated by equation 1.

The upper and the lower broken lines indicate errors of +15% and -15% respectively as regards the exact prediction of each experimental value of N_{js} . Fig. 2.16 shows the good reliability of the proposed correlation since all prediction errors

are lower than 15%. Clearly, such correlation should be considered applicable only for the cases and the system here investigated.

2.8 Conclusive remarks

Experiments on solid-liquid suspensions in a top-covered un-baffled stirred tank were performed. A novel experimental technique, namely the “*steady cone radius method*”, was devised to assist assessment of the just suspended agitation speed N_{js} .

N_{js} dependence on operating parameters such as solid concentration, particle density and mean particle diameter, fluid kinematic viscosity and system scale was investigated and compared with that predicted for baffled vessels by the well known Zwietering’s correlation. A very similar power law dependence of N_{js} on particle concentration and density difference was found, while a negligible dependence on particle diameter was observed. As a difference from baffled tanks and unsteadily stirred unbaffled vessels (Tezura et al., 2007), N_{js} was found to decrease with an increase in liquid kinematic viscosity.

Power Number versus agitation speed showed an increasing-decreasing behaviour with maximum values increasing both with solid loading and particle size. Power requirements to achieve just suspension conditions were found to be significantly smaller (by about one order of magnitude) in top-covered unbaffled tanks as compared with the more common baffled vessels, thus suggesting the former as a good choice for stirred solid-liquid systems, especially those involving large and/or heavy particles, provided that the liquid mixing time is not a limiting factor (as it occurs for many processes).

Unfortunately, N_{js} dependence on the scale factor was lower than that predicted by Zwietering for baffled vessels. Notwithstanding top-covered unbaffled vessel P_{js} values were found to be much smaller than the relevant values in baffled systems, the scale up criterion of power per unit volume showed an increase of specific power requirements with the system scale for the present case of top-covered unbaffled vessels. This finding suggests an economic convenience for radially stirred top-covered unbaffled vessels only under a certain scale.

Finally, a quite effective Zwietering-like correlation for the prediction of N_{js} in top-covered unbaffled vessels was devised by employing all the data collected during this thesis.

2.9 Nomenclature

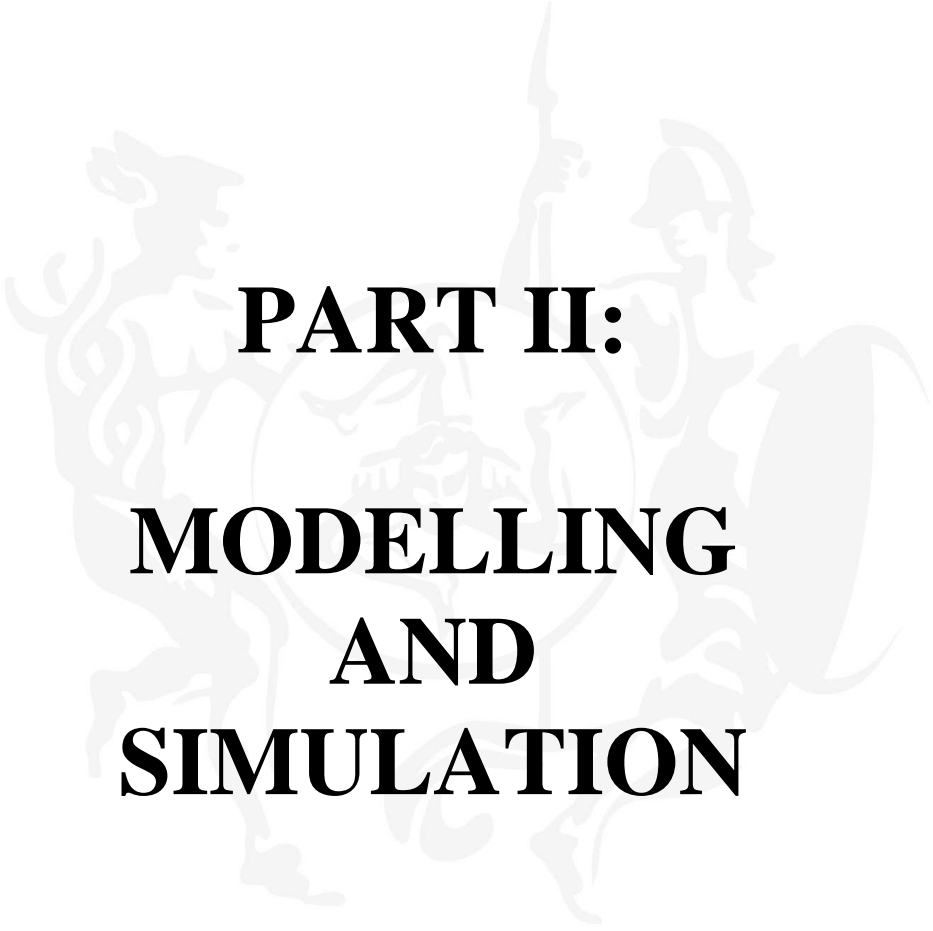
B	<i>solid mass fraction, (-)</i>
b	<i>scale factor exponent, (-)</i>
D	<i>impeller diameter, m</i>
d_p	<i>particle diameter, μm</i>
g	<i>acceleration gravity, m/sec^2</i>
H	<i>fluid height in the vessel, m</i>
N	<i>impeller speed, RPM</i>
N_{js}	<i>just suspended impeller speed, RPM</i>
N_p	<i>power number, (-)</i>
P	<i>power consumption, Watt</i>
P_{js}	<i>just suspended power consumption, Watt</i>
S	<i>geometry coefficient, (-)</i>
T	<i>tank diameter, m</i>
r_β	<i>overall particle volume fraction, (-)</i>
V	<i>volume, m^3</i>

Greek letters

ρ	<i>density, kg/m^3</i>
ν	<i>kinematic viscosity, m^2/sec</i>

Subscripts

α / L	<i>liquid phase</i>
β	<i>solid phase</i>



PART II: MODELLING AND SIMULATION

PART II: MODELLING AND SIMULATION

Introduction

Computational Fluid Dynamics is largely employed to reliably compute flows in complex geometries with multifaceted physics.

CFD now stands as an equal partner with mathematical analysis and experimental investigation. It has become such an effective tool that many industrial-researchers who previously would rely only on experiments to uncover fluid phenomena now use CFD to achieve their goals more rapidly and cost effectively. However, it is worth noting that CFD is a useless tool if a proper experimental validation is not preliminarily carried out.

The state-of-the-art of computation has advanced on many fronts. On the one hand, computer hardware itself has improved dramatically over the last half century. Nowadays, computers are very faster and more cost effective than those of several years ago. Moore's law asserting computers speedup by a factor 2 every 1.5–2 years fits well with computer performance data of the last fifty years. Furthermore, while state-of-the-art electronic chip manufacturing today uses 0.25 μ feature size technology, the path to 0.05 μ or smaller technology now seems apparent, thereby ensuring Moore's law-like speedups for the next 15 years or so. The resulting three order-of-magnitude increase of computer capability in this relatively short future time span will clearly open new perspectives for CFD.

CFD is widely employed in all engineering sectors involving fluid flows, largely supporting the advancement of knowledge in aerospace, environmental, hydraulic, mechanical, chemical and biochemical engineering just to name some of the most relevant fields.

As far as chemical engineering is concerned, almost all unit operations involving one or more fluids (i.e. single or multi-phase flows) benefits today from CFD modelling and simulation. With reference to the case of the present PhD thesis, it must be said that CFD has been successfully employed to investigate solid-liquid

suspension in stirred tanks, with many research efforts devoted to this topic over the past decades. Notwithstanding all these studies, a universally applicable and accepted CFD model for simulating suspension phenomena in vessels agitated by stirrers does not exist yet. Moreover, practically all the CFD models developed so far address the particle distribution and liquid flow field simulations, conversely, none of them directly focus on the complex phenomenon of solid suspension.

The main goal of this section is to contribute in filling the lack of knowledge in this field by directly addressing the modelling of suspension phenomena via CFD methodologies.

In order to accomplish this ambitious aim, an insight into the modelling of partial suspension regime was necessary. During partial suspension regime, some particles are motionless on the bottom while other are in motion suspended on or off the vessel bottom. At each impeller speed a specific equilibrium between suspended and unsuspended particles arises and the available interfacial area for possible mass transfer processes consequently changes.

Firstly, an attempt was made to model a solid-liquid suspension during start-up: a start-up intrinsically encompasses the suspension phenomenon during its occurrence. In addition, it represents a first insight into partial suspension conditions modelling problems and difficulties.

Secondly, a CFD model able to predict the particle suspension behaviour under partial suspension conditions was developed and successfully applied to tanks stirred by a standard Rushton turbine.

Finally, a reliable criterion based on the former CFD predictions was proposed aiming at providing a universally valid tool which could drive solid-liquid contactor design and operation.

CHAPTER 3

DENSE OFF-BOTTOM SUSPENSION DYNAMICS

3.1 Abstract

Computational Fluid Dynamics (CFD) modelling of solid liquid suspension is an issue of primary importance. It is difficult to simulate the behaviour of this type of systems especially when the solid loading is high (dense suspension). Modelling via CFD techniques the suspension phenomenon represents a way to enhance knowledge of the complex particle suspension mechanism. In order to accomplish this objective a dense solid-liquid off-bottom suspension inside a baffled mechanically stirred tank equipped with a standard Rushton turbine was investigated. Particularly, the dynamic evolution of the suspension from start up to steady state conditions has been determined by both visual experiments and computational fluid dynamics. The prediction of this evolution practically coincide with the modelling of suspension phenomenon just during its development.

As far as CFD modelling features are concerned, a classical Eulerian-Eulerian Multi Fluid Model along with the “homogeneous” k- ϵ turbulence model was adopted to simulate suspension dynamics. In these systems the drag inter-phase force affects both solid suspension and distribution. Therefore, different computational approaches were tested in order to compute this term. Simulation results were compared with images obtained from the real system and a good agreement was found. The soundness of the proposed approach is further validated by comparing predicted concentration profiles with literature data for the case of a similar geometry.

3.2 Literature review

Reliable design, optimum performance and accurate control of solid liquid contactors are closely dependent on a thorough understanding of their fluid-flow

dynamics. Modelling of such systems would lead to the prediction of the best geometrical and operative characteristics able to guarantee minimum power consumption and maximum efficiency that is a good mixing which allows for an efficient contacting between the two phases without requiring high relevant costs. Because of the high industrial relevance, a significant effort has been devoted to model the phenomena involved. First modelling studies aimed to predict the minimum impeller speed for complete solid suspension (Baldi et al., 1987), more recently authors attention has been focused on the entire flow field study and therefore on the solid particle distribution.

In recent years Computational Fluid Dynamics (CFD) has been increasingly employed as a fundamental tool to critically analyze solid-liquid flows and related phenomena. The most common approaches employed to simulate two-phase systems by CFD are the Eulerian-Eulerian approach and the Eulerian-Lagrangian approach (Crowe et al., 1996).

Eulerian-Eulerian approach assumes the two phases as two interacting interpenetrating continua existing contemporaneously in each place of the computation domain thus resulting in similar conservation equations for the two phases. Continuity and momentum equations are solved contemporaneously (using the same discretization scheme) and separately for both phases (Micale et al., 2000; Micale et al., 2004; Montante and Magelli, 2005; Montante and Magelli, 2007; Darelius et al., 2008; Ochieng and Lewis, 2006b; Fletcher and Brown, 2009; Laurenzi et al., 2009; Holbeach and Davidson, 2009; Laurenzi et al., 2009; Tamburini et al., 2009; Chen et al., 2010). Adopting an Eulerian framework for the particle phase, i.e. considering particles as a continuum, leads to a sophisticated modelling of the relevant physical aspects affecting particle motion and behaviour as well as their reciprocal interactions with the liquid phase. These aspects are modelled via suitable inter-phase terms included within the momentum equations. Several research efforts were accordingly devoted to the estimation of such parameters (Tsuo and Gidaspow, 1990; Gidaspow, 1994; Lopez de Bertodano, 1998; Gibilaro, 2001; Van Wachem et al., 2001; Ljungqvist and Rasmuson, 2001; Fan et al., 2005; Khopkar et al., 2006; Ochieng and Onyango, 2008; Holbeach and

Davidson, 2009; Tamburini et al., 2009; Hosseini et al., 2010). Notably, Eulerian-Eulerian approach is not suitable in the case of poly-dispersed particle systems, where it would be necessary to define a number of different solid phases (one for each particle diameter), which in turn require solution and closure of the relevant momentum balance equations. The Algebraic Slip Mixture (*ASM*) model (Altway et al., 2001) is a version of the most accepted Eulerian-Eulerian method. As the Eulerian-Eulerian approach, *ASM* assumes (for a two-phase system) that both phases exist at all points of the domain as interpenetrating continua. Differences regard the considered equations: *ASM* accounts for continuity and momentum equations for the mixture, volume fraction equation for the dispersed phase and an algebraic equation for the slip velocity between the two phases. Since a unique equation is considered for momentum, the slip velocity algebraic equation allows the two phases to move with different velocities.

In the Eulerian-Lagrangian approach the fluid is treated as a continuum by solving the Navier-Stokes (*NS*) equations, either averaged or not, while the dispersed phase is considered in terms of individual representative point-particles whose trajectories are individually tracked (through the *NS* solved flow field) by solving the equation of motion for each of them (Decker and Sommerfeld, 1996; Lain et al., 2002; Derksen, 2003; Bosse et al., 2005; Zhang and Ahmadi, 2005; Hartmann et al., 2006; Guha et al., 2008). The equation of motion accounts for all the forces acting on particles. Coupling of Eulerian and Lagrangian part resolutions is necessary to account for phase interactions: influence of dispersed phase on the continuum one is modelled via reliable source terms inserted within the conservation equations which must be sampled during the Lagrangian tracking. Eulerian and Lagrangian part are solved sequentially till the achieve of a converged solution. Clearly, it is necessary to perform ensemble averages in each computational cell in order to get local average properties (i.e. volume fraction, velocity, etc). The most important advantage of the Lagrangian modelling of the solid phase with respect to the Eulerian one is that the solid phase keeps its particle nature. This allows the modelling of the physical effects affecting particle motion (i.e. particle-turbulence interactions, particle-wall collisions, inter-particle interactions) which can be

properly dealt with on the basis of physical principles (Gouesbet and Berlemont, 1999). Derksen (2003) stated that Eulerian-Lagrangian simulations are very useful to study the influence of modeling assumptions concerning phase interactions. Moreover, a particle size distribution can be easily encountered by using a given distribution function for the injected particles. Unfortunately, the computational needs (time and memory space) required by the Lagrangian particle tracking are very large and directly related to the number of tracked particles (linearly proportional without taking into account particle-particle collisions; super-linearly proportional if particle-particle collisions are taken into account), a drawback bounding the use of this approach to fairly low solid loadings (Derksen, 2003). In particular Decker and Sommerfeld (2004) stated that this approach can provide good predictions only for low solid volume fraction ($\leq 5\%$).

As far as direct comparison of the two approaches is concerned, literature is lacking in information. Eulerian-Eulerian frameworks are preferred by industry as they are capable to solve multiphase problems with sufficient accuracy and faster than Eulerian-Lagrangian ones. Tamburini et al. (2009) asserted that Eulerian-Eulerian approaches, involving the classical Multi Fluid Model (MFM), are often preferred to the Eulerian-Lagrangian ones because of their simplicity, lower computational requirements, faster numerical resolution and capability to deal with high solid loading conditions (dense suspensions). However, only Guha et al. (2008) addresses directly the issue so far, by comparing a *LES*-based Eulerian-Lagrangian approach with a standard *RANS*-based Eulerian-Eulerian model for the case of a dilute (1% volume by volume overall solid hold-up) solid-liquid suspension in a baffled tank stirred by a radial impeller. Authors compared, with relevant experimental data, the CFD results obtained either by Large Eddy Simulations (*LES*), based on an Eulerian-Lagrangian framework, either by a standard Eulerian-Eulerian approach. Being *LES* a more accurate approach to solve the fluid Navier-Stokes equations, in such dilute conditions the Eulerian-Lagrangian approach provided better agreement with tangential component of the azimuthally averaged velocities and turbulent kinetic energy experimental data than the Eulerian-Eulerian approach.

Recently, various simulation attempts have been made to study the behaviour of dense suspensions inside stirred tanks showing a good agreement between experiment and numerical predictions for steady state systems (Brucato et al., 2002; Micale et al., 2004; Montante and Magelli, 2005; Khopkar et al., 2006).

It is worth noting that dense suspensions require a correct modelling of both solid-liquid and particle-particle interactions.

Several studies highlight the importance of correctly describing the interaction between phases by specifying inter-phase momentum exchange terms such as Basset force, virtual mass force, lift force and drag force. Ljungvist and Rasmuson (2001) stated that drag is the most important of the investigated inter-phase momentum transfer terms, even if they obtained this result in very dilute solid-liquid systems. Much effort has been made in recent years in order to better specify the influence of drag force on both solid suspension and distribution (Ochieng and Onyango, 2008). Some works focused their attention simply on the drag coefficient investigating its dependence on turbulence and particle characteristics and concentration (Montante and Magelli, 2007; Khopkar et al., 2006; Montante and Magelli, 2005; Ochieng and Onyango, 2008; Gidaspow, 1994; Brucato et al., 1998a); others dealt with the inter-phase drag coefficient dependence on solids concentration for the case of dense suspensions (Ochieng and Onyango, 2008; Gidaspow, 1994). Fewer efforts have been devoted so far to the problem of particle-particle interactions (Derksen, 2003; Ochieng and Onyango, 2008; Gidaspow, 1994).

This chapter follows up these recent studies and deals with a topic not yet investigated: transient start-up conditions study. More precisely the aim was to numerically predict the transient behaviour of an off-bottom suspension in the case of a dense solid-liquid system, from its initial motionless condition till the attainment of steady state conditions.

Given the high solid particle concentration (dense suspension) here considered, the choice of an Eulerian-Eulerian approach has been compulsory for the purpose of present Chapter.

Computational results were qualitatively compared with experiments in order to validate the adopted modelling approach. The qualitative comparison regards mainly the clear liquid layer height observed during the transient. The clear liquid layer formation is a phenomenon which has been already investigated both by experimental (Hicks *et al.*, 1997) and computational (Micale *et al.*, 2004) studies showing the dependence of its extension on the tank geometry, impeller speed and solid loading.

3.3 Physical system

The experimental system consisted of a cylindrical, flat-bottomed, baffled tank with vessel diameter $T=0.19\text{m}$ and liquid height equal to $1.5\cdot T$, as depicted in Fig. 3.1. A standard six bladed Rushton turbine was used in the suspension experiments. A close off-bottom impeller clearance was chosen in order to ensure a "single-loop" flow configuration (Montante *et al.*, 1999). The liquid level (H) was higher than usual ($H=1.5T$, instead of $H=T$) in order to widen the range of stirrer speed velocities for which the clear liquid existence is clearly observed (Hicks *et al.*, 1997).

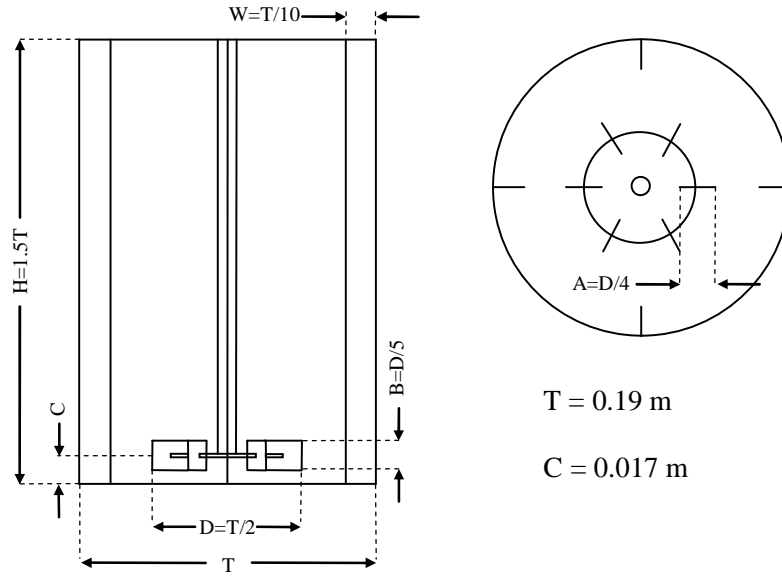


Fig. 3.1: Stirred vessel employed.

Deionised water and silica particles with diameter ranging between 212 and 250 μm were employed. Solid measured density was 2580 kg/m^3 . The solid particle loading was equal to 2 kg corresponding to an average solid weight fraction of 21.5% w/w (9.6% v/v). The particle bed laying on the bottom under no agitation conditions was experimentally measured and found to have a void fraction of about 38%.

It is worth noting that at start-up, before mixing operation starts, the impeller is completely submerged by the solid particles.

Experimental information regards both the transient and the steady state behaviour of the off-bottom suspension. Digital images were recorded using a high resolution digital camera at 19 frames per second until steady state conditions were achieved after 50-100 impeller full revolutions (Micale *et al.*, 2004). Only selected series of snapshots, sufficient to characterize the start-up transitory, will be

presented in the following: they are relevant to 1, 2, 5, 10, 20 and 50 full revolutions. The digital camera was placed in two different positions: just in front of the vessel in order to follow the dynamic evolution of the clear liquid layer height (or equally the suspension height) and at an inclined upper frontal position to record more specific phenomena like the initial impeller uncovering.

Impeller speed was set at 380 RPM (corresponding to a Reynolds number of about 57000) both in experiments and in simulations and it was sufficient to get fully suspended conditions at steady state (a just suspended speed of about 260 RPM was found by the usual *1 second criterion*). With the combination of a DC motor (Mavilor MS6) and a speed controller (Infranor) adopted, it was observed experimentally that the impeller swiftly reached the speed of 380 RPM within a time corresponding to less than 0.04 seconds (i.e. about 1/4th of a full revolution at 380 RPM).

3.4 CFD modelling

All CFD simulations were performed by adopting the Eulerian-Eulerian Multi Fluid Model. This model solves the continuity and momentum equations for a generic multi-phase system and therefore allows the determination of separate flow field solutions for each phase simultaneously. The particle phase was treated as a separate dispersed phase, occupying disconnected regions of space in the continuous liquid phase.

The system is always considered as Newtonian, the relevant continuity equations for both phases are:

$$\frac{\partial}{\partial t}(r_\alpha \rho_\alpha) + \vec{\nabla} \cdot (r_\alpha \rho_\alpha \vec{U}_\alpha) - \frac{\mu_t}{\sigma} \nabla^2 r_\alpha = 0 \quad (3.1)$$

$$\frac{\partial}{\partial t}(r_\beta \rho_\beta) + \vec{\nabla} \cdot (r_\beta \rho_\beta \vec{U}_\beta) - \frac{\mu_t}{\sigma} \nabla^2 r_\beta = 0 \quad (3.2)$$

where the last term models the turbulent dispersion of the two phases. In these equations subscripts α and β refer to the continuous and dispersed phases respectively, r is volumetric fraction, ρ is density, U is mean velocity, μ_t is turbulent viscosity, σ is turbulent Schmidt number. This last was set to 0.8 in all simulations.

Obviously:

$$r_\alpha + r_\beta = 1 \quad (3.3)$$

Momentum equations are:

$$\begin{aligned} \frac{\partial}{\partial t}(r_\alpha \rho_\alpha \vec{U}_\alpha) + \vec{\nabla} \cdot \left(r_\alpha \left\{ \rho_\alpha \vec{U}_\alpha \otimes \vec{U}_\alpha - (\mu_\alpha + \mu_t) [\vec{\nabla} \vec{U}_\alpha + (\vec{\nabla} \vec{U}_\alpha)^T] \right\} \right) = \\ = r_\alpha (\vec{B} - \vec{\nabla} P) + \vec{M}_{\alpha\beta} \end{aligned} \quad (3.4)$$

$$\begin{aligned} \frac{\partial}{\partial t}(r_\beta \rho_\beta \vec{U}_\beta) + \vec{\nabla} \cdot \left(r_\beta \left\{ \rho_\beta \vec{U}_\beta \otimes \vec{U}_\beta - (\mu_\beta + \mu_t) [\vec{\nabla} \vec{U}_\beta + (\vec{\nabla} \vec{U}_\beta)^T] \right\} \right) = \\ = r_\beta (\vec{B} - \vec{\nabla} P) + \vec{M}_{\beta\alpha} \end{aligned} \quad (3.5)$$

In these equations, B is body force, μ is viscosity, P is pressure (the solid and the liquid phases share the same pressure field) and M is momentum inter-phase transfer term.

Interactions between the two phases were directly modelled only by inter-phase drag force terms within the momentum equations (two-way coupling). Moreover, fluid-particle interactions as well as particle-particle interactions were modelled by the adoption of an *excess solid volume correction (ESVC)* algorithm which will be detailed in paragraph 3.4.2.

The numerical system of equations so far presented is mathematically closed: there are nine equations and nine unknowns: two volumetric fractions, six velocity

components and the pressure (momentum transfer terms, i.e. inter-phase drag force are known). As concerns the turbulence closure, Montante and Magelli (2005), for suspensions with a solid concentration up to 6% v/v, and Micale et al. (2004), for suspensions with a solid concentration up to about 14% v/v, have shown that the “homogeneous” k - ε turbulence model provides a fair representation of the solid distribution in high density stirred reactors. In the homogeneous k - ε turbulence model the two phases share the same k and ε value and the transport equations for k and ε have no inter-phase turbulence transfer terms.

In relation to these simplifications the turbulence model equations are:

$$\frac{\partial}{\partial t}(\rho k) + \vec{\nabla} \left[\rho \vec{U} k - \left(\mu + \frac{\mu_t}{\sigma_k} \right) \vec{\nabla} k \right] = S_k \quad (3.6)$$

$$\frac{\partial}{\partial t}(\rho \varepsilon) + \vec{\nabla} \left[\rho \vec{U} \varepsilon - \left(\mu + \frac{\mu_t}{\sigma_\varepsilon} \right) \vec{\nabla} \varepsilon \right] = S_\varepsilon \quad (3.7)$$

where

$$S_k = \mu_t \vec{\nabla} \vec{U}_\alpha \left(\vec{\nabla} \vec{U}_\alpha + \left(\vec{\nabla} \vec{U}_\alpha \right)^T \right) - \rho \varepsilon \quad (3.8)$$

$$S_\varepsilon = C_1 \frac{\varepsilon}{k} \mu_t \vec{\nabla} \vec{U}_\alpha \left(\vec{\nabla} \vec{U}_\alpha + \left(\vec{\nabla} \vec{U}_\alpha \right)^T \right) - C_2 \rho \frac{\varepsilon^2}{k} \quad (3.9)$$

All physical properties figuring in the previous equations are the “mixture” averaged properties.

$$\rho = r_\alpha \rho_\alpha + r_\beta \rho_\beta \quad (3.10)$$

$$\vec{U} = \frac{1}{\rho} (r_\alpha \rho_\alpha \vec{U}_\alpha + r_\beta \rho_\beta \vec{U}_\beta) \quad (3.11)$$

$$\mu_t = \rho C_\mu \frac{k^2}{\varepsilon} \quad (3.12)$$

3.4.1 Inter-phase Drag Force and Drag Coefficient

As far as momentum exchange between phases is concerned, inter-phase drag forces in the presence of a high particle concentration have a crucial role in determining suspension height and particle distribution. In fact dense particle effects have an important influence on the inter-phase drag force since interactions among particles arise and interactions between phases consequently change. The case considered in this chapter has a high solid loading, besides, local particle concentration undergoes outstanding variations during the entire transient: solid are completely packed at start-up and better distributed at steady state.

In order to account for solid concentration effect on the inter-phase drag force the following three different equations were adopted:

- for low solid fractions ($0 < r_\beta < r_{\beta_min}$)

$$\begin{aligned} \vec{M}_{\alpha\beta} &= C_{\alpha\beta} (\vec{U}_\beta - \vec{U}_\alpha) = \\ &= \left[\frac{3}{4} \frac{C_D}{d_p} r_\beta \rho_\alpha |\vec{U}_\beta - \vec{U}_\alpha| \cdot (1 - r_\beta)^{-1.65} \right] (\vec{U}_\beta - \vec{U}_\alpha) \end{aligned} \quad (3.13)$$

where d_p is particle diameter, and C_D is the drag coefficient. Eq.(3.13) is utilized if the solid volume fraction is lower than a fixed value r_{β_min} ; in practice with this equation the drag inter-phase term is calculated by the standard $C_{\alpha\beta}$ formulation along with Gidaspow's correction for dense particle effects (Gidaspow, 1994);

- for solid volumetric fractions variable from r_{β_max} to the maximum value r_{β_packed} , Eq.(3.14) is used ($r_{\beta_max} < r_{\beta} < r_{\beta_packed}$)

$$\begin{aligned}\bar{M}_{\alpha\beta} &= C_{\alpha\beta} (\bar{U}_{\beta} - \bar{U}_{\alpha}) = \\ &= \left[150 \frac{r_{\beta}^2 \mu_{\alpha}}{(1-r_{\beta}) d_p^2} + 1.75 \frac{r_{\beta} \rho_{\alpha} |\bar{U}_{\beta} - \bar{U}_{\alpha}|}{d_p} \right] (\bar{U}_{\beta} - \bar{U}_{\alpha})\end{aligned}\quad (3.14)$$

Here $C_{\alpha\beta}$ is obtained in practice *via* the well known Ergun equation (Ergun, 1952), typically used to describe closely packed fixed-bed systems;

- for intermediate volume fractions ($r_{\beta_min} < r_{\beta} < r_{\beta_max}$)

$$\bar{M}_{\alpha\beta} = \left[C_{\alpha\beta}(r_{\beta_min}) + \frac{C_{\alpha\beta}(r_{\beta_max}) - C_{\alpha\beta}(r_{\beta_min})}{r_{\beta_max} - r_{\beta_min}} (r_{\beta} - r_{\beta_min}) \right] (\bar{U}_{\beta} - \bar{U}_{\alpha}) \quad (3.15)$$

i.e. a linear interpolation was employed thus avoiding any discontinuity in calculating $C_{\alpha\beta}$ from the two previous expressions. On the basis of Eq.(13) and Eq.(14) validity fields, r_{β_min} and r_{β_max} were set to 0.35 and 0.45 respectively, as long as a monotonic dependence of $C_{\alpha\beta}$ vs r_{β} was obtained, as shown in Fig.3.2A.

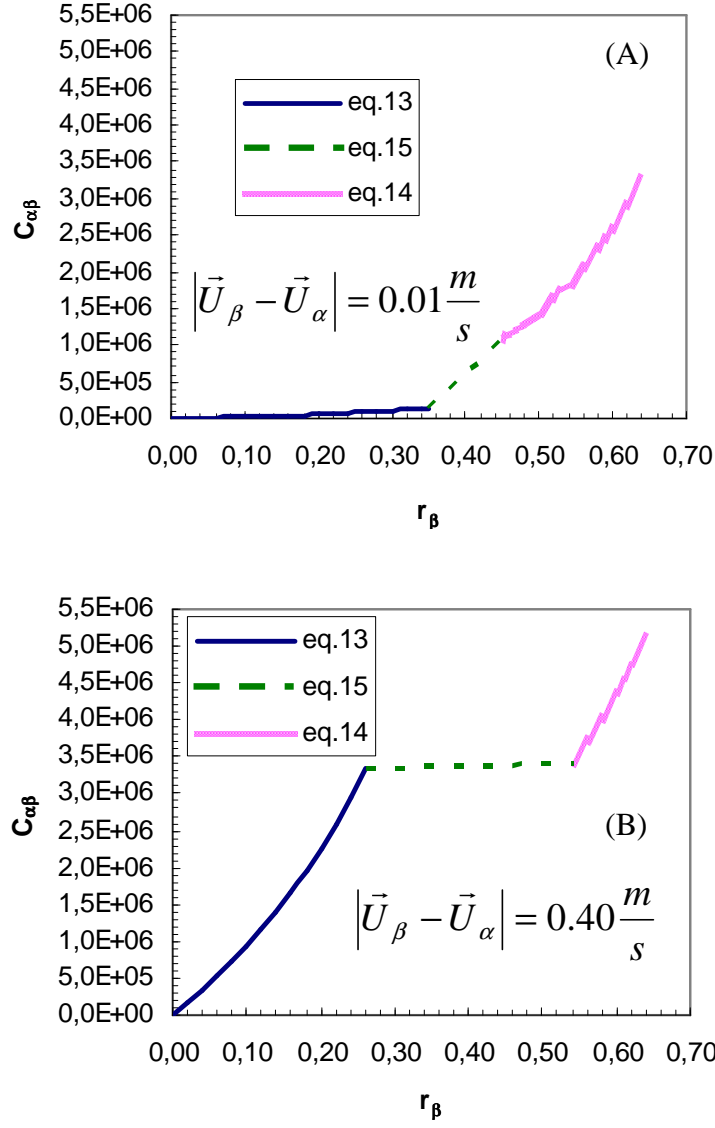


Fig. 3.2: The complete $C_{\alpha\beta}(r_\beta)$ function at two different slip velocity values.

Where the slip velocity was so large that a non-monotonic dependence would have resulted, the validity range for Eq.(3.15) was suitably enlarged in order to avoid it, as shown in Fig.3.2B. The critical slip velocity value requiring this

enlargement is about 0.05 m/s. The typical slip velocity range observed in the vessel is 0-0.2 m/s, but in some cases the slip velocity during the transient reached up to 0.5 m/s. It is worth noting that the enlargement requirement occurs only when a fixed value for C_D is chosen (see the *fixed- C_D* approach below).

Eq.3.13 and Eq.3.15 involve the specification of an input value for the drag coefficient. Here a choice of approaches were used to correctly model the influence of slip velocity and free stream turbulence on the drag coefficient (C_D).

- The simplest one computes it as for a single particle settling at its terminal velocity (~ 3 cm/s) in a quiescent fluid on the basis of the standard drag curve (for the particle-fluid system here employed $C_D=6.01$). This approach will be named *fixed- C_D* .

- Another approach considers a C_D variable in each cell in relation to the slip velocity: here C_D is calculated by the Clift *et al* correlation (Clift et al., 1978), Eq.(16), where cell slip velocity was used for the Reynolds number calculation. This approach will be called as *slip- C_D* .

$$C_D = \frac{24}{\frac{\rho_\alpha d_p |\vec{U}_\beta - \vec{U}_\alpha|}{\mu_\alpha}} \left(1 + 0.2 \left(\frac{\rho_\alpha d_p |\vec{U}_\beta - \vec{U}_\alpha|}{\mu_\alpha} \right)^{0.63} \right) =$$

$$= \frac{24}{\text{Re}_p} (1 + 0.2 \text{Re}_p^{0.63}) \quad (3.16)$$

- In the last case, named *turb- C_D* , free-stream turbulence influence upon drag inter-phase force was accounted for by implementing Brucato *et al* correlation (Brucato et al., 1998a)

$$C_{D,turb} = C_D \left[1 + 8.67 \times 10^{-4} \left(\frac{d_p}{\lambda} \right)^3 \right] \quad (3.17)$$

where C_D was computed by Eq.(16) and λ is the well known Kolmogorov length scale, obtained by the following Eq. (18).

$$\lambda = \left[\frac{\left(\frac{\rho_\alpha}{\mu_\alpha} \right)^3}{\varepsilon} \right]^{\frac{1}{4}} \quad (3.18)$$

Here ε is the mechanical power dissipation per unit mass of fluid phase, directly computed by the k- ε turbulence model.

The above expressions were implemented in the code through the use of a User Fortran subroutine available for this purpose in Ansys-CFX4.4 (*USRIPT*).

3.4.2 Computational approaches and numerical simulations

For all Reynolds Average Navier Stokes simulations here presented, the numerical solution was obtained by adopting the commercial finite-volume method code CFX release 4.4, developed by AEA Technology.

A $24 \times 69 \times 32$ (azimuthal \times axial \times radial) finite volume structured grid was used to discretize the domain region. Therefore the total number of cells is equal to 52992. In the azimuthal direction, thanks to symmetry, only half of the vessel was simulated, with 24 equally-spaced angular subdivisions. The other half of the tank was simulated imposing periodic boundary conditions along the azimuthal direction. The computational grid adopted has a smaller cell spacing in the lower part of the vessel, near the impeller, where the largest gradients of flow quantities are expected (see Fig.3.3).

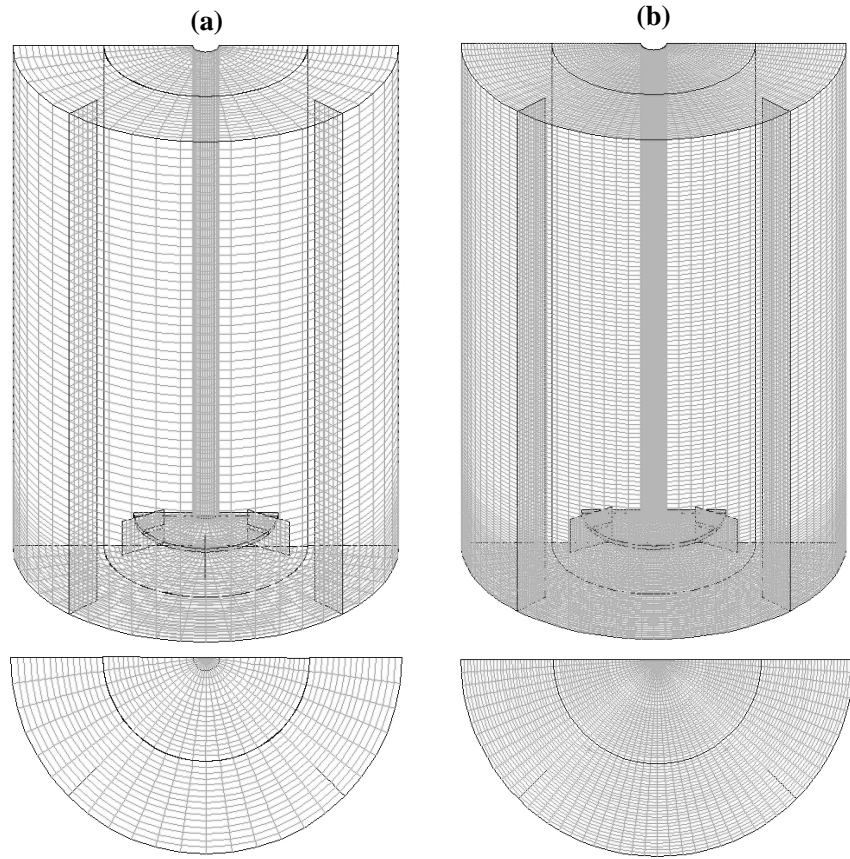


Fig. 3.3: Computational grids adopted: a) standard grid; b) fine grid.

The coarse grid was used in order to keep computational needs low. However, a eight times finer grid $48 \times 138 \times 64$ (azimuthal \times axial \times radial) was also used to check whether results were affected by grid-dependence. Altogether this second grid encompassed 423936 cells.

In order to compare our results with literature data, a third grid of 61272 cells ($24 \times 69 \times 37$) (azimuthal \times axial \times radial) was created to discretize the stirred

vessel employed by Micheletti et al. (2003) with $C/T=0.15$ to carry out the relevant simulation.

Two main approaches are usually employed to model impeller-baffle relative motion: the *Multiple Frames of Reference* (MRF) and the *Sliding Grid* (SG):

- *Multiple Frames of Reference* (MRF) (Luo et al., 1994)

The flow domain is divided into two cylindrical, not overlapping sub-domains, each meshed as a separate block. For these blocks two different frames of reference are used: the one including the impeller which rotates integrally with the impeller itself and the other including the baffles which is fixed to the tank. Flow variables relevant to the interface between these sub-domains are generally unsteady with the exception of a specific radial location where they do not change appreciably and can be assumed steady. This assumption leads to the possibility of predicting the entire flow field thoroughly the tank by means of steady-state calculations thus guaranteeing a huge computational time saving. Rotating and stationary steady-state equations are solved separately, while the boundary surface (limiting the two sub-domains) coupling is allowed by means of velocity transformations. In accordance to the former assumption, the radial position of such a surface is not arbitrary and must be chosen carefully.

- *Sliding Grid* (SG) (Murthy et al., 1994)

The full domain is divided into two meshed blocks: one moving with the impeller and the other motionless. It is worth noting that the two sub-domains share the same inertial frame of reference: it is the inner domain which rotates with time.

This moving grid was allowed to slide relative to the still one, with no mesh distortion, interacting with it along a surface of slip (i.e. the one separating the two sub-domains). The two regions are coupled at this interface by means a sliding-grid algorithm which takes into account the relative motion between the two blocks and performs conservative interpolations to obtain flow variables and face fluxes across the surface. Clearly, simulations have to be carried out in a time-dependent fashion.

MRF method resolves the RANS equations under steady state condition (Brucato *et al.*, 1998b), therefore in this chapter it was almost compulsory to utilize the SG approach as a dynamic transient had to be investigated. The black internal cylinders in the grids of Fig.3.3 show the sliding surface limits; the black curve lines in the bottom tank, depicted in the same figures, represent the projection of the sliding surface on the bottom tank.

Alternative modelling approaches concerning the impeller-baffles relative motion that are not so used nowadays and that were accordingly not taken into account in the present thesis are the *Impeller boundary Condition (IBC)* method, the *Inner-Outer Iterative Procedure (IO)*, the *Circumferential Averaging (CA)* model, the *Clicking Sliding Grid* method (CSG), *Moving Deforming Mesh (MDM)* method, the *Computational Snapshot (CS)* approach and the *Momentum Source (MS)* method:

- *Impeller boundary Condition (IBC)*

It is the simplest steady state approach whereby all equations are solved in an inertial reference frame. A “black box” is defined for the volume containing the impeller (Gosman *et al.*, 1992; Barrue *et al.*, 2001) and velocity, turbulent kinetic energy and turbulent kinetic energy dissipation axial profiles (azimuthally averaged) are imposed on the vertical cylindrical surface swept by the impeller blade tip. Such profiles are deduced by an experimental gathering of anemometry data. Naturally, the main drawbacks of this method concern, on the one hand, the need of experimental data yielding *IBC* a not fully predictive method (Guha *et al.*, 2008) and, on the other hand, the influence that experimental data have on the flow field prediction (Ranade, 1995). Also, extension of this approach to multi-phase flow in stirred vessel is not feasible as it is practically not possible to obtain (from experiments) accurate boundary conditions at the impeller for such type of systems (Ranade, 1997). Eventually, it is not able to capture the details of the flow between the impeller blades (Ranade, 1997).

- *Inner Outer (IO)*

Two different region partially overlapping are defined for the tank domain: the one *inner* containing the impeller and the other *outer* containing baffles and lateral wall. As in the MRF approach two different frames of reference are considered: one moving integrally with the impeller for *inner* region, the other motionless for the *outer* domain. *IO* approach is a steady state method consisting in an iterative procedure. Firstly, the *inner* zone is simulated by imposing arbitrary boundary conditions on the interface cells, as an example, a motionless fluid. Velocity and other variables are therefore calculated in all this region. Among these data, those relevant to the impeller contour are used as a numerical input for a simulation of the *outer* domain (as already seen in the *IBC* method) which provides information on the entire tank flow field (with the exception of the volume occupied by the impeller) as well as velocity, turbulent kinetic energy and turbulent kinetic energy dissipation estimations on the *inner* boundary surface. These values are employed as boundary conditions for a successive *inner* iteration and so on, until a satisfactory numerical convergence is achieved. Notably, data used as boundary conditions have to be azimuthally averaged and corrected for the relative motion because of the two different frames of reference employed (Wang et al., 2004). Finally, it is worth noting that the two regions are partially overlapping in order to allow the convergence of the *inner* and *outer* simulations within the iterative procedure. The location and the boundaries of this overlap region are quite arbitrary (Brucato et al., 1998b). This approach was improved by Wang and Mao (2002) and lately applied by Fan et al. (2005) to simulate a turbulent solid-liquid two-phase flow and the orientation of slender particle within a stirred vessel.

- *Circumferential Averaging (CA)*

It is a variation of the more common and used MRF method. The difference between MRF and CA regards the coupling of variables at the two sides of the interface: in CA approach each cell of the inner side of the interface sees the variables circumferential averaged in all the cells on the other side and vice versa. Clearly, it is more approximated with respect to the MRF approach. However, it can

constitute a good choice if applied to problems where the flow variables do not vary significantly in the azimuthal direction at the zone interface (Aubin et al., 2004).

- Clicking Sliding Grid (CSG) (Böhm et al., 1998)

It is a transient approach being a different version of the most common Sliding Grid method. In SG calculation the mesh is allowed to deform, conversely, in CSG the lines of the grid belonging to the rotating domain interface have to coincide with the grid lines of the stationary domain at the end of each time step. This continuous grid alignment requires that the time step must be chosen suitably, in accordance with the impeller (i.e. rotational domain) rotational speed (Sommerfeld and Decker, 2004). This approach was adopted recently by Yapici et al. (2008) who investigated the effect of the Rushton type turbine design factors on agitated tank flow characteristics by means of *Large Eddy Simulations* along with a standard Smagorinsky model (Smagorinsky, 1969).

- Moving Deforming Mesh (MDM) (Perng and Murthy (1993)

This approach based on a moving-deforming mesh technique was developed by Perng and Murthy (1993) and employed for the time-dependent simulation of the flow in mixing tanks. Also, it was implemented in the commercial CFD package FLUENT. A single mesh and a single reference frame were used for stationary and moving parts, but the grid cells associated with the impeller rotated with it, causing the interfacial mesh to deform. When mesh deformation became acute, the grid was re-generated locally and information was transformed to the new mesh in a conservative fashion. The grid motion was accounted for by transforming the time derivatives in Eulerian conservation equations into a Lagrangian form. No comparisons between CFD simulations adopting this approach and corresponding experimental data were found in literature.

- Computational Snapshot (CS)

The characteristics of the flow induced by an impeller are mainly due to pressure and centrifugal forces: impeller speed determines centrifugal force

magnitude while the impeller blade shape generates the pressure forces that are responsible for the direction and characteristics of impeller discharge stream. The pressure forces generated by the blade rotation causes suction of fluid at the back side of the impeller blades and equivalent ejection of fluid from the front side of the blades. An intrinsically transient sliding mesh method manages to correctly simulate such ejection and suction phenomena. *Computational Snapshot* method developed by Ranade and Dommeti (1996) models the same phenomena within a steady state framework by keeping the impeller blades fixed at one particular position with respect to the baffles (similar to taking a snapshot of the rotating impeller). Ejection and suction are modelled through the adoption of suitable mass source terms for the computational cells on the front side of the blades and mass sink terms for the computational cells on the back side of the blades. In practice, even though the flow generated by an impeller is inherently unsteady in the stationary frames of reference, these source terms are expected to lead to predicted results equivalent to a snapshot of this inherently unsteady flow.

- *Momentum Source (MS)*

This model is not so utilized. It is based on aerofoil aerodynamics and it can be successfully applied when the axial flow is prevailing with respect to the radial flow within the stirred vessel. This method was employed by Xu and McGrath (1996) who compared MS-CFD predictions with relevant *Laser Doppler Anemometry (LDA)* data stating that the momentum source model can be applied with confidence for predictions of mean velocities in stirred tank reactors.

Performances of *IBC*, *IO*, and *SG* were critically discussed by the well known work of Brucato et al. (1998b) where *SG* method was found to provide better results although it requires higher computational costs.

Coupling of pressure and velocity was obtained by the SIMPLEC algorithm. The hybrid-upwind discretization scheme was employed for the advective terms.

The table 3.1 shows the physical properties of the two phases as set in the simulation.

	Liquid (water)	Solid (silica)
Density [kg/m ³]	1000	2580
Viscosity [Pa·s]	10 ⁻³	10 ⁻³
Particle diameter [m]	-	2.31·10 ⁻⁴
Mean volumetric fraction	0.904	0.096
Volumetric fraction at max packing	0.38	0.62
Turbulent Schmidt Number	0.8	0.8

Tab. 3.1: Physical parameters of the two phases modelled.

At the beginning of the simulation all the solid phase is placed over the bottom of the tank with a fixed initial packing level of 0.62 v/v (i.e. the value of r_{β_packed} measured for the investigated particle system). To avoid r_{β_packed} to be exceeded during the simulations an ad-hoc algorithm, named *excess solid volume correction* (Lettieri et al., 2003), was implemented inside the CFD code. This correction operates as a posteriori redistribution of the solid volume in excess for each cell where the volume fraction exceeds r_{β_packed} .

As a difference from the original version (i.e. 2-D fluidized bed), in this thesis the algorithm was applied for the first time for 3D stirred tanks, in addition it was implemented at the end of each iteration of the SIMPLEC algorithm inside the User Fortran subroutine *USRCVG* of the Ansys-CFX4.4 code.

The algorithm does not remove the over-packing issue, but rather rearranges the volume fraction distribution and ensures the excess of solids to be carried towards cells where no excess is present. In other words it performs a transport of the solids from the cells where $r_{\beta} > r_{\beta_packed}$ towards the nearest domain regions where no excess exists.

More precisely, at the end of each iteration, the amount of solid volume exceeding r_{β_packed} (i.e. r_{β}^{ex}) (if present) is calculated cell by cell:

$$r_{\beta_{i,j,k}}^{ex} * V_{cell_{i,j,k}} = (r_{\beta_{i,j,k}} - r_{\beta_packed}) * V_{cell_{i,j,k}} \quad (3.19)$$

This quantity has to be equally redistributed within the surrounding cells (six if the central cell is not placed next to boundaries or topological elements) (Fig.3.4):

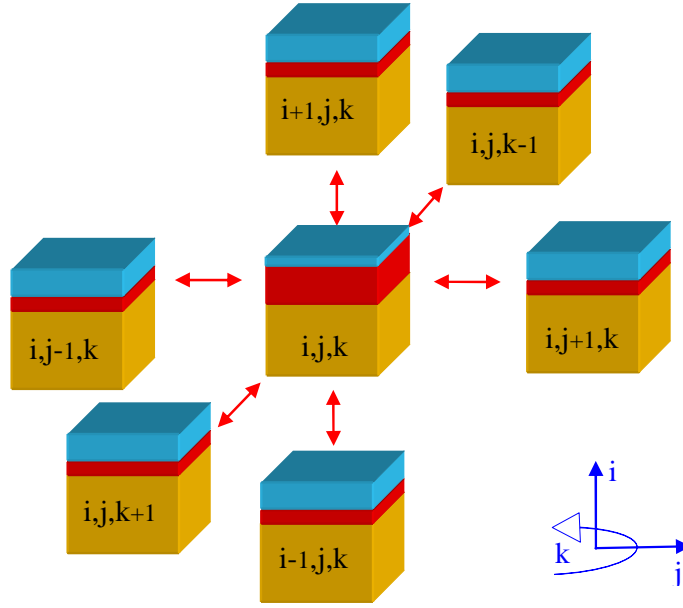


Fig. 3.4: ESVC algorithm operation scheme (the red layer represents the excess of solids) .

The new value of r_{β} is calculated by the present algorithm in accordance with the following equation:

$$\begin{aligned}
 (r_{\beta_{i,j,k}})^{new} = & (r_{\beta_{i,j,k}})^{old} - r_{\beta_{i,j,k}}^{ex} + \left(\frac{r_{\beta_{i+1,j,k}}^{ex}}{6} \right) * \frac{V_{cell_{i+1,j,k}}}{V_{cell_{i,j,k}}} + \left(\frac{r_{\beta_{i-1,j,k}}^{ex}}{6} \right) * \frac{V_{cell_{i-1,j,k}}}{V_{cell_{i,j,k}}} + \\
 & + \left(\frac{r_{\beta_{i,j+1,k}}^{ex}}{6} \right) * \frac{V_{cell_{i,j+1,k}}}{V_{cell_{i,j,k}}} + \left(\frac{r_{\beta_{i,j-1,k}}^{ex}}{6} \right) * \frac{V_{cell_{i,j-1,k}}}{V_{cell_{i,j,k}}} + \left(\frac{r_{\beta_{i,j,k+1}}^{ex}}{6} \right) * \frac{V_{cell_{i,j,k+1}}}{V_{cell_{i,j,k}}} + \\
 & + \left(\frac{r_{\beta_{i,j,k-1}}^{ex}}{6} \right) * \frac{V_{cell_{i,j,k-1}}}{V_{cell_{i,j,k}}}
 \end{aligned} \tag{3.20}$$

Notably, if cells are placed next to boundaries (i.e. bottom, lateral wall, etc) or topological elements (i.e shaft, baffles etc), it will be taken into account that the number of surrounding cells has to be changed accordingly.

Moreover, the first azimuthal computational cell ($\theta = 0$, i.e $K=0$) and the last one ($\theta = \pi$, $K=NK$) (for each radial and axial position) are considered neighbouring within the algorithm indexing in order to allow the exchange of solids across the periodic boundary.

The effect of introducing the *excess solid volume correction (ESVC)* algorithm is shown in Fig.3.5, where maps of solid distribution on the tank bottom during the first impeller revolution are reported. When such algorithm was not implemented, the solid volume fraction exceeded the physical packing value r_{β_packed} in several regions of the tank bottom as shown in Fig. 3.5-1.

On the contrary, when the *ESVC* algorithm was implemented, the physical maximum solid volume fraction was not exceeded anywhere over the whole tank bottom (Fig. 3.4-2).

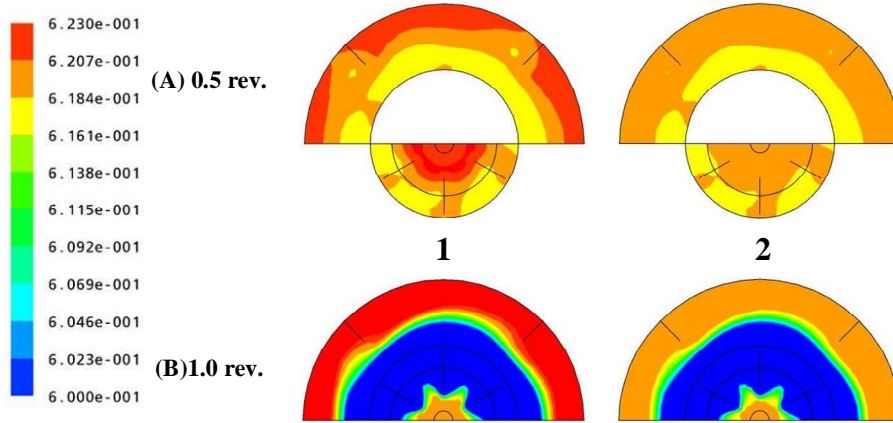


Fig. 3.5: Particle distribution at tank bottom: influence of the *ESVC* algorithm:
1) without *ESVC* algorithm; 2) with *ESVC* algorithm.

Simulations were conducted using two different time steps. A finer TS_1 was used during the first ten revolutions to better follow the initial system evolution, while a ten fold time step TS_2 was utilized for simulating the system from the 10th impeller revolution on. TS_2 corresponds to the time impeller needs to rotate by an angle equal to the azimuthal length of a single computational cell. Therefore each of the first ten revolutions require 480 time steps, while each of the last ninety require 48 time steps. It is worth nothing that such a small time step value TS_1 was needed, in the first simulation stages, in order for the *ESVC* algorithm to guarantee an effective control of maximum packing.

The number of iteration per time step was set to 30 with the aim of following the transient as closely as possible as well as to enhance the number of times (per time step) in which the *excess solid volume correction* algorithm acts. Under these conditions residuals did practically settle before passing to the next time step, i.e. in the present simulation 30 internal iterations per time steps were always more than sufficient to get fully settled values of the residuals.

3.5 Results and discussion

Simulation results and visual experimental information are reported in Fig.3.6 and in Fig.3.7. The various rows shows pictures of the suspension after 1, 2, 5, 10, 20, 50 complete impeller revolutions respectively, that is from a still almost motionless condition to steady-state. In fact, no appreciable variations in suspension height and solid distribution were visible after the 50th revolution.

The first and the last column of Fig.3.6 are experimental snapshots of the suspension, acquired by placing the camera at different tilt angles: precisely a front view images and a tilted up-front view are reported in column 1 and 5 respectively. In column 2 of Fig.3.6 and in all columns of Fig.3.7 the computational results are depicted. They show solid volume fraction distributions on a diametrical vertical plane midway between subsequent baffles; the legend range sweeps from 0 to twice the value of the mean particle volumetric fraction (i.e. 0.192 v/v). All simulation results were obtained, using Eqs. 13, 14, 15 for computing the drag force, while the drag coefficient model was: the *fixed*- C_D for column 2 of Fig.3.6, and for column 1 and 2 of Fig.3.7, the *slip*- C_D for column 3 of Fig.3.7, and the *turb*- C_D for column 4 of Fig.3.7.

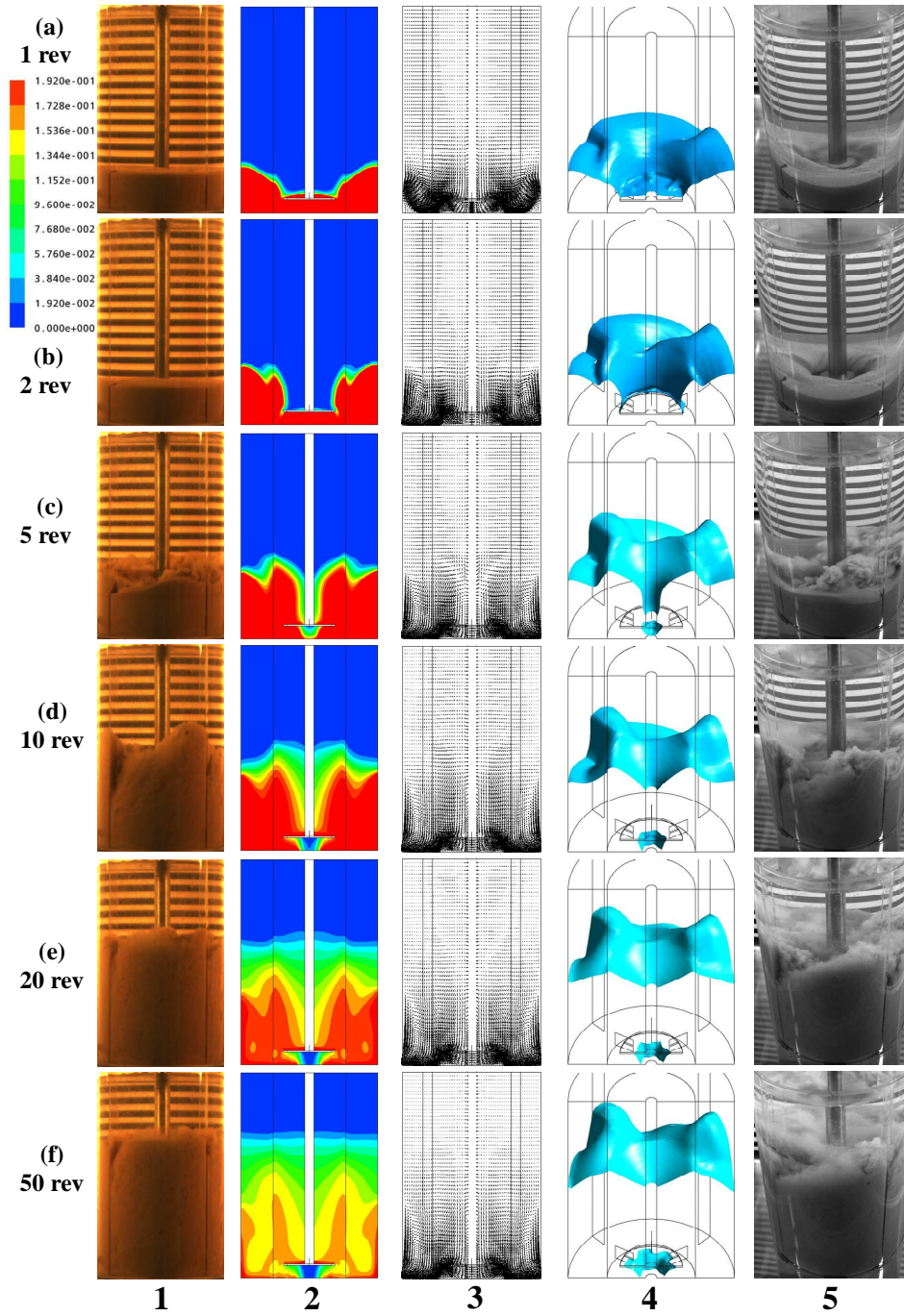


Fig. 3.6: Time evolution of particle off-bottom suspension from start-up to steady state: 1) experimental front view; 2) $fixed-C_D$ simulated distribution on a vertical plane midway between baffles; 3) simulated velocity vector plot; 4) simulated iso-surface at a solid volume fraction of 0.1; 5) experimental tilted view.

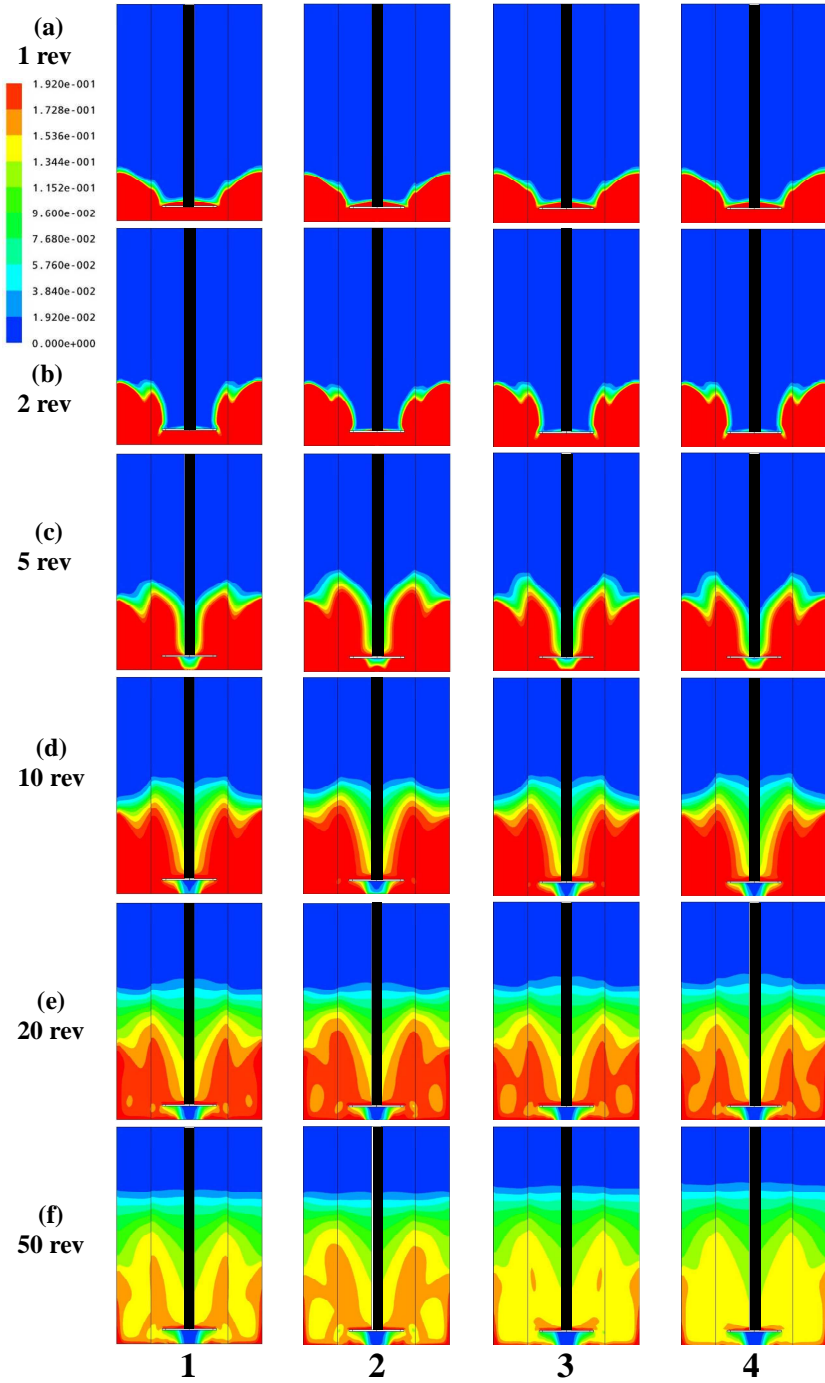


Fig. 3.7: Simulated particle distributions on a vertical diametrical plane midway between baffles. Comparison among different simulations approaches: 1) *fixed- C_D* ; 2) *fixed- C_D* and finer computational grid; 3) *slip- C_D* ; 4) *turb- C_D* .

After one impeller revolution from start, both experimental and computational results (first row of Fig.3.6) present a decrease in suspension height in the central part of the tank upon the impeller disk, thus generating a partial impeller uncovering: solid particles over the impeller disk move towards more peripheral zones. This impeller uncovering phenomenon is particularly visible in the two tilted images (columns 4 and 5 of Fig.3.6) and becomes complete and clearly observable after two impeller revolutions (row b of Fig.3.6). This partial and total impeller uncovering is very well predicted by the simulation while, during these first two revolutions, suspension height near the side wall is slightly overestimated. This may well depend on some drag overestimation when using the Ergun equation under high particle concentration conditions. As a matter of fact, the Ergun equation holds true for fluids moving through rigid and steady fluid-solid interfaces. The mobility of particles under suspended, yet highly concentrated, conditions might well result into lower forces exchanged between the two phases with respect to Ergun equation predictions.

The other computational snapshots, relevant to 5, 10, 20, 50 complete impeller revolutions respectively, highlight a very good agreement of time-dependent predicted suspension height with corresponding experimental images. Overall, it can be stated that a good prediction of the entire transient solid distribution was obtained. This suggests that a simple modelling of inter-phase drag is practically sufficient to correctly predict the suspension height of a solid-liquid suspension in radially agitated baffled tank.

Velocity vector plots, shown in column 3 of Fig.3.6, clearly follow the suspension evolution. In the first two revolutions, velocities are significant only near the impeller, where fluid and particles start to move. In the subsequent revolutions velocities diffuse towards the upper part of the tank, being however always limited to the zone where particles are present.

Column 4 of Fig.3.6 reports simulation results in the form of the iso-surface at $r_{\beta}=0.1$ and thus shows the volume of the tank containing a significant concentration

of solid particles. The choice of $r_\beta=0.1$ is quite arbitrary but it gives a very good idea of the interface separating the high concentration zone from the clear liquid region.

The 3-D nature of such a surface provides other useful information. By means of this column the computational initial impeller uncovering and the dynamic “puffs” of particles behind baffles are better observable. These “puffs” are well predicted by the simulations, thus confirming the reliability of model results, as shown in graphs d4 and d5 of Fig.3.6.

As far as other drag coefficient approaches are concerned, the *slip- C_D* and the *turb- C_D* are presented in columns 3 and 4 of Fig.3.7 respectively. The introduction of the model *turb- C_D* , produces a little increase in suspension height. Model *slip- C_D* , does not yield any significant difference with respect to model *fixed- C_D* .

In any case, no significant variations among the chosen computational approaches are appreciable, each of them manages to correctly follow the transient, providing a very good prediction of suspension height dynamic evolution too.

An important issue was to verify the total absence of any grid-dependence, in fact all the results so far presented are obtained by the coarse grid. The computational images depicted in column 2 of Fig.3.7 are obtained using the finer grid, they are very similar to those of column 1, thus suggesting limited grid-dependence, as far as particle distribution is concerned. This is further confirmed by the radially averaged steady-state axial particle concentration profiles depicted in Fig.3.8, where only minor changes can be observed despite the large grid variation.

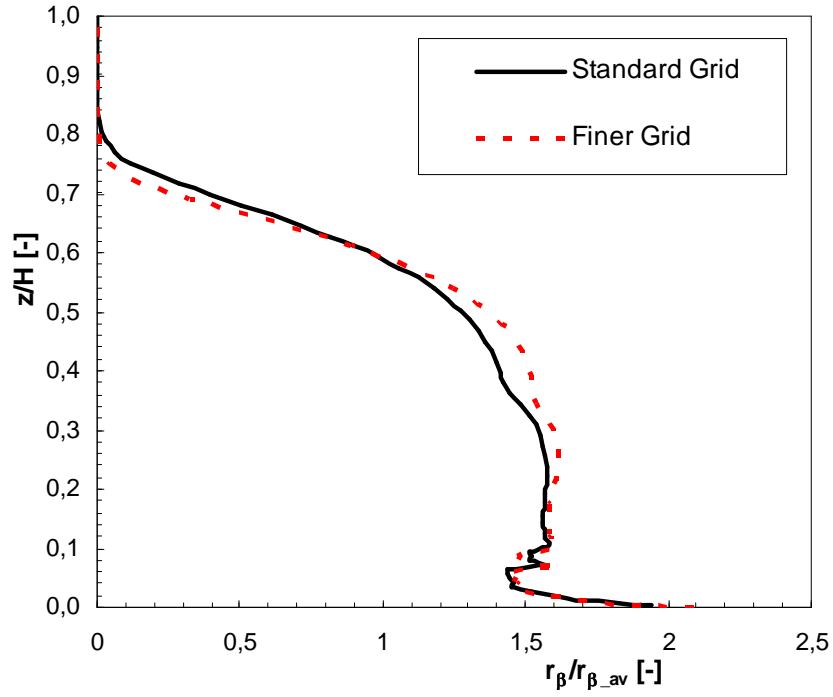


Fig. 3.8: Steady-state radially-averaged axial profiles of particle concentration on a vertical plane midway two subsequent baffles: comparison between standard and fine grid.

Finally, in order to further test model reliability, in Fig.3.9 experimental data by Micheletti *et al.* (2003) are compared with relevant CFD predictions. In the above mentioned figures steady state local axial profiles of particle concentration at a radial position $r/T=0.35$ and midway between subsequent baffles, are presented.

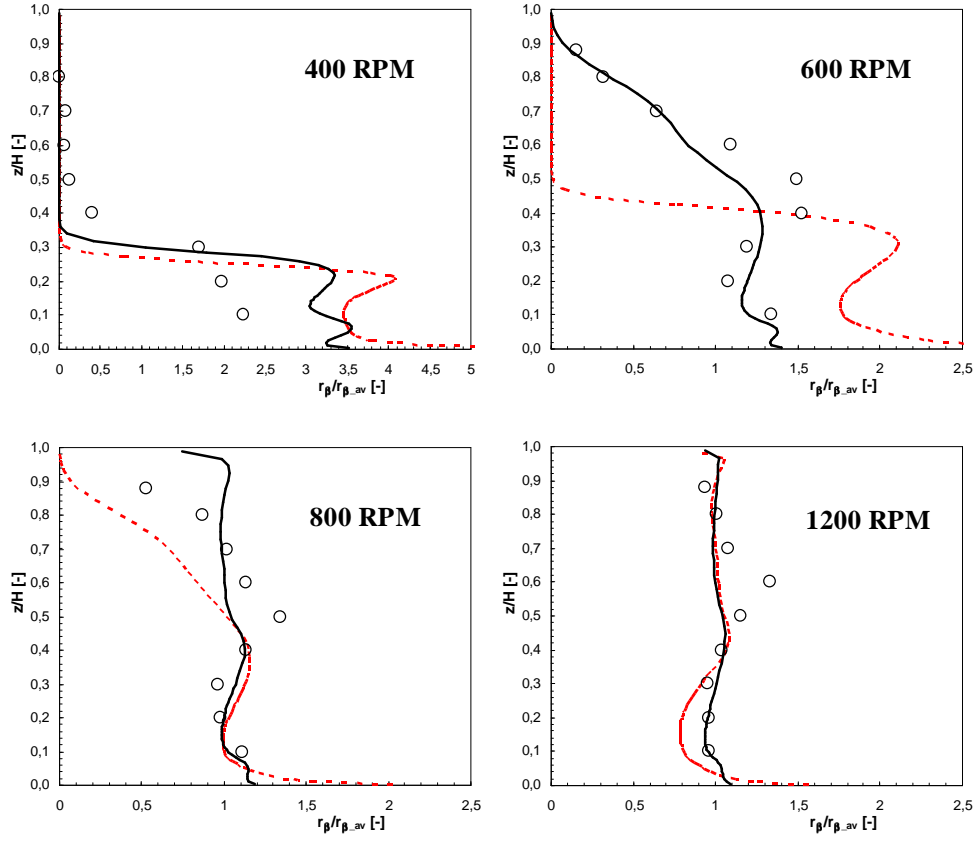


Fig. 3.9: Steady state local axial profile of particle concentration (midway between subsequent baffles and at radius = 0.35T). Symbols: Micheletti et al. (2003) experimental data; dotted line: *fixed- C_D* CFD results; solid line: *turb- C_D* CFD results.

Each image shows the comparison between Micheletti et al. data (2003) and, both *fixed- C_D* (with $C_D=1.50$ for the particles-liquid system involved) and *turb- C_D* , computational data. It can be observed there that simulation results agreement with experimental data is poor at 400 RPM. It is however important to note that, according to Micheletti et al. (2003), at this agitation speed fully suspended conditions are not achieved. Clearly the presence of a layer of solids steadily lying on the tank bottom cannot be simulated within the present model, as it could have

been expected. As concerns the results data obtained at N=600, 800 and 1200 RPM (all pertaining to fully suspended conditions) a better agreement, comparable if not better than that obtained by Derksen (2003), can be observed between experimental data and simulation results.

Notably, *turb- C_D* simulations give rise to better agreement than the *fixed- C_D* simulation, particularly for the 400 and 600 RPM cases, thus confirming the importance of correcting drag force for free stream turbulence effects (Brucato *et al.*, 1998a; Montante and Magelli, 2005). The apparent discrepancy with the above quoted unimportance of turbulence drag correction in the case of the transient simulations is clearly the result of two factors both resulting in a negligible $C_{D,turb}/C_D$ ratio (1.11 for the transient simulations versus 2.89, 5.45, 9.56 and 22.14 at 400, 600, 800 and 1200 RPM respectively for Micheletti *et al.*' vessel simulations). The first factor is the smaller specific power input, i.e. the smaller turbulent dissipation (0.22 W/kg for the transient simulations versus 0.15, 0.48, 1.15 and 3.84 W/kg at 400, 600, 800 and 1200 RPM respectively for Micheletti *et al.*' case, all computed by the k- ϵ turbulence model) implying larger λ (46 μm versus 50, 38, 30 and 23 μm at 400, 600, 800 and 1200 RPM respectively). The second factor is the smaller particle size (231 μm versus 655 μm) selected for the case of the transient simulation.

In interpreting the results shown in Fig.3.9, it should be kept in mind that any effect of the drag model is not local: in particular, the r_β distribution in the upper region of the vessel does not, or not only, depend on the drag effects in the same volume, but rather on the particle-fluid interactions and dispersion in the entire vessel volume. As a matter of fact the local particle concentration increase observable in the upper region of Fig.3.9 at 800 RPM are clearly the result of more particles reaching that region, due to drag changes and better dispersion capability in the lower part of the tank.

Also the low influence of the C_D model in the 1200 RPM case is explained by the fact that, at this high speed, the solid volume fraction has attained an almost uniform value throughout the vessel height thus making any further effect of the model negligible.

Overall, the present results indicate that particle distribution in dense solid-liquid suspensions in stirred tanks is a phenomenon mainly controlled by gravity, inertial and inter-phase drag forces. When these are properly modelled, the simple simulation approach adopted in this chapter gives rise to satisfactory agreement with experimental results even with the (apparently complex) transient behaviour of dense suspensions.

3.6 Final remarks

The transient behaviour of an off-bottom solid-liquid suspension during start-up in a stirred fully baffled tank was investigated by means of a rather simple CFD methodology purposely formulated and tested. Relevant experimental data were acquired to validate the modelling approach. Literature data were also employed to further test model reliability.

The Eulerian-Eulerian Multi Fluid Model along with the standard homogeneous k - ϵ turbulence model was adopted inside the commercial CFD code Ansys-CFX4.4. The sliding grid algorithm was used to simulate the impeller rotation in the fully baffled tank.

Particle-particle and particle-fluid interactions strongly affect particle distribution, and therefore require an effective modelling of relevant phenomena. Here particle fluid interactions were assumed to be limited to drag force exchange, with this last able to deal with the high solid concentrations near tank bottom, the intermediate concentration levels inside the suspension and the low concentration region in the upper clear liquid layer, as well as with free-stream turbulence effects. Particle-particle interaction modelling was computed by the adoption of an excess particle concentration treatment (*ESVC* routine) that inhibited particle concentration from getting significantly larger than maximum particle packing.

Results were found to be in satisfactory agreement with experiments, though room for further improvement exists. The agreement observed between simulation results and experiment suggests that the modelling approaches here adopted are able

to capture the main factors affecting particle distribution in stirred dense systems, which are therefore confirmed to involve mainly inertial, drag and body forces.

3.7 Nomenclature

B	<i>body force, N/m^3</i>
C	<i>impeller clearance, m</i>
$C_{a\beta}$	<i>inter-phase drag term, $kg/(m^3 \cdot s)$</i>
C_D	<i>drag coefficient, (-)</i>
D	<i>impeller diameter, m</i>
d_p	<i>particle diameter, m</i>
H	<i>height of fluid in vessel, m</i>
k	<i>turbulent kinetic energy, m^2/s^2</i>
M	<i>inter-phase terms, N/m^3</i>
N	<i>agitation speed, RPM</i>
N_{js}	<i>just suspended agitation speed, RPM</i>
NI	<i>number of computational cell in the axial direction, (-)</i>
NJ	<i>number of computational cell in the radial direction, (-)</i>
NK	<i>number of computational cell in the azimuthal direction, (-)</i>
r	<i>volumetric fraction, (-)</i>
r_{β}^{ex}	<i>solid volumetric fraction exceeding maximum packing value, (-)</i>
$r_{\beta}^{ex \text{ total}}$	<i>the sum of r_{β}^{ex} for all the domain computational cells, (-)</i>
$r_{\beta\text{-packed}}$	<i>solid volumetric fraction maximum packing value, (-)</i>
P	<i>pressure, Pa</i>
Re	<i>Reynolds number, (-)</i>
S	<i>source term</i>
T	<i>tank diameter, m</i>
U	<i>velocity, m/s</i>
V_{cell}	<i>computational cell volume, m^3</i>

Greek letters

α	<i>liquid phase</i>
β	<i>solid phase</i>
ε	<i>turbulent dissipation, W/kg</i>
λ	<i>Kolmogorov length scale, m</i>
μ	<i>viscosity, Pa·s</i>
ρ	<i>density, kg/m³</i>
σ	<i>turbulent Prandtl number, (-)</i>

Subscripts

α	<i>liquid phase</i>
β	<i>solid phase</i>
t	<i>turbulent</i>

CHAPTER 4

INCOMPLETE SUSPENSION REGIME MODELLING

4.1 Abstract

This chapter represents the further development of the investigation carried out in Chapter 3. Predicting the transient behaviour of a dense solid-liquid suspension during start-up was a first attempt to get a deep insight into the complex mechanism of suspension. In fact, during the first phases of the start-up, some particles are motionless on the tank bottom and others start suspending. The suspension degree increases with time till all the particles are in motion and complete suspension conditions are achieved.

Suspension starts within the incomplete suspension regime, therefore CFD modelling of this regime could lead to a better understanding of the forces and the effects which cause some particles to suspend while others remain still on the vessel bottom.

The prediction of a dense solid-liquid suspension dynamics during start-up already allowed to partially deal with the incomplete suspension regime. It is the aim of the present chapter to perform a specific research effort focusing on the study of this regime.

Reliable and accurate CFD modelling of this regime would lead to a deeper knowledge of the suspension phenomenon as well as to the possibility of predicting the minimum impeller speed for complete suspension N_{js} .

In addition, it is worth noting that investigating the filleting regime could constitute a focus of primary importance by an industrial point of view since many industrial stirred vessels operate at impeller speeds lower than N_{js} (Oldshue, 1983; Rieger et al., 1988).

A lot of research efforts have been devoted so far to the assessment of the minimum impeller speed able to guarantee the suspension of all particles. Conversely, only little attention has been paid to the evaluation of the amount of

solid particles that are suspended at impeller speeds lower than N_{js} : in some cases the loss in available interfacial area between particles and liquid could be reasonably counterbalanced by a decreased mechanical power input. This consideration leads to the need to evaluate the percentage of suspended solids at different impeller rotational speeds in order to quantify the economical advantage linked to the adoption of an incomplete suspension regime inside the stirred tank.

The present chapter deals with Computational Fluid Dynamics simulations of dense solid-liquid partial suspensions in baffled stirred tanks and particularly focuses on the prediction of the amount of suspended particles at a number of angular velocities encompassing both the filleting and the complete suspension regime. An Eulerian-Eulerian Multi Fluid Model coupled with a standard k- ϵ turbulence model were adopted for CFD simulations. Both Sliding Grid and Multiple Reference Frame approaches were employed to simulate the impeller-tank relative rotation. In addition, a number of numerical approaches were tested and the relevant results were critically discussed. A lot of experimental data were used for validation purposes: data collected by using the Pressure Gauge Technique (Brucato et al., 1997), snapshots of the simulated tank and literature data. Comparison between CFD predictions and all experimental data showed a very good agreement.

4.2 Literature review

Information on the quality of suspension is of greatest importance for the design and control of reactors involving mixing of solid particles in a liquid (Zwietering, 1958; Chapman et al., 1983; Rewatkat et al., 1991). Therefore, modelling the fluid dynamics of solid liquid suspensions in stirred tanks is an issue of crucial importance.

The choice of design parameters ensuring an adequate solid suspension is still an open problem for design engineers. All the industrial applications involving transport phenomena between solids and liquid require the contacting interfacial area has to be maximized. It means that mixing operation must guarantee a complete suspension of particles, keeping at the same time an impeller speed not too high in

order to allow acceptable energy consumptions. The well known compromise between these two aspects is represented by the choice of the minimum impeller speed required for the complete off-bottom suspension of solid particles in the vessel (N_{js}), a very important parameter for industrial mixing process design and optimization whose assessment has been focused by many research efforts (Zwietering, 1958; Nienow, 1968; Baldi et al., 1978; Bohnet and Niesmak, 1980; Chapman et al., 1983; Raghava Rao et al., 1988; Rewatkar et al., 1991; Armenante et al., 1998). As a matter of fact, although all these works succeeded in determining, in a more or less accurate way, N_{js} values, they did not give any quantitative information on the incomplete suspension conditions. This is rather surprising since in a number of industrial cases a $N < N_{js}$ is usually chosen as operative condition (Oldshue, 1983; Rieger et al., 1988), in fact the energy savings due to a lower operative agitator speed can counterbalance the loss active interfacial area. In particular Brucato and Brucato (1998) stated that at impeller speeds of about 80% of the N_{js} estimated by Zwietering's criterion (no particles resting on the vessel bottom for more than 1 second) practically all particles but a few are already suspended thereby achieving large and installation cost savings without significantly affecting the solid-liquid mixing performance.

Therefore, the knowledge of the amount of the suspended solids at different impeller speeds (*suspension curves*) is a topic of primary importance.

So far, most researchers have focused their attention on the evaluation of N_{js} , but only few efforts have been devoted on the estimation of *suspension curves* (Biddulph, 1990; Brucato et al. 1997; Brucato and Brucato, 1998; Micale et al. 2002). Brucato and Brucato (1998) utilized a technique based on the "twin system" concept (Brucato and Rizzuti, 1989) for the determination of the fraction of unsuspended solid particles at impeller speeds lower than N_{js} . This technique was considered reliable when the fraction of unsuspended solids is lower than 0.5, but too demanding in terms of experimental work. Conversely, Brucato et al. (1997) and Micale et al. (2002) proposed a novel technique, namely the Pressure Gauge Technique (*PGT*), able to assess the percentage of suspended solids in a stirred tank, at a given impeller speed, by means of pressure measurements on the tank bottom.

Although such experimental approach is simple and reliable, the adoption of computational fluid dynamics (CFD) would result less onerous and time consuming in providing similar information on a variety of systems. In fact, CFD investigations give more detailed data on the flow field than classical experimental techniques so that a deeper understanding and a better application of solid suspension theories can be obtained (Rieger and Dittl, 1994). Furthermore, though CFD constitutes a powerful tool which can be used to obtain deep insights into complex multiphase flow problems, it is necessary to validate the model predictions with corresponding experimental data before the model can be reliably used for industrial reactor design and operation.

In accordance with my knowledge no CFD works devoted to the issue of suspension curves exist in literature. Also, only a few works deal with CFD simulations of solid-liquid suspensions within stirred vessels at impeller speeds lower than the minimum for complete suspension (*partial suspension conditions*) (Kee and Tan, 2002; Oshinowo and Bakker, 2002; Ochieng and Lewis, 2006a; Murthy et al., 2007; Kasat et al., 2008; Panneerselvam et al., 2008; Hosseini et al., 2010b). Most of them focused on the prediction of N_{js} without devoting with the proper attention to the filleting regime modelling issue.

In particular, Kee and Tan (2002) proposed a CFD approach for predicting N_{js} based on the observation of the simulated transient profiles of solid volume fraction for the layer of cells adjacent to the vessel floor. They performed two-dimensional (2-D) simulations of a flat-bottomed mixing tank employing both a six-bladed disc turbine (Lightnin R100TM) and a three-bladed propeller (Lightnin A310TM). Experimentally validated velocity vectors for both impellers were taken by the *MixSim library* of *Fluent code* (Fluent Inc., Lebanon, USA). Notwithstanding the excessive simplification of adopting a 2-D approach for a complex turbulent 3-D system like a stirred tank as well as the total absence of a proper experimental validation of the computational model, CFD results appeared to be quite good. As a matter of fact, because of the criterion they chose to distinguish sediments from

suspended particles, the adoption of a 3-D approach would have led to large computational costs.

Oshinowo and Bakker (2002) investigated via CFD the performance of hydrofoil impellers and a 45° pitched-blade turbine under different agitation speeds. Solid volume fraction and velocity distribution, suspension cloud height and liquid phase mixing times were predicted.

Ochieng and Lewis (2006a) employed both Computational Fluid Dynamics and experimental techniques such as Laser Doppler Velocimetry (*LDV*) and Optical Attenuation Technique (*OAT*) in order to investigate the off-bottom solid suspension in an elliptical-bottomed and fully baffled tank stirred by a hydrofoil propeller (Mixtec HA735). They used these numerical and empirical methods in close conjunction with themselves inside a “tedious procedure” to predict N_{js} value for a number of cases thus resulting in a not fully predictive technique. Cloud heights were predicted as well and a corresponding empirical correlation was proposed on the basis of the mixing features identified by the CFD and the experimental methods.

Murthy et al. (2007) adopted the Eulerian multi-fluid model along with the standard k - ϵ turbulence model to perform steady state (Multiple Reference Frames) simulations of gas-liquid, solid-liquid and gas-liquid-solid flows in a stirred tank testing different impeller types (Rushton turbine, 45° pitched blade down and up-flow turbines). Influence of solid loading, particle size, superficial gas velocity and sparger design were investigated as well. Authors proposed a method for the evaluation of N_{js} via CFD based on the value of the standard deviation of solid concentration in accordance with the definition of the standard deviation due to Bohnet and Niesmak (1980). Good predictions were obtained.

Also Kasat et al. (2008) employed the standard deviation of solid concentration in order to evaluate solid-liquid suspension regime/quality again in accordance with the criterion proposed by Bohnet and Niesmak (1980). More precisely, they carried out MRF simulations of a flat-bottomed baffled slurry tank stirred by a Rushton turbine. Simulations were performed by adopting the Multi Fluid Model (MFM) along with the homogeneous k - ϵ model for the turbulence closure. The model was

further extended aiming at understanding the influence of suspension quality on the liquid-phase mixing process which occurs in the stirred slurry tank. In particular, a criterion to evaluate mixing time by CFD was proposed and applied to the entire vessel as well as only to the top clear liquid layer at any suspension regime. Results showed that the very small velocities encountered in the top clear liquid layer are responsible of a low mixing within this zone thus resulting, on its turn, into an increase in the total mixing time.

Panneerselvam et al. (2008) carried out steady state simulations focusing on the study of solid suspension in a gas–liquid–solid elliptical bottomed baffled stirred vessel. Firstly solid-liquid and gas-liquid flow were investigated separately: CFD results were validated qualitatively with literature experimental data in terms of axial and radial profiles of solid velocity in liquid–solid suspension and liquid velocity in gas–liquid dispersion for different operating conditions. Concerning gas–liquid–solid flows, the CFD predictions were compared quantitatively with purposely collected experimental data in the terms of critical impeller speed for just suspended conditions. In particular, authors assessed the critical impeller speed experimentally both by visual observations and by *Power Number* (N_p) versus impeller speed plot analysis. CFD simulations were performed at the assessed just impeller speeds and the corresponding standard deviation of solid volume fractions and cloud height were calculated to check/validate simulation reliability. Influence of particle size, impeller design and air flow rate were investigated.

Hosseini et al. (2010b), investigated by both experiments (by visual observation and Electrical Resistance Tomography) and simulations solid-liquid suspensions within a transparent flat-bottomed tank provided of four equally spaced baffles placed with gaps from vessel walls. They assessed impeller torque, cloud height, N_{js} and the degree of homogenization founding a good agreement between experimental and CFD data. Also, authors addressed the CFD model to quantify the homogenization degree dependence on impeller speed, impeller design (three different axial flow impellers, i.e. Lightnin A100TM, A200TM, A310TM), impeller off-bottom clearance, particle diameter, and particle density.

All of these scientific works deal with CFD simulations at impeller speeds both lower (*partial suspension conditions*) and higher (*complete suspension conditions*) than the N_{js} value without making any comment on the presence of still particles lying on the bottom. In addition, experimental data relevant only or mainly to complete suspension conditions are employed for the CFD modelling validation, i.e. a proper validation of the modelled partial suspension conditions is not performed.

In a solid-liquid mixing operation it is necessary to avoid the accumulation of particles in some locations as well as to know where only the liquid phase is present. Therefore, there is a need not only to know the amount of solids suspended at different speeds or the impeller speed at which the solid particles become fully suspended, but also to gain information on the quality of the solid distribution within the tank. A reliable prediction of such an information is of crucial importance for an accurate design and testing of a solid-liquid stirred system. However, in accordance with my knowledge, it is not easy to find such a type of data in literature for partial suspension conditions because of the slight industrial interest on this particular regime.

Although CFD prediction of the partial suspension regime could apparently seem not so interesting by an industrial point of view, it can lead to a deeper knowledge of the complex phenomenon of particle suspension within an agitated liquid thus possibly resulting in a better design of pertinent solid-liquid contact equipment.

Scope of the present chapter was to carry out CFD simulations on incomplete-to-complete suspension regimes in stirred tanks in order to numerically predict suspension curves as well as to increase the knowledge degree of particle suspension phenomenon.

Three different types of experimental data were accordingly used for the validation of the proposed CFD model:

- data concerning the fraction of suspended solid particles collected by PGT;
- snapshots of the investigated vessel for both qualitative and quantitative comparison;

- literature data (Micheletti et al., 2003) regarding local axial profiles of solid concentration.

It is worth noting that, for the first time, CFD simulations dealing with the incomplete suspension conditions are validated by means of purposely collected experimental data.

4.3 Experimental information

The experimental system consisted of a cylindrical flat bottomed baffled tank with the vessel diameter $T = 0.19\text{m}$ equal to the total liquid height H , as depicted in Fig. 4.1.

A standard six-bladed Rushton turbine with $D=T/2$ was used in the suspension experiments. It was set at a distance from the vessel bottom equal to $1/3$ of H . Deionised water and glass ballottini with diameter ranging between 212 and $250\ \mu\text{m}$ were employed. Solid measured density was $2500\ \text{kg/m}^3$. The solid particle loading was equal to $1.6\ \text{kg}$ corresponding to an average solid weight fraction (ratio of solid mass to liquid mass) 33.8% $w_{\text{solid}}/w_{\text{liquid}}$ ($=11.9\%$ $v_{\text{solid}}/v_{\text{total}}$). The particle bed lying on the bottom void fraction (under no agitation conditions) was experimentally measured resulting in about 40% . Influence of particle concentration and particle mean diameter on the simulation procedure reliability was checked: the solid loading was decreased to $0.8\ \text{Kg}$ (16.9% $w_{\text{solid}}/w_{\text{liquid}}$ $=5.95\%$ $v_{\text{solid}}/v_{\text{total}}$) to evaluate concentration effect and $500\text{-}600\ \mu\text{m}$ glass ballottini particles with the concentration of 33.8% $w_{\text{solid}}/w_{\text{liquid}}$ were employed to verify particle mean diameter influence.

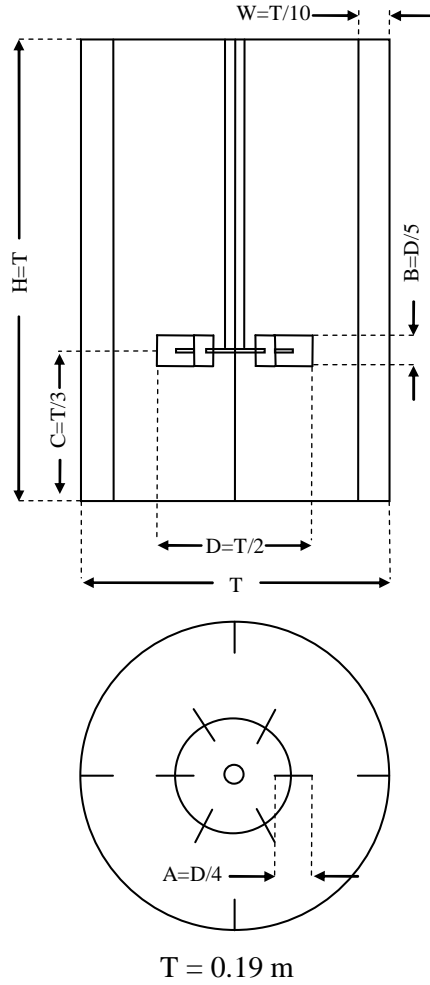


Fig. 4.1: Stirred tank.

4.3.1 Pressure Gauge Technique (PGT) apparatus and fundamentals

The impeller shaft was driven by a DC motor (Mavilor MS6) provided with a speed control loop (Infranor). An optical tachometer was employed to independently measure the impeller rotational speed. A pressure gauge constituted of a simple

inclined manometer is connected to a given point of the vessel bottom allowing pressure readings to be taken. This point was placed azimuthally midway between two subsequent baffles and radially midway between the axis and the lateral wall. A hole in the vessel bottom transmitted the local pressure value to a dead chamber directly connected to the pressure gauge (Fig.4.2).

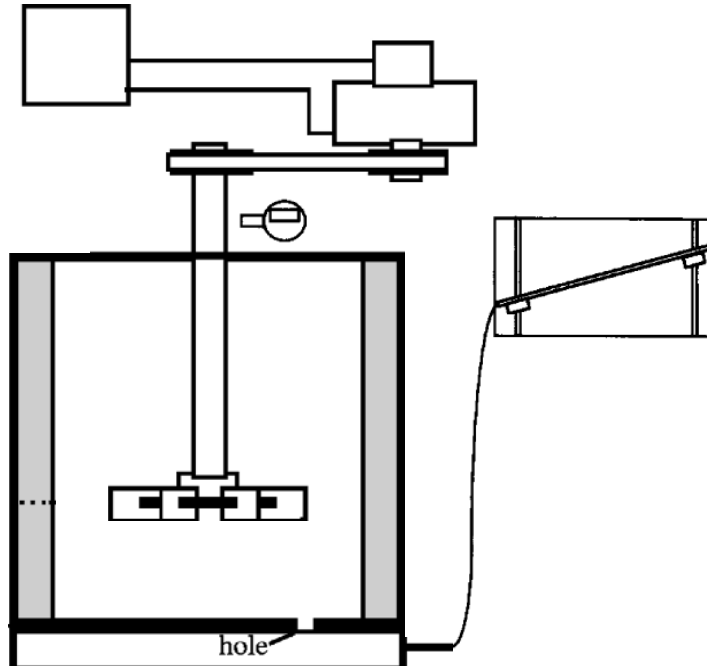


Fig. 4.2: Experimental set-up: PGT apparatus.

When system is not stirred, all the particles rest still on the vessel bottom and the measured pressure clearly results proportional to the height of the liquid inside the vessel. This pressure is considered as the reference pressure and it is subtracted from the readings obtained at higher agitation speeds. In fact, when some or all of the particles are suspended, a pressure enhancement due to the increase of the fluid

apparent density is measured. It is possible to numerically link this increase to the amount of suspended solids by means of the following equation:

$$\Delta P_\beta = \frac{V_\beta (\rho_\beta - \rho_\alpha) g}{A_{bottom}} = \frac{1 - \rho_\alpha / \rho_\beta}{\pi T^2 / 4} M_\beta \quad (4.1)$$

where A_{bottom} is the vessel bottom area, ΔP is the observed pressure increase and M_β is the mass of suspended solids.

The value of pressure increase assessed at a given impeller speed would be easily converted through equation 4.1 into the corresponding mass of suspended solids. Actually, increasing agitation speed, also the dynamic head effects due to the liquid motion inside the vessel under agitated conditions give a contribution to the measured pressure enhancement. These effects were taking into account, assessed and subtracted from the measured total pressure, thus obtaining the pressure increase due only to the solid suspension. Eventually, the M_β values found in this way were translating into fractional solid suspension data. Full details on the technique can be found in Brucato et al., 1997 and Micale et al., 2002.

4.3.2 Snapshots of the investigated vessel

In order to provide additional experimental data for a further validation of the CFD modelling procedure, a number of images of the operating system were collected by employing a commercial digital camcorder (Sony, model DCRTRV530E PAL). Two different set of images were collected for each experimental case previously presented: the camera was placed below the vessel bottom and in front of the lateral wall. The first set of images shows the unsuspended solids on the vessel bottom, i.e. the shape which the sediment assumes on this surface, similarly, the front snapshots show the shape of the sediment placed on the lateral wall. In order to correctly distinguish the still particles from the

moving ones, images were taken with high capture times (i.e. low shutter speeds): in this way still particles are well defined while the moving ones appear to be blurred.

4.4 Numerical modelling

Reynolds Average Navier Stokes (RANS) simulations were carried out by using the commercial finite-volume method code CFX4.4 (AEA technology). The adopted numerical approach for the simulation of the two-phase system was the Eulerian-Eulerian *Multi Fluid Model (MFM)* where the two phases are assumed to coexist at every point in space in the form of interpenetrating continua. It solves the continuity and momentum equations for the two-phases separately and simultaneously, the coupling between the two phases is obtained through pressure and inter-phase exchange terms. The particle phase was treated as a separate dispersed phase, occupying disconnected regions of space in the continuous liquid phase.

4.4.1 Equations of motion

Assuming phases to be incompressible, for each one, the continuity equation is written as a function of its own volume fraction:

$$\frac{\partial}{\partial t}(r_{\alpha}\rho_{\alpha}) + \vec{\nabla} \cdot (r_{\alpha}\rho_{\alpha}\vec{U}_{\alpha}) = 0 \quad (4.2)$$

$$\frac{\partial}{\partial t}(r_{\beta}\rho_{\beta}) + \vec{\nabla} \cdot (r_{\beta}\rho_{\beta}\vec{U}_{\beta}) = 0 \quad (4.3)$$

where the subscripts α and β refer to the continuous and dispersed phases respectively, r is volumetric fraction, ρ is density and U is mean velocity.

Clearly,

$$r_{\alpha} + r_{\beta} = 1 \quad (4.4)$$

The momentum balance equations are:

$$\frac{\partial(r_\alpha \rho_\alpha \vec{U}_\alpha)}{\partial t} + \vec{\nabla} \cdot (r_\alpha \rho_\alpha \vec{U}_\alpha \otimes \vec{U}_\alpha) = \vec{F}_\alpha \quad (4.5)$$

$$\frac{\partial(r_\beta \rho_\beta \vec{U}_\beta)}{\partial t} + \vec{\nabla} \cdot (r_\beta \rho_\beta \vec{U}_\beta \otimes \vec{U}_\beta) = \vec{F}_\beta \quad (4.6)$$

where F_α and F_β are the net forces acting respectively on the liquid and the solid phase. They are the sum of the viscous term, the pressure gradient, the gravity force, and the momentum inter-phase transfer term:

$$\vec{F}_\alpha = \vec{\nabla} \cdot \left(r_\alpha (\mu_\alpha + \mu_t) \left(\vec{\nabla} \vec{U}_\alpha + (\vec{\nabla} \vec{U}_\alpha)^T \right) \right) - r_\alpha \vec{\nabla} P + r_\alpha \rho_\alpha \vec{g} + \vec{M}_{\alpha\beta} \quad (4.7)$$

$$\vec{F}_\beta = \vec{\nabla} \cdot \left(r_\beta \mu_\beta \left(\vec{\nabla} \vec{U}_\beta + (\vec{\nabla} \vec{U}_\beta)^T \right) \right) - r_\beta \vec{\nabla} P + r_\beta \rho_\beta \vec{g} + \vec{M}_{\beta\alpha} \quad (4.8)$$

In these equations, g is acceleration gravity, μ is viscosity, P is pressure (the solid and the liquid phases share the same pressure field) and M is momentum inter-phase transfer term. In the rotating frame, the centrifugal and Coriolis forces were obviously included as body forces in the above equations, when the *Multiple Frames of Reference* method (MRF) (Luo et al., 1994) is adopted. Conversely, in *Sliding Grid* approach (SG) (Murthy et al., 1994) the flow equations for the rotating domain are written with respect to the absolute reference frame since it is the grid which rotates: this results in including additional accelerations terms being completely equivalent to the former body forces, typical for non-inertial frames. Notably, time derivative terms are not solved when the MRF approach is adopted.

It is worth noting that no turbulent viscous terms were considered for the solid phase. Usually, in literature the two phases are considered to share the same

turbulent viscosity (generally computed by means of the homogeneous k- ϵ turbulence model) and satisfactory results can be obtained in a number of cases (Micale et al., 2000; Micale et al., 2004; Khopkar et al., 2006; Kasat et al., 2008; Tamburini et al., 2009; Hosseini et al., 2010b). Conversely, for the case here presented, simulations were carried out at very different impeller speeds even at impeller speeds very much lower than N_{js} when many particles lie on the bottom: in such conditions. The inclusion of the turbulence viscosity term in the momentum balance equation for the solid phase would generate a strong underestimation of the amount of particles lying motionless on the vessel bottom (see results and discussion section). In other words, the inclusion of turbulent viscosity would be wrong in an environment where resting particles are surrounded by other resting particles, thus being not at all affected by the action of turbulent viscous stresses. Of course a molecular viscosity for the solid phase had to be however accounted for, in order to avoid numerical convergence problems. A molecular viscosity equal to the liquid one was chosen as suggested by literature (Micale et al., 2004; Murthy et al., 2007). Moreover, it is important to stress that the presence of a still sediment with a very high local value of solid concentration produced problems of numerical convergence thus resulting in the practical impossibility of adopting different approaches such as the *Solid Pressure Model* (Bouillard et al., 1989) or the *Granular Kinetic Theory* (Gidaspow, 1994).

4.4.2 Inter-phase transfer terms

Fluid-particle interactions as well as particle-particle interactions were modelled by the adoption of the excess solid volume correction (*ESVC*) algorithm (introduced in Chapter 3) which will be described in the following.

Interactions between the two phases were directly modelled only by inter-phase drag force terms within the momentum equations (two-way coupling):

$$\vec{M}_{\alpha\beta} = C_{\alpha\beta} (\vec{U}_{\beta} - \vec{U}_{\alpha}) = \left[\frac{3}{4} \frac{C_D}{d_p} r_{\beta} \rho_{\alpha} |\vec{U}_{\beta} - \vec{U}_{\alpha}| \right] (\vec{U}_{\beta} - \vec{U}_{\alpha}) \quad (4.9)$$

$$\bar{M}_{\beta\alpha} = C_{\beta\alpha} (\bar{U}_{\alpha} - \bar{U}_{\beta}) = C_{\alpha\beta} (\bar{U}_{\alpha} - \bar{U}_{\beta}) \quad (4.10)$$

where $C_{\alpha\beta}$ is inter-phase drag coefficient and d_p is particle mean diameter. Other inter-phase momentum exchange terms such as Basset force, virtual mass force and lift force give generally a low contribute to solid-liquid hydrodynamics especially if the particle density ratio to liquid is more than 2 (Tatterson, 1991) and they are consequently neglected (Ljungqvist & Rasmuson, 2001; Montante et al., 2001; Murthy et al., 2007; Panneerselvam et al., 2008). More precisely, Basset force, arising only in unsteady flows because of the development of a boundary layer around particles, was found to have a magnitude much smaller than the drag force. Moreover, a very little influence of lift force and virtual mass force on the simulated solid hold-up profile was found by Ljungqvist and Rasmuson (2001) for the case of a dilute solid-liquid suspension.

4.4.3 Turbulence closure

Obviously, the continuity and momentum equations written are time averaged and a turbulence model is required to guarantee they are able to describe turbulent conditions. The well known $k-\varepsilon$ turbulence model (Launder and Spalding, 1972; Launder and Spalding, 1974) was adopted as it is robust, economical, and rapid, besides it gives stable calculations and reasonable results for many flow domains (Hosseini et al., 2010b). It is commonly employed to simulate the turbulence within single/multi phase stirred vessels even though it is not able to predict with high accuracy turbulent quantities in rotating flows (Ciofalo et al., 1996) because of the presence of anisotropic turbulence (Ng et al., 1998). It is well known that the $k-\varepsilon$ turbulence model assumes the isotropy for turbulence (Murthy and Joshi, 2008) while the turbulence in the discharge stream of the impeller is anisotropic (Hockey and Nouri, 1996; Mishra et al., 1998; Aubin et al., 2001). Generally, results obtainable by the $k-\varepsilon$ turbulence model are in a good agreement with relevant experimental data as far as main bulk flow characteristics are concerned, on the

contrary, even pronounced deviations from experimental measurements concerning turbulent quantities could be obtained in the impeller region (Ng et al., 1998; Yeoh et al., 2004). Moreover, k - ε model usually overestimates the eddy viscosity. Murthy and Joshi (2008) asserted that k - ε model works well when the flow is unidirectional that is less swirl and weak recirculation as in the case of tanks stirred by hydrofoil impellers. Improved CFD predictions of turbulent quantities can be obtained by a modified k - ε model named *zonal modelling* (Sahu et al., 1998) whereby, practically, domain is divided in different zones and different k - ε model parameter (i.e. C_μ , C_1 and C_2) are utilized for each of them. Actually, it is important stressing that Jenne and Rauss (1999) focused on the effect provided by different time scales and anisotropy on the standard k - ε turbulence model without obtaining any significant improvement.

For anisotropic turbulence modelling, the adoption of the anisotropic *Reynolds Stress Model (RSM)* (which calculates each Reynolds stress separately without requiring any eddy viscosity) could constitute a valid alternative (Ciofalo et al., 1996) even though it has got various drawbacks: it can produce a long and difficult numerical convergence, it has got non-universal model parameters, it is computationally expensive (by an order of magnitude as compared to the k - ε model), it does not capture the time dependent nature of the flow and it often provides no considerable improvements in the prediction of turbulent quantities (i.e turbulent kinetic energy) (Armentante and Chou, 1996; Sheng et al., 1998; Murthy and Joshi, 2008). Aubin et al. (2004) asserted that the discrepancy of predicted turbulent quantities (both by k - ε and *RSM* model) with relevant experimental data may depend on Reynolds averaging.

Accordingly, the adoption of a *Large Eddy Simulations (LES)* provide better results in many cases (Derksen and Van den Akker, 1999; Aubin et al., 2004; Hartmann et al., 2004; Micheletti et al., 2004; Yeoh et al., 2004; Alcamo et al., 2005; Guha et al., 2008; Yapici et al., 2008). *LES* leads to a higher accuracy in prediction by modeling only the smallest turbulent scales, which tend to be more isotropic, while fully resolving the turbulence at the larger scales (Murthy and Joshi, 2008). In particular Derksen and Van den Akker (1999) stated that only Large Eddy

Simulations can predict turbulent kinetic levels which are in accordance with corresponding experimental data for a flow driven by a Rushton turbine. Results that were confirmed later by Hartmann et al. (2004).

Deksen (2003) asserted that *LES* leaves less room for speculation in modelling the turbulence (see *zonal modelling* as an example) and the motion of particles immersed in the flow than the *RANS* based turbulence models. Yianneskis's research group (Micheletti et al., 2004; Yeoh et al., 2004) compared *LES* with *RANS* based turbulence modelling concluding that *RANS* approach can yield reasonable results away from the regions close to the impeller and that the *LES* approach is better than *RANS* as far as prediction reliability of global turbulent energy dissipation rate ε is concerned. However, recently Coroneo et al. (2011) affirmed that much finer computational grids than those usually adopted for *RANS* simulations are required to reduce numerical uncertainties concerning turbulent quantities prediction to negligible values. Murthy and Joshi (2008) investigated by both *LDA* measurement and CFD a fully baffled tank comparing the capability of the three turbulence models (i.e. *k- ε* , *RSM*, *LES*) to predict the fluid velocities and turbulent kinetic energy for the case of several impeller designs. Summarizing, *RSM* simulates well all the mean flow characteristics, while the standard *k- ε* model fails to predict the mean flow associated with a strong swirl. Further, both of them underestimate the turbulent kinetic energy profiles in the proximity of the impeller. Conversely, *LES* approach is able to predict with a good accuracy all the fluid flow variables. Unfortunately, such a type of model is very computational demanding (Derksen, 2003), especially in two-phase systems with high concentrations of the dispersed phase (like in the case of the present PhD work) thus limiting its use to single phase or dilute two-phase cases (Derksen, 2003; Guha et al., 2008). Similarly, the direct solving of a two-phase flow field under turbulent conditions through *Direct Numerical Simulation (DNS)* (i.e. computing directly eddies of all sizes without any equation averaging, the temporal of *RANS* or the spatial of *LES*) goes beyond the present and foreseeable future computational possibilities (Hartmann et al., 2006).

In the present formulation the standard k - ε model was adopted accordingly and it was used to account only for the turbulence of the continuum phase in accordance with the formerly presented momentum equations (eq. 4.7 and 4.8): k and ε transport equations were solved only for the liquid phase and they were not taken into account for the particle phase.

$$\frac{\partial}{\partial t}(\rho_\alpha k) + \vec{\nabla} \left[\rho_\alpha \vec{U}_\alpha k - \left(\mu_\alpha + \frac{\mu_t}{\sigma_k} \right) \vec{\nabla} k \right] = S_k \quad (4.11)$$

$$\frac{\partial}{\partial t}(\rho_\alpha \varepsilon) + \vec{\nabla} \left[\rho_\alpha \vec{U}_\alpha \varepsilon - \left(\mu_\alpha + \frac{\mu_t}{\sigma_\varepsilon} \right) \vec{\nabla} \varepsilon \right] = S_\varepsilon \quad (4.12)$$

where

$$S_k = \mu_t \vec{\nabla} \vec{U}_\alpha \left(\vec{\nabla} \vec{U}_\alpha + \left(\vec{\nabla} \vec{U}_\alpha \right)^T \right) - \rho_\alpha \varepsilon \quad (4.13)$$

$$S_\varepsilon = C_1 \frac{\varepsilon}{k} \mu_t \vec{\nabla} \vec{U}_\alpha \left(\vec{\nabla} \vec{U}_\alpha + \left(\vec{\nabla} \vec{U}_\alpha \right)^T \right) - C_2 \rho_\alpha \frac{\varepsilon^2}{k} \quad (4.14)$$

$$\mu_t = \rho_\alpha C_\mu \frac{k^2}{\varepsilon} \quad (4.15)$$

Notwithstanding no turbulence exchange terms have been clearly considered, interactions between phases turbulence are accounted for in the drag force term which includes the influence of liquid free-stream turbulence on the particle drag coefficient C_D (see paragraph 4.4.1).

4.4.4 Drag Coefficient C_D

Particle drag coefficient C_D was considered variable in each cell in relation to the slip velocity between phases: C_D is calculated by the Clift et al. correlation (1978) where the cell slip velocity was used for the Reynolds number calculation:

$$C_D = \frac{24}{\frac{\rho_\alpha d_p |\vec{U}_\beta - \vec{U}_\alpha|}{\mu_\alpha}} \left(1 + 0.2 \left(\frac{\rho_\alpha d_p |\vec{U}_\beta - \vec{U}_\alpha|}{\mu_\alpha} \right)^{0.63} \right) =$$

$$= \frac{24}{Re_p} (1 + 0.2 Re_p^{0.63}) \quad (4.16)$$

This approach will be called as C_{D-slip} . Notably, when Re_p is higher than 1000 the drag coefficient is equal to 0.44.

It is known that the drag coefficient of small particles exhibiting a Stokesian behaviour is not affected by free stream turbulence (Clift *et al.*, 1978). On the contrary for particles falling in all other regimes, drag coefficients in turbulent fluids depend on both particle and flow field characteristics (Clift *et al.*, 1978). Notwithstanding these crucial findings, the effect of turbulence eddies on the motion of the dispersed phase is often ignored by assuming a standard drag coefficient as applied to quiescent flow thus may leading to large errors in the simulation of the dispersed phase concentration profile of an industrial flow under turbulent conditions (Doroodchi et al., 2008). The effect of turbulence is that of modifying the interactions between particles and fluid by modifying the flow field around the particle with respect to the case of absence of free stream turbulence. This effect leads to an increase of particle drag if the turbulence scale is small enough when compared to particle size. In fact, only micro-scale turbulence features appear to affect particle drag while the macro-scale turbulence is not involved in the drag increase phenomenon. Accordingly, the extent of such increase depends on particle and fluid physical properties as well as on turbulence intensity. (Brucato et al.

1998a). In order to take into account the bulk prevailing turbulence influence upon drag inter-phase, two different correlations were implemented: Brucato et al. (1998a) correlation and Pinelli et al. (2001) correlation:

$$C_{D,turb}^{Brucato} = C_D \left[1 + 8.67 \times 10^{-4} \left(\frac{d_p}{\lambda} \right)^3 \right] \quad (4.17)$$

$$C_{D,turb}^{Pinelli} = C_D \left[0.6 + 0.4 \tanh \left(16 \frac{\lambda}{d_p} - 1 \right) \right]^{-2} \quad (4.18)$$

where λ is Kolmogorov length scale, computable by the following relation:

$$\lambda = \left[\frac{\left(\frac{\rho_\alpha}{\mu_\alpha} \right)^3}{\varepsilon} \right]^{\frac{1}{4}} \quad (4.19)$$

where the turbulent dissipation ε is directly obtained by the turbulence model.

These approaches will be called as $C_{D-turb-Brucato}$ (or simply $C_{D,turb}$) and $C_{D-turb-Pinelli}$ respectively. The C_D coefficient of equations 4.17 and 4.18 is calculated by equation 4.16. The above expressions were implemented in the code through the use of a *User Fortran subroutine* available for this purpose in Ansys-CFX4.4 (*USRIPT*). A comparison of the two former correlations is depicted in the following figure.

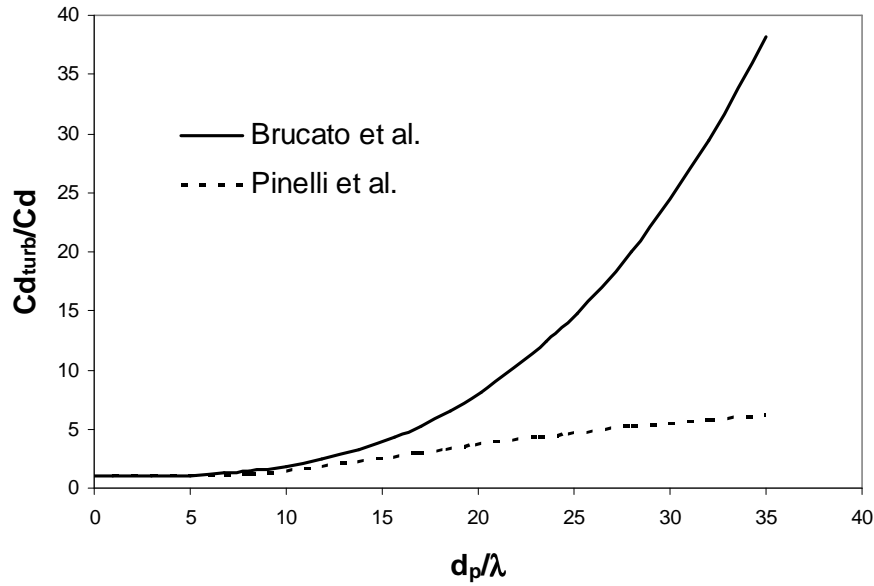


Fig. 4.3: Liquid free stream turbulence effect on particle-liquid drag coefficient: comparison between Brucato et al. (1998a) and Pinelli et al. (2001) correlation..

It shows that the two approaches provide the same effect for d_p/λ ratio being approximately lower than 10. When this ratio is higher than this value, the two curves diverge and the drag coefficient predicted by Brucato et al. correlation appears to be much higher, especially for high ratio d_p/λ . These two correlations are the most used in CFD scientific works dealing with solid-liquid suspension in stirred tanks even though they do not take into account the influence of particle density (Doroodchi et al., 2008). With this regard, recently Lane et al. (2005) proposed a different approach whereby the ratio of the “turbulent” terminal velocity to the “stagnant” terminal velocity (i.e. a ratio proportional to the square root of the ratio between the corresponding drag coefficients) was found dependent on the *Stokes Number*. This dimensionless number was considered as the ratio of the *particle relaxation time* (times a particle spends to respond to an interacting eddy) to the *turbulent integral time scale*. They supposed a decreasing-increasing trend with a minimum for the ratio of the turbulent terminal velocity to the stagnant one versus

the Stokes Number, but they validate such relation with experimental data only in the initial “decreasing” part (low Stokes Number). Doroodchi et al. (2008) dealt with the experimental confirmation of Lane et al. (2005) correlation at high Stokes Numbers (the “increasing” part). Results confirmed the decreasing-minimum-increasing trend hypothesized by Lane et al. (2005), but they refuted the global validity of Lane et al. (2005) correlation thus leaving room for future studies and improvements.

4.5 Other tested modelling procedures

4.5.1 Dense Particle Effect approach (DPE)

This approach presents only a difference with respect to the modelling procedure presented so far (that is the *reference modelling procedure*): here inter-phase drag force term equation includes an additional factor which accounts for particle-particle interactions in dense suspensions (i.e. high solid loading): this factor is Gidaspow’s correction for dense particle effect (Gidaspow, 1994):

$$\begin{aligned}\vec{M}_{\alpha\beta} &= C_{\alpha\beta} (\vec{U}_{\beta} - \vec{U}_{\alpha}) = \\ &= \left[\frac{3}{4} \frac{C_D}{d_p} r_{\beta} \rho_{\alpha} |\vec{U}_{\beta} - \vec{U}_{\alpha}| * (1 - r_{\beta})^{-1.65} \right] (\vec{U}_{\beta} - \vec{U}_{\alpha})\end{aligned}\quad (4.20)$$

As shown by the equation 4.20, increasing solid volume fraction leads to an enhancement of drag force as a consequence of higher particle-particle interactions. In fact, higher solid loading means higher number of particles and particle collisions thus resulting in a variation of interactions between the two phases.

4.5.2 Homogeneous k - ϵ approach (*Turb-Turb*)

This modelling procedure is practically almost identical to the reference modelling procedure: the difference regards the turbulence closure: here both phases are considered turbulent, that is even in the momentum equation of the solid phase, a

turbulent viscosity figures so that a coupling of turbulence between phases issue arises. Notably, about turbulence prediction in multi-phase systems in literature three different extensions of standard k - ε turbulence model (*homogeneous*, *per phase* or *dispersed*) are encountered. In *homogeneous* approach, only a couple of k and ε equations are solved, where the physical properties of the mixture are adopted, the two phases share the same k and ε (and the same eddy viscosity) value and the transport equations for k and ε have no inter-phase turbulence transfer terms. In *per phase* formulation, the turbulence model equations are solved for all the phases present. Additional terms referring to the modelling of inter-phase transport of k and ε have to be included in the equations relevant to each phase. Alternatively, in *dispersed* approach, turbulence is first simulated for continuous phase and then Tchen's theory of dispersion of discrete particles by homogeneous turbulence (Hinze, 1975) is used to estimate the turbulent quantities of the dispersed phase. Montante and Magelli (2005) have studied the influence of these three formulations on predicted results. They have observed that using more computationally demanding approaches like *per phase* formulation does not lead to any significant improvement over the mixture formulation. Furthermore, literature shows that for a number of cases dealing with dense suspension in stirred tanks (Montante et al., 2001; Micale et al., 2004; Montante and Magelli, 2005; Khopkar et al., 2006; Kasat et al., 2008; Tamburini et al., 2009), *homogeneous* k - ε turbulence model provides a fair representation of the solid distribution throughout the vessel. Therefore, in accordance with all these literature suggestions, a *homogeneous* k - ε turbulence model was employed within the *Turb-Turb* approach. Equations 4.11, 4.12, 4.13, 4.14, 4.15 remain practically the same, but all physical properties figuring in these previous equations have to be the “mixture” averaged properties. As examples:

$$\rho = r_\alpha \rho_\alpha + r_\beta \rho_\beta \quad (4.21)$$

$$\vec{U} = \frac{1}{\rho} (r_\alpha \rho_\alpha \vec{U}_\alpha + r_\beta \rho_\beta \vec{U}_\beta) \quad (4.22)$$

Finally, no dense particle effect is taken into account in this approach.

4.5.3 Modified $C_{\alpha\beta}$ approach (*Mod- $C_{\alpha\beta}$*)

This modelling procedure was described in Chapter 3 and consists in the adoption of the Eulerian-Eulerian MFM model. The main difference with respect to other approaches mentioned so far concerns the coupling between phases via inter-phase drag force: different local solid concentrations affect the drag force value, so inter-phase interactions and solid distribution throughout the tank consequently change. In order to account for this influence three different equations were used, each one for a specific solid volumetric fraction range:

- low volumetric fractions ($0 < r_\beta < r_{\beta_min}$):

the drag force is computed by the equation 4.20 i.e. the standard $C_{\alpha\beta}$ formulation along with Gidaspow's corrective term for dense particle effects;

- high volumetric fractions ($r_{\beta_max} < r_\beta < r_{\beta_packed}$):

the code uses Ergun's equation (Ergun, 1952), typically used to deal with closely packed fixed-bed systems.

$$\begin{aligned} \bar{M}_{\alpha\beta} &= C_{\alpha\beta} (\bar{U}_\beta - \bar{U}_\alpha) = \\ &= \left[150 \frac{r_\beta^2 \mu_\alpha}{(1 - r_\beta) d_p^2} + 1.75 \frac{r_\beta \rho_\alpha |\bar{U}_\beta - \bar{U}_\alpha|}{d_p} \right] (\bar{U}_\beta - \bar{U}_\alpha) \end{aligned} \quad (4.23)$$

- intermediate volume fractions ($r_{\beta_min} < r_\beta < r_{\beta_max}$):

for this range a linear interpolation of the two previous equations was used in order to avoid any discontinuity in $C_{\alpha\beta} - r_\beta$ relation: this unphysical behaviour would occur if only equation 4.20 and 4.23 were employed. In addition, adopting this

interpolation with r_{β_min} and r_{β_max} set to 0.35 and 0.45, along with a C_D computed via slip velocity, guarantees a monotonic dependence of $C_{\alpha\beta}$ vs r_β .

$$\vec{M}_{\alpha\beta} = \left[C_{\alpha\beta}(r_{\beta_min}) + \frac{C_{\alpha\beta}(r_{\beta_max}) - C_{\alpha\beta}(r_{\beta_min})}{r_{\beta_max} - r_{\beta_min}} (r_\beta - r_{\beta_min}) \right] (\vec{U}_\beta - \vec{U}_\alpha) \quad (4.24)$$

As far as turbulence modelling is concerned, *Mod- $C_{\alpha\beta}$* approach adopts the previously described “homogeneous” k- ϵ turbulence model. For full details about this approach refer to the Chapter 3.

Finally, it is important to underline that all the numerical approaches presented in this paragraph embody the influence of liquid free stream turbulence on drag coefficient referring to Brucato et al. correlation (1998a).

4.6 Numerical details

Coupling of pressure and velocity was obtained by the *SIMPLEC* algorithm. The hybrid-upwind discretization scheme was employed for the advective terms. Central differences were employed for all diffusion terms.

Impeller to baffle relative motion was modelled in two different ways: by adopting two different frames of reference (*MRF*) or by coupling the MFM with a sliding mesh (*SG*).

4.6.1 Discretization of the computational domain

In accordance to the axial symmetry of the system, only half of the tank was simulated, the other part was taken into account within the simulations by imposing periodic boundary conditions along the azimuthal direction. This domain was discretized by a coarse finite volume structured computational grid (Fig. 4.4) which encompasses 53760 cells (hexahedrons): 70 along the axial direction (*NI*), 32 along

the radius (NJ) and 24 along the azimuthal direction (NK). Fig.4.4 shows that cell spacing is suitably reduced in the proximities of the impeller where larger gradients of the variables are expected.

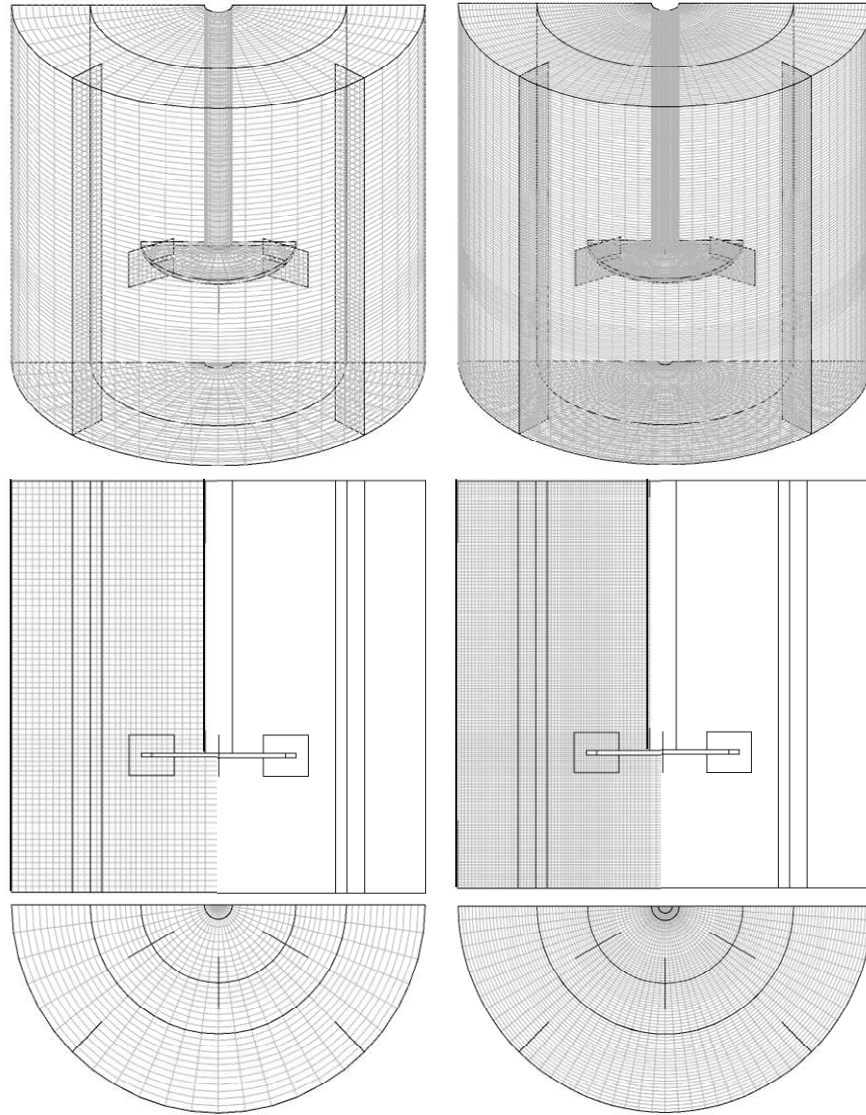


Fig. 4.4: Computational grids: the coarse one on the left, the finer on the right.

Notwithstanding this grid clearly presents a fairly coarse subdivision, the simulations obtained in this way did not be affected by noteworthy residual grid dependence, as will be discussed in the paragraph 4.7. This grid was adopted for the standard computations in consideration of its low demand of computational resources. However, an eight times finer grid was adopted in order to check the presence of any grid dependence. It encompasses 430080 cells distributed as $140 \times 64 \times 48$ along the axial, radial and azimuthal direction respectively. SG/MRF surface was set in accordance with the assumptions of Luo et al. (1994) at the radial position $R/\text{radius} = 0.62$ as purposely shown in Fig.4.4.

Furthermore, in order to validate the modelling approach with literature data, a third grid was created to discretize the stirred vessel employed by Micheletti *et al.* (2003) with $C=T/3$ and suitable simulations were carried out.

4.6.2 Initial conditions, time step and number of iterations

At the beginning of each simulation all particles were placed on the tank bottom with an initial volume fraction of $0.60 v_{\text{solid}}/v_{\text{total}}$ (*packed conditions*), corresponding to the experimentally assessed maximum packing ($r_{\beta\text{-packed}}$), also being a typical value for mono-dispersed spherical particles (Kee and Tan, 2002). Anyway, effect of such a critical initial condition on simulations results was addressed by carrying out some simulations with a different and numerically simpler initial condition, i.e. solid particles homogeneously distributed throughout the vessel (*initial homogeneous condition*) which constitutes the most common choice in literature (Ochieng and Lewis, 2006a). It is worth noting that both bottom lifting and avoidance of settling phenomena are essential for solid suspension mechanism (Mersmann et al., 1998) while assuming a particle homogeneous distribution as initial condition is likely to account only for the avoidance of settling phenomenon thus neglecting the bottom lifting one (Ochieng and Lewis, 2006a). Moreover, as far as initial condition on

velocity is concerned, both phases were considered completely still at the beginning of all simulations.

The time step employed for the transient sliding grid simulations was equal to the time which impeller needs to sweep of an angular azimuthal length equal to a single computational cell (*one cell time step*). For all the transient cases 100 revolutions were considered more than sufficient to reach steady state conditions since no appreciable variations in solid distribution were found before reaching the 100th revolution. Therefore, for the case of the coarse grid, 4800 time steps were required for concluding each simulation. The number of iteration per time step was set to 30 with the aim of allowing residuals to settle before passing to the next time step as well as to enhance the number of times (per time step) in which the *ESVC* algorithm acts. In addition, some simulations were performed with different time steps in order to evaluate time step influence on numerical predictions: a time step equal to the time impeller needs to sweep of an azimuthal length equal to half a cell (*half cell time step*) and a time step equal to the time impeller needs to rotate of an angle of 180 degrees (*180° time step*) were adopted thus requiring 9600 time steps and 200 time steps respectively to encompass 100 impeller revolutions.

As far as steady state Multiple Reference Frame simulations are concerned, 8000 iterations were found to be sufficient for allowing variable residuals to settle to very low and negligible values for all the investigated cases. Also, 8000 iterations are sufficient to guarantee that *ESVC* algorithm avoids the overcoming of the maximum physically allowed packing value for solid phase.

Notably, simulations of cases where impeller speed is high require a higher number of total time steps for the case of SG simulations and a higher number of total iterations for the MRF simulations with respect to the simulations where the impeller speed is lower: the former cited values (4800 time step, 8000 iterations) were chosen in order to be appropriate for all the cases here presented.

Baffles and impeller blades were considered as thin surfaces. No slip boundary conditions were assumed for all the tank boundaries with the exception of the top surface where free slip conditions were employed. Notably, the presence of very small magnitudes of the liquid velocities near the top surface leads to negligible

difference in the results predicted with no slip or free slip (Kasat et al., 2008) or symmetry boundary conditions at the top.

4.6.3 Excess Solid Volume Correction Algorithm (ESVC)

As previously described, one of the problem concerning the adoption the Eulerian-Eulerian *MFM* in its own standard formulation regards the possibility of obtaining r_β value greater than the maximum physically allowed packing value r_{β_packed} . In order to avoid r_{β_packed} to be exceeded during the simulations, the *Excess Solid Volume Correction (ESVC)* algorithm, already used and described in Chapter 3, was adopted.

As shown in the Chapter 3, this correction operates as a posteriori redistribution of the solid volume in excess for each cell where the volume fraction exceeds r_{β_packed} : at the end of each iteration, after the code has finished its calculation and has distributed the solid volumetric fractions throughout the computational domain, the *ESVC* operates in each cell by zeroing its excess of solids and redistributing it along the surrounding cells.

As a difference from the algorithm described in the Chapter 3 in the present chapter, *ESVC* algorithm has been further optimized:

a) it is applied at the end of each iteration of the SIMPLEC algorithm inside an iterative procedure. More precisely, it works iteratively or until the total mass which exceeds r_{β_packed} is reduced to one hundredth of its initial value or two hundreds times. This limit value of two hundreds operation was chosen aiming to avoid too much high computational times for each simulation and significant variation of the system dynamics;

b) it is able to perform the redistribution of solid volumetric fractions exceeding r_{β_packed} even across the SG/MRF surface.

An in-depth description of the algorithm improvement declared in point (b), is provided in the following. In CFX 4.4 it is not possible to manage equations dealing

with cells belonging to different domains. As previously described the tank volume is divided in two different domains named *Box In* and *Box Out* separated by the SG/MRF surface. Practically, it is not possible to write equation 3.20 for *Box In* cells neighbouring this surface because equation requires an excess amount relevant to the corresponding *Box Out* cells and vice versa. This drawback was overcome by defining two vectors called *Excess Store* (Fig.4.5): The amount of r_{β}^{ex} which would have to be transferred from a generic *Box In* cell is preventively stored in this vector (the red part of *Excess Store* in Fig.4.5) and successively considered within the equation 3.20 for the corresponding *Box Out* cell (red arrows in Fig.4.5). Similarly a r_{β}^{ex} value, which has to be transferred towards the inner domain, is stored in the *Excess Store* vector (the yellow part of *Excess Store* in Fig.4.5) and then inserted into equation 3.20 for the neighbouring *Box In* cell.

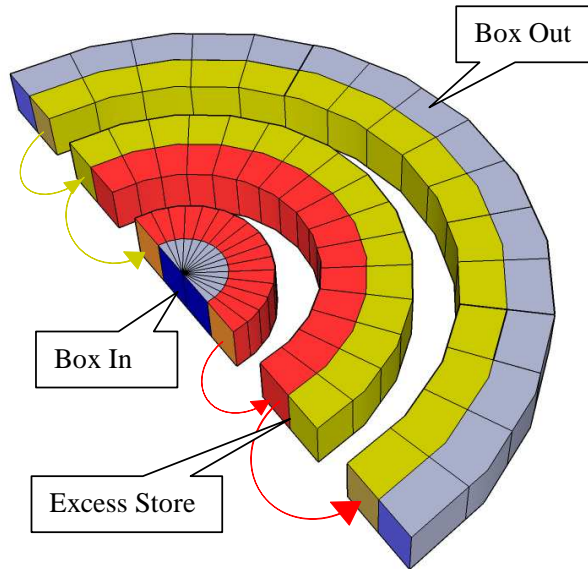


Fig. 4.5: Excess exchange across SG/MRF surface.

This procedure requires other refinements if a SG approach is employed: in fact in sliding grid simulations the Box In rotates in accordance with the impeller speed instead of the Box Out which remains still. This relative rotation implies that a generic cell of Box Out has a neighbouring Box In cell which changes with time and vice versa. An example is plotted in Fig.4.6 where two different generic instants are considered. In order to simplify explanation, it can be assumed a time step equal to the time impeller needs to sweep a single azimuthal computational cell. When system is in the position showed by Fig.4.6a, Box In cell 1 has to exchange solid excess with Box Out cell 2, likewise Box In cell $NK-1$ is coupled with Box Out cell NK , Box In cell NK has to exchange excess with Box Out cell 1 and so on. This behaviour is clearly periodic with a period of 180 degrees as Fig.4.6b shows. *ESVC* algorithm was refined with the implementation of an ad-hoc index-linking for Box In and Box Out as well as for the inner and the outer part of Excess Store.

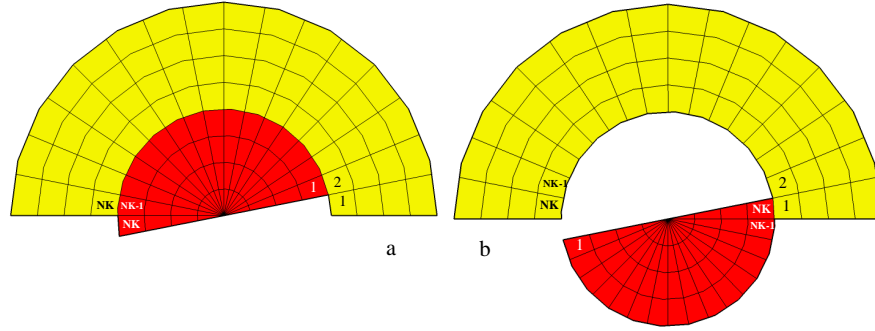


Fig. 4.6: Relative rotation of inner and outer domain in SG simulations.

The algorithm does not remove the over-packing issue, but rather rearranges the volume fraction distribution and ensures the excess of solids to be carried towards cells where no excess is present. Naturally, it is worth noting that, operating at the end of each iteration, its action has to be kept as small as possible, thus preventing the correction from altering significantly the dynamics of the system. In fact *ESVC*

algorithm does not operate more than two hundred times, thus keeping the total amount of transferred mass very low (always below 2% even in the worst cases).

Fig.4.7 shows an example of *ESVC* algorithm operation for the case of 231 μm at the highest (i.e. most critical) solid concentration of 33.8% $w_{\text{solid}}/w_{\text{liquid}}$: two generic SIMPLEC iterations relevant to initial impeller rotations (when most solid are resting on the bottom and the over-packing issue is most critical) in SG calculations are considered.

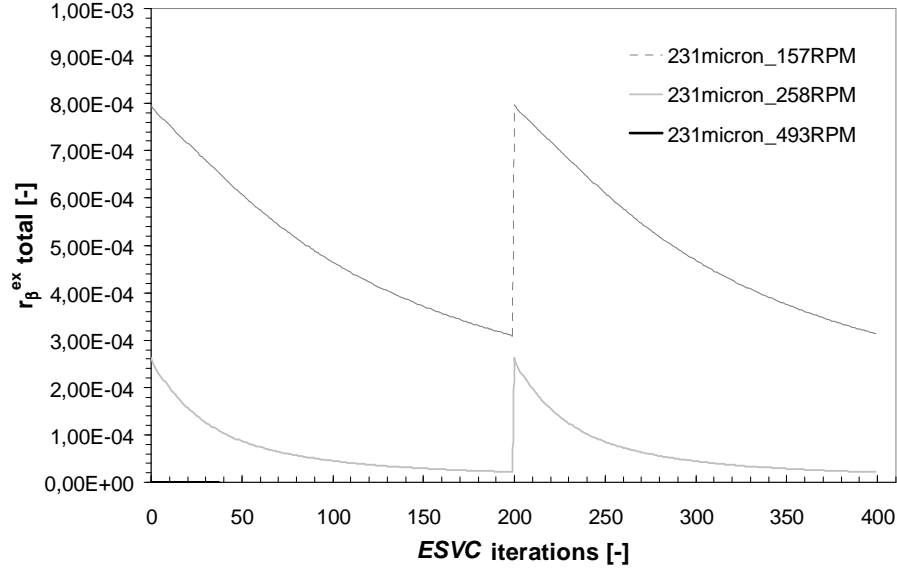


Fig. 4.7: *ESVC* operation during two generic SIMPLEC iterations.

$r_{\beta}^{ex total}$ is the sum of r_{β}^{ex} for all the domain computational cell.

As a matter of fact, when impeller velocity is low (157RPM in the figure), solids prefer to stay still over the bottom, thus resulting in a higher $r_{\beta}^{ex total}$ and a more massive operation of *ESVC* algorithm. Both for 157RPM and 258RPM cases, 200 hundreds *ESVC* iteration for each SIMPLEC iteration are reached, on the contrary, at 493RPM the amount of still particles is very low thus leading to a

reduction of r_{β}^{ex} total of one hundredth before reaching the maximum number of two hundreds iterations.

Finally, effect of employing *ESVC* algorithm within simulations is considered and discussed. Fig.4.8 shows a comparison of r_{β} distribution results obtained by employing *ESVC* algorithm (Fig.4.8b) and without employing it (Fig.4.8a) for the case of highest solid loading (and particle diameter equal to 231 μ m) at the very low impeller speed of 90 RPM. r_{β} values refer to a vertical diametrical plane placed midway two subsequent baffles. When *ESVC* algorithm is not adopted solids tend to over-pack themselves on the bottom thus showing volumetric fraction values which overcome the maximum r_{β_packed} value and even reach the value of one (Fig.4.8a). Conversely, if a *ESVC* algorithm is employed the over-packing issue is handled and the r_{β} distribution figured in Fig.4.8b does not show values significantly higher than the maximum physically allowed one r_{β_packed} .

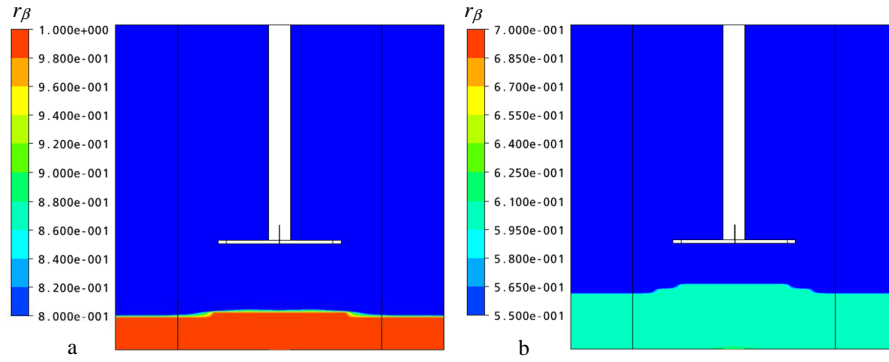


Fig. 4.8: 231 μ m, 33.8% w_{solid}/w_{liquid} , 90RPM: solid volumetric fractions on a vertical diametrical plane: a) without employing *ESVC* algorithm, b) employing *ESVC* algorithm.

The improvements of *ESVC* algorithm presented in this chapter were necessary for the simulation of partial suspension conditions. As a difference from the case

presented in the Chapter 3, here particles rest on the bottom in all the cases where $N < N_{js}$. If *ESVC* algorithm improvements were not be implemented, unphysical results would be obtained (i.e. volumetric fractions exceeding r_{β_packed} as well as possible discontinuity of solid volume fraction level in the correspondence of the *MRF/SG* surface).

Finally, it is worth noting that the *ESVC* routine, inhibiting particle concentration from getting significantly larger than maximum particle packing, represents a way to model particle-particle interactions (Tamburini et al., 2009).

4.7 Unsuspended Solid Criterion (USC)

As a matter of fact, it is necessary to establish a criterion aiming at correctly distinguishing the suspended particles from the unsuspended ones. Velocity is the first variable one may think to use as a benchmark: if a particle exhibits a value of velocity equal to 0.0, it should be considered as unsuspended.

Unfortunately, all simulations, even at very low impeller speeds, provide solid velocities very small but different from zero thus leading to the unique possibility of choosing a velocity value as small as arbitrary as a cut off value: if particle velocity was lower than this limit value, particle would be considered unsuspended. In relation to these considerations, adopting another variable to establish a not arbitrary criterion could constitute a better choice.

In accordance with *PGT* fundamentals, solids can be considered suspended if they contribute to increase the mean density of the suspension by lifting and moving away from the tank bottom. When solids lie still on the bottom they show their maximum volumetric fraction r_{β_packed} (Kee and Tan, 2002). Clearly, it is highly improbable for particles to be suspended while preserving this local value of r_{β} , in fact it is quite likely that particles are distributed during the suspension process, thus showing a r_{β} lower than r_{β_packed} . Therefore the simulation procedure compute as unsuspended all the solids which show a solid volumetric fraction $r_{\beta} = r_{\beta_packed}$ inside a computational cell. This criterion will be indicated in the following as *Unsuspended Solid Criterion (USC)*.

Clearly, this criterion could be improved by adding other conditions, but it represents a good simple starting point. Notably, this criterion could underestimate the amount of unsuspended particles because it is possible that some particles can stay on the bottom isolated from each other, but being likely a few, this percentage is quite low and can be reasonably neglected. As a matter of fact, in relation to the modus operandi of this criterion, a finer grid would guarantee a more precise estimation of the unsuspended solids.

In addition, a suitable binary scalar named *sedim* was purposely prepared in order to allow visualizations of the sediment during post-processing: if particles inside a cell are considered as unsuspended by *USC* criterion, the scalar *sedim* assumes a value equal to 1.0, otherwise it is equal to 0.0.

4.8 Results and analysis

As far as experimental results are concerned, each data set (Fig.4.9) shows the typical behaviour presented in the works of Brucato et al. (1997) and Micale et al. (2002): plotting the fraction of the suspended solids versus agitation speed a S-shaped curve was obtained for all of the investigated cases.

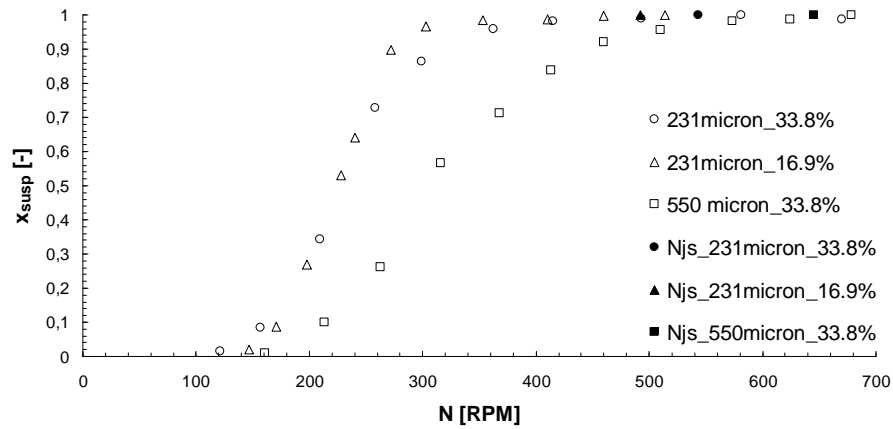


Fig. 4.9: Experimental suspension curves for the following cases: \circ 212-250 μm glass ballottini particles with a solid loading of 33.8%^{w/w}; Δ 212-250 μm glass ballottini particles with a solid loading of 16.9%^{w/w}; \square 550-600 μm glass ballottini particles with a solid loading of 33.8%^{w/w}. Corresponding solid symbols indicate the relevant N_{js} values assessed by Zwietering's correlation (1958).

The collected data show that higher particle diameter and concentration lead to higher unsuspended solid fractions at a given agitation speed as expected. Also, suspended solid fractions being equal about to 1 (corresponding to the achievement of complete suspension conditions) show the same behaviour (particle suspension is favoured by smallest particles and lower solid loadings) emphasizing the soundness of the experimental procedure. Actually, complete suspension conditions are achieved at impeller speeds being lower than the corresponding ones predicted by Zwietering's correlation (solid symbols in Fig.4.9). Zwietering's correlation is conservative, but more mechanical power demanding: with respect to an industrial point of view, it is not important that no particles are still on the bottom for more than a second, but it is crucial that the amount of unsuspended solids is negligible if compared to the total solid-loading.

Anyway, further details and discussion on experimental suspension curves can be found in Brucato et al. (1997) and Micale et al. (2002) and are not reported here.

4.8.1 PGT curves

Fig. 4.10 shows the prediction of the suspension curve by SG transient simulations: Despite the simplicity of the suspension criterion, simulation results appear to be in fair agreement with experimental data: simulation data present the same "S" curve trend and are close to the corresponding experimental data even if there is a slight overestimation, especially for the intermediate impeller rotational speeds. In the same figure two different approaches are compared: C_{D-slip} and C_{D-turb} .

Brucato

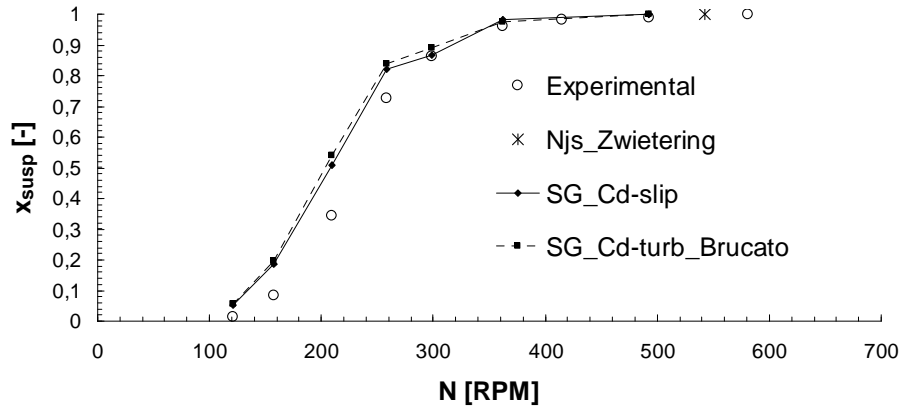


Fig. 4.10: Simulated vs experimental suspension curve for the case of 212-250 μm glass ballottini particles with a solid loading of 33.8%^{w/w}.

No significant variations are appreciable as expected: in fact, particle diameter is small and impeller speeds are not so high, thus leading to low enhancements of C_D (for the case of 493RPM the ratio $C_{D\text{-turb-Brucato}}$ to C_D was equal to 1.48, see Table 4.1 for further details). Results identical to those provided by $C_{D\text{-turb-Brucato}}$ approach are given by $C_{D\text{-turb-Pinelli}}$ approach because, as previously described, both approaches provided practically identical C_D enhancements for d_p/λ lower than 10.

Investigated vessel						Micheletti et al. data (2003)							
231 μm			550 μm			655 μm							
N [RPM]	dp/λ	C _{D,turb} /C _D	Brucato et al. correlation		Pinelli et al. correlation		N [RPM]	dp/λ	C _{D,turb} /C _D	Brucato et al. correlation		Pinelli et al. correlation	
			N [RPM]	dp/λ	C _{D,turb} /C _D	dp/λ				C _{D,turb} /C _D	N [RPM]	dp/λ	C _{D,turb} /C _D
121	2,78	1,02	122	6,89	1,28	6,92	1,12	400	14,54	3,66	14,77	2,49	
157	3,33	1,03	161	8,24	1,49	8,27	1,25	500	17,58	5,71	17,45	3,11	
209	4,18	1,06	213	9,91	1,84	9,92	1,49	600	20,55	8,53	19,88	3,66	
258	5,03	1,11	263	11,79	2,42	11,76	1,83	700	23,10	11,69	22,83	4,27	
299	5,64	1,16	316	13,83	3,29	13,74	2,26	800	25,45	15,30	26,50	4,95	
362	6,44	1,23	368	15,71	4,36	15,60	2,69	900	27,87	19,77	27,51	5,12	
493	8,21	1,48	413	17,08	5,32	16,98	3,01	1000	29,68	23,68	29,98	5,51	
			460	18,62	6,60	18,42	3,33	1100	32,57	30,95	31,82	5,78	
			510	20,21	8,15	19,94	3,67						
			624	23,64	12,46	23,21	4,35						
			678	25,20	14,87	24,71	4,63						

Tab. 4.1: Influence of liquid free stream turbulence on drag coefficient

4.8.2 Concentration maps

The good quality of predictions is also visible in Fig.4.11 where contour plots of r_β for the same case were depicted: at low agitation speed (157RPM) most particles lie on the bottom; at 258RPM, many of them suspend but without reaching the highest part of the tank; finally, at 493RPM suspension is very near to be complete and particles distribute following the liquid main flow and describing the typical double loop configuration.

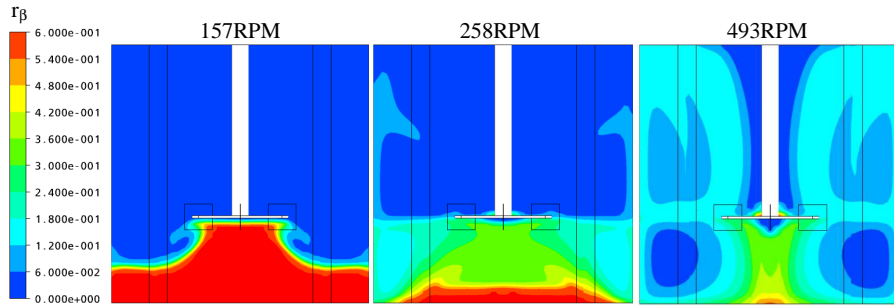


Fig. 4.11: Contour plots of solid volumetric fractions on a vertical diametrical plane at three different impeller speeds for the case of 231 μm ballottini particles at 33.8%^{w/w}.

Fig.4.12 refers to the same cases described in Fig.4.11, it shows a three dimensional representation of the scalar *sedim*, plot upon the solid volumetric fraction contours of the former figure. The iso-volume figured in Fig.4.13 represents the domain zones where the scalar *sedim* is equal to one: such a volume practically corresponds to the 3-D visualization of the sediment estimated by simulations.

As Fig.4.12 shows, the amount of sediment is reduced by increasing impeller rotational speed. When impeller is motionless, solids lie on the bottom as sediment without showing any particular shape. At 157RPM the flow discharged by the impeller starts to profile the sediment (as showed also by vector plots, Fig.4.13)

which assumes a volcano-like shape. The build-up of a solid heap at the centre of the vessel floor is a characteristic phenomenon of the fluid-flow pattern imposed by radial flow impellers like the Rushton turbine (Kee and Tan, 2002; Kasat et al., 2008). At 258RPM the sediment predicted by simulations shows a particular form which is experimentally visible by observing the vessel bottom (see Paragraph 4.8.11): impeller rotates counter clockwise, so near the lateral wall the sediment is present only in the part placed in front of the baffles (which cover it from the liquid flow). Finally, at 493RPM only a negligible amount of sediment is still present.

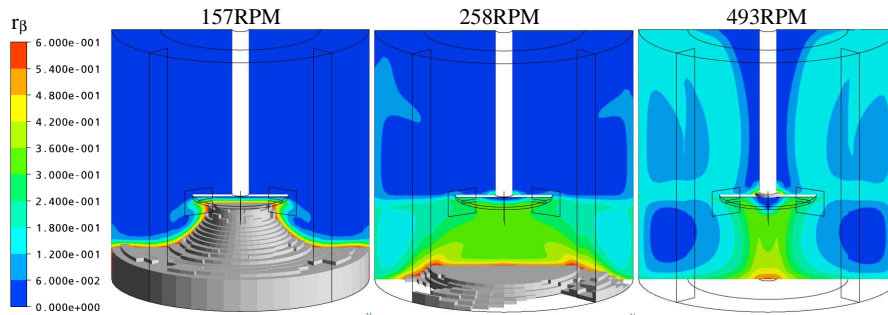


Fig. 4.12: 3-D scalar *sedim* plot upon contour plots of solid volumetric fractions on a vertical diametrical plane at three different impeller speeds for the case of 231 μm ballottini particles at 33.8% w/w .

4.8.3 Velocity vector plots

In Fig.4.13 velocity vector plots are depicted: in this figure a vector whose length is $T/4$ has got a magnitude equal to v_{tip} . The external contour of the scalar *sedim* is also included in the same figure. When impeller speed is low, particles constitute a fictitious bottom thus resulting in a very low impeller clearance (i.e. *false bottom effect*) (Kasat et al. (2008); Brucato et al., 2010) which leads to the formation of a single recirculation loop. In fact, Galletti et al. (2003) focused on the flow pattern transition with impeller clearance variations in a stirred vessel and

observed the transition of two-loop structure to single-loop structure for a radial flow impeller with a decrease in the impeller off-bottom clearance. This phenomenon was observed by other authors as well (Micale et al., 2004; Tamburini et al., 2009). Actually, vectors do not show a perpendicular direction to the impeller blades, but they move downwards obliquely, following the profile described by the sediment as can be seen in the first two plots (i.e. 121RPM and 157RPM cases). The phenomenon of single-loop fluid flow pattern as well as the oblique velocity vectors in the presence of a motionless sediment is also observable in the work of Kasat et al. (2008). Moreover, by observing carefully the first two figures it seems that another recirculation loop is however present (inside the sediment), even if very low velocities are visible. Therefore, one would state that the flow split do not occur on the impeller plane, but on a lower plane prescribed by the sediment height. This phenomenon as well as the false bottom effect vanishes at higher impeller angular velocity, when the sediment height is further reduced: at 209RPM velocity vector plots show a double loop configuration, but the lower loop appears to be smaller because of the sediment presence which gives rise to a reduced impeller clearance. At 258 RPM, flow velocity vectors manage to reach the vessel bottom, but the presence of motionless particles in the central part of the bottom causes an early closure of the recirculation thus producing again a ring loop with reduced size. Eventually, at 493RPM, where a not appreciable amount of still particles is present, the velocity vector plot shows the double loop flow pattern configuration, typical for the radial flow impellers.

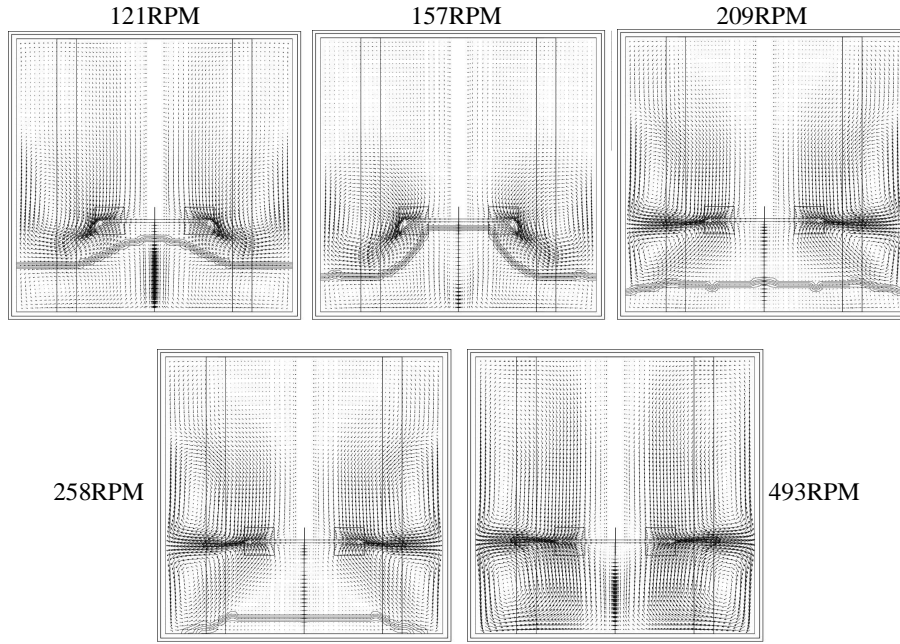


Fig. 4.13: Velocity vector plots with the indication of scalar *sedim* on a vertical diametrical plane at different impeller speeds for the case of 231 μm ballottini particles at 33.8% w/w .

4.8.4 Time step dependence

Influence of time step length on results was addressed. The simulations presented in Fig.4.10 were carried out again by halving time step duration: it corresponds to the time impeller needs to rotate of an angle equal to half a computational cell (*half cell time step*). Suspension curve result do not show any difference and are not presented.

Anyway, the quantity of unsuspended particles is an overall data, in order to properly check the time step influence, it would be better to compare local data as well. Indeed, Fig.4.14 shows two generic radially averaged axial profiles of normalized solid concentration. By observing the profiles it is clear that neither solid

concentration profiles show any appreciable variation thus confirming that the adoption of the *one cell time step* is sufficient for the transient simulations.

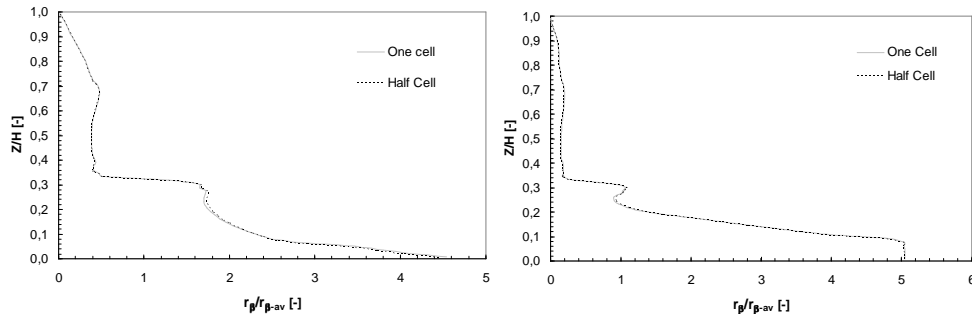


Fig. 4.14: Radially averaged axial profiles of solid concentration: comparison of different time step lengths for two different cases. On the left: 231 μm , 33.8%^{w/w} at 258RPM; on the right: 550 μm , 33.8%^{w/w} at 263RPM.

4.8.5 Sliding Grid versus Multiple Reference Frames

SG transient simulation results were compared with the MRF steady state approach. The comparison is depicted in Fig.4.15. Results are practically identical with the only exception of the 157RPM case. Suspension starts in a massive way at an impeller rotational speed close enough to 157RPM, so it represents a very delicate phenomenon for CFD simulations. By the way, results confirm the soundness of adopting a MRF approach for further analysis, thus guaranteeing a large computational time saving.

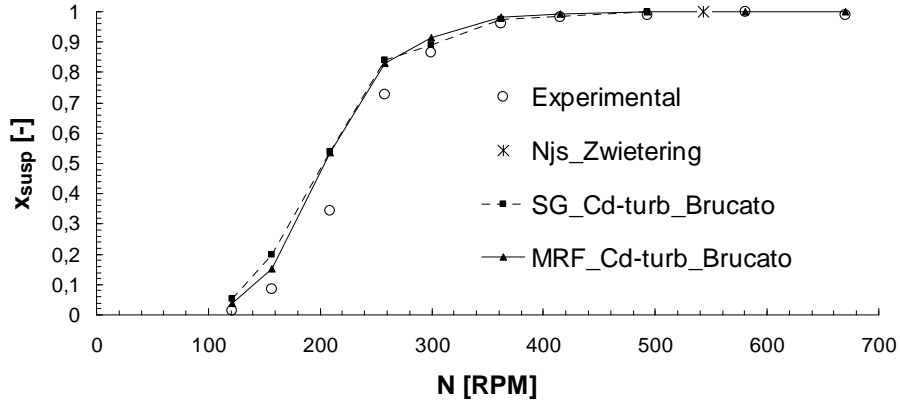
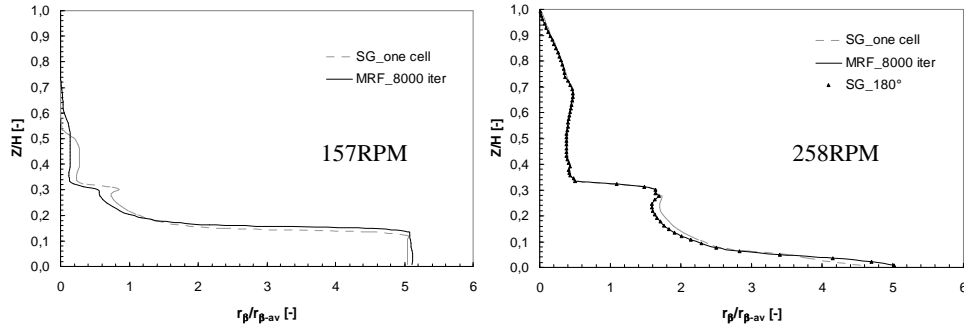


Fig. 4.15: Comparison of SG and MRF simulations with suspension curve for the case of 212-250 μm glass ballottini particles with a solid loading of 33.8%^{w/w}.

Also in this case, the comparison has embodied the observation of radially averaged axial profiles of normalized solid volumetric fractions (Fig.4.16): SG and MRF profiles are very similar for all the cases here investigated, a quite little difference is observable only at the highest impeller speeds, actually it regards merely the upper part of the vessel thus guaranteeing the goodness of predicting suspension curves by MRF simulations.



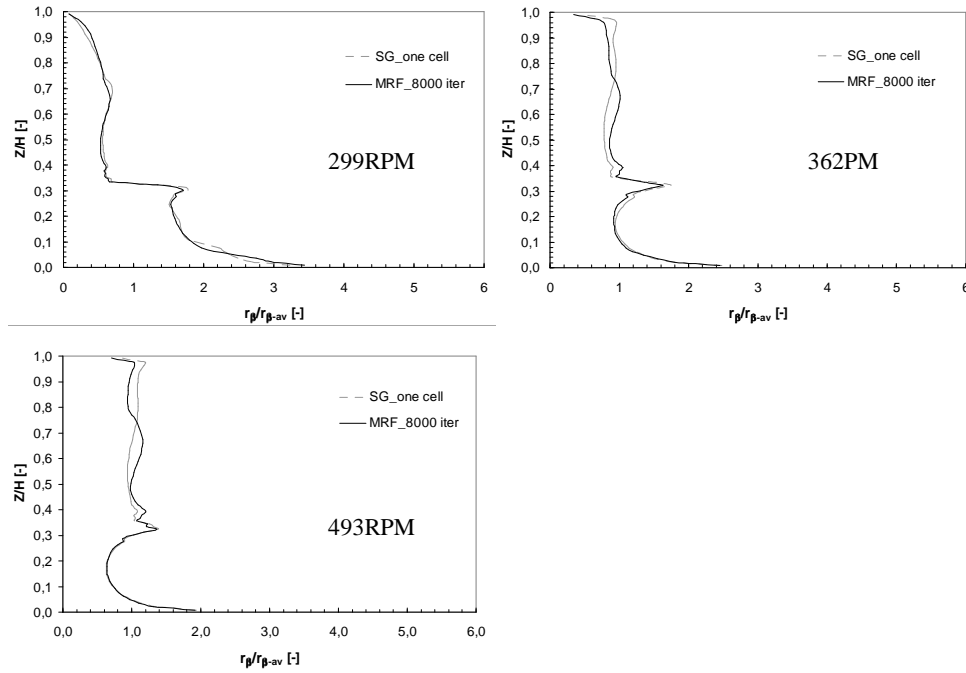


Fig. 4.16: Comparison of SG and MRF simulations with radially averaged axial profile of normalized solid volumetric fraction for the case of 212-250 μm glass ballotini particles with a solid loading of 33.8% w/w .

4.8.6 Initial conditions

All the simulations were carried out imposing particles packed at r_{β_packed} on the bottom as initial condition. It can likely be considered as the more realistic condition for the start-up of a solid-liquid stirred tank: initiating a simulation with the particles settled at the bottom is more representative of the actual physical situations. Also, it is comparable with the Lagrangian approach (Derksen, 2003) where particles are released from the bottom of the tank. On the other hand, such condition hides a lot of complexities by a computational point of view, mainly concerning numerical convergence problems. Therefore, it was considered worth checking if results were affected by some influence of such a critical initial condition. Some simulations

were carried out again, but imposing a *homogeneous initial condition* for solid volumetric fractions: the comparison plotted in Fig.4.17 shows that the results obtained by considering the two different conditions are perfectly identical.

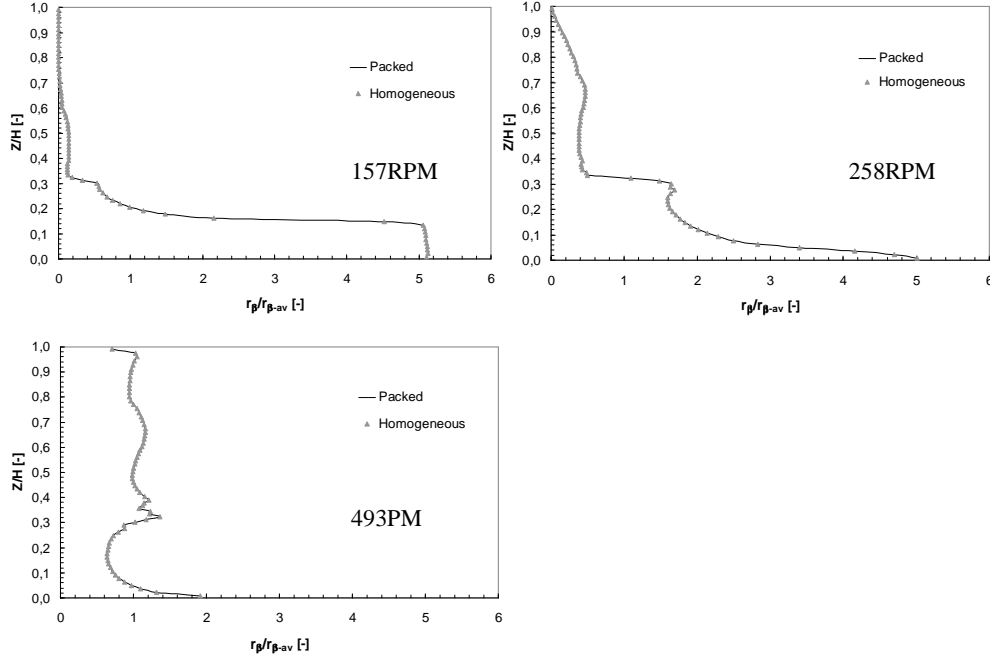


Fig. 4.17: Radially averaged axial profile of normalized solid volumetric fraction for the case of 212-250 μm glass ballottini particles with a solid loading of 33.8%^{w/w}: comparison of different initial conditions.

4.8.7 Grid dependence analysis

Verifying the total absence of any grid-dependence was another important issue, in fact all the results so far presented are obtained by employing the coarse grid.

A check of computational result grid dependence was performed for the case of 212-250 μm glass ballottini particles with mean solid concentration of 33.8%^{w/w}. Results concerning suspension curve prediction by adopting the coarse (53760) and

fine (430080) computational grids are presented in Fig.4.18. An accurate analysis of the results between these two grids highlights some discrepancies, however, the extent of numerical differences were judged acceptable for the purpose of the present PhD work. In particular the suspended solid fraction data predicted by employing the fine grid appear to be a bit lower than the corresponding coarse grid data for the case of intermediate impeller speeds.

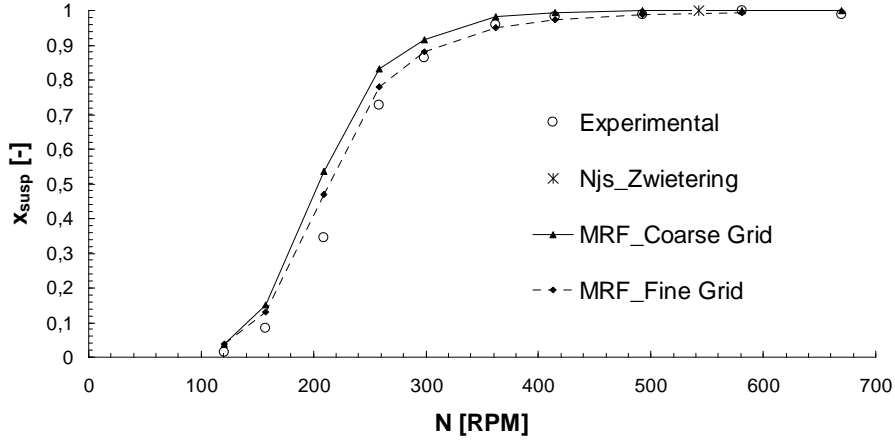


Fig. 4.18: Comparison of MRF simulations (with $C_{D-turb-Brucato}$) with experimental data with two different computational grids for the case of 212-250 μm glass ballottini particles with a solid loading of 33.8% w/w .

A further confirmation of the previous statement on the reliability of the results generated by the coarse grid is shown in Fig.4.19 where comparisons of normalized axial profiles for the two grids at different impeller speeds are reported: profiles are very similar for all the impeller speeds thus strengthening the idea that a higher discretization degree and a consequently more accurate resolution does not provide different results. Moreover, it is worth noting that the small difference observable at the lower part of the vessel for the case of 157RPM it is allegedly linked to the *ESVC* algorithm operation: in order to keep *ESVC* algorithm global effect identical

in the case of different grids (that is, when the total number of computational cells changes), the number of times when it operates would be changed accordingly. In fact, a higher computational cell number means a reduced cell size thus implying a lower exchange of r_{β}^{ex} for each cell, or, in other words, a smaller shift of excess towards zones where no excess is present. So, the two hundreds operation times should be increased when a finer grid is employed.

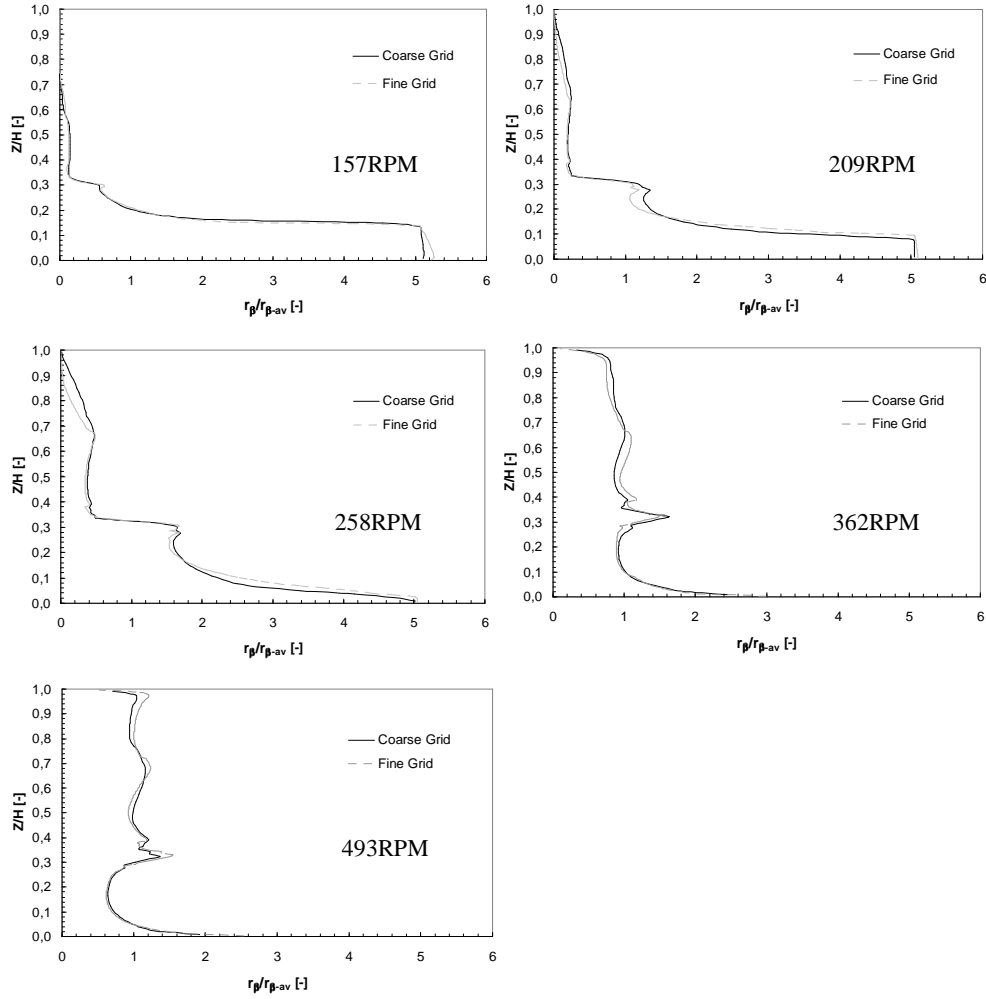


Fig. 4.19: Radially averaged axial profile of normalized solid volumetric fraction for the case of 212-250 μm glass ballottini particles with a solid loading of 33.8%^{w/w}: comparison between the coarse and fine grid.

4.8.8 Solid loading

As far as influence of particle concentration on the presented model reliability is concerned, the simulation results, depicted in Fig.4.20, follow quite well the experimental data. Predicted fractions of suspended solids are close enough to the experimental ones even if a fairly overestimation was found especially for the lower impeller speeds: also this time, it is allegedly due to the delicacy of the suspension starting. If one starts to operate the system, at very low impeller speed only a very low amount of solid particles is suspended; conversely, increasing agitation speed, but keeping it still low, suddenly, suspension phenomenon occurs in a massive way and a lot of solids get suspended. This initial condition is very critical by a computational point of view, thus leading to a great difficulty in simulating it properly. However, as a matter of fact, the numerical approach presented here was found able to reliably predict suspension curves even at a lower mean solid concentration.

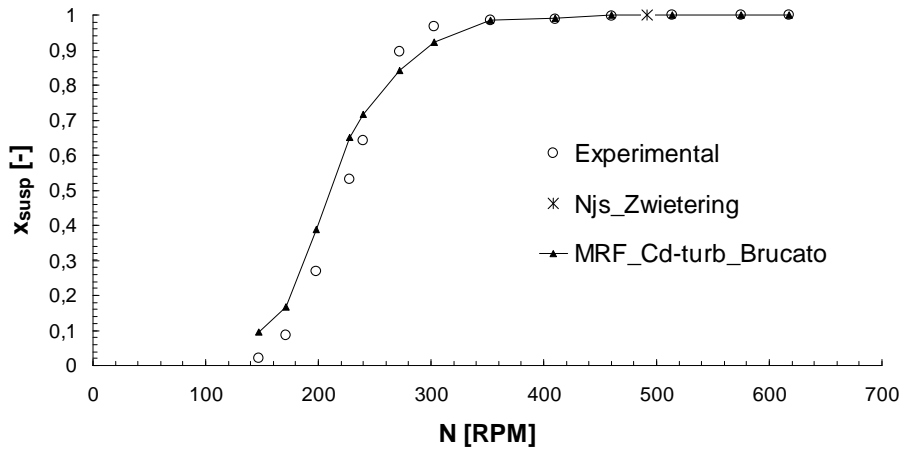


Fig. 4.20: MRF simulations versus experimental data for the case of 212-250 μm glass ballottini particles with a solid loading of 16.9%^{w/w}.

4.8.9 Particle diameter and drag coefficient

Numerical model capability of predicting solid particles diameter influence on solid suspension curves was also investigated. Three different approaches: C_{D-slip} , $C_{D-turb-Brucato}$ and $C_{D-turb-Pinelli}$ were depicted and compared in Fig.4.21 for this purpose. As a matter of fact, higher particle diameter suspension requires higher impeller speeds to achieve complete suspension conditions thus intrinsically resulting in higher ratio d_p/λ (higher d_p and lower λ) and leading to a greater influence of the liquid free-stream turbulence on the drag coefficient. Neglecting such influence provides inconsistent results as C_{D-slip} approach data show: even at very high impeller speeds, it is impossible to achieve a complete suspension regime as the fraction of suspended solid particles does not reach or asymptotically approach the desired value equal to 1.0. As far as $C_{D-turb-Brucato}$ and $C_{D-turb-Pinelli}$ are concerned, they clearly provide different enhancements of C_D , differences which further grow for high impeller speeds (i.e smaller λ , and higher ratio d_p/λ). For the case of the lowest impeller speed investigated case (122RPM) the ratio C_{D-turb} to C_D are very similar (see Table 4.1) : 1.28 and 1.12 according with Brucato et al. (1998a) and Pinelli et al. (2001) correlation respectively. Conversely, significant discrepancies between the two approaches are found for the case of the highest impeller speed (678RPM): the ratio $C_{D-turb-Brucato}$ to C_D is 14.87 while the ratio $C_{D-turb-Pinelli}$ to C_D results equal to 4.63 (see Table 4.1).

Observing Fig.4.21 data, it can be stated that both turbulent approaches fairly overestimate the fraction of suspended solids especially in correspondence of the suspension beginning but the $C_{D-turb-Pinelli}$ approach seems to follow better the experimental data at high rotational speeds. Brucato et al. correlation (1998) was obtained by fitting, experimental data whose highest particle diameter was 425-500

μm , lower than the 500-600 μm one. The equation chosen for this fitting has a form which does not extrapolate sensibly for high ratios of d_p/λ (Lane et al., 2005).

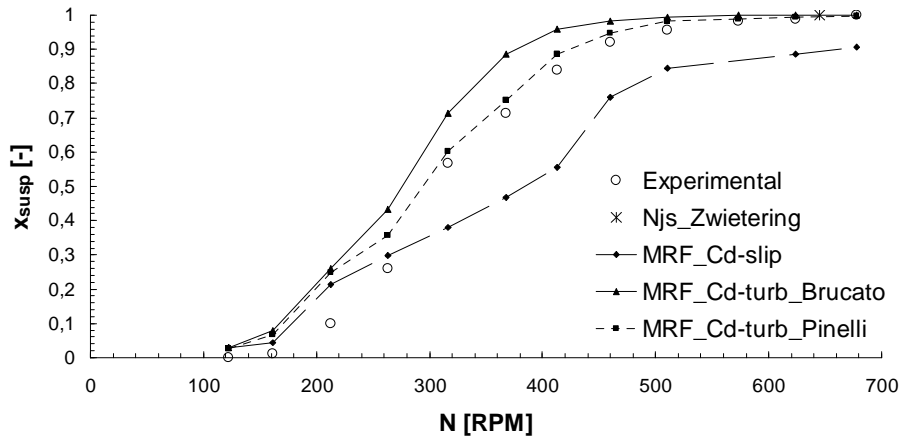


Fig. 4.21: Comparison of different MRF simulation approaches with experimental data for the case of 500-600 μm glass ballottini particles with a solid loading of 33.8%^{w/w}.

4.8.10 Alternative modelling approaches

As mentioned in Paragraph 4.5, other modelling approaches were adopted to predict suspension curves: results are presented in Fig.4.22.

No one of the tested approaches provides satisfactory results: all of them significantly overestimated the experimental data, especially at very low impeller speeds. In this regard, also some predictions of Hosseini et al. (2010b) concerning cloud height and homogenization degree show a similar overestimation at the lower impeller speeds even if the tank and impeller design they employed were different from those of the present thesis.

The *Dense Particle Effect* approach provides better results because it is able to predict the “S” shaped trend of the suspension curve. Unfortunately the drag force enhancement due to dense particle effect may determine an overestimation in

momentum exchange between phases thus providing a suspended solid fraction higher than the experimental one. Influence of the dense particle effect term should be higher when local r_β is higher, so one may expect a greater influence at low RPM when particle distribution degree is very small. Actually, when particles are packed lying on the bottom as sediment they show the same r_β value equal to $r_{\beta\text{-packed}}$, so the drag force enhancement is consequently the same in the cells where sediment is presence, independently of impeller speed. When impeller speed is very low, the drag force is not sufficient to suspend particles (even if the enhancement occurs) because the slip velocity between the liquid flow and the sediment is still too low. Increasing agitation speed, slip velocity increases (liquid velocity increases, while solid velocity remains still low) and the drag force reaches its critical value for the suspension of a large fraction of particles (i.e. when the curve starts to go upwards with a large slope). When a *DPE* approach is employed the drag force reaches its critical value at lower impeller speeds than the reference modelling approach, thus yielding an overestimation of the amount of suspended particles.

Conversely, in the case of *homogeneous k-ε turbulence model (Turb-Turb)* approach, differences in predictions are due to the effect of the presence of a turbulent viscosity for the solid phase as well, whose values are shared with the liquid phase. This approach likely yields an overestimation of the convective term in the solid phase momentum equation especially in the computational cells where a still sediment is present, thus providing a premature suspension of solid particles from the vessel bottom.

Finally, for the case of *Mod- $C_{\alpha\beta}$* approach results indicate a dramatically high overestimation of the experimental data. Actually, in the cells where $r_\beta = r_{\beta\text{-packed}}$, *Mod- $C_{\alpha\beta}$* approach makes use of Ergun's equation for the drag force assessment: sediment is assumed as a fixed bed through which liquid can flow. Unfortunately, Ergun's equation is not so satisfactory because simulations results show that the sediment has a very low velocity but it moves anyhow. Ergun's equation provides drag forces much higher than those yielded by the first equation of this approach thus leading to even higher over-predictions.

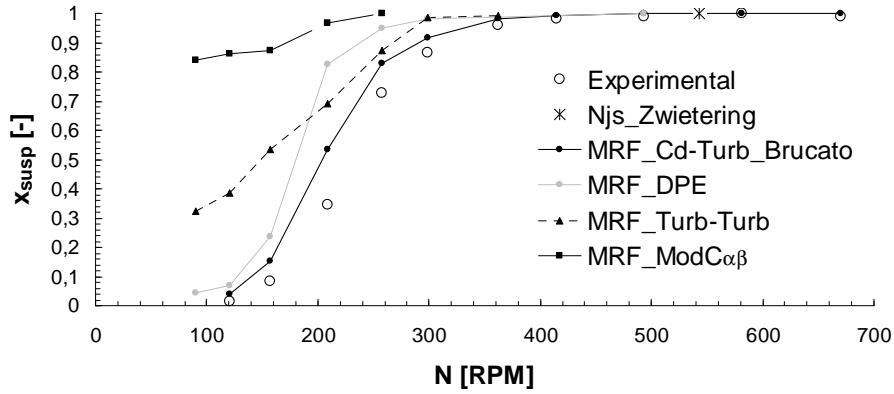


Fig. 4.22: MRF simulations versus experimental data for the case of 212-250 μm glass ballottini particles with a solid loading of 33.8%^{w/w}; comparison of different modelling approaches.

It is worth noting that all these considerations concern the prediction of the amount of solid particles lying on the bottom, conversely the suspension curve data do not provide any information on particle distribution throughout the vessel so that a comparison of these approaches about solid distribution prediction capability can be made only by employing other experimental data (see Paragraph 4.8.12).

4.8.11 Snapshots of the investigated vessel

Both frontal and inferior snapshots of the investigated vessel were taken.

- *Inferior snapshots*

Inferior snapshots were used for a qualitative validation of computational predictions: an example is provided in Fig.4.23.

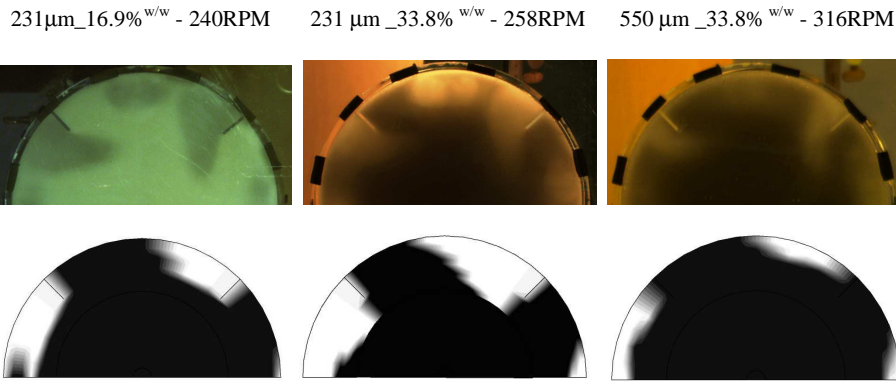


Fig. 4.23: Qualitative comparison of sediment bottom shape between CFD scalar *sedim* (on the bottom) and experimental snapshots (on the top).

Sediment shape visible on the bottom is qualitatively quite well predicted by simulations: still particles are found in front of the baffles, while no sediment is present behind the baffles in accordance with the anticlockwise impeller rotation. Furthermore, unsuspended particles are observable in the middle part of vessel bottom as expected for a system stirred by a radial impeller. Actually, CFD sediment shape images are not identical to the experimental ones, maybe a more accurate flow field calculation by a Large Eddy Simulation would guarantee better results as sediment shape strongly depends on the flow patterns on the vessel bottom.

Unfortunately, a good comparison at higher velocities than those of the former figure were not possible: although high acquisition times were adopted (equal to one second), images appear too blurred and it is not possible to clearly distinguish moving particles from the still ones: as a difference with unbaffled stirred vessels (Brucato et al., 2010), at high impeller speeds, in baffled tanks particles are not permanently still on the bottom because a continuous particle replacement occurs thus leading to a greater difficulty in distinguishing fillets from suspended particles by image/video acquisition procedures.

- Frontal snapshots

As far as frontal snapshots are concerned, they were used both for a qualitative and quantitative comparison with relevant CFD data. At very low impeller speed, when suspension is not started yet in a massive way, it is possible to experimentally observe the 3D sediment shape, a similar corresponding information can be obtained by the 3D visualization of the contour plot of scalar *sedim* (on a vertical diametrical plane placed midway two different baffles) provided by CFD simulations: comparison is depicted in Fig.4.24.

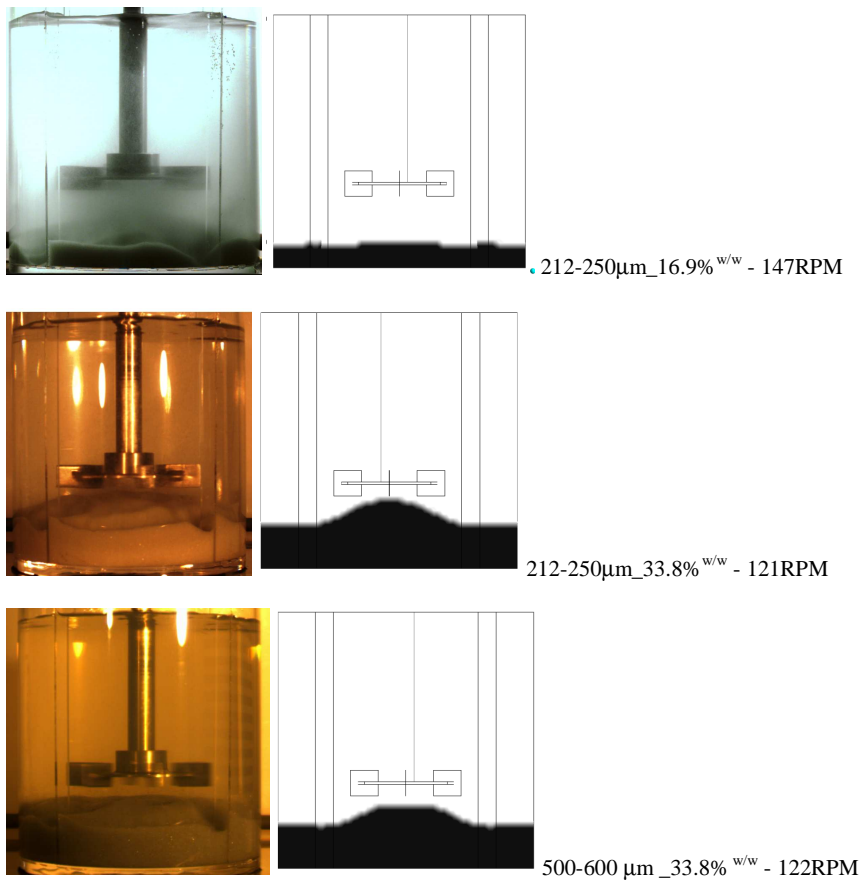


Fig. 4.24: Qualitative comparison of sediment shape: CFD predictions on the right and experimental snapshots on the left.

A heap of particles (typical of solid-liquid systems stirred by radial impellers) is visible in the central part of the vessel underneath the impeller for all the three cases. Such experimental evidence is predicted by CFD simulations in the high solid loading cases, instead of the CFD 16.9%^{w/w} case where no heap of particles is observable.

Quantitative validation by experimental snapshots regards the sediment which is observable on the lateral wall at low and intermediate impeller speeds. More precisely, the height that the sediment visible on this boundary surface assumes midway two subsequent baffles was assessed both in experimental snapshots and in CFD scalar *sedim* contour plots for comparison purposes.

As an alternative, being the height of the settled bed uneven, one may think to use for comparison the area that the sediment placed on the lateral wall shows; unfortunately, in some cases it is not simple to mark this area with a good accuracy so that it would lead to a poor reliability of the measure. The same choice for particle bed height assessment was made by Zhu and Wu (2002).

Fig.4.25 shows the experimental assessments of the normalized sediment height at different rotational speeds. Naturally, at 0RPM both the 33.8%^{w/w} cases show the same initial normalized h_{sed} while the 16.9%^{w/w} case shows a lower value equal to half of the 33.8%^{w/w} one as expected.

Increasing agitation speed, the observable trends follow faithfully the considerations made for Fig.4.9: lower solid particle diameter and concentration aid suspension. Because of the lower number of particles involved, the case with the lowest concentration shows the lowest normalized sediment height at a given agitation speed. In addition, increasing agitation speed but keeping it very low normalized h_{sed} values for the 16.9%w/w case show a smaller decrease than the other cases likely because of the lower number of solid particles involved. Particle diameter has a greater effect than particle concentration on solid suspension as well

as on normalized h_{sed} as suggested by Zwietering's correlation (1958): in fact the impeller speeds at which the sediment disappears from the lateral wall is closer for 212-250 μm glass ballottini particle cases than the 500-600 μm one.

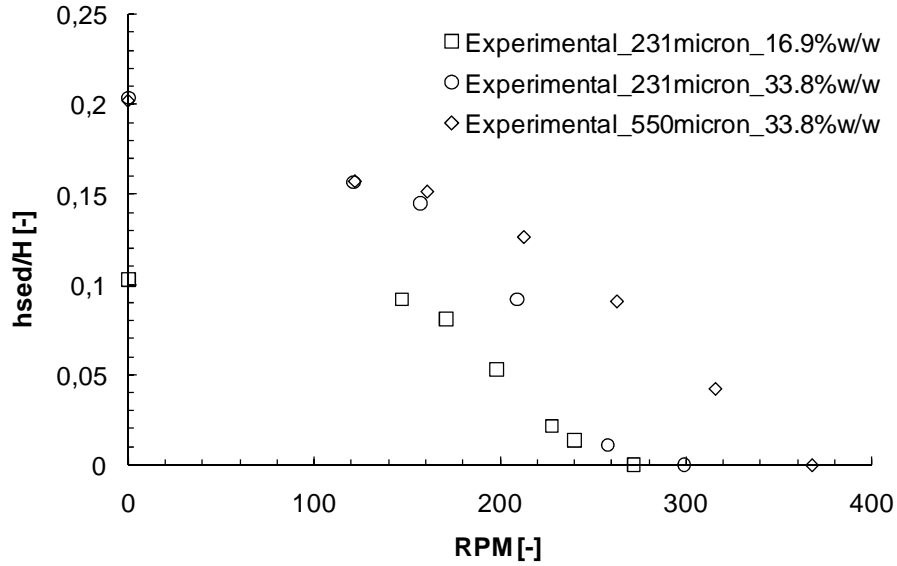


Fig. 4.25: Height of the sediment visible on the lateral wall, assessed in the middle of two subsequent baffles.

The same simulation set carried out with the aim to simulate the suspension curves was also employed to predict the normalized sediment height value as a further model validation.

Figs. 4.26, 4.27 and 4.28 show that, also in this case, simulations were in a very good agreement with relevant experimental results: practically all the presented experimental data are obtainable by CFD simulations with a good precision degree.

Fig.4.26 shows that experimental data are very well predicted even if a little overestimation at low impeller speeds however exists.

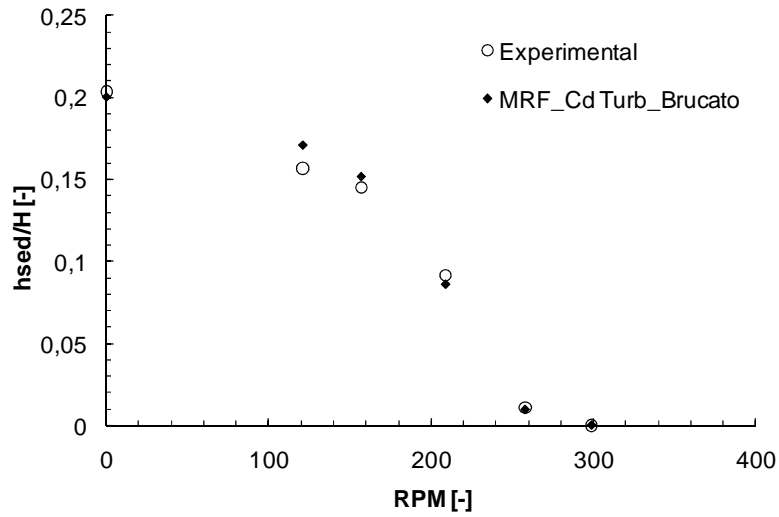


Fig. 4.26: Simulated versus experimental normalized suspension height for the case of 212-250 μm glass ballotini particles with a solid loading of 33.8% w/w .

Conversely, CFD simulations provide a little under-prediction at low impeller speeds for the lower solid concentration case (Fig.4.27).

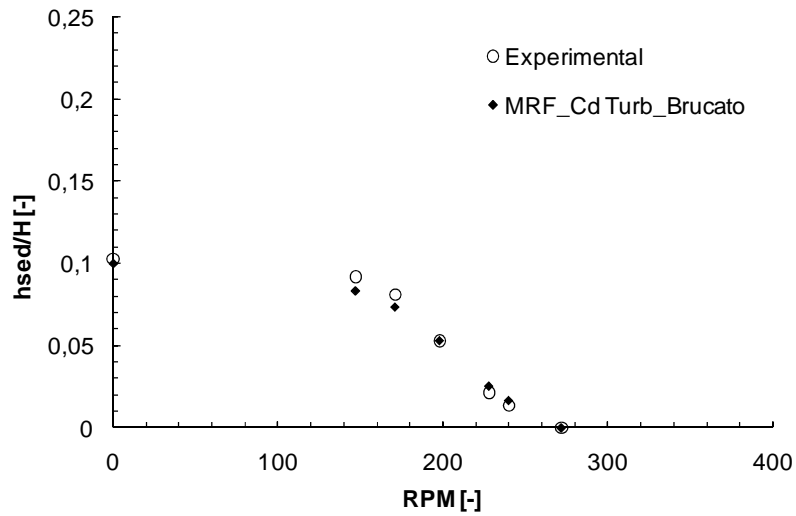


Fig. 4.27: Simulated versus experimental normalized suspension height for the case of 212-250 μm glass ballottini particles with a solid loading of 16.9%^{w/w}.

Eventually, even the normalized sediment height relevant to the high particle diameter case were very well predicted by CFD simulations (Fig.4.28) with the exception of 316RPM value where a moderate underestimation is observable. Notably, no significant differences between the two drag modelling were found, because the impeller speeds investigated are quite low thus providing similar drag coefficient enhancements (see Tab.4.1).

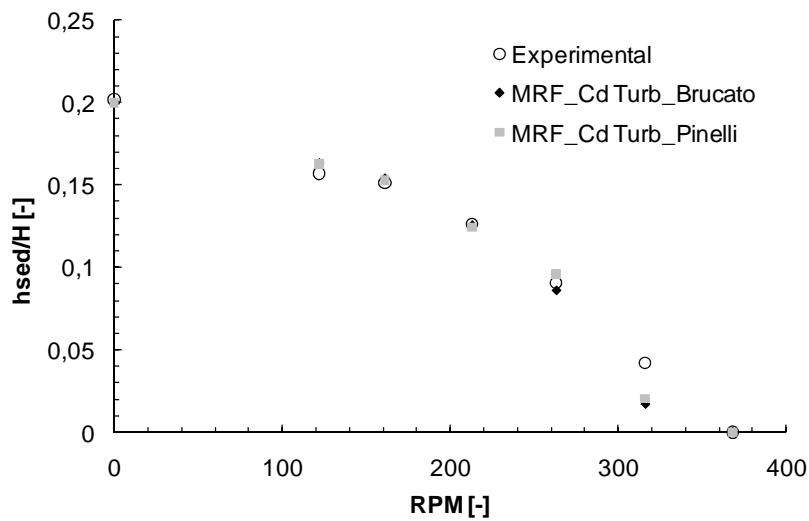


Fig. 4.28: Comparison of two MRF simulation approaches with experimental normalized suspension height for the case of 500-600 μm glass ballottini particles with a solid loading of 33.8%^{w/w}.

For the reference case of 231 μm glass ballottini particles with 33.8%^{w/w}, a comparison of different modelling techniques was performed and depicted in Fig.

4.29. Results confirm the trend already seen in Fig.4.22 for the case of suspension curve data predictions.

Mod- $C_{\alpha\beta}$ approach provides the worst results since, even at low impeller speeds, the normalized h_{sed} values are very lower than the experimental ones. In addition, increasing the agitation speed a very poor decrease of sediment height is observable. *DPE* approach provides good predictions only at low impeller speeds and high underestimations of experimental data at higher velocities, as already seen in Fig.4.22. *Turb-Turb* approach provides under-predicted h_{sed} data in all the investigated range with the exception of 258RPM where an overestimation occurs. With this regard, it is worth noting that *DPE* and *Turb-Turb* predicted data show the same “inversion” also observable in Fig.4.22: before 200RPM, *DPE* approach gives better results than *Turb-Turb* approach, conversely, opposite considerations have to be made at impeller speeds higher than 200RPM. As formerly discussed, this phenomenon may be linked to the Gidaspow’s corrective term which provides higher local value of inter-phase drag force whose effect becomes preponderant on the enhanced convective *Turb-Turb* term only after a certain impeller speed.

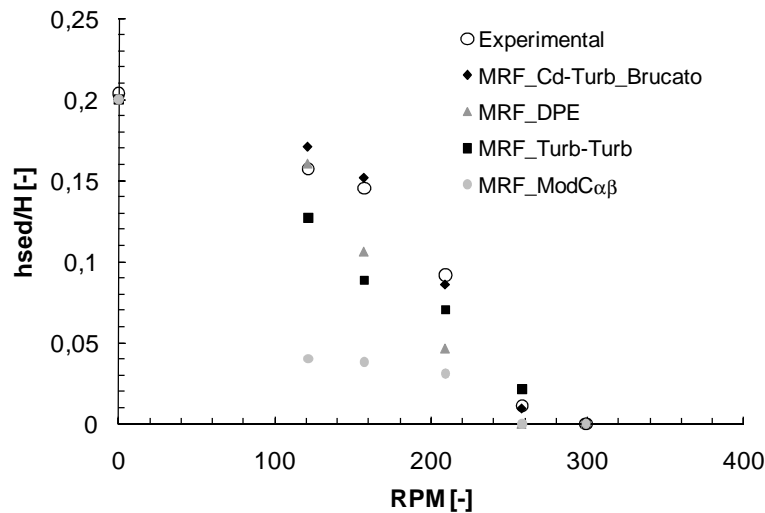


Fig. 4.29: MRF simulations versus experimental normalized suspension height for the case of 212-250 μm glass ballottini particles with a solid loading of 33.8%^{w/w}: comparison of different modelling approaches.

4.8.12 Validation with literature data

Experimental data employed so far for quantitative validation purposes are strictly linked to the amount of solid particles lying on the vessel walls (bottom and lateral wall), but they do not provide information on a quantitative description of the particle distribution over the vessel.

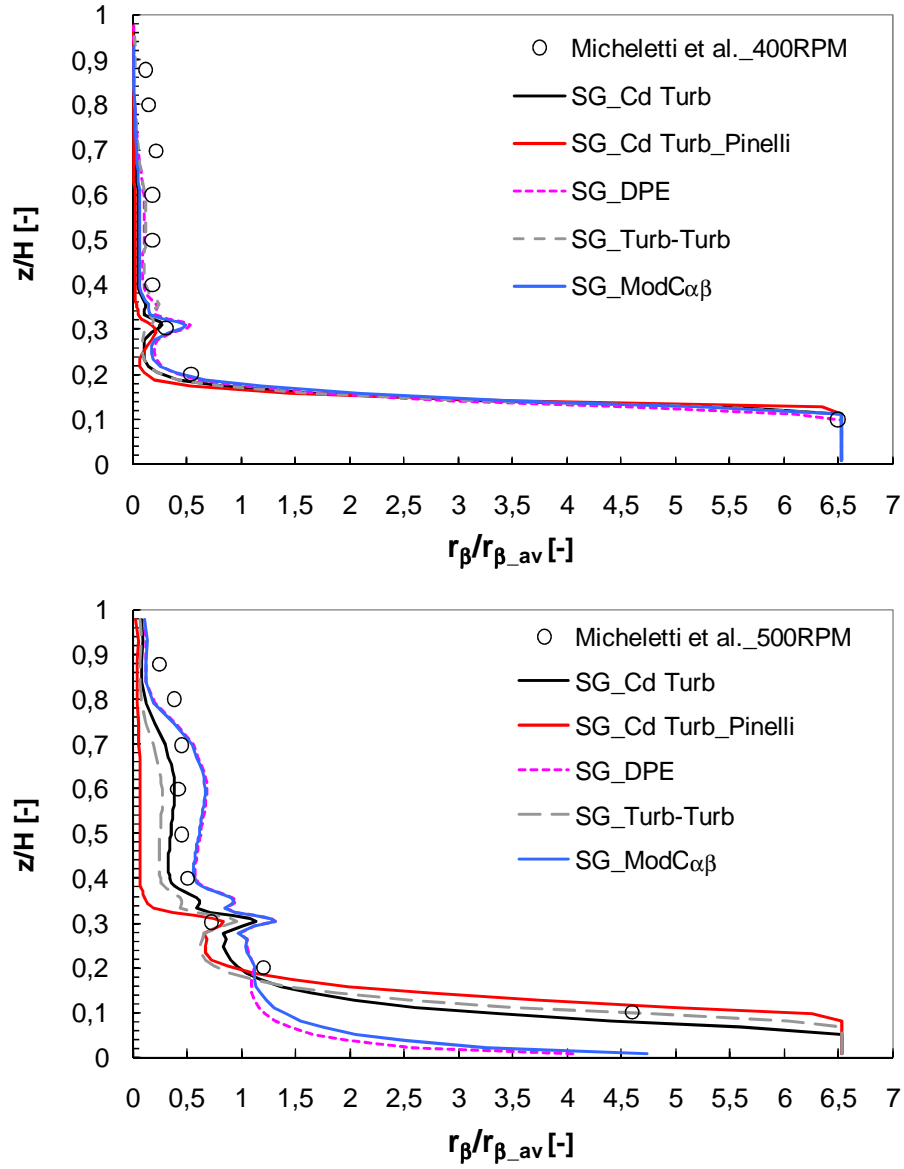
Therefore axial profiles of solid concentrations found in literature for a similar system (Micheletti et al., 2003) were employed for a further model validation.

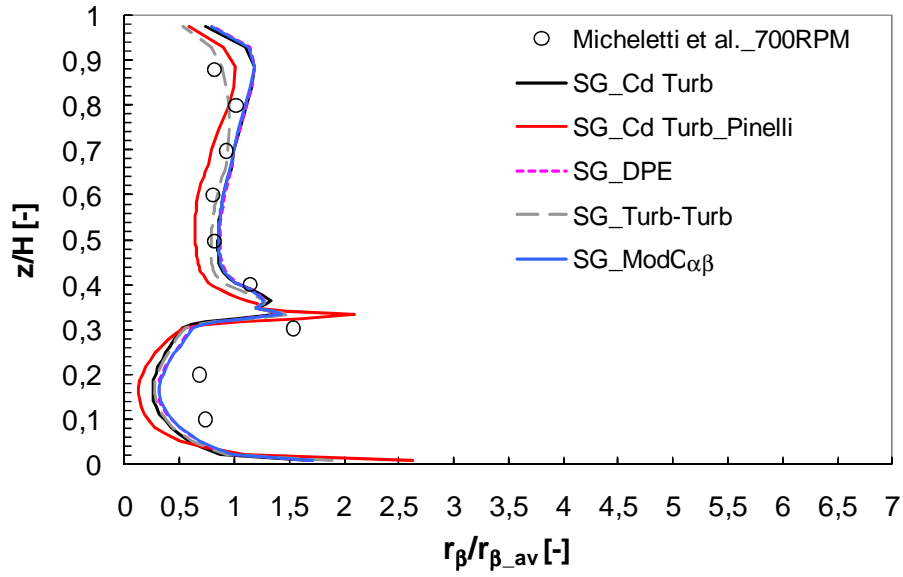
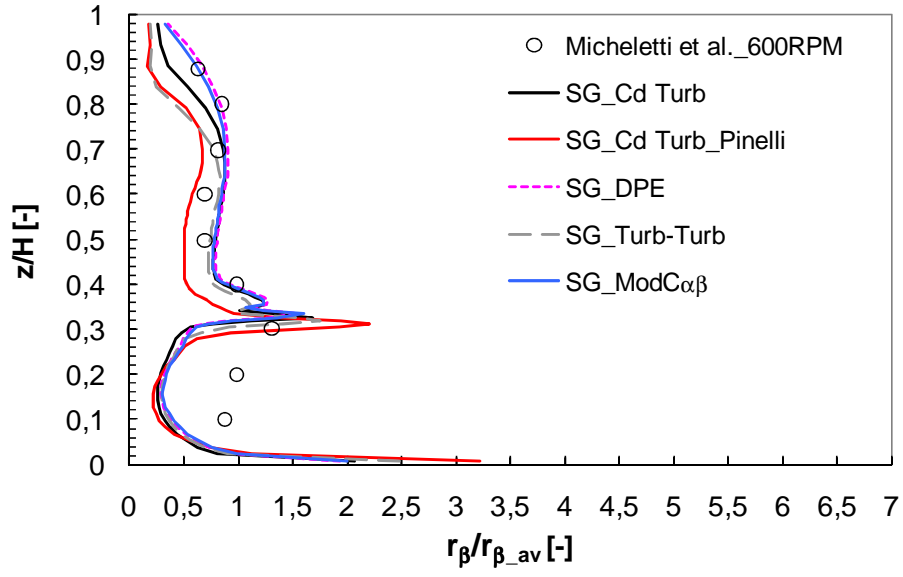
More precisely, local steady state normalized solid concentrations measurements at a radial position $R/T=0.35$, midway between subsequent baffles and at different heights of the tank were collected by Micheletti et al. (2003) using a conductivity probe with the aim of studying the quality of particle distribution.

Average solid volumetric fraction was 9.2%^{v/v}, D was equal to $T/3$ and glass particles whose diameter range was 600-710 μm were employed, other details can be found in the relevant literature (Micheletti et al., 2003).

Reliable simulations were carried out in order to simulate these data for comparison purposes. A *Sliding Grid* approach was adopted even if slight discrepancies between SG and MRF approaches were formerly found (as shown in Figs. 4.15 and 4.16). A comparison of data concerning solid concentration values at different vessel heights requires a more accurate calculation, especially if different modelling approaches (i.e. *Turb-Turb*, *Mod- $C_{\alpha\beta}$* , etc.) have to be carefully compared: as known in literature (Ochieng and Lewis, 2006a; Panneerselvam et al., 2008) a transient CFD simulation approach based on the fully predictive SG algorithm accounts for the temporal variations in the mixing tank thus providing better predictions of the liquid flow field and solid suspension than the MRF steady state framework.

Comparisons between Micheletti et al.' experimental data (2003) and relevant CFD simulation results were depicted in Fig.4.30 for different impeller speeds.





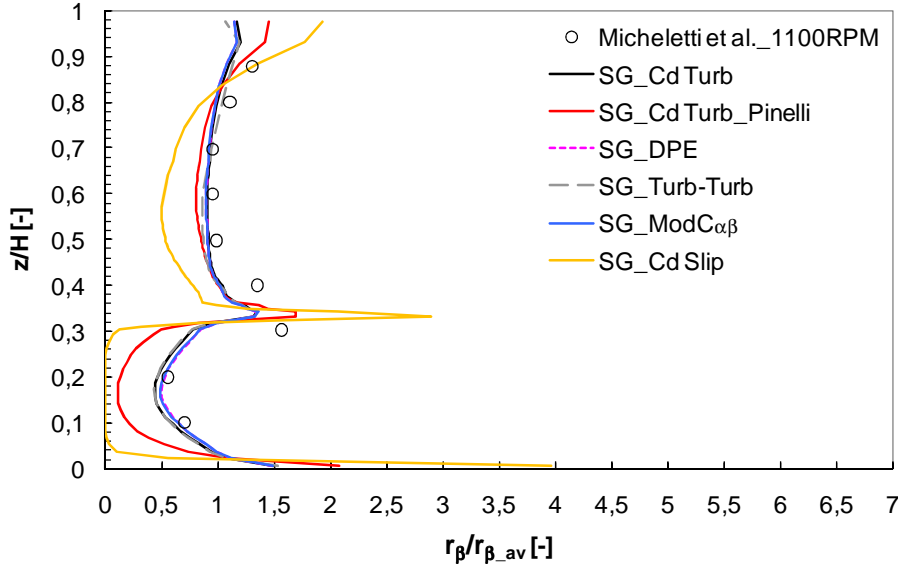


Fig. 4.30: Steady state local axial profiles of particle concentrations (midway between subsequent baffles and at $R = 0.35T$) for different impeller speeds.

At 400RPM all of the tested approaches manage to predict with high accuracy the experimental profile: no appreciable differences among results provided by the various approaches are visible. The presence of particles with a volumetric fraction corresponding to the maximum allowed one (i.e. 0.6) is very well predicted by CFD simulations: the normalized r_β value showed by all approaches is equal to 6.52 which multiplied by the average solid volumetric fraction (i.e. 0.092) just gives back the r_{β_packed} value. Actually, CFD simulation for the 400RPM cases do not provide any particle presence in the upper part of the vessel where experimental data show the presence of a small but not negligible amount of solid particles.

At 500RPM first differences among approaches can be found. $C_{D_turb_Brucato}$ and $Turb-Turb$ approaches provide similar results following very well the experimental profile: more precisely $C_{D_turb_Brucato}$ is a bit closer to Micheletti et al.' data than $Turb-Turb$ approach in the upper part of the vessel while it results further in the

lower part. $C_{D_turb_Pinelli}$ approach gives good predictions in the lower part of the vessel, but it seems not able to correctly predict the distribution of particles in the tank at heights higher than the impeller plane one. DPE and $Mod-C_{\alpha\beta}$ approaches provide similar results: even if they provide good predictions in the upper part of the vessel, they do not manage to predict the amount of particles placed in the proximity of the vessel bottom. The drag force enhancement due to Gidaspow's dense particle effect factor (computed by both the two approaches) produces an additional effect on suspension thus leading to a premature particle suspension. These two approaches show a little difference between each other in the lower part of the tank allegedly because of Ergun's equation effect which is a peculiarity of $Mod-C_{\alpha\beta}$ approach. Even at 500RPM the amount of particles present in the upper part of the vessel is slightly underestimated by all of the CFD simulations.

At 600RPM all the approaches provide the same results under the impeller plane showing an underestimation of experimental data. Actually, the CFD data of the various approaches show little differences just over the bottom thus resulting in different fractions of unsuspended particles (see Fig.4.31). As far as the upper part of the vessel is concerned no big differences between experimental and all computational data are visible even if the adoption of Gidaspow's correction (DPE and $Mod-C_{\alpha\beta}$) seems to generate better predictions for z/H higher than 0.8.

At 700RPM over the impeller plane a good agreement with the experimental profile is visible for all the tested computational approaches even if the upper experimental point is better predicted by the $Turb-Turb$ approach. Under the impeller plane, the figure shows an underestimation of experimental data whose amplitude appears to be lower than the corresponding 600RPM case one. Also, the underestimation provided by $C_{D_turb_Pinelli}$ is higher than that of the other approaches, and the value of solid volumetric fraction just over the bottom is higher as well.

The N_{js} calculated by Micheletti et al. (2003) by means of Zwietering's correlation was found to be equal to about 988RPM so that all the experimental profiles discussed so far are relevant to partial suspension conditions. Therefore in the case of 1100RPM the impeller speed is higher than N_{js} but lower than the speed necessary for the achievement of homogeneous suspension conditions: in other

words, the case of 1100RPM is representative of the commonly investigated regime of complete suspension. Fig.4.30 shows that all of the tested approaches with the exception of $C_{D_turb_Pinelli}$ follow very well the experimental data: it is worth noting that the under-predictions formerly seen under the impeller plane for the 600RPM and 700RPM cases completely disappear in the present case. As already discussed for the 700RPM case, even in this case, $C_{D_turb_Pinelli}$ approach provides data lower than the experimental ones under the impeller plane as well as normalized r_β values higher than other approaches ones just on the tank bottom. The C_{D_slip} approach was also tested in this case of 1100RPM. This approach was formerly found to be unable to provide a fraction of suspended solids equal to one even at very high impeller speeds. Now, it provides high under-prediction of particle distribution degree thus showing underestimations of experimental data both over and under the impeller plane while an improbable very high r_β value is visible on the vessel bottom.

It is very worth noting that such a comparison with experimental axial profiles represents the first attempt in literature to predict the solid distribution in a stirred tank under partial suspension conditions: the adoption of some approaches different from the common ones is justified by this objective.

The suspension curves relevant to these formerly presented profiles are depicted in Fig.4.31 in order to provide a complete comparison of the different approaches. It is worth noting that no experimental data are available for validation in this case.

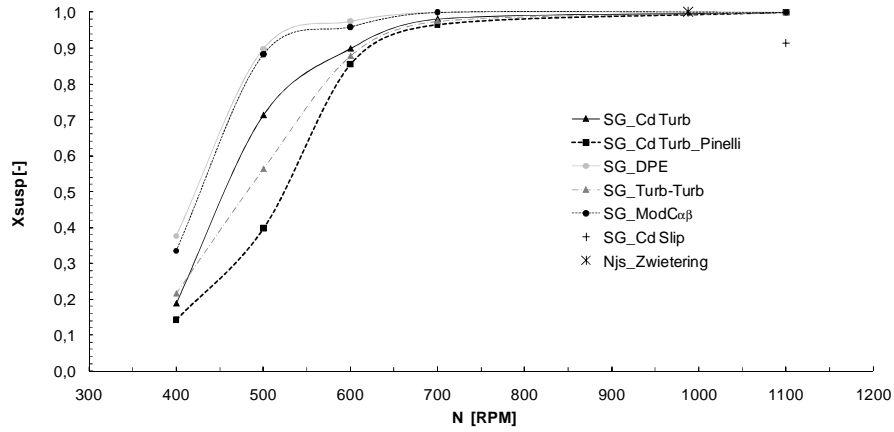


Fig. 4.31: SG suspension curve data for the case of 600-710 μm glass particles with a solid loading of 9.2%^{v/v}: comparison of different modelling approaches.

Fig.4.30 confirms that *DPE* and *Mod- $C_{\alpha\beta}$* approaches overestimate the particle suspension degree even just over the bottom thus resulting in a possibly too high suspended solid fractions especially at low impeller speeds. As previously seen, even if there is not a large difference with other approaches (with the exception of the 500RPM case) *$C_{D_turb_Pinelli}$* approach gives the lowest x_{susp} . *$C_{D_turb_Brucato}$* and *Turb-Turb* approaches provide very similar values of suspended solid fractions with the exception of the 500RPM case where a large difference is observable. Finally, Fig.4.31 shows that even in this case, at 1100RPM, i.e. an impeller speed higher than N_{js} , *C_{d_slip}* approach is not able to provide a fraction of suspended particles equal to one, thus resulting in a not physical outcome.

Summarizing all of the results presented so far, it can be stated that the reference modelling approach, i.e. *$C_{D_turb_Brucato}$* is capable to predict with fair accuracy both the suspension curves and the local axial profiles although predicted x_{susp} could result overestimated when particles with high diameter were employed. *$C_{D_turb_Pinelli}$* provides lower enhancement of particle drag coefficient at high d_p/λ so that it can predict very well the amount of still particles lying on the bottom but it is not so suitable in predicting with high reliability the particle distribution throughout the vessel, especially at high impeller speeds. *C_{d_slip}* approach employment leads to unphysical data thereby confirming the need of computing the effect of liquid free stream turbulence on particle drag coefficient.

Turb-Turb approach seems to be capable to correctly predict local axial profiles at any agitation speed, conversely it does not provide good predictions of x_{susp} . It is worth noting that the vessels employed in this present Chapter and in the Micheletti et al.' work (2003) are fairly different as far as the ratio D/T is concerned: our system has a D/T = 1/2 while Micheletti et al.' one has a D/T = 1/3. Radial impellers

generate considerable turbulence and shear rates which are preferentially concentrated in the impeller neighbourhood: as previously showed, solid sediment could be located very close to the impeller. In addition, the predictions of velocities, especially just over the vessel bottom, is very complex and critical so that perhaps the adoption of a *LES* resolution could provide even more reliable results (Guha et al., 2008) and consequently better clarify the phenomenon. By the way, it is worth underlining that the validity of choices regarding the adoption of a suitable turbulence model for a dense solid-liquid stirred system could be demonstrated only by means of a validation with experimental data concerning the velocities of both the phases (even under partial suspension regime).

DPE and *Mod- $C_{\alpha\beta}$* approaches make use of Gidaspow's correction for dense particle effect which can lead to good results in several cases (Ochieng and Onyango, 2008; Tamburini et al., 2009) where impeller speeds higher than N_{js} are adopted: if partial suspension conditions are dealt with, the employment of such a term can provide overestimations of the inter-phase drag force thus leading to an over-predictions of x_{susp} as well as of particle distribution degree, especially at intermediate impeller speeds: in fact, when impeller speeds are low, slip velocities are low as well so that dense particle correction cannot provide appreciable effects. Furthermore, for the case of *Mod- $C_{\alpha\beta}$* approach, drag force overestimation within the solid sediment area can be dangerously enhanced by the adoption of Ergun's equation notwithstanding its employment at high local volume fractions is suggested by literature (CFX-4 Documentation; Ochieng and Onyango, 2008; Busciglio et al., 2009; Holbeach and Davidson, 2009).

On overall, the comparison among the *reference case* simulation results, the alternative modelling approaches results and experiments, indicate that prediction of the fraction of unsuspended solids at all agitation speeds requires suitable modelling of the key factors controlling the onset of suspension. Conversely, the prediction of solid particle distribution within the vessel would require the development of a model where other key physical factors different from those controlling the onset of suspension play a major role. This has been confirmed by the difficulty in the

formulation of one only model which is universally capable of reliably and accurately predicting both the amount of unsuspended solids resting on the vessel bottom and the distribution of solid particles within the suspension volume. However the model C_{D-turb} appeared to work adequately for the largest variety of cases so far investigated in the present PhD work resulting in satisfactory predictions of both the fraction of motionless particles and the distribution of the suspended ones.

4.9 Conclusions

CFD simulations of dense solid-liquid suspensions within flat bottomed vessels stirred by a standard Rushton turbine were performed with the objective of numerically predicting the percentage of unsuspended solids and the particle distribution at different impeller speeds (covering partial to complete suspension regime). These simulations were carried out with the commercial code CFX4.4 by adopting the fully predictive Eulerian-Eulerian Multi Fluid Model along with the standard k- ϵ model in order to simulate the two-phase flow and the liquid phase turbulent flow, respectively. The transient Sliding Grid (SG) or the steady state Multiple Reference Frame (MRF) approach was used to simulate the impeller to baffles relative rotation. Inter-phase momentum exchange terms have been approximated only by the inter-phase drag forces. Two different correlations were implemented and tested in order to account for the effect of liquid free stream turbulence on drag coefficient. Finally, a grid dependence analysis was performed. A number of experimental data were purposely collected or taken by literature in order to validate simulation results. Particularly, three different types of data were used for the CFD approach validation:

- data concerning the fraction of suspended solid particles collected by *Pressure Gauge Technique*;
- snapshots of the investigated vessel for both qualitative and quantitative comparison;

- literature data (Micheletti et al., 2003) regarding local axial profiles of solid concentration.

Influence of solid loading and particle diameter were investigated. The SG and MRF approaches were compared and no significant differences were found. Grid dependence was found low and more than acceptable. Taking into account the influence of turbulence on drag coefficient was considered necessary to get correct predictions for the higher particle size cases. Comparison between CFD predictions and practically all experimental data showed a very good agreement, notwithstanding the simple modelling approach here adopted. Some other modelling approaches were tested and critically compared. Overall, results suggest that drag force has a crucial role in determining the suspension of particles from the vessel bottom and their distribution throughout the tank. Although suspension of particles in a liquid within a stirred system was found to be allegedly due to “turbulence bursts” on the vessel bottom (Baldi et al., 1978), it seems that the suspension phenomenon should be modeled not only by carrying out a good prediction of turbulence on the vessel bottom, but also and above all by an accurate computation of the inter-phase drag terms. This suggests that the particle suspension and distribution in dense solid-liquid suspensions in stirred tanks at partial to complete suspension conditions is a phenomenon mainly controlled by gravity, inertial and inter-phase drag forces. Eventually, even though systems stirred at speeds lower than N_{js} are not as interesting as systems under complete or homogeneous suspension conditions by an industrial point of view, they however deserve attention, since the correct prediction of solid motion under the filleting regime leads towards a deeper knowledge of the complex particle suspension mechanism.

4.10 Nomenclature

A_{bottom}	vessel bottom area, m^2
$C_{\alpha\beta}$	inter-phase drag term, $kg\ m^{-3}s^{-1}$
C_D	drag coefficient, (-)
$C_{\mu} C_1 C_2$	k - ε model parameter, (-)

D	<i>impeller diameter, m</i>
d_p	<i>particle mean diameter, m</i>
F	<i>force (Nm^{-3})</i>
g	<i>gravitational constant, m s^{-2}</i>
H	<i>liquid height, m</i>
h_{sed}	<i>height sediment assumes on the lateral wall midway two subsequent baffles, m</i>
k	<i>turbulent kinetic energy, $\text{m}^2 \text{s}^{-2}$</i>
M	<i>inter-phase term, Nm^{-3}</i>
M_β	<i>mass of suspended solids, kg</i>
N	<i>rotational impeller speed, RPM</i>
N_{js}	<i>just suspension speed, RPM</i>
N_p	<i>power number, (-)</i>
NI	<i>number of computational cell in the axial direction, (-)</i>
NJ	<i>number of computational cell in the radial direction, (-)</i>
NK	<i>number of computational cell in the azimuthal direction, (-)</i>
P	<i>pressure, (N m^{-2})=Pa</i>
ΔP_β	<i>pressure increase due to solid suspension, (N m^{-2})=Pa</i>
R	<i>tank radius, m</i>
r	<i>volumetric fraction, (-)</i>
$r_{\beta, \text{av}}$	<i>average solid volumetric fraction value, (-)</i>
r_β^{ex}	<i>solid volumetric fraction exceeding maximum packing value, (-)</i>
$r_\beta^{\text{ex total}}$	<i>the sum of r_β^{ex} for all the domain computational cells, (-)</i>
$r_{\beta\text{-packed}}$	<i>solid volumetric fraction maximum packing value, (-)</i>
Re_p	<i>particle Reynolds number, (-)</i>
T	<i>tank diameter, m</i>
U	<i>velocity, ms^{-1}</i>
v_{tip}	<i>tangential speed of the impeller blade tip, m s^{-1}</i>
x_{susp}	<i>fraction of suspended solid, s (-)</i>

Greek letters

ε	<i>turbulent dissipation, W Kg^{-1}</i>
λ	<i>Kolmogorov length, m</i>
μ	<i>viscosity, Pa s</i>
ρ	<i>density, Kg m^{-3}</i>
σ	<i>turbulent Prandtl number, $(-)$</i>

Subscripts

α	<i>liquid phase</i>
β	<i>solid phase</i>
t	<i>turbulent</i>

CHAPTER 5

N_{js} PREDICTION

5.1 Abstract

This chapter represents the arrival point of the modelling efforts carried out in the previous Chapters 3 and 4.

Chapter 3 allowed a first insight into the modelling via CFD techniques of suspension phenomena in solid-liquid agitated systems, while in Chapter 4 an in-depth CFD modelling of partial suspension conditions and particle suspension mechanism was set up. Particularly, in Chapter 4 a CFD model able to adequately simulate particle suspension at impeller speeds either lower or higher than the minimum speed for complete suspension was provided.

Therefore, it is quite obvious to continue these modelling efforts by trying to predict N_{js} values making use of the same CFD model presented in Chapter 4.

Transient Reynolds Averaged Navier Stokes simulations along with the Sliding Grid algorithm were carried out. Liquid turbulence was modelled by the standard k- ϵ model. Coupling between phases was accounted for *via* inter-phase drag terms. Effect of free-stream turbulence on drag coefficient was taken into account by means of the two correlations employed in Chapter 4.

In the scientific literature it is possible to find a number of methods to estimate N_{js} , most of which based on experimental information, while some specifically based on CFD techniques. Some of all these methods are used and discussed throughout the present Chapter in order to compare their reliability. In addition, another method based on the *Unsuspected Solid Criterion* (USC, see paragraph 4.6.2) is presented and its capability of predicting N_{js} is critically discussed.

Only few efforts have been devoted so far to a critical analysis of N_{js} assessment methods (Rieger and Dittl, 1994), moreover, a universally accepted CFD methodology concerning this topic does not exist yet. This lack in scientific literature is addressed by the present Chapter which has two main aims:

- using the CFD model presented in Chapter 4 in conjunction with some N_{js} assessment criteria to check whether any of these is able to provide results showing a good agreement with Zwietering's ones.
- provide a good strategy able to allow the design of mixing apparatuses for solid-liquid suspension by means of Computational Fluid Dynamics.

The choice of the correlation to compute the effects of free stream turbulence on the drag coefficient was found to have a large influence on N_{js} predictions. However, an acceptable agreement between CFD predicted N_{js} and the Zwietering's correlation was found only for some methods, while all other methods were found to be unsuited to provide correct N_{js} values via CFD for the tested cases. These findings suggest that it may be safer to base the design of solid-liquid contactors via CFD referring only to unsuspended solid fractions as well as to the *sufficient suspension criterion* and *speed N_{ss}* instead of the traditional N_{js} value.

5.2 Literature review

Efficient solid-liquid contacting is crucial for the optimization of many industrial processes: the main objective of this contact is to maximize the available particle surface area for reaction or transport processes. This task can be fulfilled by avoiding particle accumulation at any position in the apparatus chosen for the solid-liquid contact. Being particle density higher than the liquid one, particle suspension apparatus performance is often measured in terms of the fraction of the particles resting on system bottom for a specified interval of time (Baldi et al., 1978).

As already emphasized in previous Chapters, in mechanically agitated stirred tanks this criterion leads to the definition of the minimum agitation speed for all particle suspension N_{js} as the impeller speed allowing the particle-bottom time contact to be shortened enough to consider a sufficient liquid replacement around particles.

Scientific studies have produced several methods as well as different criteria to assess this important parameter: they are reviewed and classified in the followings.

5.2.1 Vessel-bottom observation method or Zwietering's method

The most famous and used N_{js} assessment method based on visual observation was provided by Zwietering (1958): in accordance to its criterion N_{js} is defined as the minimum impeller speed at which all solid particles do not rest motionless on vessel bottom for more than 1-2 seconds. This criterion was consequently called “one second criterion”. Zwietering employed glass and Perspex transparent fully baffled vessels in order to allow vessel-bottom observations and ascertain whether particles were completely suspended. Observations can be made easy by illuminating the vessel-bottom with a photoflood light (Chapman et al., 1983) and looking through a mirror placed underneath the tank (Zwietering, 1958).

Most of scientific works dealing with N_{js} evaluation by visual observations refer to Zwietering's work: its criterion as well as its method are in fact largely employed in literature (among the others, Nienow, 1968; Chapman et al., 1983; Buurman et al., 1986; Barresi and Baldi, 1987a; Wong et al., 1987; Raghava Rao et al., 1988; Rewatkar et al., 1991; Armenante et al., 1992; Ibrahim and Nienow, 1996; Armenante and Nagamine, 1998; Armenante et al., 1998; Ibrahim and Nienow, 1999; Fangary et al., 2002; Foucault et al., 2004; Ibrahim and Nienow, 2004) even nowadays (Ren et al., 2008; Van der Westhuizen and Deglon, 2008; Sardeshpande et al., 2009, Ibrahim and Nienow, 2010).

A particular application of the present method was proposed by Ghionzoli et al. (2007). They investigated the effect of vessel-bottom roughness on N_{js} . Since the rough bottom was clearly not transparent, the tank was illuminated and observed from the side. In addition it was inserted in a squared trough in order to avoid optical distortion. This choice was possible as the last point of particle suspension was the fillets between the base and the cylindrical wall.

As already stated by several authors (Nienow, 1992; Micale et al., 2001; Kasat and Pandit, 2005) Zwietering criterion is not particularly efficient under an economical point of view: in baffled stirred tanks, before complete suspension conditions are achieved, a small amount of particles stays in stagnant regions of the vessel bottom (i.e. region where the liquid recirculation is weak like vessel periphery

near the baffles or the tank centre) forming fillets. The amount of particles involved in the fillets may be quite small, even insignificant under a practical point of view. Impeller speed has to be increased greatly to allow all these fillets to suspend off the bottom, thus suggesting that neglecting these fillets could guarantee large agitation cost savings. In particular, Zhu and Wu (2002) asserted that it is sometimes necessary to dramatically increase the impeller speed (up to 20-50%) to lift statistically insignificant particles, often easily doubling energy consumptions. Furthermore, Sharma and Shaikh (2003) stated that any increase of impeller speed aiming to rake particles out of the fillets tends to homogenize particle concentration in the vessel-bulk first before the fillets were eliminated. In accordance with these considerations some authors (Nienow, 1992; Sharma and Shaikh 2003, Kasat and Pandit, 2005) suggested that the criterion for the N_{js} assessment should be applied to the vessel-bottom bulk without considering the fillet suspension from the periphery (corner sites).

On one hand Zwietering's criterion has the advantage of being very simple, but, on the other hand it requires a transparent vessel and it is not so reliable. Being this method based on visual observations along with temporal considerations, it is affected by an intrinsic subjectivity: measurements depend on operator sensitivity indeed. Even for the same observer, errors were estimated to be in the range $\pm 5\%$ (Chapman et al., 1983; Hicks et al., 1997; Armenante and Nagamine, 1998) for the case of dilute solid-liquid suspension. In this regard Rieger and Dittl (1994) state that Zwietering's method is based only on a single measurement closely linked to a subjective determination of the time during which the particles rest at the vessel bottom. Determining this time is difficult especially in fine particle suspension where the layer gradually diminishes (Rieger and Dittl, 1994). Moreover, method reliability dramatically decreases when high solid loadings are employed, up to become practically unreliable in the case of dense suspension. In this regard, Oldshue and Sharma (1992) stated that no data can be reliably reproduced for solid loading higher than $8\%^{w/w}$. Similarly, Sardeshpande et al. (2009), stated that Zwietering criterion application via vessel-bottom observations becomes difficult at

high particle concentrations even with increased impeller speed because differentiation from the partly suspended to just suspended condition was gradual. Thus, identification of N_{js} was difficult and impractical at high solid loadings.

5.2.2 Liquid free surface observation method

This method is quoted here only for the sake of completeness. It is applied only to solid-liquid stirred systems where floating particles are to be drawn down. The criterion is practically identical to Zwietering's one but the observations are carried out at the liquid-free surface. This variant was proposed by Joosten et al. (1977) and indicated in literature as the "*Joosten visual method*" (Kuzmanic et al., 2008). In accordance to this method N_{js} is defined as the speed at which all stagnant zones of floating particles at the liquid surface have just disappeared.

Clearly, main advantages (simplicity) and disadvantages (subjectivity) are very similar to the traditional Zwietering's method.

5.2.3 Particle bed height method

This method is based on the observation of the vessel-lateral wall. When impeller speed is lower than the minimum for complete suspension, by frontal inspection of a baffled stirred tank a sediment, that is a particle bed with a certain height, is visible. It is therefore possible to measure such height, that clearly decreases as impeller speed increases.

N_{js} is defined as the impeller speed at which the height of the settled bed is zero and a reduction in impeller speed causes particles to settle (Hicks et al, 1997; Zhu and Wu, 2002).

Actually, some years before Hicks et al. (1997) and Zhu and Wu (2002), other authors (Havelkova, 1987; Rieger and Dittl, 1994) proposed a similar method which couples this type of measurements with others taken from vessel bottom. Practically, both the height and the base (inner diameter of the sediment annulus) of the lateral particle bed were contemporaneously measured. In this case N_{js} was defined as the impeller speed at which sediment height at the vessel wall was zero and the radius of the particle cleaned area on the vessel bottom reached the vessel diameter. Rieger

and Ditl (1994) found that this phenomenon occurred contemporaneously, i.e. at the same impeller speed chosen as N_{js} thus resulting in practically identical results with the method dealing with sediment height assessment only.

Particle bed height method is quite simple. It is more labor-intensive (Rieger and Ditl, 1994) than Zwietering's one but, on the other hand, it is able to provide more objective results. As far as disadvantages are concerned, being the flow pattern in the tank quite complex and bed surface consequently uneven (Zhu and Wu, 2002), bed height measurements could be not so reliable. Furthermore, this particular behaviour regarding last particles suspending from the bottom periphery, is strongly dependent on the impeller type employed as well as on system geometrical configuration (bottom shape, impeller clearance, aspect ratio, etc) thus limiting method universality.

5.2.4 Cloud height method

Cloud Height method was proposed by Einkenkel and Mersmann (1977) and it is based on visual observations of the cloud of particles from a front view of the vessel. More precisely, the height (from the bottom named *Cloud Height*) of the interface separating suspension from the clear liquid layer was measured at different impeller speeds. In relation to Einkenkel and Mersmann' (1977) definition, N_{js} is chosen as the impeller speed at which the cloud height shows a sudden change.

Some years after, Zehner and Tebel (1984) and more recently Kraume (1992) carried out other cloud height versus impeller speed measurements and proposed a different definition for N_{js} . They defined N_{js} as the impeller speed at which the height of suspended particle cloud was approximately 90% of the total liquid height. Sardeshpande et al. (2009) found that, quantitatively, the N_{js} obtained from this method and Zwietering's one are found to agree with each other within $\pm 8\%$. Conversely, Kraume (1992) stated that N_{js} estimated by the present method is approximately 20-25% higher than that predicted by Zwietering's method.

This method is as simple as other visual methods, but it can lose effectiveness if a wide particle distribution is employed inside the vessel: in fact small particles can

reach the top of the tank (after suspension) before the bigger ones lift off the vessel-bottom thus resulting in an erroneous estimation of N_{js} .

Micheletti et al. (2003) investigated a flat-bottomed tank equipped with a Rushton turbine: they found that (when the impeller was placed at a clearance $C=T/3$) suspension height was equal to the liquid height, even at relatively low impeller speeds.

Another example of the poor generality of this method is provided by Kasat and Pandit (2005) who affirmed that results can significantly differ for small particle size ($<300\text{ }\mu\text{m}$). In this regard, Micheletti et al. (2003) stated that with smaller particles there is typically no clear layer almost at any speed, and with larger ones, there is a clear layer near the top of the vessel which however may disappear at a speed of $N \ll N_{js}$.

Furthermore, as already discussed for particle bed height, also cloud top may well be uneven, which affects measurement reliability. As an example Rewatkar et al. (1991) observed that, at N_{js} , particles were suspended up to the liquid surface in the regions behind the baffles. Conversely, on the other side of the baffle, suspension height was approximately equal to half of the liquid height. Between two consecutive baffles there was a continuous increase in the suspension height moving azimuthally along the vessel lateral wall in the direction of impeller rotation (from the first baffle towards the consecutive one).

5.2.5 Power Number method

This method is based on the observation of the variation of *Power Number* with respect to impeller rotational speed. As briefly described in Chapter 2, Rewatkar et al. (1991) and Raghava Rao et al. (1988) consider as N_{js} the impeller speed beyond which N_p remains constant with impeller speed.

Actually, the two research groups found different N_p versus N curve trends. Rewatkar et al. (1991) observed that at very low impeller speeds N_p decreases with N as the fillets present on vessel bottom and at the vessel periphery reshape vessel bottom so promoting a more streamlined flow. Increasing N , the amount of particles lifting off the bottom increases, so leading to an increase of the average suspension

density seen by the impeller, and in turn in an increase of N_p . After complete suspension conditions were achieved, no further increase in N_p value was observed. Conversely, Raghava Rao et al. (1988) and Micheletti et al. (2003) observed a monotonic trend of N_p versus N . In particular Micheletti et al. (2003) observed that when most particles were motionless on the bottom, N_p increased slowly with N also remaining lower than that for water only as suspension was not started yet. As in the case of Rewatkar et al. (1991), increasing impeller speed led to a fast N_p increase because of average suspension density effects.

Raghava Rao et al. (1988) compared N_{js} valued obtained by this method with those obtained by Zwietering's method finding differences of about $\pm 5\%$.

As a difference with respect to Rewatkar et al. (1991) and Raghava Rao et al. (1988), who employed disc and pitched blade turbines, other authors proposed different criteria for N_{js} definition. For a tank equipped with a propeller Bohnet and Niesmak (1980) found an increasing-decreasing behaviour of N_p with a relative maximum that was suggested to practically coincide with N_{js} . For the case of a tank stirred by Rushton and pitched blade turbines investigated via CFD, Panneerselvam et al. (2008) found instead a decreasing-increasing trend of N_p versus N curves and N_{js} was chosen as the abscissa of the curve relative minimum.

In addition, for unbaffled stirred vessels a completely different trend was found in the present work, as described in Chapter 2.

Even if methods based on power number have the advantage of being applicable to opaque stirred systems, the above different behaviours of N_p versus N for different impeller/tank configurations suggest that they could be affected by a poor universality and their application should be done carefully.

5.2.6 Mixing Time method

Also this method can be used for non-transparent systems. It makes use of the variation of *Mixing Time* θ_{mix} (time necessary to achieve a predefined level of homogeneity of a tracer within a mixing vessel) with the impeller speed (Rewatkar et al., 1991). N_{js} evaluation requires a comparison between θ_{mix} versus N curves: the

one assessed for the liquid only case, the other for the solid-liquid suspension case. For single-phase systems (liquid only) θ_{mix} always decreases while increasing N . When particles were present, θ_{mix} was found to be higher than the corresponding value for liquid only at any N . This behaviour is due to the fact that the liquid phase in the vicinity of settled solids is relatively stationary as compared with the bulk liquid. Increasing impeller rotational speed, higher mixing times for the two-phase system were observed maybe because of the energy dissipation at the solid-liquid interface which reduces the energy dissipation for the liquid circulation (reduction in the average circulation velocity) (Kasat and Pandit, 2005) and it is not consequently available for the mixing process. When complete suspension conditions were achieved the difference between *Mixing Time* values in the presence and in the absence of solid particles exhibited a maximum. The impeller speed value at which this maximum occurred was defined as N_{js} .

Rewatkar et al. (1991) found that differences between N_{js} values measured by this method and by Zwietering's one are about $\pm 5\%$.

Later on Micheletti et al. (2003) suggested that no link exists between *Mixing Time* measurements and N_{js} . As a matter of fact they observed that in some cases the peak in the graph θ_{mix} versus Re occurred when the impeller speed was only 1/3 of the expected N_{js} value. Similarly Harrop et al. (1997) reported a maximum mixing time up to 6 times that measured for water alone at speeds well below the just suspended speed calculated using Zwietering's criterion, thus suggesting the poor universality of the method.

5.2.7 Radioactive tracer method

This method employs radioactive particles to track solid motion within the solid-liquid stirred vessel (Rewatkar et al., 1991). Clearly radioactive tracer physical properties have to be identical to those of the tracked particles. As already seen for the PEPT technique, this tracer emits γ -rays which are detected by means of a scintillation detector placed outside the vessel. The digital signals (*count rate*) given by the tracer particles were continuously monitored with respect to the impeller speed. Increasing the impeller speed, the *count rate* continuously decreased as more

and more particles got suspended. At a certain impeller speed, *count rate* suddenly fell and remained practically constant. This particular speed was considered as N_{js} .

Also in this case, deviations of about $\pm 5\%$ with respect to Zwietering's method were found.

This technique can be successfully employed for dished bottom vessels and in general for opaque systems. Detector position should be chosen carefully (Rewatkar et al., 1991), as the scintillation count rate depends on it. In this regard, Rewatkar et al. (1991) stated that for Disc Turbine the optimal detector position was at the centre of the vessel below the tank, while for Pitched Blade Turbine the best position was below the bottom at the periphery of the vessel.

Finally, although such method appears to be quite promising, it is not so convenient because of high costs and safety issues (due to radioactive emissions).

5.2.8 Local Particle Concentration method

This method is based on the measurement of local particle concentration just above vessel bottom. N_{js} is assessed by observing the curve of this concentration (r_β) against impeller rotational speed. Bourne and Sharma (1974) were the first who adopted this method. They proposed that N_{js} could be ascertained as the impeller speed at which the curve r_β versus N shows a maximum. At low impeller speeds, most particles rest motionless over vessel bottom so resulting in low particle concentrations at the monitoring point. Increasing impeller speed, ever larger portions of the particles originally resting on the bottom get suspended making particle concentration at the measurement point to increase up to the achievement of complete suspension conditions. By further increasing impeller rotational speed, particles get better distributed throughout the vessel and local particle concentration starts to decrease.

Musil (1976) adopted the same method to mixed crystallizers. He observed that a maximum does not always occur: r_β versus N curves were in fact found to show either a maximum for small diameter impellers or a rough slope change for large diameter impellers, at N_{js} .

According to Bourne and Sharma (1974) when the measuring position is changed, the maximum occurs at the same impeller speed value. Similarly, Musil and Vlk (1978) found that the exact location for measurements (within vessel bottom quarter) had little or no effect on the registered mean values of particle concentration and hence on the derived N_{js} values. As a difference Musil (1976) data showed different N_{js} values at different monitoring point positions as well as no maximum or sharp slope change for the highest position thus suggesting a poor reliability of this method.

Particle concentration measurement for N_{js} assessment has been done in different ways in literature: Bourne and Sharma (1974) adopted a sample withdrawal technique concluding that different diameters of the sampling tube can provide different values of solid concentration, but the same values of N_{js} (maximum occurred at the same value of impeller speed even if concentration values were different). Musil (1976) carried out solid concentration measurement by an optical method based on light absorption (see Chapter 1). Musil and Vlk (1978) made use of an electrical conductivity probe.

5.2.9 Acoustic Emission method

This recent method is based on the assessment of *Acoustic Emission* (AE) signals that solid particles emit when they impact the wall (Ren et al., 2008). Multiscale analysis showed that AE signals in the microscale correspond to the random movements of the particles which are not suspended. AE signals in the mesoscale are corresponding to the solid-liquid interactions which are mainly linked to the movement of suspended particles in the stirred tank. AE signals in the macroscale (not dealt with by the authors) are due to overall conditions of the stirred tank. In accordance with these considerations, increasing agitation speed, starting from motionless conditions, causes that more and more particles are getting suspended thus resulting in a corresponding decrease of the energy fraction of the microscale and in a corresponding increase of the energy fraction of the mesoscale.

N_{js} evaluation method can be easily explained referring to the microscale AE energy only. When impeller speeds are quite low particles start to leave the stagnant

zone and AE microscale energy is allegedly linked to their random collisions with the wall. Increasing a little the impeller speed causes an increase of the local concentration of the particles which randomly hit the vessel wall thus resulting in a slight increase of AE microscale energy. Increasing further agitation speed makes sure more and more particles get suspended (“shift” to the liquid phase): random collisions decrease and interactions between liquid and solid phase enhance. Clearly this phenomenon leads AE microscale energy to decrease consequently (and AE mesoscale energy to increase). When impeller speed approaches N_{js} value the AE microscale energy begins to decrease very slowly with N (energy distribution is nearly constant). Hence authors, investigating the trend of the energy fraction of AE microscale energy against impeller speed, defined N_{js} as the impeller speed at which this abrupt slope change occurred (“turning point” of the graph).

Results collected by this acoustic method were compared by authors with corresponding results obtained by visual methods and average relative errors of only 4.28% were found.

5.2.10 Variation Coefficient method

This method is based on the *Variation Coefficient* σ (it is commonly and erroneously called standard deviation) of solid concentration defined by Bohnet and Niesmak (1980) (Chapter 1, eq. 1.7) and largely employed in literature (Einenkel, 1980; Barresi and Baldi, 1987a; Rieger et al., 1988; Oshinowo and Bakker, 2002; Khopkar et al., 2006; Murthy et al., 2007; Kasat et al., 2008; Panneerselvam et al., 2008; Hosseini et al., 2010b).

$$\sigma = \sqrt{\frac{1}{n} \sum_{i=1}^n \left(\frac{r_{\beta-i}}{r_{\beta-av}} - 1 \right)^2} \quad (5.1)$$

In fact, it represents a parameter suitable to assess the homogeneity suspension quality: starting from motionless impeller and increasing agitation speed, the variation coefficient value first reduces sharply. After just off-bottom suspension

conditions are attained the variation coefficient reduces gradually. Hence, a homogeneity degree increase (better suspension quality) is assessable by a reduction of the variation coefficient value. Variation coefficient values at various impeller speeds can be divided in three different regions based on the quality of suspension (Bohnet and Niesmak, 1980). For homogeneous suspensions (practically uniform particle concentrations throughout the vessel) the variation coefficient value was found to be smaller than 0.2 ($\sigma < 0.2$). For complete suspension conditions (all particles suspended but without attaining a homogenous distribution within the tank) the variation coefficient value varied between 0.2 and 0.8 ($0.2 < \sigma < 0.8$). For incomplete suspension conditions (particles not completely suspended) the variation coefficient value was higher than 0.8 ($\sigma > 0.8$).

In accordance with the present method, N_{js} can practically be defined as the impeller rotational speed at which the variation coefficient approaches approximately the 0.8 value.

As a matter of fact, it is difficult to attain exactly the same value of variation coefficient for different system types thus resulting in a practical difficulty of exactly identifying the N_{js} value by this method (Kasat et al., 2008).

5.2.11 Pressure Gauge Technique method

This method makes use of the fraction of suspended solids (x_{susp}) estimated by means of the *Pressure Gauge Technique* (PGT) already described in Chapter 4. Brucato et al. (1997) and Micale et al. (2002) showed that, plotting x_{susp} against impeller speed N , a S-shaped curve can be obtained for all the investigated cases. This curve can be fitted by means of a Weibull function controlled by two parameters N_{min} and N_{span} :

$$x_{susp} = 0 \quad \text{for } N < N_{min} \quad (5.2a)$$

$$x_{susp} = 1 - \exp \left[- \left(\frac{N - N_{min}}{N_{span}} \right)^2 \right] \quad \text{for } N \geq N_{min} \quad (5.2b)$$

These two parameters have also a physical meaning: N_{min} is the impeller speed at which the suspension phenomenon starts, N_{span} is an impeller speed such that twice its value gives the range of N in which most of the suspension phenomenon takes place. It can be immediately recognized that at $(N - N_{min}) = 2 N_{span}$ the value of x_{susp} is 0.982 so that at this agitator speed less than 2% of the particles is still lying on the bottom. It is worth observing that these few particles are allegedly to be subjected to random motion from time to time so that the consequent renewal of the liquid phase in their proximity may well allow them to participate in the exchange processes occurring in the vessel. In any case, their lack of participation in the mass transfer processes cannot be considered significant (Micale et al., 2002).

These considerations led authors to the definition of the *sufficient suspension criterion*: particle suspension was considered sufficient when about the 98% of particles got suspended and a corresponding *sufficient suspension impeller speed* was consequently defined:

$$N_{ss} = N_{min} + 2N_{span} \quad (5.3)$$

Clearly, this particular impeller speed is somewhat equivalent to the Zwietering's N_{js} though not coincident and very similar to the 98% suspension criterion proposed by Chaudacek (1982).

In this regard, Brucato et al. (1997) compared N_{ss} experimental values with corresponding N_{js} calculated by means of Zwietering's correlation. Zwietering's N_{js} values were found to be in general significantly greater than the N_{ss} experimental values, as also found by Chaudacek (1982). N_{js} values were estimated to be up to 50% higher than N_{ss} ones (average increase of about 30%). The suspension of the last 2% of solid particles requires an increase of agitation speed which corresponds to a dramatic increase of power requirements (mechanical power increases with the

cube of impeller speed). This evidence justifies the adoption of Zwietering's criterion and correlation only for those cases where any unsuspended fillet (even if below 2% of the total particles) may represent a significant operating trouble. This actually occurs in the case of many crystallization processes. In all other cases, the adoption of the sufficient suspension criterion, based on *PGT* technique, instead of conventional Zwietering's visual criterion for complete off-bottom suspension is shown to result into important savings in agitation costs.

Recently, the *PGT* method has been adopted by Selima et al. (2008) for the case of a conical bottomed tank. With respect to Brucato et al. (1997), they found N_{ss} values more similar to those of Zwietering. The maximum difference was found to be about 17% and in many cases differences lower than the 5% were found.

Unlike the *Local Particle Concentration method*, the present method gives information about the overall values, rather than the local values of particle concentration in the tank (Kasat and Pandit, 2005). Furthermore, this *PGT* method can be applied to large scale systems where even more reliable results can be obtained (Micale et al. 2002).

Finally, in accordance with Kasat and Pandit (2005) the adoption of the *Sufficient Suspension Criterion*, based on the pressure measurements technique, in place of the conventional visual criterion for complete off-bottom suspension is shown to result into important savings in agitation costs.

5.2.12 Large scale methods

- *Contact method* (Rieger et al., 1980)

This particular method is suited for non-transparent vessels as in the case of large scale tanks where traditional visual methods cannot be applied. It is based on the adoption of a rod which is inserted inside the tank to be investigated. At the end of this rod a flat baffle perpendicular to it is fixed in order to allow unsuspended particle layer measurements. Complete suspension conditions are considered achieved when no particle layer is found. Clearly only a single position of the vessel bottom is investigable.

- Radiation method (Ditl and Rieger et al., 1984)

This method makes use of a scintillation probe (placed under the bottom of the stirred tank) which allows the measurement of the motionless particle layer height. Increasing impeller speed, the particle layer height decreases consequently and the pre-recorded frequency of impulses decreases. It approaches a constant value when complete suspension conditions are achieved. As the *Contact Method*, the present method is useful for not transparent large scale mixing tanks, but, even in this case, the measurement regards only a single spot of the bottom.

- Bottom Apparent Velocity method (Buurman et al., 1986)

Authors adopted a Doppler velocity meter by which they were able to observe a sharp transition between a stationary and a moving sand layer at about 1 cm from the vessel bottom. When this transition occurs, just suspension conditions are considered achieved. This method was used by the authors both at laboratory scale and at large scale, even if a distinct transition is observable only in a large scale mixing vessel (because sand layers are thinner at the laboratory scale). Finally authors assessed N_{js} at a laboratory scale both by this method and by Zwietering's one finding values diverging approximately by 1%.

5.2.13 Theoretical methods

Some authors attempted to model theoretically the complex phenomenon of solid suspension within a solid liquid system agitated by a stirrer (Baldi et al., 1978; Rieger and Ditl, 1982; Voit and Mersmann, 1986; Wichterle, 1988; Mersmann et al., 1998)

Among these scientific works Baldi et al. (1978) introduced a theoretical model to determine N_{js} based on the assumption that the energy needed to suspend a particle from the bottom is proportional to that of turbulent vortices.

Conversely, Wichterle (1988) proposed a theoretical model based on the balance between the upward flow velocity and the particle settling velocity. Eventually, Mersmann et al. (1998) formulated a theoretical prediction of N_{js} by

distinguishing and modelling two different processes: the “avoidance of settling” and “the off-bottom” lifting.

Among all these theoretical models, the one by Mersmann et al. (1998) seems to have a more general validity than the others even if more and more experimental data would be needed to assess its universal validity.

5.2.14 Computational Fluid Dynamics method

Although Computational Fluid Dynamics methodologies have been popularly adopted to simulate the flow field in stirred tanks, only a few scientific efforts have been devoted to the prediction of N_{js} via CFD.

Kee and Tan (2002) performed 2-D transient simulations of a solid-liquid stirred tank (other details can be found in Chapter 4) monitoring during the transient the solid volume fraction r_β for the layer of cells adjacent to the vessel floor. They proposed as N_{js} the impeller speed at which:

- all the transient r_β profiles (i.e. r_β versus time) exhibited steady-state behaviour;
- the steady state values of r_β were approximately 50% of the initial packed volume fraction (about 0.6 in their case)

Authors considered these numerical conditions as a numerical interpretation of Zwietering’s criterion: in fact if particles were firstly suspended and then sunk motionless on the bottom for a considerable time before being picked up again, the quantity of solids being circulated would not be constant and the r_β profiles would be un-steady. Moreover, if complete suspension conditions were not achieved, some fillets or heaps of solid would be present and the corresponding r_β profile would show the maximum packing value. Kee and Tan (2002) adopted also the *Local Particle Concentration method* of Bourne and Sharma (1974) to validate the former methodology. Both methods showed a good agreement with Zwietering’s correlation (Zwietering, 1958; Nienow, 1968): predicted N_{js} values showed a maximum error of about 12%.

Murthy et al. (2007) predicted N_{js} values for a three-phase (gas-liquid-solid) stirred tank by adopting the *Variation Coefficient method* of Bohnet and Niesmak (1980). Authors assessed the variation of σ with impeller speed and noted that there was a sharp reduction of σ as the impeller speed approached N_{js} . For three reference cases, N_{js} was experimentally measured and a σ of about 0.75 was provided by corresponding CFD simulations. Therefore, N_{js} was identified as the impeller speed at which the variation coefficient exhibited a value of 0.75. Authors concluded that the suggested value of σ held for different impeller designs and over a wide range of particle size, solid loading and superficial gas velocity.

Wang et al. (2004) adopted three different methods to predict N_{js} . The first method was the *Local Particle Concentration method* of Bourne and Sharma (1974). The second method was based on the inspection of the *axial velocity of solid phase* (u_B) in the computational cells closest to the tank bottom at different impeller speeds. When a standard Rushton turbine is employed and its speed is gradually increased, the last particles which suspend are placed at the centre of the tank bottom: the main flow at the vessel bottom is from the periphery towards the centre, thus making this position as the most difficult for particle suspension. According to this second criterion, when the axial velocity of solid phase in the cells placed at the centre of the tank bottom is definitely positive, all particles are considered suspended. The third method regarded the monitoring of the *variation of particle concentration* against impeller speed again at the centre of the tank bottom. Just off-bottom suspension conditions were considered to be achieved when the solid volume fraction in this vessel position showed some value lower than the maximum packing one. It is worth noting that the same authors criticized this last method. They asserted that the definition of the exact volume fraction corresponding to the suspension was a subjective choice, thus considering the second method better than the third.

Kasat et al. (2008) investigated a tank stirred by a radial impeller trying to predict N_{js} by means of the *Cloud Height method* of Kraume (1992). They employed

the predicted iso-surfaces of the average solid concentration to assess cloud height. More precisely cloud height was defined as the distance of the highest point of the average solid concentration iso-surface from vessel bottom. Clearly, N_{js} was identified as the impeller speed at which cloud height reached 90% of the total liquid height. They found a good agreement with an experimental N_{js} for the case of Yamazaki et al. (1986) data.

Ochieng and Lewis (2006a) proposed a quite peculiar method for the prediction of N_{js} based on experimental measurements. The maximum bottom radius covered by the particles, when the impeller was running at N_{js} , was experimentally determined. The mean solid concentration at this radial position and at the experimentally assessed N_{js} was determined by the CFD simulation and then the subsequent predictions of the N_{js} were based on the attainment of the same mean solid concentration at the same radial position. Although the CFD simulations under-predicted N_{js} especially for the larger particles, a good agreement with experimental N_{js} values was found (deviations of about 6%).

In order to predict N_{js} values via CFD Hosseini et al. (2010b) employed a method already adopted by Mak (1992). This method is based on the evaluation of the mean solid concentration at a horizontal plane located 1 millimetre above the bottom of the tank. This value is taken at different impeller speeds so that a graph (mean particle concentration at that height versus impeller speed) can be provided. Two tangents to the curve are drawn at the points having maximum and minimum slopes. N_{js} is defined as the impeller speed corresponding to the point at which the two tangents cross each other. This method was applied both to experimental and computational data and a very good agreement was found.

The issue of predicting N_{js} by means of computational fluid dynamics is addressed within this chapter. Some of the methods presented so far were employed aiming at evaluating and comparing their applicability and performance.

5.3 Numerical modelling and details

The model described and validated in Chapter 4 was adopted here for N_{js} predictions. It is summarized briefly in the following.

RANS simulations were carried out by using the commercial finite-volume method code CFX4.4 (AEA technology). The Eulerian-Eulerian MFM was employed. As transient profiles had to be obtained from simulations (because Kee and Tan method was tested) it was compulsory to perform only transient simulations by means of the Sliding Grid approach.

The $k-\varepsilon$ turbulence model was adopted to account for the turbulence of the liquid phase.

Coupling between phases was obtained via pressure and inter-phase drag force. Effect of free stream turbulence on drag coefficient was taken into account: both Brucato et al. (1998a) and Pinelli et al. (2001) correlations were (alternatively) utilized in order to compare the effects on N_{js} prediction.

For full numerical details, please refer to paragraph 4.6.

In order to be sure about the reliability and the applicability of the present CFD modelling procedure, the same cases already modelled in Chapter 4 were employed, though this time with a different purpose.

Therefore, as already seen in Chapter 4, there are four cases investigated:

- deionized water and 212-250 μm glass ballottini particles, 11.90% $v_{\text{solid}}/v_{\text{total}}$;
- deionized water and 212-250 μm glass ballottini particles, 5.95% $v_{\text{solid}}/v_{\text{total}}$;
- deionized water and 500-600 μm glass ballottini particles, 11.90% $v_{\text{solid}}/v_{\text{total}}$;
- Micheletti et al. (2003): deionized water and 600-710 μm glass particles, 9.20% $v_{\text{solid}}/v_{\text{total}}$;

It is important to underline that, as in Chapter 4, all the presented cases were modelled by adopting Brucato et al. correlation (1998a), whereas, Pinelli et al. correlation (2001) was employed only for the cases with the highest particle size (550 μm and 655 μm). Clearly the first three cases refer to the system described in

section 4.3, while the forth refers to the system investigated by Micheletti et al. (2003) (also described in Chapter 4)

N_{js} predictions required a number of simulations: many of these are the same simulations already shown in Chapter 4, others (i.e. at other impeller speeds) were added in order to complete the work. As an example, being the N_{js} predicted by Zwietering's correlation (equation 2.1) the reference value, more simulations were carried out at impeller speeds close to this value.

5.4 Case Description and Analysis of Results

Before starting the description and the discussion of each single case it is worth noting that not all the N_{js} assessment methods can be easily implemented inside a CFD model. As an example, incorporating Zwietering's criterion is difficult inside an Eulerian-Eulerian framework (Panneerselvam et al., 2008). In fact, in accordance with Oshinowo and Bakker (2002) the criterion that solid particles remain motionless on the bottom of the vessel for less than 1-2 seconds is meaningless from a computational stand point.

All the predicted N_{js} values will be compared with those predicted by means of Zwietering's correlation (equation 2.1). In fact, all the cases presented have a very high solid loading and visual assessment of N_{js} values could have led to errors even larger than those affecting Zwietering's correlation.

5.4.1 Cloud height method

This method requires the measurement of the cloud height at a given impeller speed. The extrapolation of this measurement from CFD simulation constitutes a delicate operation.

In fact, the most common method for this extrapolation makes use of an iso-surface (Fig.5.1) of solid volume fraction (Oshinowo and Bakker, 2002; Kasat et al., 2008; Tamburini et al., 2009). On its turn, this representation via iso-surface requires the choice of a suitable solid volume fraction value. The average height of the iso-surface (and so the cloud height) is dramatically dependent on this choice: similar

reference values of solid volume fraction can provide very different iso-surfaces and consequently different cloud heights. In addition, in literature a commonly accepted value of solid volume fraction for the iso-surface generation does not exist: as an example, Tamburini et al. (2009) adopted a $r_\beta=0.1$, conversely Kasat et al. (2008) adopted as r_β the average solid volume fraction of their system. All these considerations suggest that the “free” choice of the solid volume fraction for the iso-surface generation is a first operation that can alter the significance of the method.

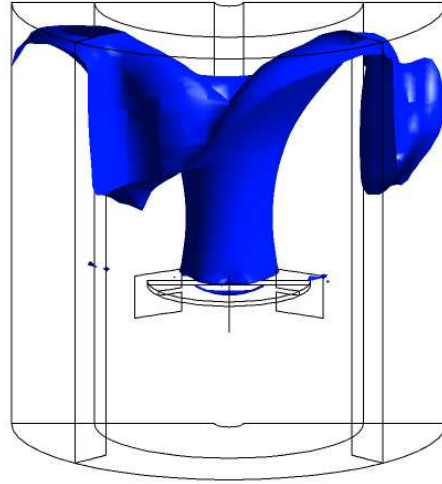


Fig. 5.1: Example of a cloud height representation via iso-surface with $r_\beta=0.015$

Unfortunately, the former is not the sole problem, another weak point of the method concerns the iso-surface shape and the consequent choice of the cloud height. In other words, as already written in paragraph 5.2.4 and observed in fig. 5.1, the iso-surface is uneven and its height between two different baffles can significantly change (Rewatkar et al., 1991). Hence, different choices are possible: one may consider the average height of the iso-surface as the cloud height, or may

take the highest iso-surface point as the cloud height (Kasat et al., 2008). Clearly, the arbitrariness of this choice contributes to further reduce the approach reliability.

Actually, the iso-surface is not the unique methodology to infer cloud height *via* CFD. A different methodology was adopted by Ochieng and Lewis (2006a). It makes use of the axial profile of solid volume fraction. As showed in Fig. 5.2, the cloud height was identified by a point of inflection on the curve. It is worth noting that such a methodology could be affected by a poor precision. In fact, if the point of inflection is far away from the ordinate axis, cloud height will be strongly underestimated.

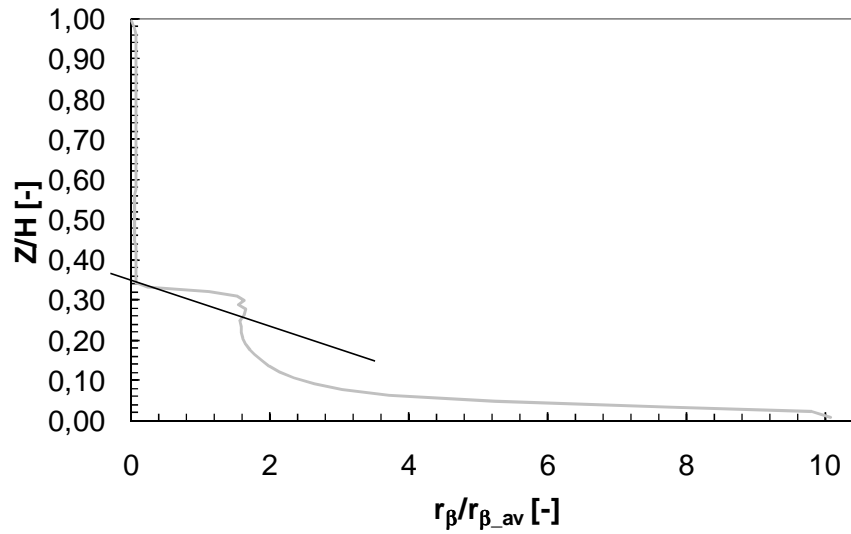


Fig. 5.2: Example of the cloud height measurement methodology

In order to avoid this possibility and in order to adopt a reliable methodology it would be necessary to know exactly the minimum r_β value which determines the opaqueness of a hypothetical corresponding transparent experimental apparatus. Unfortunately this threshold value depends on particle type, size, etc.

By the way, the cloud height was evaluated by adopting the point of inflection methodology. Results for the case of 231 μm particles and 11.9%^{v/v} as solid loading are depicted in Fig. 5.3. The horizontal line is drawn at Cloud height /H=0.9 and it is necessary to assess N_{js} value.

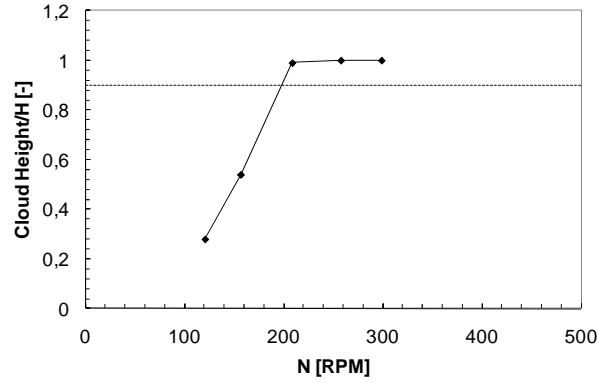


Fig. 5.3: Normalized cloud height predictions for the case of 231 μm glass particles, 11.9%^{v/v}

In fact, N_{js} is defined as the abscissa of the intersection point between the horizontal line and the line fitting the cloud height points.

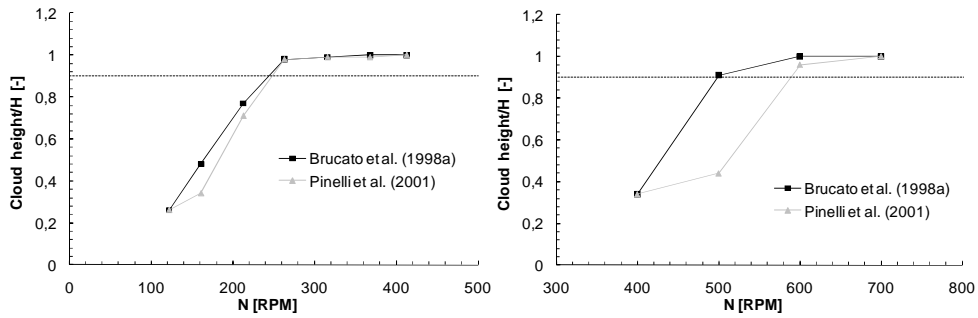


Fig. 5.4: Drag-turbulence correlation effect. On the left: 550 μ m glass particles, 11.9% v/v ; on the right: Micheletti et al. (2003) case.

Fig. 5.4 shows the effect of the two different correlations for drag coefficient on the N_{js} prediction via *Cloud Height method*. No appreciable difference are observable for the case of 550 μ m glass particles, while significant differences were found for Micheletti et al. (2003) case.

The exact N_{js} values are showed in Tab.5.1.

	231 μ m 5.95% v/v	231 μ m 11.9% v/v	550 μ m 11.9% v/v Brucato et al. correlation	550 μ m 11.9% v/v Pinelli et al. correlation
N_{js} Zwietering	492 RPM	543 RPM	645 RPM	645 RPM
N_{js} CFD	300 RPM	200 RPM	245 RPM	250 RPM
Deviation %	-39.0%	-63.2%	-62.0%	-61.2%
x_{susp} (N_{js} CFD)	~ 0.92	~ 0.54	~ 0.32	~ 0.30

	Micheletti et al. (2003) Brucato et al. correlation	Micheletti et al. (2003) Pinelli et al. correlation
N_{js} Zwietering	988 RPM	988 RPM
N_{js} CFD	500 RPM	590 RPM
Deviation %	-49.4%	-40.3%
x_{susp} (N_{js} CFD)	~ 0.71	~ 0.83

Tab. 5.1: N_{js} predictions: *Cloud Height method* case.

As shown in Tab. 5.1 the predicted N_{js} values are quite far from the expected values calculated by Zwietering's correlation thus suggesting that suspension reaches the liquid free surface at impeller speeds very lower than N_{js} .

It is worth noting that the same feature was observed also during the experiments showed in Chapter 4 thus confirming the soundness of predictions. In addition, as already written, other authors observed a similar behaviour, especially for the case of small particles (Micheletti et al., 2003).

As a difference, observing Hosseini et al. (2010b) data, it appears that the condition Cloud height/H=0.9 is attained in that case at an impeller speed higher than the just suspension speed. Similarly, most results presented by Hicks et al. (1997) show that the just suspension conditions are achieved when the ratio Cloud height/H is lower than 0.9.

Moreover, Tab. 5.1 contains another important information concerning the predicted fraction of suspended solid particles at an impeller speed equal to the N_{js} value estimated by the present *Cloud Height method*: in case of adoption of this method, for the cases here presented the fraction of suspended particles would be too small, especially for 550 μ m glass particles.

Results and relevant considerations suggest that the present method is not suitable for assessing suspension speed. The same conclusion was reached by Rieger and Dittl (1994): they observed that the *Cloud Height method* could not be used in some cases where the suspension-liquid interface (after the beginning of the suspension state) immediately reaches as far as the liquid level; they also observed that in many cases the particle cloud reaches the liquid level (and not 90% of it) well before complete suspension conditions were attained.

5.4.2 Particle Bed Height method

The *Particle bed height method* requires the CFD prediction of the height of the sediment placed on the lateral walls of the vessel. The measurement of this height was already done in Chapter 4, by means of the adoption of the scalar *sedim* and it is not shown again here (see paragraph 4.8.11)

As a matter of fact, the measurement of particle bed height involves the same problem already described and discussed for cloud height measurement, i.e. the irregularity of the sediment height between two subsequent baffles. The distance from the vessel bottom of the highest sediment point was taken as particle bed

height. Notably, CFD sediment heights were validated by corresponding experimental data in Chapter 4.

Fig.5.5 shows the normalized particle bed height predicted by employing the scalar *sedim* and already shown in Chapter 4.

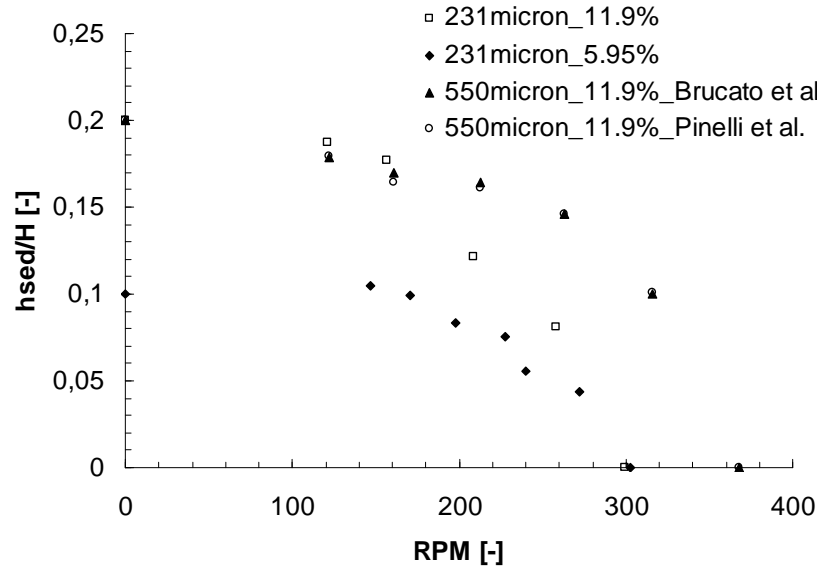


Fig. 5.5: Normalized particle bed height predictions.

It is important to remember that N_{js} is defined as the minimum impeller speed, among the investigated ones, at which the particle bed height was zeroed. Actually it exists the possibility that the chosen N_{js} is not the minimum of all the possible impeller speeds, but only the minimum among the investigated ones. It could be better to carry out other simulations at impeller speeds lower than the found N_{js} (and higher than the highest of the investigated impeller speeds $< N_{js}$) in order to check its validity. Clearly, the search for the most correct value requires that a number of CFD simulations are carried out at several impeller speeds, thus resulting in large CPU times.

	231 μm 5.95% ^{v/v}	231 μm 11.9% ^{v/v}	550 μm 11.9% ^{v/v} Brucato et al. correlation	550 μm 11.9% ^{v/v} Pinelli et al. correlation
N_{js} Zwietering	492 RPM	543 RPM	645 RPM	645 RPM
N_{js} CFD	303 RPM	299 RPM	368 RPM	368 RPM
Deviation %	-38.4%	-44.9%	-42.9%	-42.9%
x_{susp} (N_{js} CFD)	0.87	0.89	0.90	0.88

Tab. 5.2: N_{js} predictions: *Particle bed height method* case.

Tab. 5.2 shows that the predicted values of just off-bottom suspension speed are very lower than the expected ones. In addition, experimental snapshots of the investigated vessel (not shown here) for all the three cases shows that unsuspended particles were still present at impeller speeds higher than those at which the particle bed height reached the zero value.

Concluding, also this method cannot be considered suitable for N_{js} predictions via CFD.

5.4.3 Power Number method

The *Power Number method* needs the calculation of power requirements at a given agitation speed from the CFD simulations.

It is possible to calculate the power requirements from the dissipation of turbulent kinetic energy ϵ , which is directly provided by the k- ϵ turbulence model in each computational cell. Unfortunately, this procedure often leads to largely underestimated values of mechanical power. In fact, it is well known in literature and it was already discussed in Chapter 4 that the k- ϵ turbulence model underestimates the dissipation of turbulence kinetic energy.

A second methodology is on the contrary based on the torque measurements. More precisely, each CFD simulation directly provides the values of the torque on

each boundary of the system: by summing the torque acting on impeller and shaft and by multiplying this sum by the angular speed it is possible to get the value of the mechanical power.

In this Chapter 5, the second methodology was adopted and relevant results are shown in Figs 5.6 and 5.7.

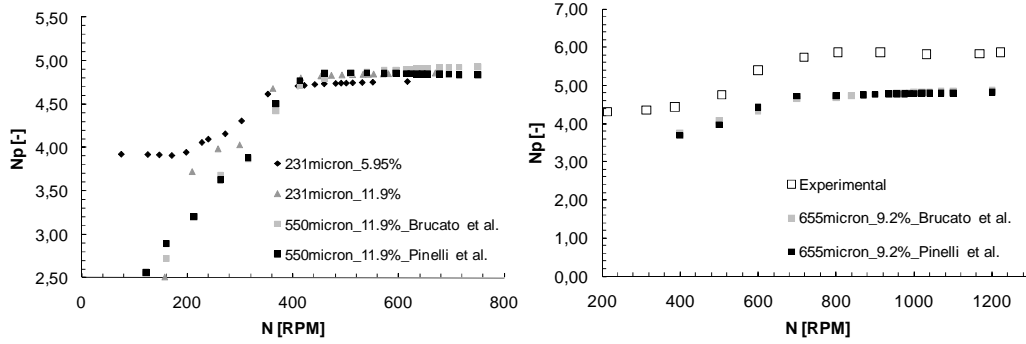


Fig. 5.6: Power Number vs impeller speed (N_p calculated by the density of suspension)

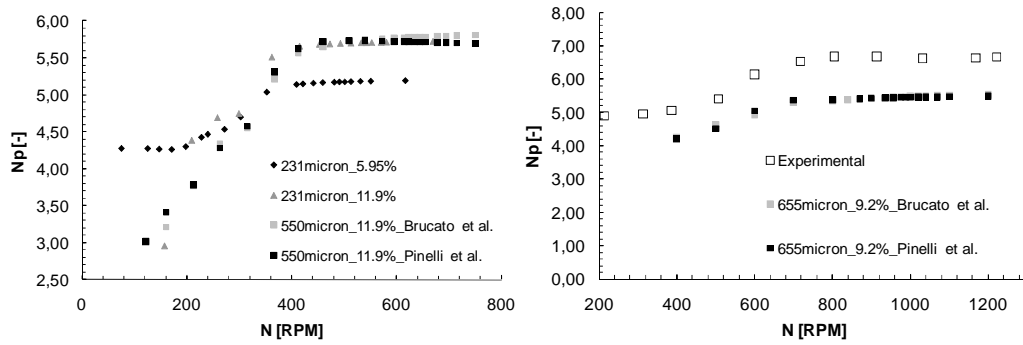


Fig. 5.7: Power Number vs impeller speed (N_p calculated by the density of liquid)

As observed by Micheletti et al. (2003) the adoption of the suspension density for the calculation of Power Number leads all the curves at different concentration to approach a similar value at high impeller speeds. The N_p values obtained appear to be reasonable. In particular the N_p predictions for the case of Micheletti et al. (2003) are compared with their relevant experimental data in the same figures: the experimental and computational trends are practically the same even if a certain underestimation of experimental data is observable. In this regard, it is important to underline that this under-prediction of experimental power number is a typical problem of CFD simulations adopting the k- ϵ turbulence model. As an example, Kasat et al. (2008) and Panneerselvam et al. (2008) found computational values of N_p lower than 4 for a standard geometry stirred tank stirred by a Rushton turbine whose typical N_p is higher than 5.

Notably, the trend is the most important information for N_{js} predictions, conversely, the specific values of N_p are not important for the present aim.

These trend do not present any minimum or maximum, therefore the predicted N_{js} should be defined as the minimum impeller speed at which N_p approaches some constant value. Unfortunately, the N_p trends depicted in the former figures do not “strictly” approach a constant value. In some of the presented cases N_p seems to continuously increase with N . A similar behavior is also observable in Kasat et al. (2008) data.

Although this increase is quite low, it makes it difficult to adopt the former criterion for N_{js} assessment. This problem was addressed and a modified criterion was proposed: N_{js} was defined as the minimum impeller speed at which the first derivative of the function $N_p = N_p(N)$ approaches a constant and very low value (Fig. 5.8).

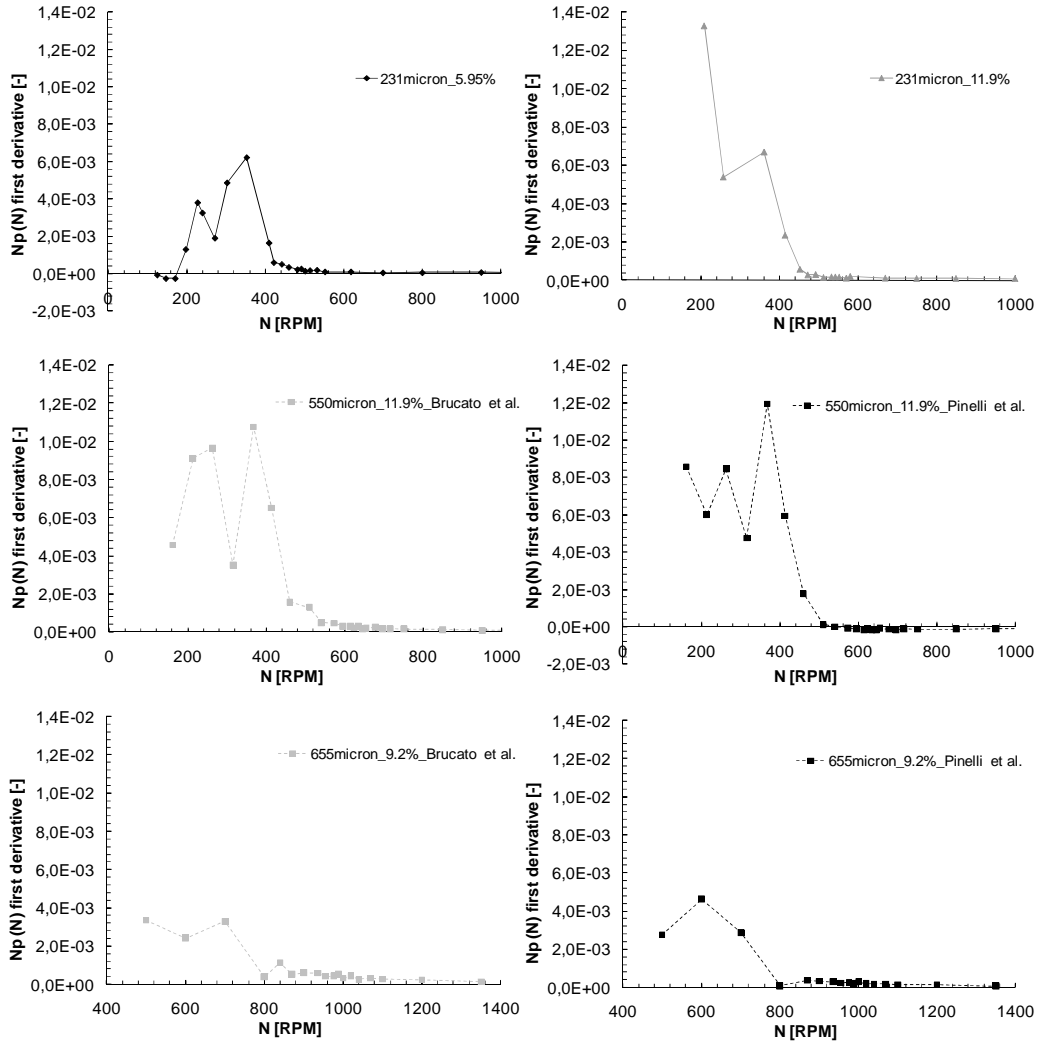


Fig. 5.8: First derivative of N_p vs N

Notably, a rigorous procedure would require the definition of the quoted “very low value”, which, in its turn, would inevitably lead to an arbitrary choice.

By the way, results of the proposed modified criterion are shown in Tab. 5.3.

	231 μm 5.95% ^{v/v}	231 μm 11.9% ^{v/v}	550 μm 11.9% ^{v/v} Brucato et al. correlation	550 μm 11.9% ^{v/v} Pinelli et al. correlation
N_{js} Zwietering	492 RPM	543 RPM	645 RPM	645 RPM
N_{js} CFD	500 RPM	500 RPM	600 RPM	600 RPM
Deviation %	+1.6%	-7.9%	-7.0%	-7.0%
$x_{\text{susp}} (N_{js} \text{ CFD})$	~ 1.00	~ 0.99	~ 0.99	~ 0.99

	Micheletti et al. (2003) Brucato et al. correlation	Micheletti et al. (2003) Pinelli et al. correlation
N_{js} Zwietering	988 RPM	988 RPM
N_{js} CFD	1040 RPM	960 RPM
Deviation %	+5.3%	-2.8%
$x_{\text{susp}} (N_{js} \text{ CFD})$	~ 1.00	~ 0.99

Tab. 5.3: N_{js} predictions: *Power Number method* case.

All the predicted N_{js} values agree quite well with the relevant Zwietering's ones, with a maximum deviation smaller than 8%. In addition all the suspended solid fractions are larger than 0.99 thus confirming that the criterion correctly predicts the achievement of complete suspension conditions.

Despite the arbitrary choice required by the modified criterion, *Power Number method* guarantees good predictions. Unresolved doubts about this method concern this arbitrary choice as well as the shape of N_p versus N curves which can be different for different systems thus negatively affecting the universality of the method.

5.4.4 Local Particle Concentration method

The present method makes use of the solid volumetric fraction variation with impeller speed. The first point to be taken into account concerns the choice of the monitoring points for solid volume fraction assessment. As already written in the literature review section, some authors stated that N_{js} predictions via *local particle concentration method* are independent of the position of monitoring points. Conversely, other authors disagreed with this point.

The choice made here was that of monitoring solid volumetric fraction variation with impeller speed at several positions, namely:

- the same positions adopted by Bourne and Sharma in their work (1974);
- the same position monitored by Kee and Tan (2002) in their work;
- the same positions chosen by Wang et al. (2004) in their work.

A total of seven different points were therefore considered for the monitoring, all azimuthally placed midway two subsequent baffles. In Fig. 5.9 it is possible to observe the exact positions of the monitoring points.

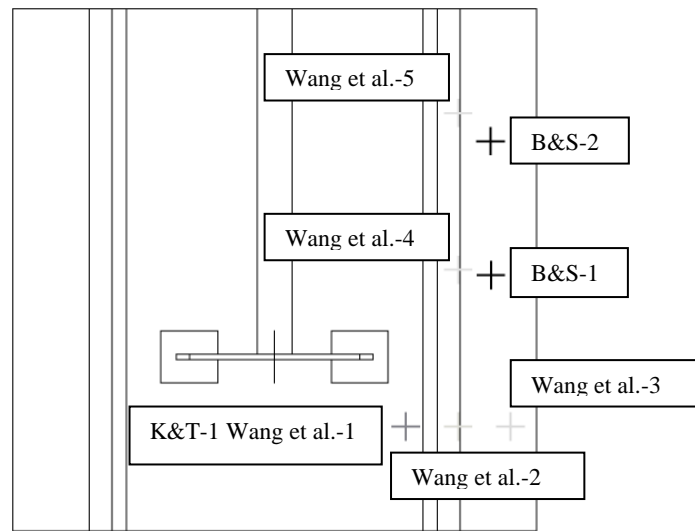
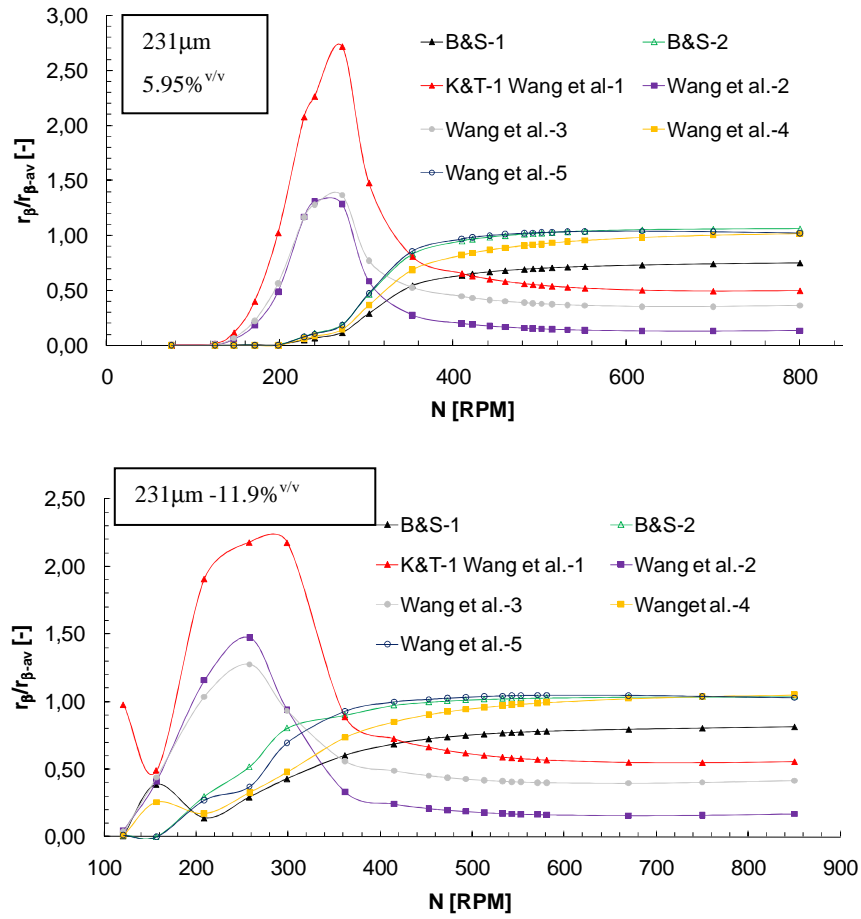
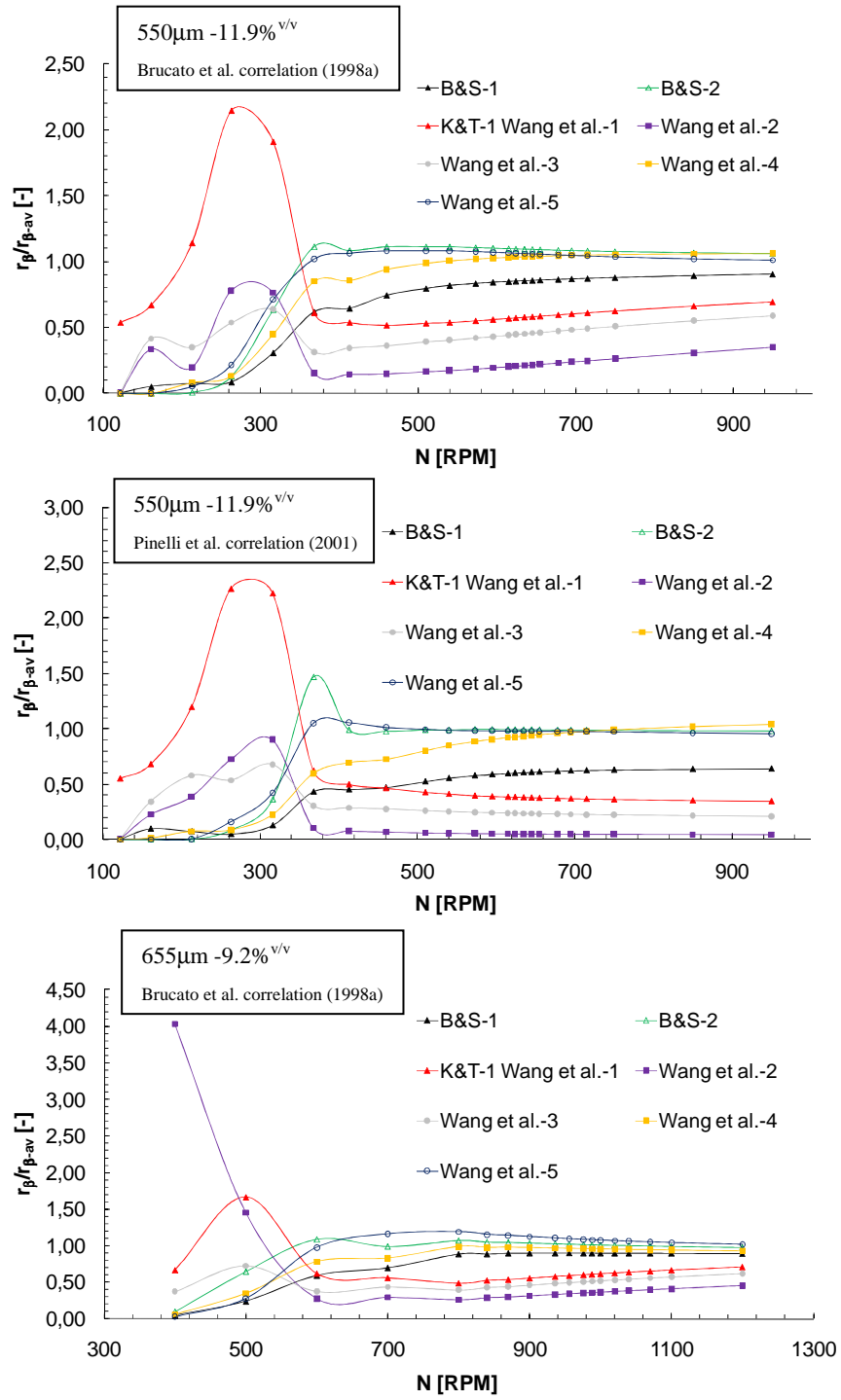


Fig. 5.9: Monitor point position and definition

As it can be observed, the point chosen by Kee and Tan (2002) coincides with one of the points adopted by Wang et al. (2004).

The trends of normalized solid volumetric fractions versus impeller speeds at all points for all the investigated cases are showed in Fig.5.10.





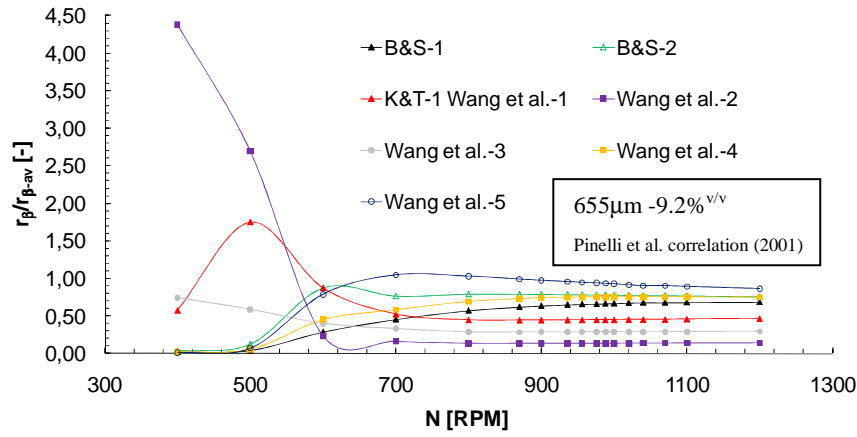


Fig. 5.10: Normalized solid volume fractions versus impeller speed at the established monitor points

All the graphs of Fig.5.10 show that the trend is dependent on the position of the monitor point: in particular, for each investigated case, some of the curves have a maximum that occurs at different impeller speeds (only the curve of 231 μ m cases show relative maxima at the same impeller speed), while other curves show no increasing-decreasing behaviour. Moreover, the maxima occur at very low impeller speeds which are far from the complete suspension conditions. In this regard, Rieger and Dittl (1994) observed that, in all investigated cases, the maximum concentration is reached at an impeller speed lower than N_{js} . The same authors concluded that the *local particle concentration method* is not suitable for assessing just off-bottom suspension speed.

As an alternative, observing Fig. 5.10, one may think to define N_{js} as the minimum impeller speed at which all the solid volumetric fractions attain some final constant value. In this case, the assessed N_{js} values would be closer to the expected ones. Actually, in some cases r_β appears to change indefinitely with N , without approaching any constant value. In addition, in systems where homogeneous suspension conditions are achievable, r_β is expected to change with N up to the

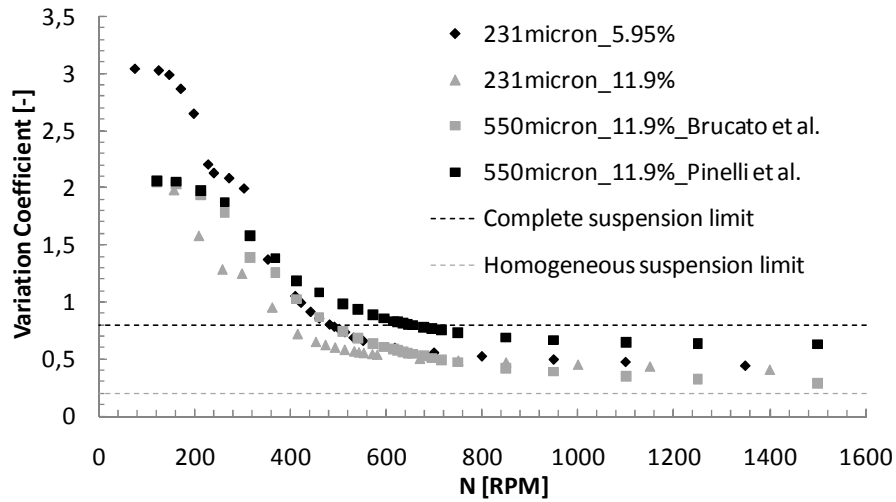
attainment of this regime where in all the computational cells r_β should approach the final mean volume fraction $r_{\beta_{av}}$.

The above results suggests that the *local particle concentration method* for N_{js} predictions is not applicable to all system configurations.

5.4.5 Variation Coefficient method

This method requires the calculation of the variation coefficient σ by means of equation 5.1 (Bohnet and Niesmak, 1980). The variation coefficient was calculated using the values of r_β stored at all computational cells, but for the cells belonging to the shaft and to the impeller (where no fluid or particles are present).

The predicted values of σ at different impeller speeds are shown in Fig. 5.11 where the horizontal lines represent the threshold values proposed in the literature to characterize the different suspension regimes.



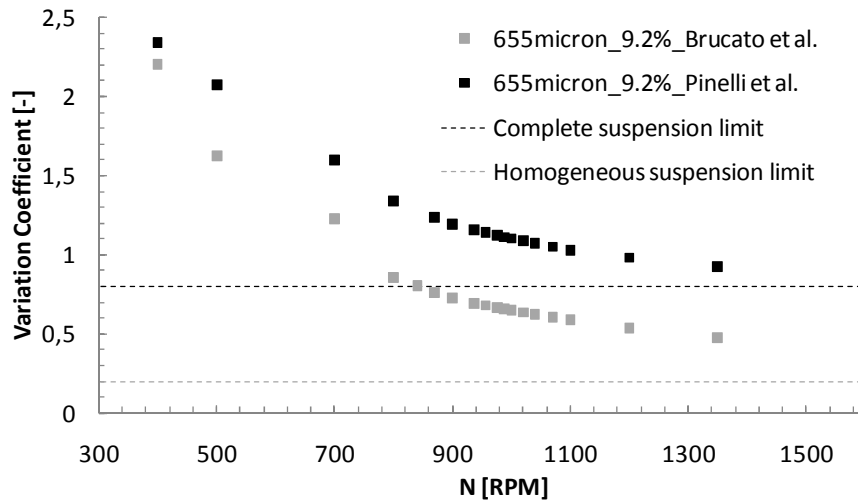


Fig. 5.11: Variation coefficient versus impeller speed.

The figure shows that all the cases but one (655mm, 9.2%, Pinelli et al. correlation) attain complete suspension conditions at high impeller speeds as the corresponding σ are lower than the 0.8 cut off value.

Murthy et al. (2007) observed a sharp reduction of σ when the impeller speed approaches N_{js} , but this is not the case for the present results. However, defining N_{js} as the minimum impeller speed at which a sharp reduction of the trend σ versus N is observed could lead to arbitrary choices or to imprecise values of N_{js} .

Being $\sigma = 0.8$ the cut-off value between incomplete and complete suspension regime, N_{js} was defined as the minimum impeller speed able to guarantee a $\sigma = 0.8$.

Relevant results are summarized in Tab. 5.4.

	231 μ m 5.95% ^{v/v}	231 μ m 11.9% ^{v/v}	550 μ m 11.9% ^{v/v} Brucato et al. correlation	550 μ m 11.9% ^{v/v} Pinelli et al. correlation
--	-------------------------------------	-------------------------------------	--	--

N_{js} Zwietering	492 RPM	543 RPM	645 RPM	645 RPM
N_{js} CFD	485 RPM	400 RPM	485 RPM	650 RPM
Deviation %	-1.4%	-26.3%	-24.8%	+0.8%
x_{susp} (N_{js} CFD)	~0.99	~0.98	~0.98	~1.00

	Micheletti et al. (2003) Brucato et al. correlation	Micheletti et al. (2003) Pinelli et al. correlation
N_{js} Zwietering	988 RPM	988 RPM
N_{js} CFD	840 RPM	>1'350 RPM
Deviation %	-15.0%	>+36.6%
x_{susp} (N_{js} CFD)	~0.99	1.00

Tab. 5.4: N_{js} predictions: *Variation Coefficient method* case.

They show that good predictions are obtainable in some cases, while in others, large deviations from Zwietering's values are present. Particularly, for Micheletti et al. (2003) system modelled by means of Pinelli et al. correlation (2001) it is not possible to assess any N_{js} value for the investigated range of impeller speeds. It is worth noting that in the case of 231 μ m-11.9%, even though a deviation higher than 25% was found, the fraction of suspended solids was about 0.98 thus suggesting that despite the underestimation of N_{js} the resulting operating condition would not be unreasonable.

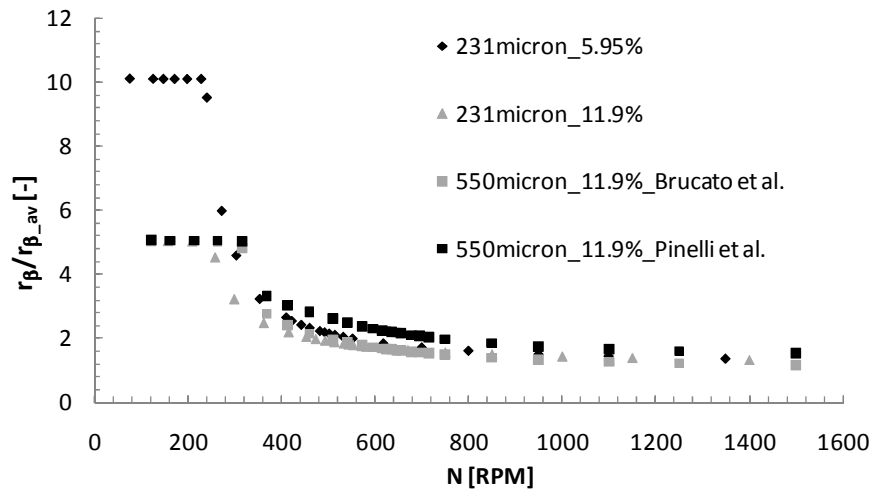
As far as the *Variation Coefficient method* reliability is concerned, both Kasat et al. (2008), Rieger and Dittl (1994) and Rieger et al. (1988) found that the values of σ achieved at N_{js} in different cases differ significantly. Similarly, Panneerselvam et al. (2008) found the same results for a three phase system. In particular Rieger and Dittl (1994) judged the present method as being unsuitable for determining complete off-bottom suspension speed.

A rigorous procedure, as that of Murthy et al. (2007), would require the evaluation of the Variation Coefficient value at the experimentally assessed N_{js} for

given system properties and configuration. Successively, this “validated” σ could be used to predict N_{js} for similar systems. Being this procedure not fully predictive, it cannot be considered as a universally acceptable method for N_{js} predictions.

5.4.6 Mak (1992) and Hosseini et al. (2010b) or Intersection method

As already described in section 5.2.14, the present method makes use of average solid volume fractions at 1millimetre height from vessel bottom. This value is plotted against impeller speed as shown in Fig. 5.12 for all the cases here investigated.



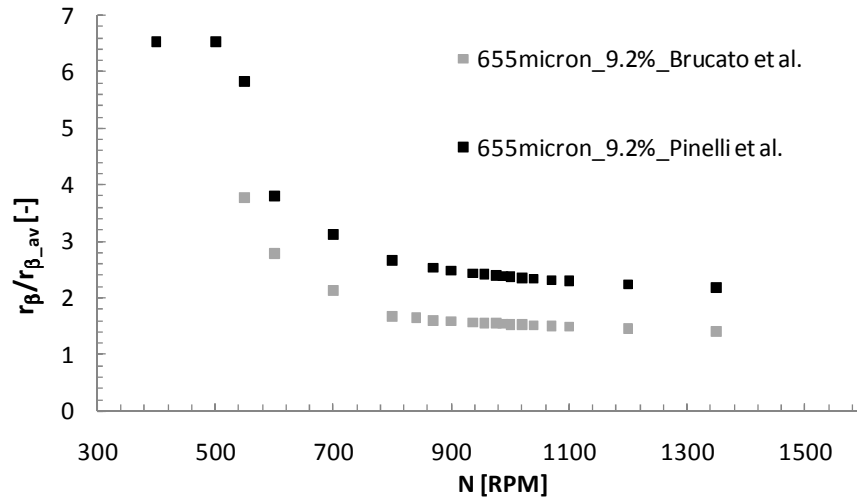


Fig. 5.12: Normalized solid volume fraction versus impeller speed.

The N_{js} assessment methodology based on the data of Fig. 5.12 is described in Fig. 5.13: the abscissa of the intersection point represents the N_{js} value predicted by the present method.

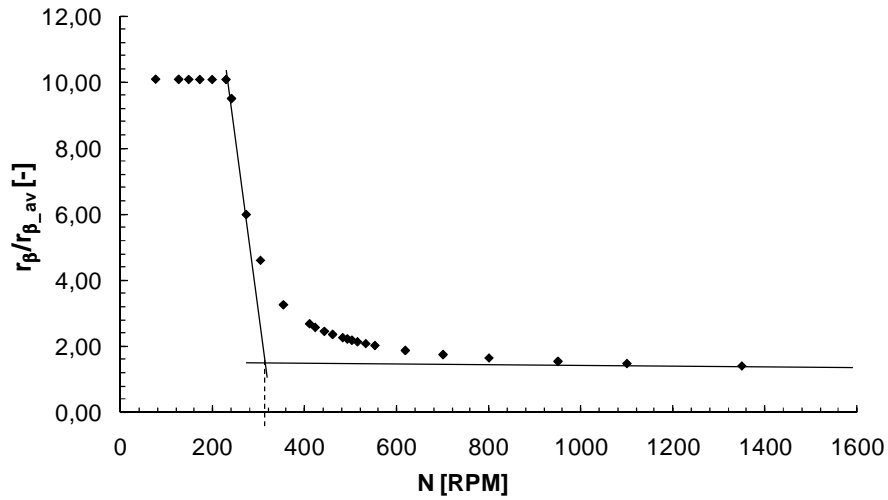


Fig. 5.13: N_{js} prediction methodology (231 μ m-5.95%^{v/v} case).

This procedure was applied to all the investigated cases and corresponding results are showed in Tab.5.5

	231 μ m 5.95% ^{v/v}	231 μ m 11.9% ^{v/v}	550 μ m 11.9% ^{v/v} Brucato et al. correlation	550 μ m 11.9% ^{v/v} Pinelli et al. correlation
N_{js} Zwietering	492 RPM	543 RPM	645 RPM	645 RPM
N_{js} CFD	315 RPM	360 RPM	420 RPM	420 RPM
Deviation %	-36.0%	-33.7%	-34.9%	-34.9%
x_{susp} (N_{js} CFD)	~0.94	~0.97	~0.96	~0.93

	Micheletti et al. (2003) Brucato et al. correlation	Micheletti et al. (2003) Pinelli et al. correlation
N_{js} Zwietering	988 RPM	988 RPM
N_{js} CFD	590 RPM	635 RPM
Deviation %	-40.3%	-35.7%
x_{susp} (N_{js} CFD)	~0.89	~0.89

Tab. 5.5: N_{js} predictions: *Intersection method* case.

The table shows that for all the investigated cases very large under-prediction of N_{js} were found thus suggesting the inapplicability of the present method for systems agitated by a standard Rushton turbine. Actually, both Mak (1992) and Hosseini et al. (2010b) applied this N_{js} assessment procedure to systems stirred by axial impellers like the Lightnin A100 (marine propeller), A200 (pitched blade turbine) and A310 (high efficiency propeller).

Moreover, the fraction of suspended solids at the assessed N_{js} are too low thus suggesting that complete off-bottom suspension conditions are far from being achieved.

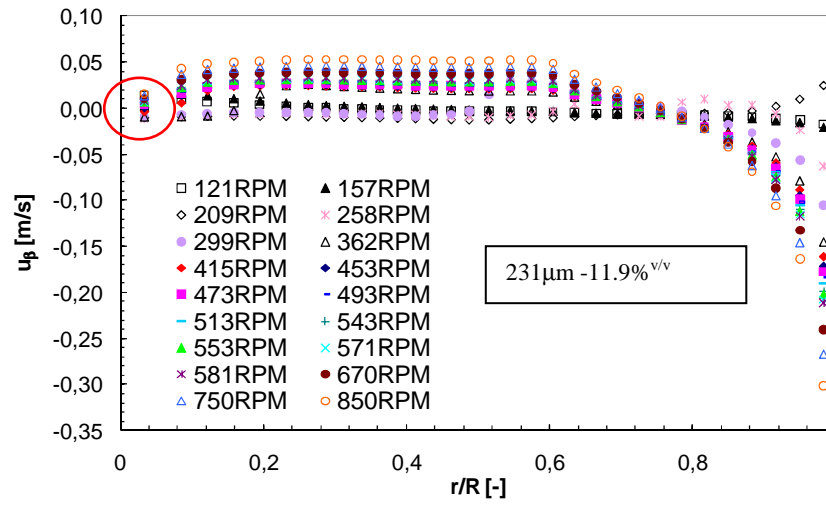
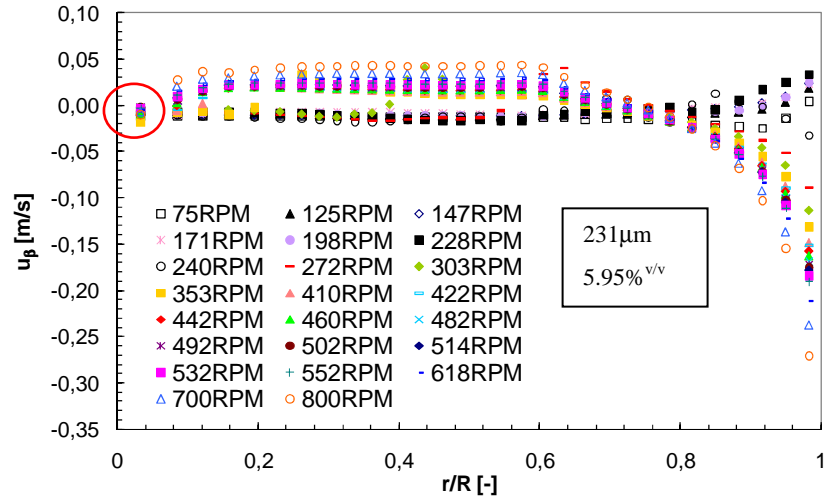
Concluding, the *Intersection method* cannot be considered successfully applicable to all vessel-impeller combinations for N_{js} predictions via CFD.

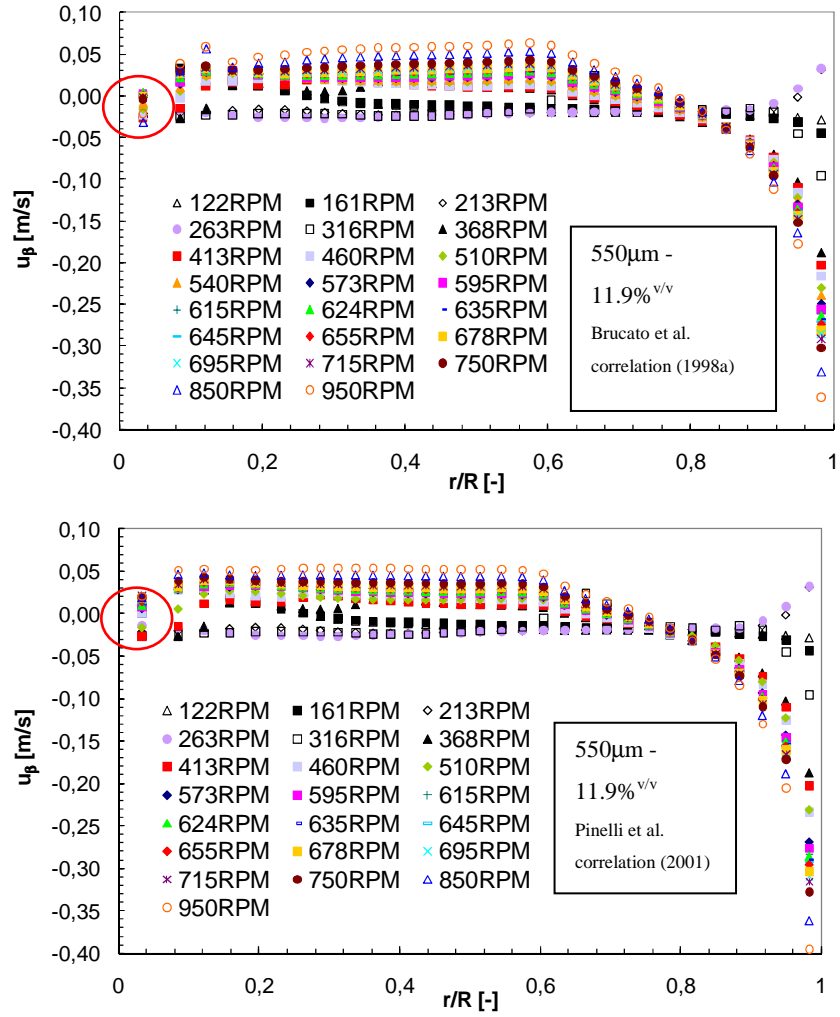
5.4.7 Wang et al. (2004) or Particle Axial Velocity method

In accordance with this method proposed by Wang et al. (2004), N_{js} is defined as the minimum impeller speed at which the particle axial velocity is found to be positive in the “final suspension region”. This region represents the area on the vessel bottom from which the last resting particles get suspended. All the investigated cases here presented are relevant to standard geometry tanks equipped by a Rushton turbine with $D=T/2$, so that the “final suspension region” is located at the centre of the vessel bottom.

Therefore, in order to assess the reliability of the present method, radial profiles of solid axial velocity on the vessel bottom are provided (as prescribed by Wang et al., 2004) and they are shown in Fig. 5.14. It is worth noting that these radial profiles are taken at a middle point between two subsequent baffles. Notably, azimuthally averaged radial profiles provide the same N_{js} predictions.

Observing each of these profiles (starting from the one at the lowest impeller speed) in correspondence of the zone indicated by the red circle (in Fig. 5.14) it is possible to recognize the first profile where u_β in this zone is positive. If also the u_β of the following profiles (i.e. those relevant to higher impeller speeds) are positive, the impeller speed corresponding to the first profile is considered as N_{js} .





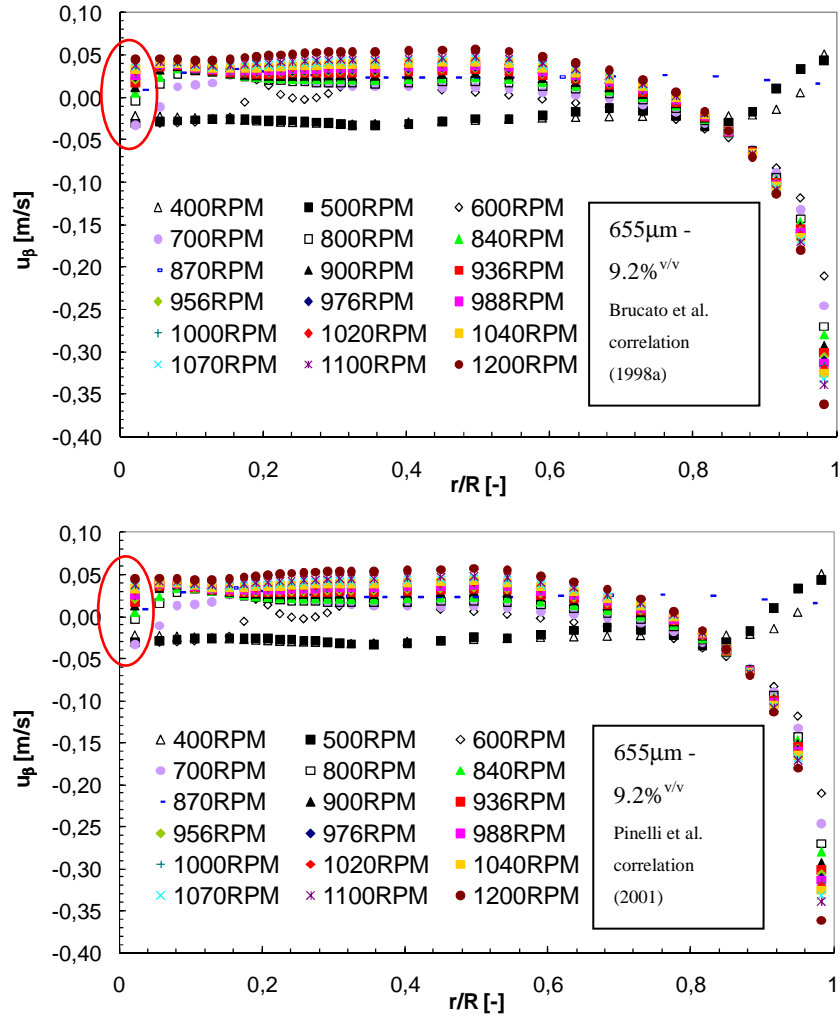


Fig. 5.14: u_β radial profiles midway two subsequent baffles.

As an example, two profiles of the 231 μm - 11.9% v/v case are separately shown in Fig. 5.15, the one at an impeller speed below N_{js} , the other exactly at N_{js} .

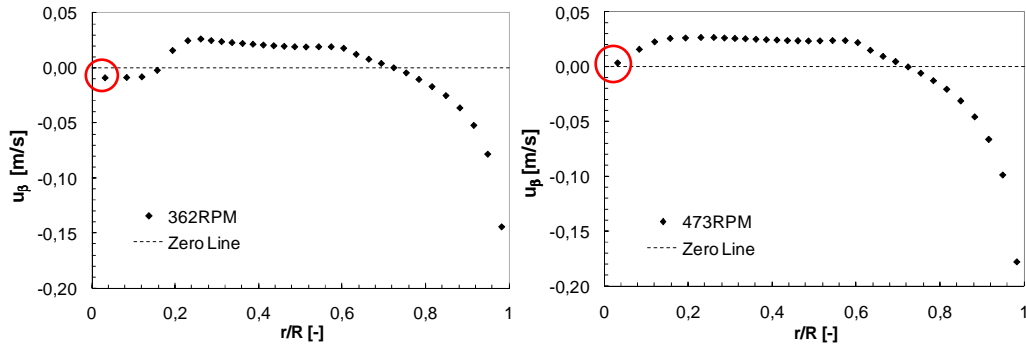


Fig. 5.15: 231 μm -11.9%^{v/v} case: two u_β radial profiles midway two subsequent baffles showed as example. On the left the profile at a $N < N_{js}$; On the right the profile at $N = N_{js}$.

As a matter of fact, some radial profiles (the ones corresponding to low impeller speeds) shown in Fig.5.14 showed a solid axial velocity which is positive at a radial position close to the lateral wall. This finding is not surprising: in fact, when the impeller speed is quite low, most particles rest on the bottom thus reducing the effective impeller clearance (false bottom effect). As already seen in Chapter 4, this occurrence leads the flow field to a single loop configuration. Particularly, velocity vectors move obliquely downwards from the impeller blade, reach the bottom and then they move upwards when the lateral wall is reached.

	231 μm 5.95% ^{v/v}	231 μm 11.9% ^{v/v}	550 μm 11.9% ^{v/v} Brucato et al. correlation	550 μm 11.9% ^{v/v} Pinelli et al. correlation
N_{js} Zwietering	492 RPM	543 RPM	645 RPM	645 RPM
N_{js} CFD	>800 RPM	473 RPM	595 RPM	573 RPM
Deviation %	>62.6%	-12.9%	-7.7%	-11.2%
x_{susp} (N_{js} CFD)	-----	~0.99	~0.99	~0.99

	Micheletti et al. (2003) Brucato et al. correlation	Micheletti et al. (2003) Pinelli et al. correlation
N_{js} Zwietering	988 RPM	988 RPM
N_{js} CFD	840 RPM	700 RPM
Deviation %	-15.0%	-29.1%
$x_{susp}(N_{js} \text{ CFD})$	~ 0.99	~ 0.96

Tab. 5.6: N_{js} predictions: *Particle Axial Velocity method* case.

The predicted N_{js} values are lower than the expected ones, but deviations are not so high. More precisely, the cases where the effect of free stream turbulence on the drag coefficient was modelled by the Pinelli et al. correlation (2001) show a higher deviation up to 30% for the Micheletti et al. (2003) system case. In addition, it was not possible to assess any N_{js} value in the case of the lowest solid loading case since the particle axial velocity showed a negative value on the centre of the vessel bottom for all the investigated impeller speeds.

This finding suggests that there are some cases for which the present method cannot be applied.

This method requires the exact knowledge of the exact zone from which the last resting particles get suspended. In the case of a standard geometry tank stirred by a Rushton turbine, this area is well known. Conversely, this area will be completely unknown (without corresponding experimental data) if an unusual impeller and/or an uncommon impeller position are employed. Fortunately, the CFD model of Chapter 4 (here coupled with the present N_{js} assessment method) was demonstrated suitable to predict quantity and position of unsuspended solid particles, thereby allowing the knowledge of the position from which the last motionless particles get suspended.

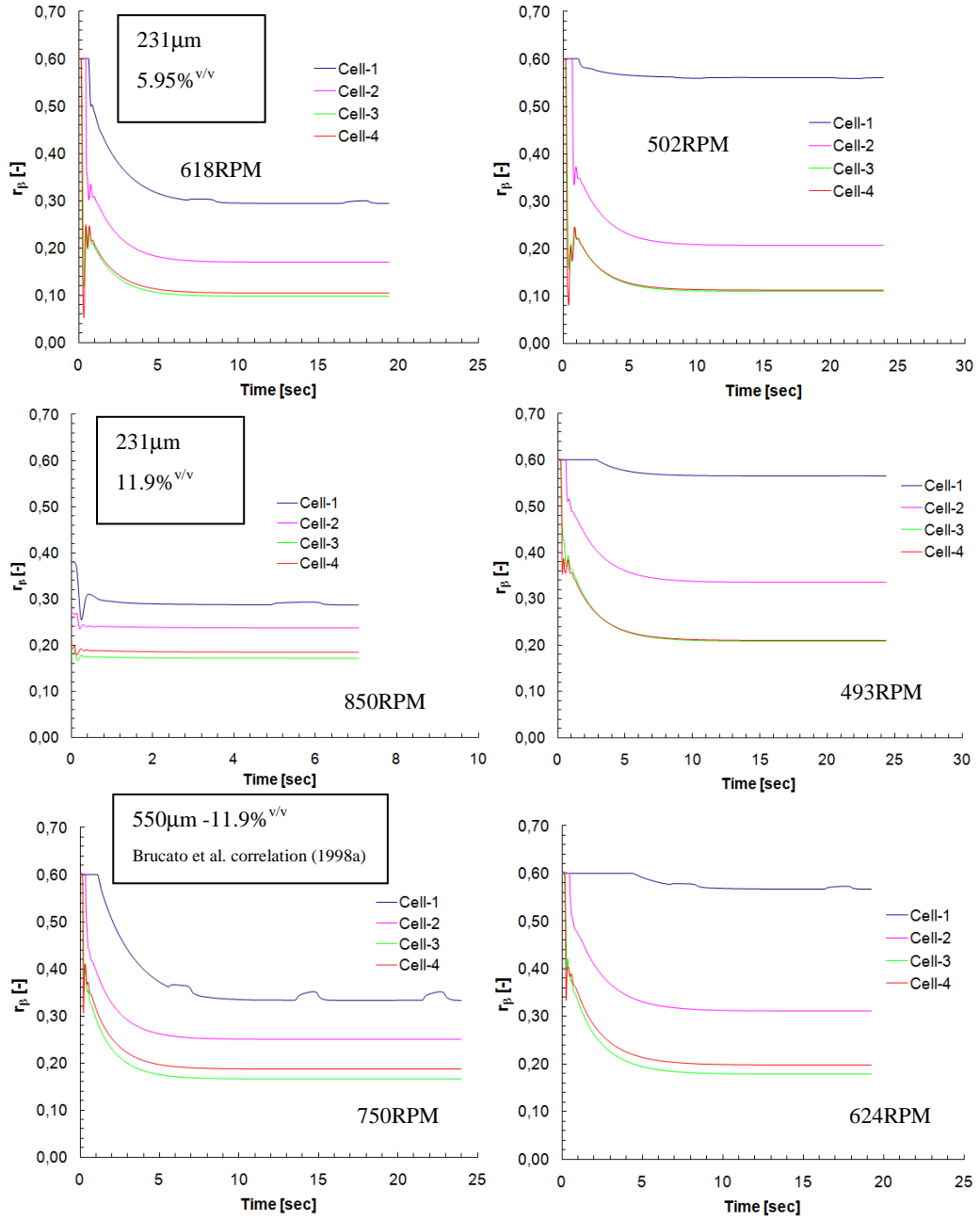
5.4.8 Kee and Tan (2002) or Transient r_β Profile method

This method is based on the monitoring of r_β with time. In particular only some cells placed on the vessel bottom are monitored during transient. All these cells are placed midway two subsequent baffles and belong to the first axial row cells, i.e. they belong to the group of cells which are located just on the bottom. The radial position of these computational cells is defined in the following:

- cell-1 position: (axial; radial) = (0; 0);
- cell-2 position: (axial; radial) = (0; T/8);
- cell-3 position: (axial; radial) = (0; 3T/8);
- cell-4 position: (axial; radial) = (0; T);

In accordance with Kee and Tan (2002) criterion, the first condition that has to be fulfilled is that a constant steady-state value is attained by r_β at all selected locations. As far as the second condition is concerned, the final constant values assumed by all four r_β values must be smaller than about half of the maximum particle packing value $r_{\beta-packed}$. In this regard, it should be kept in mind that $r_{\beta-packed}=0.6$.

N_{js} is defined as the minimum impeller speed at which both of the above conditions are fulfilled. The r_β dynamics at the predicted N_{js} are shown on the left of Fig. 5.16.



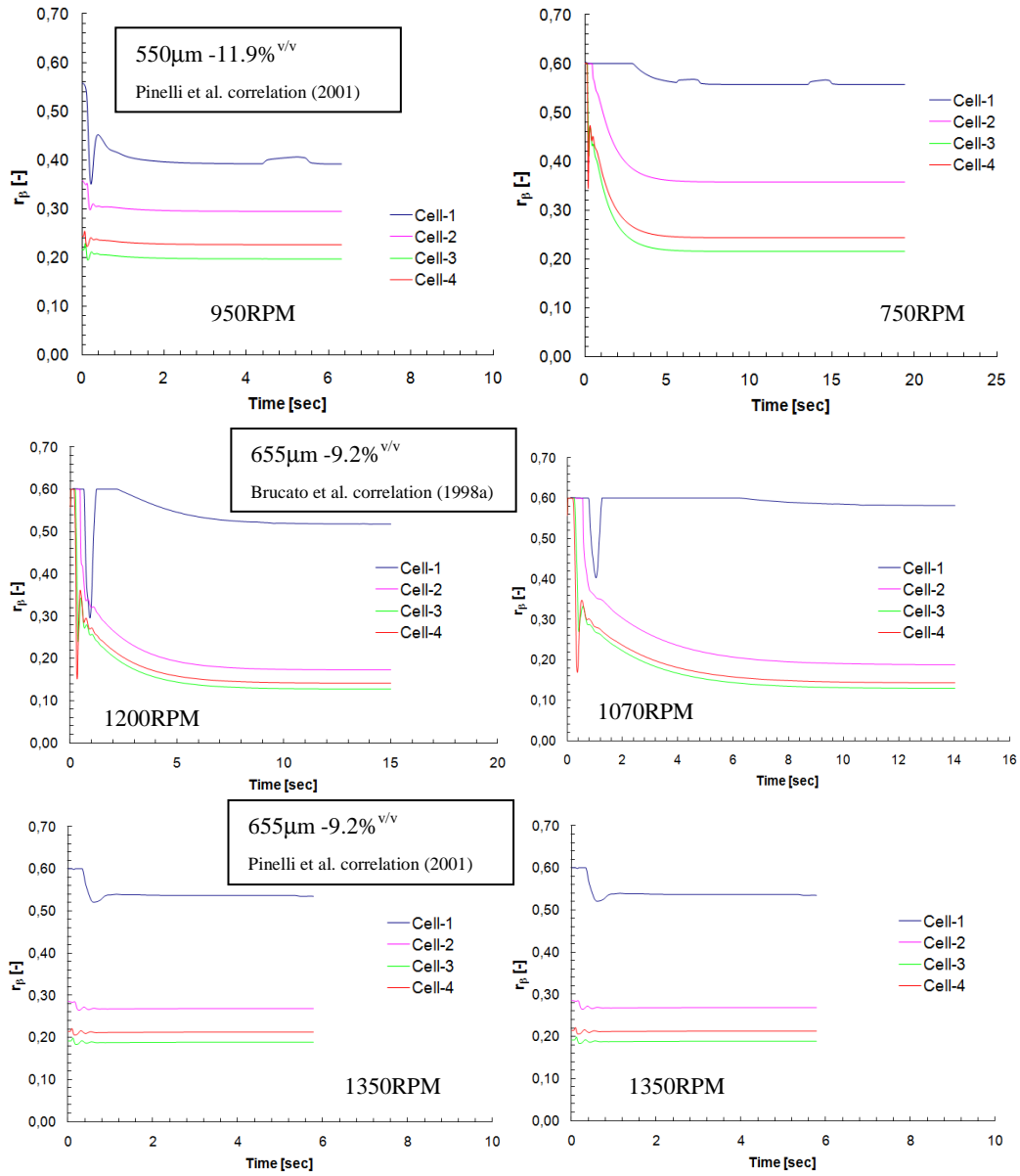


Fig. 5.16: r_{β} transient concentrations on 4 bottom locations midway between two subsequent baffles. Left: concentration dynamics at the N_{js} assessed by Kee and Tan (2002) criterion; Right: concentration dynamics at the N_{js} assessed according to the *modified* Kee and Tan (2002) criterion.

Results deriving from the application of Kee and Tan (2002) criterion are summarized in Tab. 5.7.

	231 μ m 5.95% ^{v/v}	231 μ m 11.9% ^{v/v}	550 μ m 11.9% ^{v/v} Brucato et al. correlation	550 μ m 11.9% ^{v/v} Pinelli et al. correlation
N_{js} Zwietering	492 RPM	543 RPM	645 RPM	645 RPM
N_{js} CFD	618 RPM	850 RPM	~750 RPM	>950 RPM
Deviation %	+25.6%	+56.5%	+16.3%	>+47.3%
x_{susp} (N_{js} CFD)	1.00	1.00	1.00	1.00

	Micheletti et al. (2003) Brucato et al. correlation	Micheletti et al. (2003) Pinelli et al. correlation
N_{js} Zwietering	988 RPM	988 RPM
N_{js} CFD	>1200 RPM	>1350 RPM
Deviation %	>+21.5%	>+36.6%
x_{susp} (N_{js} CFD)	1.00	1.00

Tab. 5.7: N_{js} predictions: *Transient r_β Profile method*.

As it can be seen, in some cases, no N_{js} was found for the impeller speeds here investigated: other CFD simulations at higher impeller speeds should be carried out in order to assess the relevant N_{js} values, but being these values much higher than the expected ones, their exact assessment was not considered useful. As a difference from all the other methods reviewed so far, results of Fig. 5.7 show that the predicted N_{js} values are significantly overestimated, with deviations even higher than 50%. Notably such strong overestimations in N_{js} values would result in unacceptable

over-sizing of power consumption, being the mechanical power dependent on the cube of impeller speed.

In relation to these findings, a *Modified Kee and Tan Criterion* was proposed. N_{js} was defined as the minimum impeller speed at which all the r_β profiles are steady and show a value just lower than the maximum packing one $r_{\beta-packed}$.

It may be noted that the previous choice of half of $r_{\beta-packed}$ as the threshold value clearly introduces an arbitrary choice which significantly affects the objectivity of the method. The modified criterion addresses and resolves this issue.

The transient r_β profiles at the assessed N_{js} are showed on the right of Fig. 5.16 and corresponding results are summarized in Tab. 5.8.

	231 μ m 5.95% ^{v/v}	231 μ m 11.9% ^{v/v}	550 μ m 11.9% ^{v/v} Brucato et al. correlation	550 μ m 11.9% ^{v/v} Pinelli et al. correlation
N_{js} Zwietering	492 RPM	543 RPM	645 RPM	645 RPM
N_{js} CFD	502 RPM	493 RPM	624 RPM	750 RPM
Deviation %	+2.0%	-9.2%	-3.2%	+16.3%
x_{susp} (N_{js} CFD)	~1.00	~0.99	~0.99	~1.00

	Micheletti et al. (2003) Brucato et al. correlation	Micheletti et al. (2003) Pinelli et al. correlation
N_{js} Zwietering	988 RPM	988 RPM
N_{js} CFD	1070 RPM	1350 RPM
Deviation %	+8.3%	+36.6%
x_{susp} (N_{js} CFD)	~1.00	1.00

Tab. 5.8: N_{js} predictions: *Modified Transient r_β Profile method* case.

Tab. 5.8 shows that the modified criterion leads to quite good results, as deviations of N_{js} predictions are below 10%. In accordance with this criterion, the adoption of the Pinelli et al. correlation (2001) to model the effect of turbulence on drag coefficient leads to less satisfactory predictions especially in the Micheletti et al. case (2003). The suspended solid fraction values confirm the viability of the modified criterion that can be considered suitable to assess N_{js} via CFD. A drawback of the method concerns the need of performing transient simulations so resulting in high computational costs, especially if several impeller speeds are investigated during N_{js} assessment.

5.4.9 Unsuspended Solid Criterion method

This innovative method was purposely proposed in this Chapter 5: it is based on the *Unsuspended Solid Criterion (USC)* defined in Chapter 4. In accordance with this method, N_{js} is defined as the minimum impeller speed at which the fraction of suspended solids x_{susp} reaches the value of 1.0. Results are shown in Tab. 5.9:

	231 μ m 5.95% ^{v/v}	231 μ m 11.9% ^{v/v}	550 μ m 11.9% ^{v/v} Brucato et al. correlation	550 μ m 11.9% ^{v/v} Pinelli et al. correlation
N_{js} Zwietering	492 RPM	543 RPM	645 RPM	645 RPM
N_{js} CFD	510 RPM	~620 RPM	678 RPM	850 RPM
Deviation %	+3.6%	+14.2%	+5.1%	+31.8%
x_{susp} (N_{js} CFD)	1.00	1.00	1.00	1.00

	Micheletti et al. (2003) Brucato et al. correlation	Micheletti et al. (2003) Pinelli et al. correlation
N_{js} Zwietering	988 RPM	988 RPM
N_{js} CFD	1085 RPM	~1300 RPM
Deviation %	+9.8%	+31.6%

x_{susp} (N_{js} CFD)	1.00	1.00
----------------------------	------	------

Tab. 5.9: N_{js} predictions: *Unsuspected Solid Criterion method* case.

Results are quite satisfactory and very similar to the *Modified Transient r_β Profiles method* (with the exception of 231 μ m, 11.9%) thus suggesting that the two methods are practically based on similar criteria. Also with the *USC method*, N_{js} predictions worsen when the Pinelli et al. correlation (2001) is employed.

It is worth observing that the suspension of the last few particles requires a notable increase of impeller speed. In fact, different results will be obtained if $x_{susp}=0.999$ is adopted as “*alternative*” *USC method*. Such results are depicted in Tab. 5.9.

	231 μ m 5.95% ^{v/v}	231 μ m 11.9% ^{v/v}	550 μ m 11.9% ^{v/v} Brucato et al. correlation	550 μ m 11.9% ^{v/v} Pinelli et al. correlation
N_{js} Zwietering	492 RPM	543 RPM	645 RPM	645 RPM
N_{js} CFD	507 RPM	473 RPM	624 RPM	740 RPM
Deviation %	+3.0%	-12.9%	-3.2%	+14.7%
x_{susp} (N_{js} CFD)	0.999	0.999	0.999	0.999

	Micheletti et al. (2003) Brucato et al. correlation	Micheletti et al. (2003) Pinelli et al. correlation
N_{js} Zwietering	988 RPM	988 RPM
N_{js} CFD	870 RPM	1025 RPM
Deviation %	-11.9%	+3.7%
x_{susp} (N_{js} CFD)	0.999	0.999

Tab. 5.9: N_{js} predictions: *Alternative Unsuspended Solid Criterion method* case.

Alternative Unsuspended Solid Criterion method is able to provide satisfactory results as well, even if the Pinelli et al. correlation (2001) is adopted. The comparison of Tab.5.8 and Tab. 5.9 results confirm the former consideration: the final suspension of negligible amounts of unsuspended solids can require large increase of impeller speed thus suggesting that high deviations from the expected values of N_{js} could be represented by very small percentage of unsuspended particles.

On one hand, this finding suggests that different criteria can provide satisfactory results, in fact, even though prediction deviations are large, little differences in corresponding unsuspended particle amounts can be easily found. On the other hand, little increases of the impeller speed adopted lead to energy dissipations much larger than minimum requirements.

Using CFD to predict “exactly” N_{js} is an optimization problem that would be computationally expensive (a lot of CFD simulations have to be carried out to assess the “exact” value) and often not reliable as large mistakes can be made in dependence on the method adopted for N_{js} prediction.

An alternative criterion to characterize solid-liquid suspension is needed (Oshinowo and Bakker, 2002), especially if *Computational Fluid Dynamics* techniques are employed to aid design.

5.4.10 Sufficient Suspension Speed Prediction

A possible criterion which can substitute the more common one based on the N_{js} prediction was that proposed by Brucato et al. (1997) and described in the paragraph 5.2.11. The *sufficient suspension speed* N_{ss} is the design parameter close linked to the present criterion.

The model presented in Chapter 4 and utilized in this Chapter 5 for N_{js} prediction is able to provide the amount of suspended solid particles at any agitation speed. Therefore, it was employed here to predict the N_{ss} values as well.

First of all, the experimental suspension curve data presented in Chapter 4 were fitted by a Weibull function and corresponding N_{min} and N_{span} values were assessed. Then equation 5.3 was employed to calculate the experimental N_{ss} values. Eventually, the impeller speed at which the predicted $x_{susp}=0.982$ was defined as the CFD predicted N_{ss} value.

Prediction results are shown in Tab. 5.10.

	231 μ m 5.95% ^{v/v}	231 μ m 11.9% ^{v/v}	550 μ m 11.9% ^{v/v} Brucato et al. correlation	550 μ m 11.9% ^{v/v} Pinelli et al. correlation
N_{min} Experimental	145 RPM	90 RPM	125 RPM	125 RPM
N_{span} Experimental	90 RPM	160 RPM	220 RPM	220 RPM
N_{ss} Experimental	325 RPM	410 RPM	565 RPM	565 RPM
N_{ss} CFD	351 RPM	387 RPM	462 RPM	521 RPM
Deviation %	+8.0%	-5.6%	-18.2%	-7.8%
x_{susp}	0.982	0.982	0.982	0.982

Tab. 5.10: N_{ss} predictions.

This table confirms the findings of Chapter 4: the predictions are very good for the smaller particle size cases, while for the large particle size cases, Pinelli et al. correlation (2001) allows better predictions. Clearly, no predictions of the Micheletti et al. (2003) case are provided as no experimental information concerning suspension curve are available for this case.

The goodness of predictions and the huge energy savings deriving from the adoption of the *Sufficient Suspension Criterion* suggest that the present CFD model

along with such criterion could constitute a reliable tool for solid-liquid stirred tank design and operation.

5.5 Final remarks

All methods available in literature to assess the minimum suspension speed for complete off-bottom suspension were critically reviewed throughout this Chapter. In addition, some of these methods were coupled with the CFD model presented in Chapter 4 in order to provide N_{js} assessments via CFD simulations. The capability and the reliability of these CFD-assisted methods were verified and discussed aiming at finding the CFD methodology which could be universally accepted and could represent an objective design criterion applicable to all possible systems.

An original method based on the *Unsuspended Solid Criterion* of Chapter 4 was also presented and its performance discussed.

An acceptable agreement between CFD predicted N_{js} and the Zwietering's ones was found only for some N_{js} assessment methods, while all other methods failed to provide correct N_{js} values via CFD for the cases presented in this Chapter.

Particularly, most presented CFD methods under-predicted the N_{js} values calculated by Zwietering's correlation. This behaviour had already been observed by different authors. Ochieng and Lewis (2006a) and Kee and Tan (2002) stated that CFD simulations under-predicted N_{js} especially for the larger particles ($d_p > 150\mu\text{m}$) because of the erroneous CFD assumption of particle sphericity. Conversely Wang et al. (2004) attributed this underestimation to Zwietering's correlation: it is based on a visual method which always provide N_{js} values higher than strictly needed.

Collected data suggest that the prediction of the "exact" N_{js} value by means of CFD techniques can lead to dangerous conclusions. In fact, most of the adopted N_{js} assessment methodologies have a clear drawback: they are too specific. It is common to find a CFD methodology which provides good predictions only if applied to the specific case for which it was formulated. It might be sufficient to change system physical or geometrical properties to obtain completely different results. As an example, all the methods based on the particular shape of some trend

(N_p vs N , or local r_{β} vs N , etc) might be inapplicable when different impeller or impeller to tank configurations are adopted.

Moreover, just before the attainment of complete suspension conditions, a small variation of the amount of unsuspended solid particles can be obtained by a correspondingly high increase of impeller speed. This suggests that a quite precise prediction of complete suspension conditions could be followed by really different (in percentage terms) impeller speeds and consequently agitation costs thus resulting in a poorly reliable criterion for solid-liquid apparatus design.

With the aim of defining a successful and reliable design criterion applicable to all system types and configurations, it is suggested here that basing the design of solid-liquid contactors *via* CFD on the concept of unsuspended solid fractions and the *sufficient suspension criterion*, may well be more effective than basing it on the much more troubled N_{js} prediction.

5.6 Nomenclature

U	velocity, ms^{-1}
T	tank diameter, m
H	liquid height, m
D	impeller diameter, m
C	impeller clearance, m
r	volumetric fraction, (-)
$r_{\beta_{av}}$	average solid volumetric fraction value, (-)
$r_{\beta_{packed}}$	solid volumetric fraction maximum packing value, (-)
N	rotational impeller speed, RPM
N_{js}	just suspension speed, RPM
N_{min}	agitation speed at which the suspension phenomenon starts, RPM
N_{span}	parameter that determines the width of the Weibull S curve, RPM
N_{ss}	impeller speed for sufficient suspension conditions, RPM
N_p	power number, (-)
d_p	particle mean diameter, (m)

Re	Reynolds number, (-)
k	turbulent kinetic energy, $m^2 s^{-2}$
u	axial component of velocity, $m s^{-1}$
x_{susp}	fraction of suspended solids, (-)
h_{sed}	height sediment assumes on the lateral wall midway two subsequent baffles, m

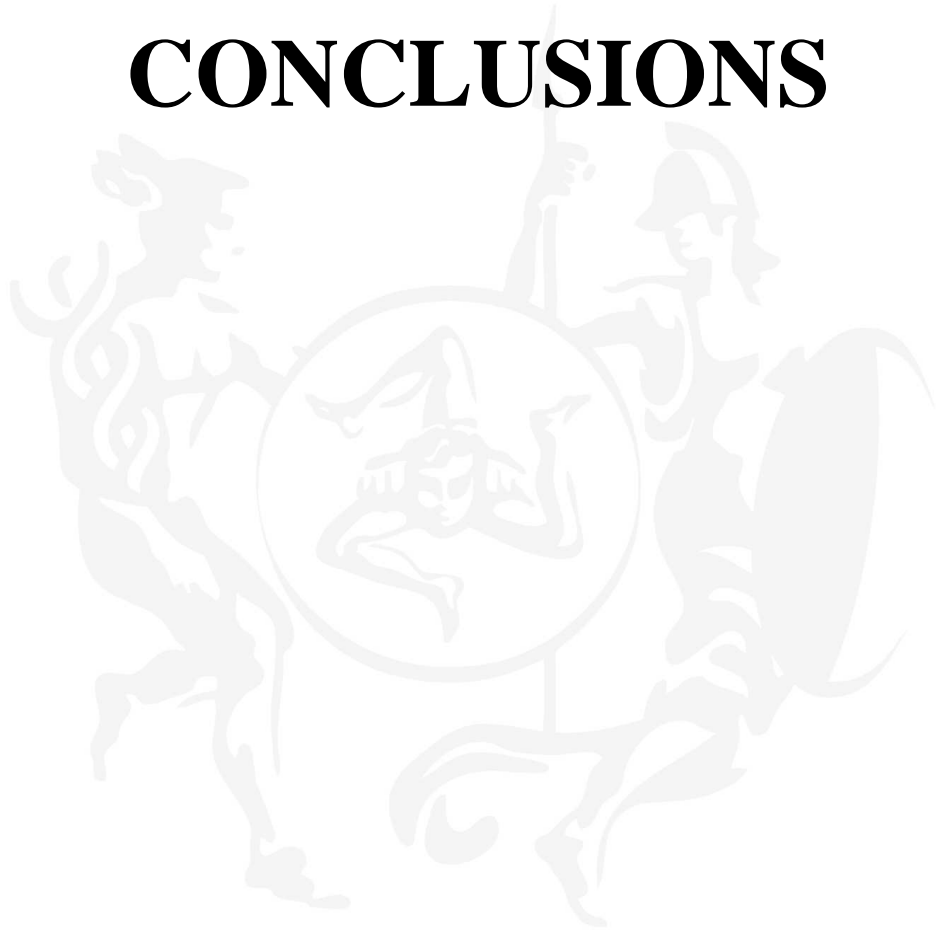
Greek letters

ε	turbulent dissipation, $W Kg^{-1}$
θ_{mix}	Mixing Time, s
σ	Variation Coefficient, (-)

Subscripts

α	liquid phase
β	solid phase

CONCLUSIONS



CONCLUSIONS

The present PhD thesis has been entirely devoted to the analysis of suspension phenomena in solid-liquid agitated systems, contributing with original experimental and computational studies in order to achieve a better understanding of such topic.

As far as experimental part is concerned, a novel very simple technique named *Laser Sheet Image Analysis* for solid concentration assessments of dilute solid-liquid suspension in stirred vessels was developed. It is non-invasive allowing to get experimental information on particle distribution without adopting any equipment inside the investigated system and consequently avoiding possible result alteration. This innovative technique appears to be very promising: it is characterized by a good reproducibility and result reliability. It is able to provide directly 2-D (composed of about 35000 point by point measurement information) solid particle concentration distribution maps in stirred tanks without requiring neither too complex and long elaborations nor too expensive measurement apparatuses. *LSIA* technique was successfully applied to solid-liquid dispersions in two different top-covered unbaffled vessels providing useful data which may constitute a good validation tool for computational studies.

Future remarks concern the further application of *LSIA* technique to other systems such as the baffled vessels. Moreover, the procedure for the production of fluorescent particles should be optimized in order to allow also the production of small particles. Finally, *LSIA* technique could be coupled to a *refractive index matching* methodology aiming at allowing its employment even for dense-opaque systems.

Investigations were also performed on the possibility of employing top-covered unbaffled stirred vessels for solid-liquid suspension instead of the more common systems provided of baffles. In particular a novel experimental technique, namely

the “*steady cone radius method*”, was devised to assist assessments of the just suspended agitation speed N_{js} . N_{js} dependence on operating parameters such as solid concentration, particle density and mean diameter, fluid kinematic viscosity and system scale was investigated and compared with that predicted for baffled vessels by the well known Zwietering’s correlation (1958). Power requirements to achieve just suspension conditions suggest an economic convenience for radially stirred top-covered unbaffled vessels only under a certain scale. Finally, a quite effective Zwietering-like correlation for the prediction of N_{js} in top-covered unbaffled vessels was devised by employing all the data collected during this thesis.

Future development of this topic should require enlargements of experimental tests encompassing different impeller types and features, system geometry and scale, etc.

As far as CFD modelling efforts are concerned, firstly an ad-hoc algorithm (*Excess Solid Volume Fraction* algorithm) was successfully implemented inside an Eulerian-Eulerian framework aiming at allowing the simulations of systems where sediments over the vessel bottom are present. As a first insight into the incomplete suspension regime, the transient behaviour of an off-bottom solid-liquid suspension during start-up in a stirred fully baffled tank was investigated by means of a rather simple CFD methodology purposely formulated and tested. Relevant experimental data were acquired to validate the modelling approach. Literature data were also employed to further test model reliability and a general satisfactory agreement with experimental data was found.

Subsequently, CFD simulations of dense solid-liquid suspensions within flat bottomed vessels stirred by a standard Rushton turbine were performed with the objective of numerically predicting the percentage of unsuspended solids and the particle distribution at different impeller speeds (covering partial to complete suspension regime) thus resulting in a reliable modelling of incomplete-to-complete suspension regime. Overall, results suggest that drag force has a crucial role in determining the suspension of particles from the vessel bottom and their distribution throughout the tank. Although suspension of particles in a liquid within a stirred

system was found to be allegedly due to “turbulence bursts” on the vessel bottom (Baldi et al., 1978), it seems that suspension phenomenon should be modeled not only by carrying out a good prediction of turbulence on the vessel bottom, but also and above all by an accurate computation of inter-phase drag terms. This implies that the particle suspension and distribution in dense solid-liquid suspensions in stirred tanks at partial to complete suspension conditions is a phenomenon mainly controlled by gravity, inertial and inter-phase drag forces.

Finally, the capability and the reliability of fully predictive CFD methods for minimum impeller speed for complete suspension were verified and discussed aiming at finding a methodology which could be universally accepted and which could represent an objective design criterion applicable to all possible systems. An original method was also proposed and evaluated. Simulation results suggest that the prediction of the “exact” N_{js} value by means of CFD technique can lead to dangerous conclusions. In fact, just before the attainment of complete suspension conditions, a small variation of the amount of unsuspended solid particles can be obtained by a corresponding high increase of the impeller speed. This implies that a quite precise prediction of complete suspension conditions could be followed by really different (in percentage terms) impeller speeds and consequently agitation costs thus resulting in a poor reliable criterion for the solid-liquid apparatus design. Accordingly to the aim of defining a design criterion that could be considered successfully and reliably applicable to all system types and configurations, it could be more suitable and prudent to drive the design of solid-liquid contactors via CFD referring only to unsuspended solid fractions as well as to the *sufficient suspension criterion* and *speed* instead of the traditional methods based on the N_{js} prediction.

As future work, it may be interesting to focus on the further testing of the present CFD-assisted criterion by applying it to different system geometry and/or characteristics in order to further validate its general applicability and reliability.

REFERENCES



REFERENCES

- Abat an, A.A., McCarthy, J.J., Vargas, W.L., 2006. Particle migration in the rotating flow between co-axial disks. *AIChE Journal*, 52 (6), 2039-2045.
- Alba, F., 1992. Method and apparatus for determining particle size distribution and concentration in a suspension using ultrasonics. US Patent No. 5,121,629.
- Alba, F., Crawley, G.M., Fatkin, J., Higgs, D.M.J., Kippax P.G., 1999. Acoustic spectroscopy as a technique for the particle sizing of high concentration colloids, emulsions and suspensions. *Colloids and Surfaces A: Physiochemical and Engineering Aspects*, 153, 495-502.
- Alban, F.B., Sajjadi, S., Yianneskis, M., 2004. Dynamic tracking of fast liquid-liquid dispersion processes with a real-time in situ optical technique. *Transactions of the Institute of Chemical Engineering, Part A, Chemical Engineering Research and Design*, 82, 1054-1060.
- Alcamo, R., Micale, G., Grisafi, F., Brucato, A., Ciofalo, M., 2005. Large-eddy simulation of turbulent flow in an unbaffled stirred tank driven by a Rushton turbine. *Chemical Engineering Science* 60, 2303 – 2316.
- Aloi L.E., Cherry, R.S., 1996. Cellular response to agitation characterized by energy dissipation at the impeller tip. *Chemical Engineering Science*, 51 (9), 1523-1529.
- Altobelli, S.A., Givler, R.C., Fukushima, E., 1991. Velocity and concentration measurements of suspensions by nuclear resonance imaging. *J. Rheol.*, 35, 721.
- Altway A, Setyawan H, Margono, Winardi S., 2001. Effect of particle size on simulation of three-dimensional solid dispersion in stirred tank. *Trans IChemE*;79 (A), 1011-1016.
- Álvarez, M.M., Arratia, P.E., Muzzio, F.J., 2002. Laminar mixing in eccentric stirred tank systems. *Canadian Journal of Chemical Engineering* 80, 546-557
- Andreussi, P., Di Donfrancesco A. and Messia M., 1988. An impedance method for the measurement of liquid hold-up in two phase flow. *Int J Multiphase Flow*, 14: 777–787.

- Andreussi, P., Paglianti A. and Silva F., 1999. Dispersed bubble flow in horizontal pipes. *Chem Eng Sci*, 54: 1101–1107.
- Angst R., Kraume M., 2005. Particle distributions in stirred solid-liquid systems. Experimental investigations in three different scales. *Chemical and Process Engineering*, 26 (3), 405-412.
- Angst R., Kraume M., 2006. Experimental investigations of stirred solid/liquid systems in three different scales: Particle distribution and power consumption. *Chem. Eng. Sci.*, 61, 2864–2870.
- Armenante, P.M., Huang, Y.-T., Li, T., 1992. Determination of the minimum agitation speed to attain the just dispersed state in solid-liquid and liquid-liquid reactors provided with multiple impellers. *Chem. Eng. Sci.*, 47, 2865-2870.
- Armenante, P.M., Chou, C.-C., 1996. Velocity profiles in a baffled vessel with single or double pitched-blade turbines, *AIChE J.* 42 (1), 42–54.
- Armenante P.M. and Nagamine, E.U., 1998. Effect of low off-bottom impeller clearance on the minimum agitation speed for complete suspension of solids in stirred tanks, . *Chemical Engineering Science.*, 53, 1757-1775.
- Armenante, P.M., Nagamine, E.U., Susanto, J., 1998. Determination of Correlations to Predict the Minimum Agitation Speed for Complete Solid Suspension in Agitated Vessels, *Can J Chem Eng*, 76: 413-419.
- Assirelli, M., Bujalski, W., Eaglesham, A., Nienow, A.W., 2008. Macro- and micromixing studies in an unbaffled vessel agitated by a Rushton turbine. *Chemical Engineering Science*, 63, 35-46.
- Aubin, J., Mavros, P., Fletcher, D.F., Bertrand, J., Xuereb, C., 2001. Effect of axial agitator configuration (up-pumping, down-pumping, reverse rotation) on flow patterns generated in stirred vessels. *Trans. IChemE*, 79A 845-856.
- Aubin, J., Fletcher, D.F., Xuereb, C., 2004. Modeling turbulent flow in stirred tanks with CFD: the influence of the modeling approach, turbulence model and numerical scheme. *Experimental Thermal and Fluid Science*, 28, 431–445.
- Baldi G., Conti R., Alaria E., 1978. Complete Suspension of Particles in Mechanically Agitated Vessels, *Chem. Eng. Sci.*, 33, 21-25.
- Bamberger, J.A., Greenwood, M. S., 2004. Using ultrasonic attenuation to monitor slurry mixing in real time. *Science Direct*, 145-148.
- Bamberger, J.A., Kytomaa, H.K., Greenwood, M.S., 1998. Slurry ultrasonic particle size and concentration characterization, in: W.W. Schulz, N.J. Lombardo (Eds.),

- Science and Technology for Disposal of Radioactive Tank Wastes, Plenum Press, New York,
- Bao Y., Hao Z., Gao Z., Shi L., Smith J.M., 2005. Suspension of buoyant particles in a three phase stirred tank, *Chem Eng. Sci.*, 60, 2283-2292.
- Barigou M., Fairhurst P.G., Fryer P.J., Pain J.P., 2003. Concentric flow regime of solid-liquid food suspension: theory and experiment. *Chemical Engineering Science*, 58, 1671-1686.
- Barigou, M., 2004. Particle tracking in opaque mixing systems: an overview of the capabilities of PET and PEPT. *Chem. Eng. Res. Des.*, 82(A9), 1258–1267.
- Barresi A. and Baldi G., 1987a. Solid dispersion in an agitated vessel. *Chemical Engineering Science*, 42 (12), 2949-2956.
- Barresi A. and Baldi G., 1987b. Solid dispersion in an agitated vessel: effect of particle shape and density. *Chemical Engineering Science*, 42 (12), 2969-2972.
- Barrue H, Bertrand J, Cristol B, Xuereb C., 2001. Eulerian simulation of dense solid-liquid suspension in multi-stage stirred vessel. *J. Chem. Eng. Japan.*, 34 (5), 585-594,.
- Bates R.L., Fondy P.L., Corpstein R.R., 1963. An examination of some geometric parameters of impeller power, *I&EC Process Design and Development*, 2 (4), 310-314.
- Biddulph, T., in “Modelling sand suspension and sedimentation for a submersible jet mixer”, Batchelor’s thesis, University of Sidney, Sydney, Australia, 1990.
- Birch D. and Ahmed N., 1997. Solid Suspension in aerated agitation vessels: role of sparger design. *Récents Progrés en Génie des Procédés*, 11 (52), 177-184.
- Böhm, M., Wechsler, K., Schäfer, M., 1998. A parallel moving grid multigrid method for flow simulation in rotor–stator configuration. *Int. J. Numer. Meth. Eng.*, 42, 175–189.
- Bohnet M. and Niesmak G., 1980. Distribution of solids in stirred suspensions. *Germ. Chemical Engineering*, 3, 57-65.
- Bolton, G.T. and Primrose, K.M., 2005. An overview of electrical tomographic measurements in pharmaceutical and related applications areas. *AAPS Pharm. Sci. Tech.*, 6 (2), E137-E143.

- Bosse, T., Kleiser, L., Härtel, C., Meiburg, 2005. E., Numerical simulation of finite Reynolds number suspension drops settling under gravity. *Physics of Fluid*, 17 (3), 037101-1-037101-17.
- Bouillard, J.X., Lyczkowski, R.W. and Gidaspow, D., 1989. Porosity distribution in a fluidised bed with an immersed obstacle. *AIChE J*, 35: 908–922.
- Bourne, J.R. and Sharma, R.N., 1974. Suspension characteristics of solid particles in propeller-agitated tanks. *Proceedings of the First European Conference on Mixing and Centrifugal Separation*, Cambridge, BHRA, Cranfield, UK, B3, 25-39.
- Brucato A., Micale G., Rizzuti L., 1997. Determination of the amount of unsuspended solid particles inside stirred tanks by means of pressure measurements, *Rec Progr Genie des Proc*, 11, 3-10.
- Brucato A. and Brucato V., 1998. Unsuspended mass of solid particles in stirred tanks. *Can. J. Chem. Eng.*, 76, 420-427.
- Brucato, A., Grisafi, F., Montante, G., 1998a. Particle Drag Coefficients in Turbulent Fluids, *Chem Eng Sci*, 53: 3295-3314.
- Brucato, A., Ciofalo, M., Grisafi, F., Micale, G., 1998b. Numerical Prediction of Flow Fields in Baffled Stirred Vessels: a Comparison of Alternative Modelling Approaches, *Chem Eng Sci*, 53: 3653-3684.
- Brucato, A., Micale, G., Montante, G., Scuzzarella, A., 2002, Experimental Investigation and CFD Simulation of Dense Solid-Liquid Suspensions in a Fully Baffled Mechanically Stirred Tank, *Proc. 10th Workshop on two-phase flow predictions*, (Merseburg, Germany, 9-12 April), pp 255-264.
- Brucato, A., Cipollina, A., Micale, G., Scargiali, F., Tamburini, 2010. A., Particle suspension in top-covered unbaffled tanks. *Chem. Eng. Sci.*, 65, 3001–3008,.
- Brunazzi E., Galletti C., Paglianti A. and Pintus S., 2004. An impedance probe for the measurements of flow characteristics and mixing properties in stirred slurry reactors. *Chemical engineering research and design*, 82, 1250-1257.
- Brunazzi, E., Paglianti, A. and Pintus, S., 2001. A capacitance probe and a new model to identify and predict the capacity of columns equipped with structured packings. *Ind Eng Chem Res*, 40: 1205–1212.
- Bubbico, R., Di Cave, S., Mazzarotta, B., 1998. Agitation power for solid-liquid suspensions containing large particles, *Can. Journ. Chem. Eng.*, 76 (3), 428-432.

- Bujalski W., Takenaka K., Paolini S., Jahoda M., Paglianti A., Takahashi K., Nienow A.W., Etchells A.W., 1999. Suspension and liquid homogenization in high solids concentration stirred chemical reactors. *Trans IChemE*, 77 (A), 241-247.
- Busciglio, A., Vella, G., Micale, G., Rizzuti, L., 2009. Analysis of the bubbling behaviour of 2D gas solid fluidized beds. Part II. Comparison between experiments and numerical simulations via Digital Image Analysis Technique. *Chem. Eng. J.*, 148, 145-163.
- Buurman, C., Resoort, G., and Plaschkes, A., 1986. Scaling-up rules for solids suspension in stirred vessels. *Chemical Engineering Science*, 41, 2865-2871.
- Ceccio, S.L. And George, D.L., 1996. A review of electrical impedance techniques for the measurement of multiphase flows. *J. Fluids Eng.*, 118, 391-399.
- CFX-4 Documentation. AEA Technology.
- Chang, J.S., Ichikawa, Y., Irons, G.A., Morala, E.C., Wan, P.T., 1984. Void fraction measurement by an ultrasonic transmission technique in bubbly gas-liquid two-phase flow. In: Delhaye, J.M., Cognet, G. (Eds.), *Measuring Techniques in Gas-Liquid Two-phase Flows*. Springer, New York, U.S.A..
- Chaouki, J., Larachi, F., Dudukovic, M.P. (Eds.) 1997. *Non-invasive monitoring of multiphase flows*. Elsevier Science B.V., Amsterdam, The Netherlands.
- Chaouki, J., Larachi, F., Dudukovic, M.P. 1997. Noninvasive tomographic and velocimetric monitoring of multiphase flows. *Industrial and Engineering Chemistry Research*, 36, 4476-4503.
- Chapman, C.M., Nienow, A.W., Cooke, M. and Middleton J.C., 1983. Particle-gas-liquid mixing in stirred vessels. Part I: particle-liquid mixing. *Chem. Eng. Res. Des.* 61, 71-81.
- Chen, T., Wu, D.-Z., Du, H.-X., Wang, L.-Q., Li, Z.-F., 2010. Numerical simulation on low-density solid-liquid mixing process. *Kung Cheng Je Wu Li Hsueh Pao / Journal of Engineering Thermophysics*, 31 (2), 271-274.
- Chudacek M.W., 1982. Formation of unsuspended solids profile in a slurry mixing vessel. *Proceedings of the 4th European Conference on Mixing*, Noordwijkerhout, The Netherlands, April 27-29. BHRA, Cranfield, U.K., 275-287.
- Ciofalo, M., Brucato, A., Grisafi, F., Torracca, N., 1996. Turbulent flow in closed and free-surface unbaffled tanks stirred by radial impellers. *Chemical Engineering Science* 51 (14), 3557-3573.

- Clift et al., Bubbles, drops and particles, 1978. Academic Press, New York, San Francisco, London.
- Considine , D.M. and Considine G.D., 1985. Process Instruments and Controls Handbook, 3rd ed., McGraw-Hill, New York.
- Coroneo, M., Montante, G., Paglianti, A., Magelli, F., 2011. CFD prediction of fluid flow and mixing in stirred tanks: Numerical issues about the RANS simulations. Computers and Chem. Eng., doi:10.1016/j.compchemeng.2010.12.007.
- Crowe, C. T., Troutt, T. R., Chung, J. N., 1996. Numerical Models for Two-Phase Turbulent Flows. Ann. Rev. Fluid. Mech., 28, 11-43.
- Cui, M.M. and Adrian, R.J., 1997. Refractive index matching and marking methods for highly concentrated solid – liquid flows. Experiments in fluids, 22, 261–264.
- Darelius, A., Rasmuson, A., vanWachem, B., Björn, I. N., Folestad, S., 2008. CFD simulation of the high shear mixing process using kinetic theory of granular flow and frictional stress models. Chem. Eng. Sci., 63, 2188-2197.
- Decker, S., Sommerfeld, M., 1996. Calculation of particles suspension in agitated vessels with the Euler-Lagrange approach, *I Chem E Symp Ser*, 140: 71-82.
- Derksen, J. J., Van den Akker, H. E. A., 1999. Large eddy simulations on the flow driven by a Rushton turbine, *AIChE J.*, 45 (2), 209-221.
- Derksen, J. J., 2003. Numerical Simulation of Solid Suspension in a Stirred Tank, *AIChE Journal*, 49: 2700-2714.
- Derksen, J.J., 2006. Long-Time solids suspension simulations by means of a large eddy approach. Chem. Eng. Res. Des., 84, 38–46.
- Distelhoff, M.F.W. and Marquis, A.I., 2000. Scalar mixing in the vicinity of two disk turbines and two pitched blade impellers. Chemical Engineering Science 55, 1905–1920.
- Ditl, P. and Rieger, F., 1984. Congress CHISA, Praha.
- Dohi N., Takahashi T., Minekawa K., Kawase Y., 2004. Power consumption and solid suspension performance of large scale impellers in gas-liquid-solid three phase stirred tank reactors, Chem. Eng. Jou., 97, 103-114.
- Doroodchi, E., Evans, G.M., Schwarz, M.P., Lane, G.L., Shah, N., Nguyen, A., 2008. Influence of turbulent intensity on particle drag coefficients. Chemical Engineering Journal, 135, 129-134.

- Dong, L., Johansen, S. T., Engh, T. A., 1994. Flow induced by an impeller in an unbaffled tank I. Experimental. *Chemical Engineering Science*, 49, 549-560.
- Dudukovic, M.P., 2002. Opaque multiphase flows: experiments and modelling. *Experimental Thermal and Fluid Science*, 26, 747-761.
- Dyakowski, T., Jeanmeure, L.F.C., Jaworski, A.J., 2000. Applications of electrical tomography for gas-solids and liquid-solids flows – a review. *Powder Technology*, 112, 174-192.
- Einenkel, W.D. and Mersmann, A., 1977. Required RPM for suspending in agitators. *Verfahrenstechnik* 11 (2), 90-94.
- Einenkel, W.D., 1980. Influence of physical properties and equipment design on the homogeneity of suspensions in agitated vessels.. *Ger. Chem. Engng.* 3 (2), 118-124.
- Ergun, S., 1952. Fluid Flow through Packed Columns, *Chem. Eng. Progress*, 48: 89-94.
- Fajner, D., Magelli, F., Nocentini, M., & Pasquali, G., 1985. Solids concentration profiles in a mechanically stirred and staged column slurry reactor. *Chemical Engineering Research and Design*, 63, 235–240.
- Fan, L., Mao, Z., Wang, Y., 2005. Numerical simulation of turbulent solid-liquid two-phase flow and orientation of slender particles in a stirred tank. *Chem. Eng. Sci.*, 60, 7045-7056.
- Fangary Y.S., Barigou M., Seville J.P.K. and Parker D.J., 2000. Fluid trajectories in a stirred vessel of non-newtonian liquid using positron emission particle tracking. *Chem. Eng. Sci.*, 55, 5969-5979.
- Fangary Y.S., Barigou M., Seville J.P.K. and Parker D.J., 2002. A Lagrangian study of solids suspensions in a stirred vessel by Positron Emission Particle Tracking (PEPT). *Chemical Engineering Technology*, 25, 521-528.
- Fishwick, R., Winterbottom, M., Parker, D., Fan, X., Stitt, H., 2005. The use of positron emission particle tracking in the study of multiphase stirred tank reactor hydrodynamics. *Canadian Journal of Chemical Engineering* 83 (1), 97-103.
- Fletcher, D.F. and Brown, G.J., 2009. Numerical simulation of solid suspension via mechanical agitation: effect of the modeling approach, turbulence model and hindered settling drag law. *Intern. Jour. of Comp. Fluid Dynam.*, 23 (2), 173-187.

- Foucault, S., Ascanio, G., Tanguy, F.A., 2004. Coaxial mixers hydrodynamics with Newtonian and non-Newtonian fluids. *Chem. Eng. Tech.*, 27, 324-329.
- Fountain, G.O., Khakar, D.V., Mezic, I., Ottino, J.M., 2000. Chaotic mixing in a bounded three-dimensional flow. *Journal of Fluid Mechanics*, 417, 265-301.
- Fournier, T. and Jeandey, C., 1993. Optimization of an experimental setup for void fraction determination by the X-ray attenuation technique, in J.M. Delhayr and G. Cognet (Eds.), *Measuring techniques in gas-liquid two-phase flows*, (pp. 199-228), Berlin, Heidelberg, New York, Tokio: Springer.
- Frijlink J., Bakker A., Smith J., 1990. Suspension of solid particles with gassed impellers, *Chem. Eng. Sci.*, 45, 1703-1718.
- Froystein, T., 1997. Flow imaging by gamma-ray Tomography: Data processing and reconstruction techniques. *Frontiers in Industrial Process Tomography II*, Delft, April 8-12.
- Fukushima, E., 1999. Nuclear magnetic resonance as a tool to study flow. *Annu. Rev. Fluid. Mech.*, 31, 95.
- Galletti, C., Brunazzi, E., Yianneskis, M., Paglianti, A., 2003. Spectral and wavelet analysis of the flow pattern transition with impeller clearance variations in a stirred vessel. *Chem. Eng. Sci.* 58, 3859-3875.
- Galletti, C., Brunazzi, E., 2008. On the main flow features and instabilities in an unbaffled vessel agitated with an eccentrically located impeller. *Chemical Engineering Science*, 63, 4494-4505.
- Ghionzoli, A., Bujalski, W., Grenville, R.K., Nienow, A.W., Sharpe, R.W., Paglianti, A., 2007. The effect of bottom roughness on the minimum agitator speed required to just fully suspend particles in a stirred vessel. *Chem. Eng. Res. Des.*, 85(A5), 685-690.
- Gibilaro, L.G., 2001, *Fluidization-Dynamics*, Butterworth-Heinemann, Oxford.
- Gidaspow, D., 1994, *Multiphase flow and fluidization*, (eds) (Academic Press, San Diego, USA).
- Godfrey, J. C. and Zhu, Z. M., 1994. Measurement of particle-liquid profiles in agitated tanks, *AIChE Symp. Ser.*, No. 299, 90: 181.
- Goldstein, R.J., *Fluid Mechanics measurements*. Taylor and Francis, DC, 1996.

- Gosman AD, Lekakou C, Politis S, Issa RI, Looney MK., 1992. Multidimensional modeling of turbulent two-phase flows in stirred vessels. *AIChE J.* ,38 (12),1946-1956.
- Gouesbet, G. and Berlemont, A., 1999. Eulerian and Lagrangian approaches for predicting the behaviour of discrete particles in turbulent flows. *Progress in Energy and Combustion Science*, 25, 133-159.
- Grisafi F., Brucato A., Rizzuti L., 1994. Solid-liquid mass transfer coefficient in mixing tanks: influence of side wall roughness, *ICHEME Symposium Series*, 136, 571-578.
- Grisafi F., Brucato A., Rizzuti L., 1998., Solid-Liquid Mass Transfer Coefficients in Gas-Solid-Liquid Agitated Vessels, *Canad. Jour. Chem Eng.*, 76, 446-455.
- Guha, D., Ramachandran, M.P., Dudukovic, M.P., Derksen, J.J., 2008. Evaluation of Large Eddy Simulation and Euler-Euler CFD Models for Solids Flow Dynamics in a Stirred Tank Reactor, *AIChE J.*, 54, 766-778.
- Guida, A., Fan, X., Parker, D.J., Nienow, A.W., Barigou, M., 2009. Positron emission particle tracking in a mechanically agitated solid-liquid suspension of coarse particles. *Chemical Engineering Research and Design*, 87 (4), 421-429.
- Guilbault, G. 1973. *Practical Fluorescence*. New York: Marcel Dekker, Inc.
- Guillard, F., Träghard, C., Fuchs, L., 2000. New image analysis methods for the study of mixing patterns in stirred tanks. *Canadian Journal of Chemical Engineering* 78, 273–285
- Guha Debangshu, Ramachandran, P.A., Dudukovic, M.P., 2007. Flowfield of suspended solids in a stirred tank reactor by Lagrangian tracking. *Chem. Eng. Sci.*, 62, 6143–6154.
- Hannoun, I. and E. List. 1988. Turbulent Mixing at a shear-free density interface. *J. Fluid. Mech.*, 189, 211-234.
- Harrop, K.L., Spanfeller, W.H., Jahoda, M., Otomo, N., Etchells, A.W.; Bujalski, W., Nienow, A.W., 1997. Impact of suspended solids on the homogenisation of the liquid phase under turbulent conditions in a stirred vessel. *Récents Prog. Génie Procédés*, 11, 52, 41.
- Hartmann, H., Derksen, J. J., Montavon, C., Pearson, J., Hamill, I.S., Van den Akker, H.E.A., 2004. Assessment of large eddy and RANS stirred tank simulations by means of LDA. *Chem. Eng. Sci.*, 59, 2419–2432.

- Hartmann, H., Derksen, J. J., Van den Akker, H.E.A., 2006. Numerical simulation of a dissolution process in a stirred tank reactor. *Chem. Eng. Sci.*, 61, 3025–3032.
- Havelkova, D., 1987. Dissertation CVUT FSI, Praha.
- Hekmat, D., Hebel, D., Schmid, H., Weuster-Botz D., 2007. Crystallization of lysozyme: from vapor diffusion experiments to batch crystallization in agitated ml-scale vessels. *Process Biochemistry*, 42, 1649–1654.
- Hemrajani R.R., Tatterson G.B., 2004. Mechanically stirred vessels. In: Paul E.L., Atiemo Obeng V.A., Kresta S.M. (Eds.), *Handbook of Industrial Mixing*. Wiley, New York. Table 6-4, p. 365.
- Herringe, R. A, 1979. The behaviour of mono-size particle slurries in a fully baffled turbulent mixer, *3rd European Conference on Mixing*, BHRA, Cranfield, U.K., Paper D1.
- Hewitt, G.F., 1978. Measurement of two phase flow parameters. Academic Press, New York, USA.
- Hicks, M.T., Myers, K.J., Bakker, A., 1997. Cloud Height in Solids Suspension Agitation, *Chem Eng Comm*, 160: 137-155.
- Hinze, J.H., *Turbulence*, 1975. McGraw-Hill, New York.
- Hirata, Y., Dote, T., Inoue, Y., 2009. Contribution of suspended particles to fluid mixing in recipro-mixing with a disk impeller. *Chem. Eng. Res. & Des.* 87 (4), 430-436.
- Hockey, R.M., Nouri, J.M., 1996. Turbulent flow in a baffled vessel stirred by a 60° pitched blade impeller. *Chem. Eng. Sci.*, 51 (19), 4405–4421.
- Holbeach, J.W., Davidson, M.R., 2009. An Eulerian-Eulerian model for the dispersion of a suspension of microscopic particles injected into a quiescent liquid. *Eng. Appl. Comput. Fl. Mech.*, 3 (1), 84-97.
- Hosseini S., Patel D., Ein-Mozaffari F. and Mehrvar M., 2010a. Study of solid-liquid mixing in agitated tanks through electrical resistance tomography. *Chem. Eng. Sci.*, 65 (4), 1374-1384.
- Hosseini S., Patel D., Ein-Mozaffari F. and Mehrvar M., 2010b. Study of solid-liquid mixing in agitated tanks through computational fluid dynamics modelling. *Ind. Eng. Chem. Res.*, 49, 4426-4435.

- Ibrahim, S. and Nienow, A.W., 1996. Particle suspension in the turbulent regime: the effect of impeller type and impeller/vessel configuration. *Chem. Eng. Res. Des.*, 74 (6), 679-688.
- Ibrahim, S. and Nienow, A.W., 1999. Comparing impeller performance for solid-suspension in the transitional flow regime with Newtonian fluids. *Chem. Eng. Res. Des.*, 77 (8), 721-727.
- Ibrahim, S. and Nienow, A.W., 2004. Suspension of microcarriers for cell culture with axial flow impellers. *Chem. Eng. Res. Des.*, 82, 1082-1088.
- Ibrahim, S. and Nienow, A.W., 2010. The effect of viscosity on particle suspension in an aerated stirred vessel with different impellers and bases. *Chem. Eng. Comm.*, 197, 434-454.
- Jenne, M., Reuss, M., 1999. A critical assessment on the use of $k-\varepsilon$ turbulence model for simulation of turbulent flow induced by a Rushton turbine in a baffled stirred tank reactor. *Chem. Eng. Sci.* 54, 3921-3941.
- Kagoshima, M. and Mann R., 2006. Development of a networks-of-zones fluid mixing model for an unbaffled stirred vessel used for precipitation. *Chem. Eng. Sci.*, 61, 2852-2863.
- Kasat, G.R. and Pandit, A.B., 2005. Review on mixing characteristics in solid-liquid and solid-liquid-gas reactor vessels. *Can. Jour. of Chem. Eng.*, 83, 618-643.
- Kasat, G. R.; Khopkar, A. R.; Ranade, V. V.; Pandit, A. B., 2008. CFD Simulation of Liquid-Phase Mixing in Solid-Liquid Stirred Reactor. *Chem. Eng. Sci.* 63, 3877-3885.
- Kee, R.C.S. & Tan, R.B.H., 2002. CFD simulation of solids suspension in mixing vessels. *Can. J. Chem. Eng.*, 80, 721-726.
- Kerker, M., 1969. The scattering of light and other electromagnetic radiation. Academic Press, New York, USA.
- Khopkar, A.R., Kasat, G.R., Pandit, A.B., and Ranade, V.V., 2006. Computational Fluid Dynamics Simulation of the Solid Suspension in a Stirred Slurry Reactor, *Ind Eng Chem Res*, 45: 4416-4428.
- Kling, K. and Mewes, D., 2004. Two-colour laser induced fluorescence for the quantification of micro- and macro-mixing in stirred vessels. *Chem. Eng. Sci.*, 59, 1523-1528.

- Kohnen, C., and Bohnet, M., 2001. Measurement and Simulation of Fluid Flow in Agitated Solid/Liquid Suspensions. *Chem. Eng. Technol.* 24, 6, 639-643.
- Kraume, M. 1992. Mixing times in stirred suspensions. *Chem. Eng. Tech.*, 15 (5), 313-318.
- Kumar, S.B., Moslemian, D., Dudukovic, M.P., 1995. A γ -ray tomographic scanner for imaging of void distribution in two-phase flow systems, *Flow Meas. Instrum.*, 6 (3), 61-73.
- Kumar, S.B., Moslemian, D., Dudukovic, M.P., 1997. Gas holdup measurements in bubble columns using computed tomography, *AIChE J.* 43 (6), 1414-1425.
- Kuzmanic N. and Ljubicic B., 2001. Suspension of floating solids with up-pumping pitched blade impellers; mixing time and power characteristics, *Chem. Eng. Jou.*, 84, 325-333.
- Lackermeier, U., Rudnik, C., Werther, J., Bredebusch, A., Burkhardt, H., 2001. Visualization of flow structures inside a circulating fluidized bed by means of laser sheet and image processing. *Powder technology*, 114, 71-83.
- Lain, S., M. Sommerfeld, and J. Kussin, 2002. Experimental Studies and Modelling of Four-Way Coupling in Particle-Laden Horizontal Channel Flow. *Int. J. Heat Fluid Flow*, 23, 647-656,
- Lamberto, D.J., Muzzio, F.J., Swanson, P.D., Tonkovich, A.L., 1996. Using time dependent RPM to enhance mixing in stirred vessels. *Chemical Engineering Science*, 51, 733-741.
- Lamberto, D.J., Álvarez, M.M., Muzzio, F.J., 2001. Computational analysis of regular and chaotic mixing in a stirred tank reactor. *Chemical Engineering Science*, 56, 4887-4899.
- Lane, G.L., Schwarz, M.P., Evans, G.M., 2005. Numerical modelling of gas-liquid flow in stirred tanks. *Chemical Engineering Science*, 60, 2203-2214.
- Larachi, F.; Chaouki, J.; Kennedy, G.; Dudukovic, M.P., 1997. Radioactive particle tracking in multiphase reactors: principles and applications. *Non-Invasive Monit. Multiphase Flows* 335-406.
- Latifi, M.A., Rode, S., Midoux, N., Storck, A., 1992. The use of microelectrodes for the determination of flow regimes in a trickle-bed reactor. *Chem. Eng. Sci.*, 47, 1955-1961.
- Lauder, B. E. and Spalding, D. B., 1972. *Lectures in Mathematical Models of Turbulence*, Academic Press: London.

- Launder, B. E. and Spalding, D. B., 1974. The Numerical Computation of Turbulent Flows. *Comput. Meth. Appl. Mech. Eng.*, 3, 269.
- Laurenzi, F., Coroneo, M., Montante, G., Paglianti, A., Magelli, F., 2009. Experimental and computational analysis of immiscible liquid-liquid dispersions in stirred vessels. *Chem. Eng. Res. Des.* 87 (4), 507-514.
- Lettieri, P., Cammarata, L., Micale, G. and Yates J., 2003. CFD Simulations of Gas Fluidized Beds Using Alternative Eulerian-Eulerian Modelling Approaches, *Int Jour Chem Reactor Eng*, 1 (A5).
- Ljungqvist, M., Rasmuson, A., 2001. Numerical Simulation of the Two-Phase Flow In an Axially Stirred Vessels, *Chem Eng Res and Des*, 79: 533-546.
- Lopez de Bertodano, M.A., 1998. Two fluid model for two-phase turbulent jets. *Nuclear Eng. Des.*, 179, 65–74.
- Lu, WM., Hsu, RC., Chien, WC., Lin, L.C., 1993. Measurement of local bubble diameters and analysis of gas dispersion in an aerated vessel with disk-turbine impeller. *Journal of Chemical Engineering Japan*, 26, 551-557.
- Luo, J.Y., Issa, R.I. and Gosman, A.D., 1994. Prediction of impeller-induced flows in mixing vessels using multiple frames of reference, *ICHEME Symp. Ser.*, 136, 549-556.
- MacTaggart, R.S., Nasr-El-Din, H.A. and Masliyah, J.H., 1993. Sample withdrawal from a slurry mixing tank. *Chemical Engineering Science*, 48, 921-931.
- Magaud, F., Souhar, M., Wild, G., & Boisson, N., 2001. Experimental study of bubble columns hydrodynamics. *Chem. Eng. Sci.*, 56, 4597–4607.
- Magelli F., Fajner D., Nocentini M. and Pasquali G., 1990. Solid distribution in vessels stirred with multiple impellers. *Chemical Engineering Science*, 45 (3), 615-625.
- Majors, P.D., Givler, R.C., Fukushima, E., 1989. Velocity and concentration measurements in multiphase flows by NMR. *J. Magn. Reson. (1969-1992)*, 85, 235.
- Mak, A.T.C., 1992. Solid-liquid mixing in mechanically agitated vessels. Ph.D. Dissertation, University of London, London.
- Maneval, J.E., Powell, R.L., McCarthy, M.J., McCarthy, K.L., 1993. Magnetic resonance imaging of multiphase systems in Particulate Two Phase Flow, edited by M. Roco. Butterworths-Heinemann, Boston.

- Mann, R., Dickin, F. J., Wang, M., Dyakowski, T., Williams, R.A., Edwards, R.B., Forrest, A.E., Holden, P. J., 1997a. Application of electrical resistance tomography to interrogate mixing processes at plant scale. *Chem. Eng. Sci.*, 52 (13), 2087-2097.
- Mann, R., Williams, R.A., Dyakowski, T., Dickin, F. J., Edwards, R.B., 1997b. Development of mixing models using electrical resistance tomography. *Chem. Eng. Sci.*, 52 (13), 2073-2085.
- Mauri R, Papageorgiou DT, 2002. The onset of particle segregation in plane couette flows of concentrated suspensions. *International Journal of Multiphase Flows*, 28, 127-136.
- Mazzarotta B., Comminution phenomena in stirred sugar suspensions, 1993. *AIChE Symposium Series*, 89, 112-117.
- McLaren White and Sumerford S.D., 1933. Studies in agitation, sand concentration as function of sand size and agitator speed, *Industrial and Engineering Chemistry*, pp. 1025-1027.
- McKee S.L., Williams R.A. and Boxman A., 1995. Development of solid-liquid mixing models using tomographic techniques. *Chemical Engineering Journal*, 56, 101-107.
- Mersmann, A and Laufhutte, H.D., 1985. Scale-up of agitated vessels for different mixing processes. *Proceedings of 5th European Conference on Mixing*, BHRA, Cranfield, Bedford, England, 273-284.
- Mersmann, A., Werner, F., Maurer, S., Bartosch, K., 1998. Theoretical prediction of the minimum stirrer speed in mechanically agitated suspensions. *Chemical Engineering and Processing* 37 (6), 503-510.
- Micale G., Carrara V., Grisafi F., Brucato A., 2000, Solids suspension in three phase stirred tanks, *Chem. Eng. Res. Des.*, 78, 319-326.
- Micale, G., Montante, G., Grisafi, F., Brucato, A., Godfrey, J., 2000. CFD simulation of particle distribution in stirred vessels. *Trans IChemE*, 78, Part A, 435-444.
- Micale G., Grisafi F., Brucato A., 2002. Assessment of particle suspension conditions in stirred vessels by means of a Pressure Gauge Technique, *Chem. Eng. Res. Des.*, 80, 893-902.
- Micale G., Grisafi F., Rizzuti L., and Brucato A., 2004. CFD Simulation of Particle Suspension Height in Stirred Vessels, *Chem Eng Res & Des*, 82(A9): 1204-1213.

- Micheletti, M., Nikiforaki, L., Lee, K.C., Yianneskis, M., 2003. Particle Concentration and Mixing Characteristics of Moderate-to-Dense Solid-Liquid Suspensions. *Ind. Eng. Chem. Res.*, 42 (24), 6236-6249.
- Micheletti, M., Baldi, S., Yeoh, S.L., Ducci, A., Papadakis, G., Lee, K.C., Yianneskis, M., 2004. On spatial and temporal variations and estimates of energy dissipation in stirred reactors. *Trans. IChemE, Part A: Chem. Eng. Res. Des.*, 82 (A9), 1188-1198.
- Micheletti, M. and Yianneskis, M., 2004. Study of fluid velocity characteristics in stirred solid-liquid suspensions with a refractive index matching technique. *Proceedings of the Institution of Mechanical Engineers, Part E: Journal of Process Mechanical Engineering* 218 (4), 191-204.
- Milliken, W.J., Gottlieb, M., Graham, A.L., Mondy, L.A., Powell, R.L., 1989. The viscosity-volume fraction relation for suspensions of randomly oriented rods. *J. Fluid Mechanics*, 202, 217.
- Mishra, V.P., Dyster, K.N., Jaworski, Z., Nienow, A.W., McKemmie, J., 1998. A study of an up- and a down-pumping wide blade hydrofoil impeller: Part I. LDA measurements. *Can. J. Chem. Eng.*, 76 577-588.
- Mondy, L.A., Graham, A.L., Majumdar, A., Bryant, 1986. Techniques of measuring particle motions in concentrated suspensions. *Int. J. Multiphase Flow*, 12, 497.
- Montante, G., Lee, KC, Brucato, A., Yianneskis, M., 1999. An Experimental Study of Double-to-Single-Loop Transition in Stirred Vessel, *Canadian Jour Chem Eng*, 77: 649-659.
- Montante, G., Micale, G., Magelli, F., Brucato, A., 2001. Experiments and CFD predictions of solid particle distribution in a vessel agitated with four pitched blade turbines. *Trans IChemE*, 79, Part A, 1005-1010.
- Montante, G., Magelli, F., 2005. Modelling of Solids Distribution in Stirred Tanks: Analysis of Simulation Strategies and Comparison with Experimental Data, *Int Jour Comp Fluid Dyn*, 19: N°3, 253-262.
- Montante, G., Bakker, A., Paglianti, A., Magelli, F., 2006. Effect of the shaft eccentricity on the hydrodynamics of unbaffled stirred tanks. *Chemical Engineering Science*, 61, 2807-2814.
- Montante, G., Magelli, F., 2007. Mixed Solids Distribution in Stirred Vessels: Experiments and Computational Fluid Dynamics Simulations, *Ind Eng Chem Res*, 46: 2885-2891.

- Murai, Y., Song, X. Q., Takagi, T., Ishikawa, M., Yamamoto, F., Ohta, J., 2000. Inverse energy cascade structure of turbulence in a bubbly flow. PIV measurement and results Japanese Society of Mechanical Engineers International Journal Series B, Fluids and Thermal Engineering, 43(2), 188–196.
- Murthy, J.Y., Mathur, S.R. and Choudhury, D., 1994. CFD simulation of flows in stirred tank reactors using a sliding mesh technique. IChemE Symp. Ser., 136, 341-348.
- Murthy, B.N., Ghadge, R.S. and Joshi, J.B., 2007. CFD simulations of gas-liquid-solid stirred reactor: prediction of critical impeller speed for solid suspension. Chem. Eng. Sci., 62, 7184-7195.
- Murthy, B.N. and Joshi, J.B., 2008. Assessment of standard k- ϵ , RSM and LES turbulence models in a baffled stirred vessel agitated by various impeller designs. Chem. Eng. Sci., 63, 5468-5495.
- Musil, L., 1976. The hydrodynamics of mixed crystallizers. Collection of Czechoslovak Chemical Communication, 41 (3), 839-852.
- Musil, L. and Vlk, J., 1978. Suspending solid particles in an agitated conical-bottom tank. Chem. Eng. Sci., 33, 1123-1131.
- Nagata, S., 1975. *Mixing Principles and Applications*. Halsted Press, New York.
- Ng, K., Fentiman, N.J., Lee, K.C., Yianneskis, M., 1998. Assessment of sliding mesh CFD predictions and LDA measurements of the flow in a tank stirred by a Rushton impeller. Trans. IChemE, Part A 76, 737–747.
- Nienow A. W., 1968. Suspension of solid particles in turbine-agitated baffled vessels. *Chem. Eng. Sci.*, 23, 1453-1459.
- Nienow A., Konno M., Bujalski W., 1986. Studies on three phase mixing: a review and recent results. *Chem. Eng. Res. Des.*, 64, 35-42.
- Nienow, A.W., 1992. “The suspension of solid particles” in “Mixing in the process Industries”. Butterworths, London, U.K., 364-393.
- Nocentini, M., Pinelli, D., Magelli, F., 2002. Dispersion coefficient and settling velocity of the solids in agitated slurry reactors stirred with multiple rushton turbines. Chem. Eng. Sci., 57, 1877-1884.
- Ochieng, A. and Lewis, A.E., 2006a. CFD simulation of solids off-bottom suspension and cloud height. Hydrometallurgy, 82, 1-12.

- Ochieng, A. and Lewis, A.E., 2006b. Nickel solids concentration distribution in a stirred tank. *Minerals Engineering*, 19, 180-189.
- Ochieng, A., Onyango, M. S., 2008. Drag Models, Solids Concentration and Velocity Distribution in a Stirred Tank, *Powder Technology*, 181: 1-8.
- Oldshue, J. Y., in "Fluid Mixing Technology", Chapter 5, McGraw-Hill, New York, NY, 1983.
- Oldshue, J.Y., and Sharma, R.N., 1992. The effect of off-bottom distance of an impeller for the 'Just Suspended Speed', N_{js} . *AIChE Symp. Ser.*, 88, 72-78.
- Oshinowo, L.M. and Bakker, A., 2002. CFD modeling of solids suspensions in stirred tank. *Proceedings of the Conference on Computational Modeling of Materials, Minerals and Metals Processing*, 205-215.
- Pacek, A. W., Ding, P., Nienow, A.W., 2001. The effect of volume fraction and impeller speed on the structure and drop size in aqueous/aqueous dispersions. *Chemical Engineering Science*, 56, 3247-3255.
- Paglianti, A. and Pintus, S., 2001. The impedance probe for the measurements for liquid hold-up and mixing time in two/three-phase stirred tank reactors. *Experiments in Fluids*, 31, 417-427.
- Panneerselvam, R., Savithri, S., Surender, G.D., 2008. CFD modeling of gas-liquid-solid mechanically agitated contactor. *Chem. Eng. Res. Des.* 86, 1331-1344.
- Pantula P.R.K. and Ahmed N., 1997. The impeller speed required for complete solids suspension in aerated vessels: a simple correlation?. *Récents Progrés en Génie des Procédés*, 11 (52), 11-18.
- Parker, D. J., Broadbent, C. J., Fowles, P., Hawkesworth, M. R., McNeil, P., 1993. Positron emission particle tracking - A technique for studying flow within engineering equipment. *Nuclear Instruments and Methods in Physics Research*, A326, 592-607.
- Parker, D.J., Forster, R.N., Fowles, P. and Takhar, P.S., 2002. Positron emission particle tracking using the new Birmingham positron camera. *Nucl Instrum Methods A*, 477(1-3), 540-545.
- Perng, C. Y. and Murthy, J. Y., 1993. A moving-deforming mesh technique for simulation of flow in mixing tanks, *A.I.Ch.E. Symp. Ser.* 89 (293)
- Pianko-Oprych, P., Nienow, A.W., Barigou, M., 2009. Positron emission particle tracking (PEPT) compared to particle image velocimetry (PIV) for studying the

- flow generated by a pitched-blade turbine in single-phase and multi-phase systems. *Chem. Eng. Sci.*, 64, 4955-4968.
- Pinelli, D., Nocentini, M., Magelli, F., 2001. Solids distribution in stirred slurry reactors: Influence of some mixer configurations and limits to the applicability of a simple model for predictions. *Chem. Eng. Sci.*, 188, 91-107.
- Powell, R.L., 2008. Experimental techniques for multiphase flows. *Physics of fluids*, 20, 040605.
- Raghava Rao K.S.M.S., and Joshi J.B., 1988. Liquid phase mixing in mechanically agitated three phase contactors. *6th European Conf. on Mixing*, Pavia, Italy: May 24-26.
- Raghava Rao K.S.M.S., Rewatkar V.B., Joshi J.B., 1988. Critical Impeller speed for solid suspension in mechanically agitated contactors. *AIChE Journal*, 34 (8), 1332-1340.
- Rammohan, A.R., Kemoun, A., Al-Dahhan, M.H., Dudukovic, M.P., 2001a. A Lagrangian description of flows in stirred tanks via computer automated radioactive particle tracking (CARPT). *Chemical Engineering Science* 56, 2629.
- Rammohan, A.R., Kemoun, A., Al-Dahhan, M.H., Dudukovic, M.P., 2001b. Characterization of single phase flows in stirred tanks via computer automated radioactive particle tracking (CARPT). *Transactions of the Institution of Chemical Engineers* 79 (A), 831-844.
- Rammohan, A. R.; Kemoun, A.; Al-Dahhan, M. H.; Dudukovic, M. P.; Larachi, F. 2001c. CARPT Dynamic Bias Studies: Evaluation of Accuracy of Position and Velocity Measurements. *Tracers and Tracing Methods*, 15 (79), 59-67.
- Rammohan, A.R., Dudukovic, M.P., Ranade, V.V., 2003. Eulerian flow field estimation from particle trajectories: numerical experiments for stirred tank type flows. *Ind. Eng. Chem. Res.*, 42, 2589-2601.
- Ranade, V.V., 1995. Computational fluid dynamics for reactor engineering. *Rev. Chem. Eng.*, 11, 229-289.
- Ranade, V.V., Dommeti, S.M.S., 1996. Computational snapshot of flow generated by axial impellers in baffled stirred vessels. *Trans. Inst. Chem. Eng.*, 74, 476-484.
- Ranade, V.V., 1997. An efficient computational model for simulating flow in stirred vessels: a case of Rushton turbine. *Chem. Eng. Sci.*, 52, 4473-4484.

- Rao, A.R. and Kumar, B., 2007. The use of circular surface aerators in wastewater treatment tanks. *Journal of Chemical Technology and Biotechnology*, 82, 101–107.
- Reiss, L. P., & Hanratty, T. J., 1963. An experimental study of the unsteady nature of the viscous sublayer. *A.I.Ch.E. Journal*, 9, 154–160.
- Ren, C., Jiang, X., Wang, J., Yang, Y., Zhang X., 2008a. Determination of Critical Speed for Complete Solid Suspension Using Acoustic Emission Method Based on Multiscale Analysis in Stirred Tank. *Ind. Eng. Chem. Res.*, 47, 5323-5327.
- Ren, C., Wang, J., Zhang, X., Yang, Y. 2008b. Measurement of slurry suspension height in stirred tank by multi-scale analysis of acoustic emission technology. *Huagong Xuebao/Journal of Chemical Industry and Engineering (China)* 59 (6), 1383-1389.
- Ren, C., Wang, J., Yang, Y., Zhang, X. 2008c. Measurement of critical suspension speed for solid particles in stirred vessel based on acoustic method. *Huagong Xuebao/Journal of Chemical Industry and Engineering (China)* 59 (8), 1986-1991
- Rewatkar V.B., Raghava Rao K.S.M.S., Joshi J.B., 1991. Critical impeller speed for solid suspension in mechanically agitated three-phase reactors. 1.Experimental part. *Ind. Eng. Chem. Res.*, 30, 1770-1784.
- Rieger, F., Ditl, P., Novak, V., 1980. Research report N° 218-11/80, CVUT FSI, Praha.
- Rieger and Ditl, 1982. Suspension of solid particles in agitated vessels. *Proceedings of the 4th European Conference on Mixing, BHRA, Cranfield, U.K.*, 263.
- Rieger, F., Ditl, P., Havelkova, O., 1988. Suspension of solid particles – Concentration profiles and particle layer on the vessel bottom. *Proceedings of the 6th European Conference on Mixing, Pavia, Italy, 24-26 May*, 251-258.
- Rieger, F. and Ditl, P., 1994. Suspension of solid particles. *Chem. Eng. Sci.* 49 (14), 2219–2227.
- Rieger, F., Novak, V., Ditl, P., 1980. Research report N° 218-2/80, CVUT FSI, Praha.
- Rode, S., Midoux, N., Latifi, M.A., Storck, A., 1994. Hydrodynamics and liquid–solid mass transfer mechanisms in packed beds operating in cocurrent gas–liquid downflow: An experimental study using electrochemical shear rate sensors. *Chem. Eng. Sci.*, 49, 1383–1401.

- Rodgers, T.L., Stephenson, D.R., Cooke, M., York, T.A., Mann, R., 2009. Tomographic imaging during semi-batch reactive precipitation of barium sulphate in a stirred vessel. *Chem. Eng. Res. Des.*, 87, 615-626.
- Rousseaux, J.M., Muhr, H., Plasari, E., 2001. Mixing and micromixing times in the forced vortex region of unbaffled mixing devices. *Canadian Journal of Chemical Engineering* 79, 697–707.
- Sahu, A.K., Kumar, P., Joshi, J.B., 1998. Simulation of flow in stirred vessels with axial flow impeller: Zonal modelling and optimization of parameters. *Ind. Eng. Chem. Res.*, 37, 2116-2130.
- Sardeshpande, M.V., Sagi, A.R., Juvekar, V.A., Ranade, V.V., 2009. Solid suspension and liquid phase mixing in solid-liquid stirred tanks. *Ind. Eng. Chem. Res.*, 48, 9713-9722.
- Sbrizzai, F., Lavezzo, V., Verzicco, R., Campolo, M., Soldati, A., 2006. Direct numerical simulation of turbulent particle dispersion in an unbaffled stirred-tank reactor. *Chemical Engineering Science*, 61, 2843–2851.
- Schmitz, D., and Mewes, D., 2000. Tomographic imaging of transient multiphase flow in bubble columns. *Chemical Engineering Journal*, 77, 99–104.
- Segre', G, Silberberg, A., 1962. Behavior of macroscopic rigid spheres in poiseuille flow. *Journal of Fluid Mechanics*, 14, 115-156.
- Selima, Y.S., Fangary, Y.S., Mahmoud, N.A., 2008. Determination of minimum speed required for solids suspension in stirred vessels using pressure measurements. *Can. Jour. of Chem. Eng.* 86 (4), pp. 661-666.
- Sessieq P., Mier P., Gruy F. and Cournil M., 1999. Solid particles concentration profiles in an agitated vessel. *Institution of Chemical Engineers, Trans IChemE*, 77 (A), 741-746.
- Shamlou, P. A. and Koutsakos, E., 1988. Solids suspension and distribution in liquids under turbulent agitation. *Chem. Eng. Sci.*, 44 (3), 539 – 542.
- Shan, X.G., Yu, G.Z., Yang, C., Mao, Z.S., Du, L.Z., Zhang, W.. G. 2008. Dispersion characteristics of solid-liquid suspension in an unbaffled stirred tank. *Guocheng Gongcheng Xuebao/The Chinese Journal of Process Engineering* 8 (1), 1-7.
- Sharma, R.N. and Shaikh, A.A., 2003. Solids suspension in stirred tanks with pitched blade turbines. *Chem. Eng. Sci.*, 58, 2123-2140.

- Shekhar, S.M. and Jayanti, S., 2002. CFD study of power and mixing time for paddle mixing in unbaffled vessels. *Trans IChemE*, 80 (A), 482-498.
- Sheng, J., Meng, H., Fox, R.O., 1998. Validation of CFD simulations of a stirred tank using particle image velocity data, *Can. J. Chem. Eng.*, 76, 611–625.
- Shan, X. G.; Yu, G. Z.; Yang, C.; Mao, Z.-S.; Zhang, W. G., 2007. Distribution characteristics of solid-liquid suspension in an unbaffled stirred tank (in Chin.). *Chin. J. Process Eng.*, 8 (1), 1-7.
- Shan, X., Yu, G., Yang, C., Mao, Z.-S., Zhang, W., 2008. Numerical Simulation of Liquid-Solid Flow in an Unbaffled Stirred Tank with a Pitched-Blade Turbine Downflow. *Ind. Eng. Chem. Res.*, 47, 2926-2940.
- Shirhatti, V.; Wang, M.; Williams, R.; Ortega, J. R., 2006. Determination of minimum agitation speed for complete solid suspension using four electrode conductivity method. Presented at The 5th International Symposium on Measurement Techniques for Multi-phase Flows, Macau, China.
- Sinton, S.W. and Chow, A.W., 1991. NMR flow imaging of fluids and solid suspensions in Poiseuille flow. *J. Rheol.*, 35, 735.
- Smagorinsky, J., 1969. General circulation experiments with the primitive equations. I. The basic experiment, *Monthly Weather Rev.*, 91, 99–164.
- Smith, J.M., “Industrial Needs for Mixing”, 1990, *Chemical Engineering Research and Design*, 68 (1), 3-6.
- Stanley, S.J., Mann, R., Primrose, K., 2002. Tomographic imaging of fluid mixing in three dimensions for single-feed semi-batch operation of a stirred vessel. *Trans IChemE*, 80 (A), 903-909.
- Stapf, S., and Han, S., 2006. *Nuclear Magnetic Resonance Imaging in Chemical Engineering*. Wiley-VCH, Manheim.
- Stephenson, D.R., Mann, R., York, T.A., 2008. The sensitivity of reconstructed images and process engineering metrics to key choices in practical electrical impedance tomography. *Meas. Sci. Technol.*, 19, 094013 (15pp).
- Sommerfeld, M. and Decker, S., 2004. State of the art and future trends in CFD simulation of stirred vessel hydrodynamics. *Chem. Eng. Technol.* 27 (3), 215–224.
- Spidla M., Sinevic V., Jahoda M., Machon V., 2005. Solid particle distribution of moderately concentrated suspensions in a pilot plant stirred vessel. *Chemical Engineering Journal*, 113, 73-82.

- Szalai, E.S., Kukura, J., Arratia, P.E., Muzzio, F.J., 2003. Effect of hydrodynamics on reactive mixing in laminar flows. *A.I.Ch.E. Journal* 49 (1), 168–179.
- Tagawa A., Dohi N., Kawase Y., 2006. Dispersion of floating particles in aerated tank reactors: minimum impeller speeds for off-surface and ultimately homogeneous solid suspension and solids concentration profiles, *Ind. Eng. Chem. Res.*, 45, 818-829.
- Takenaka, K. and Takahashi, K., 1996. Local gas hold-up and recirculation rate in an aerated vessel equipped with a Rushton impeller. *J Chem Eng Japan*, 29: 799–804.
- Tamburini, A., Cipollina, A., Micale, G., Ciofalo, M., Brucato, A., 2009. Dense solid–liquid off-bottom suspension dynamics: simulation and experiment. *Chem. Eng. Res. Des.* 87, 587–597.
- Tatterson, G. B., 1991. *Fluid Mixing and Gas Dispersion in Agitated Tanks*. McGraw-Hill: New York.
- Tezura, S., Kimura, A., Yoshida, M., Yamagiwa, K., Ohkawa, A., 2007. Agitation requirements for complete solid suspension in an unbaffled agitated vessel with an unsteadily forward–reverse rotating impeller. *Jour. Chem. Technol. Biotechnol.*, 82, 672–680.
- Thompson, V.S., Worden, R.M., 1997. Phase hold-up, liquid dispersion, and gas-to-liquid mass transfer measurements in a three-phase magnetofluidized bed. *Chemical Engineering Science*, 52, 273-295.
- Tsuo, Y.P. and Gidaspow D., 1990. Computation of flow patterns in circulating fluidized beds. *AIChE Journal*, 36 (6), 885-896.
- Uchida, S., Okamura, S., Katsumata, T., Iida, K., 1989. Measurement of solids holdup in a three-phase fluidized bed by an ultrasonic technique. *Chemical Engineering Science* 44, 196–198.
- Unadkat, H., Rielly, C.D., Hargrave, G.K., Nagy, Z.K., 2009. Application of fluorescent PIV and digital image analysis to measure turbulence properties of solid-liquid stirred suspensions. *Chem. Eng. Res. Des.*, 87, 573-586.
- Van der Westhuizen, A.P. and Deglon, D.A., 2008. Solids suspension in a pilot-scale mechanical flotation cell: A critical impeller speed correlation. *Minerals Engineering* 21 (8), 621-629.
- Van Vliet, E., Derksen, J.J., van den Akker, H.E.A., 2000. Four-dimensional laser induced fluorescence measurements of micro mixing in a tubular reactor.

- Proceedings of the 10th European Conference on Mixing, Delft, July 2–5, pp. 45–52.
- Van Wachem, B.G.M., Schouten, J.C., Van den Bleek, C.M., Sinclair, J.L., 2001. Comparative analysis of CFD models of dense gas–solid systems. *AIChE Journal* 47, 1035–1051.
- Vatanakul, M., Zheng, Y., Couturier, M. 2004. Application of Ultrasonic Technique in Multiphase Flows. *Ind. Eng. Chem. Res.*, 43, 5681-5691.
- Vatanakul, M., Zheng, Y., Couturier, M. 2005. Ultrasonic technique for measuring phase holdups in multiphase systems. *Chemical Engineering Communications* 192 (4-6), 630-646
- Virdung, T. and Rasmuson, A., 2008. Solid-liquid flow at dilute concentrations in an axially stirred vessel investigated using particle image velocimetry. *Chem. Eng. Comm.* 195 (1), 18-34.
- Voit, H. and Mersmann, A., 1986. General statement for the minimum impeller speed during suspension. *Ger. CHem. Eng.*, 9 (2), 101-106.
- Walker, D. 1987. A fluorescence technique for measurement of concentration in mixing liquids. *J. Phys. E: Sci. Instr.*, 20, 217-224.
- Wang M., Dorward A., Vlaev D. and Mann R., 2000. Measurements of gas-liquid mixing in a stirred vessel using electrical resistance tomography(ERT). *Chemical Engineering Journal*, 77, 93-98.
- Wang, W.J., and Mao, Z.S., 2002. Numerical simulation of the whole flow field in a stirred tank with a Rushton turbine using the improved inner-outer procedure. *Chinese J. Proc. Eng.*, 2 (3), 193-198.
- Wang, F., Wang., W., Mao., Z., 2004. Numerical study of solid-liquid two-phase flow in stirred tanks with Rushton impeller. (I) Formulation and simulation of flow field. *Chinese J. Chem. Eng.*, 12 (5), 599-609.
- Warsito, W., Fan L.-S., 2001. Measurement of real-time flow structures in gas–liquid and gas–liquid–solid flow systems using electrical capacitance tomography (ECT). *Chem. Eng. Sci.*, 56, 6455–6462.
- Williams, R.A. and Beck, M.S., 1995. *Process Tomography: Principles, Techniques and Applications*. Butterworth-Heinemann, Oxford, UK.
- Williams, R.A., Jia, X., McKee, S.L., 1996. Development of slurry mixing models using resistance tomography. *Powder Technology*, 87, 21-27.

- Williams, R.A., Wang, M. 2000. Dynamic Imaging of Process Plant Reactors and Separators using Electrical Process Tomography. *Oil and Gas Science and Technology* 55 (2), 185-186.
- Witcherle, K., 1988. Conditions for suspension of solids in agitated vessels. *Chem. Eng. Sci.*, 43, 467-471.
- Wittmer, S., Falk, L., Pitiot, P. and Vivier, H., 1998. Characterization of stirred vessel hydrodynamics by three-dimensional trajectory photography. *Can J Chem Eng*, 76(3): 600–610.
- Wong, C.W., Wang, J.P., Huang, S.T., 1987. Investigations of fluid dynamics in mechanically stirred aerated slurry reactors. *Can. Jour. Chem. Eng.*, 65, 412-419.
- Xu, Y. and McGrath, G., 1996. CFD predictions of stirred tank flows. *Trans. Inst. Chem. Eng.*, 74, 471–475.
- Yamazaki, H., Tojo, K., Miyanami, K., 1986. Concentration profiles of solids suspended in a stirred tank. *Powder Technology*, 48 (3), 205-216.
- Yapici, K., Karasozen, B., Schäfer, M., Uludag, Y., 2008. Numerical investigation of the effect of the Rushton type turbine design factors on agitated tank flow characteristics. *Chem. Eng. Proc.*, 47, 1340-1349.
- Yeoh, S.L., Papadakis, G., Yianneskis, M., 2004. Numerical simulation of turbulent flow characteristic in a stirred vessel using the LES and RANS approaches with the sliding/deforming mesh methodology. *Trans. IChemE, Part A: Chem. Eng. Res. Des.*, 82, 834–848.
- Yianneskis, M., Popiolek, Z. and Whitelaw, J. H., 1987. An experimental study of the steady and unsteady flow characteristics of stirred reactors. *Journal of Fluid Mechanics*, 175, 537 555.
- Yoshida, M., Kimura, A., Yanagiwa, K., Ohkawa, A., Tezura, S., 2008. Movement of solid particles on and off bottom of an unbaffled vessel agitated by unsteadily forward-reverse rotating impeller. *Journal of fluid science and technology*, 3, 282-291.
- Zehner, P. and Tebel, K.H., 1984. Hydrodynamik beim suspendieren in Ruhrbehälter. *Mischvorgänge, Freising*.
- Zhang X, Ahmadi, G., 2005. Eulerian-Lagrangian simulations of liquid-gas-solid flows in three-phase slurry reactors. *Chem Eng Sci.*, 60, 5089-5104.

- Zheng, Y, and Zhang Q., 2004. Simultaneous measurement of gas and solid holdups in multiphase systems using ultrasonic technique. *Chem. Eng. Sci.*, 59, 3505-3514.
- Zhu, Y. and Wu, J., 2002. Critical impeller speed for suspending solids in aerated agitation tanks. *Can. Jour. Chem. Eng.*, 80, 682-687.
- Zwietering T. N., 1958. Suspending of solid particles in liquids by agitators, *Chem. Eng. Sci.*, 8, 244-253.

ACKNOWLEDGMENTS

I thank Prof. Alberto Brucato and Prof. Michele Ciofalo for their example and valuable suggestions.

I thank all the people (students, roommates, colleagues, professors, etc) who share with me something of important at the University of Palermo during these three wonderful years.

I thank Giorgio and Andrea who have been both good life-friends and fine guides for my PhD activities.

I thank my brother and all my friends for their support.

I thank my mother and my uncle Franco, who have dealt with my homely duties allowing me to devote more time to my research.

I thank Lori who has always borne me with sweetness and kindness.

Last but not least, I thank my father for his constant presence and help.